Uniwersytet Mikołaja Kopernika
Wydział Fizyki, Astronomii i Informatyki Stosowanej
Instytut Astronomii

Praca doktorska
interdyscyplinarne studia doktoranckie nauk fizycznych

Multi–wavelength observations of the outer Galaxy: Identifying the impact of environment on star formation

Ngân Thị Mỹ Lê

Promotor: **prof. dr. hab. Michał Hanasz**
Co-Promotor: **dr Agata Karska**

Toruń 2023

Pracę przyjmuję i akceptuję	Potwierdzam złożenie pracy dyplomowej
______________________	______________________
data i podpis opiekuna pracy	*data i podpis pracownika dziekanatu*

"Whatever situations you run into,
always think there is something good out there"
— Dieu Duc Nguyen

Streszczenie

Powstawanie gwiazd jest powszechnym zjawiskiem w naszej Galaktyce, ale warunki fizyczne i chemiczne w obszarach ich formowania mogą się różnić w zależności od środowiska. Przykładowo, z powodu ujemnego gradientu metaliczności, oczekuje się zmniejszonych obfitości molekuł oraz pyłu wraz z odległością od centrum Galaktyki, a w efekcie innego budżetu chłodzenia oraz efektywności powstawania gwiazd. Uważa się, że również pola magnetyczne mogą regulować proces formowania się gwiazd, a ich wpływ powinno się określać osobno dla każdego obłoku.

Celem tej rozprawy jest zbadanie znaczenia pól magnetycznych oraz metaliczności w obłokach molekularnych, w których powstają nowe gwiazdy w naszej Galaktyce. Po pierwsze, scharakteryzowana zostaje morfologia oraz wielkość pól magnetycznych w najgęstszej części pobliskiego obłoku molekularnego Oph A, a także przedyskutowana rola pól magnetycznych oraz promieniowania od pobliskiej młodej gwiazdy na proces powstawania gwiazd oraz kształt obłoku. Po drugie, zbadany zostaje wpływ metaliczności na chłodzenie w liniach w zakresie dalekiej podczerwieni u głęboko zanurzonego zgrupowania gwiazd Gy 3–7 położonej w obszarze CMa-ℓ224 w zewnętrznych częściach Galaktyki. Obliczone zostały warunki fizyczne gazu (temperatura, gęstość) w zgrupowaniu, zidentyfikowana została obecność fal uderzeniowych oświetlanych przez promieniowanie ultrafioletowe oraz scharakteryzowane młode gwiazdy. Pomimo, że spodziewana metalicznosć Gy 3–7 ma wartość pośrednią pomiędzy Wielkim Obłokiem Magellana oraz otoczeniem Słońca, to nie udało się pokazać wpływu metaliczności na procesy formowania gwiazd w tym zgrupowaniu. Podobne wnioski wynikają z ostatniej części pracy, w której zbadane zostało tempo akrecji masy przez mało- i średniomasywne młode obiekty gwiazdowe w obszarze CMa-ℓ224. Policzone zostały typy widmowe tych gwiazd oraz ekstynkcja, a także nadmiar emisji w kontinuum z powodu akrecji. Tempa akrecji masy są zgodne z tymi, które zostały wcześniej zmierzone u młodych obiektów gwiazdowych znajdujących się w pobliskich obszarach formowania gwiazd. Głównym wnioskiej z pracy jest więc potrzeba przeprowadzenia bardziej systematycznych badań zewnętrznych części Galaktyki w szerokim zakresie widma oraz metaliczności, aby móc w sposób jednoznaczny zidentyfikować wpływ środowiska na procesy postawania gwiazd.

Abstract

Star formation is ubiquitous in the Galaxy, but the physical and chemical conditions in star-forming sites might differ due to environment. For example, due to the negative metallicity gradient, abundances of molecules and dust are expected to decrease with the distance from the Galactic Center, and subsequently influence the cooling budget and efficiency of star formation. Magnetic fields (B-fields) are also believed to regulate the formation of stars, and their impact shall be quantified individually for each cloud.

This thesis aims to investigate the role of B-fields and metallicity in molecular clouds, where new stars are born in our Galaxy. Firstly, we characterize the morphology and strengths of B-fields in the densest part of a nearby molecular cloud Oph A, and discuss the role of B-fields and radiation from a nearby star in regulating star formation and shaping the cloud. Secondly, we investigate the role of metallicity on far-infrared (far-IR) line cooling in the embedded cluster Gy 3–7 located in the CMa-$\ell224$ region in the outer Galaxy. We obtain gas physical conditions (temperatures, densities) across the cluster, identify the presence of shocks irradiated by ultraviolet radiation, and characterize the population of young stars. Even though the metallicity of Gy 3–7 is expected to be intermediate between the Large Magellanic Cloud and the Solar neighborhood, we do not find the impact of low metallicity on star formation in this cluster. Similar conclusions are reached in our final investigation of mass accretion rates of low- and intermediate-mass young stellar objects (YSOs) in the CMa-$\ell224$ region. We calculate the spectral types of those young stars and extinction, as well as the excess continuum emission due to accretion. Mass accretion rates are in good agreement with those found for YSOs in the nearby star-forming regions. We conclude that a systematic, multi-wavelength study of the outer Galaxy, covering a broad range of metallicities, is necessary to confidently identify the impact of environment on star formation.

Contents

Chapter 1

Introduction

Galaxies constitute of stars, gas, dust, and dark matter. All of the baryonic matter in between stars is referred to as the interstellar medium (ISM). The ISM consists of 99% gas and about 1% solid dust grains. The most abundant components of atomic gas in the ISM are hydrogen and helium, which account for ~70% and 28% of its mass, respectively. The remaining 2% of the gas is contributed by other heavier elements (e.g., carbon, nitrogen, oxygen).

The gas in the ISM can be found in a variety of chemical forms (i.e., neutral, ionized, or molecular) in the gas phase or solid state, which are closely linked with the physical conditions (e.g., temperature, density, radiation field). In general, there are five gaseous phases of the ISM (Klessen & Glover 2016, Table 1.1): i) The warm neutral medium (WNM) consisting mainly of warm, $\sim 10^4$ K atomic gas with densities of ~ 0.5 cm^{-3}and ionization fraction of ~0.1; ii) the cold neutral medium (CNM) with temperatures of ~100 K, gas densities of a few dozen cm^{-3}, and ionization fraction of $\sim 10^{-4}$; iii) the hot ionized medium (HIM) – the component of hot ($\sim 10^6$ K), fully ionized gas with densities of ~0.01 cm^{-3}; iv) the warm ionized medium (WIM) with similar temperatures and densities as in the WNM but higher ionization; and v) the molecular gas, found in the cold and dense phase of the ISM, with temperatures of ~10–20 K, densities $\gtrsim 100$ cm^{-3}, and ionization fraction well below 10^{-4}. The conditions in the molecular gas favor the formation of stars, which is the main subject of this thesis.

Dust grains constitute about 1% of the ISM but play a fundamental role in various physico-chemical processes. In the ISM, dust grains are considered a mixture of primarily silicate and carbonaceous compounds, including polycyclic aromatic hydrocarbons (PAHs). Typical grains in the ISM have sub-micron sizes (~0.1 μm), but can significantly grow in dense gas of protoplanetary disks (Testi et al. 2014). Dust grains absorb and scatter the stellar radiation in ultraviolet (UV) and optical regimes, and subsequently, re-emit the excess energy in the infrared (IR) and (sub)millimeter domains. Thus, dust is a powerful tool to probe the properties of the dense ISM where the stars and planets form. The polarization of starlight (Hall 1949; Hiltner 1949) and polarized thermal dust emission (Hildebrand 1989) have revealed that dust grains are aspherical and partially aligned with the interstellar magnetic fields (B-fields). Thus, dust polarization has been widely used to trace magnetic fields in various astrophysical environments, from diffuse ISM to dense molecular clouds as well as in protoplanetary disks (see reviews by Draine & Weingartner

Table 1.1: Summary of physical properties of various phases of gas in the ISM. Adapted from Klessen & Glover (2016).

Component	Temperature (K)	Density (cm^{-3})	Ionization fraction
Warm neutral medium (WNM)	10^4	$\sim$0.5	$\sim$0.1
Cold neutral medium (CNM)	100	20–50	10^{-4}
Hot ionized medium (HIM)	10^6	0.01	1.0
Warm ionized medium (WIM)	10^4	$\sim$0.5	1.0
Molecular gas	10–20	$\gtrsim$100	$\ll 10^{-4}$

1997; Lazarian 2007; Andersson et al. 2015; Hennebelle & Inutsuka 2019).

1.1 Molecular clouds

Molecular gas consists primarily of molecular hydrogen (H_2), the most abundant molecule in the galaxies, and carbon monoxide (CO), which is a factor of $\sim 10^4$ less common (Frerking et al. 1982). Observations of the Milky Way have shown that molecular clouds have sizes of 1–100 pc and masses ranging from 10^2 to 10^6 solar masses ($M_\odot$), with typical volume densities from 10 to 1000 cm^{-3} (Duarte-Cabral et al. 2021). One of the earliest theories of the formation of the molecular cloud is based on the coagulation model, where collisions of smaller discrete clouds can lead to the coagulation of small molecular clouds to form a larger cloud (Oort 1954). This model, however, was not able to explain the formation of so-called Giant Molecular Clouds (GMCs) with $M \gtrsim 10^5 M_\odot$ that need $\geq$100 Myrs to form, much longer than their age (Blitz & Shu 1980). The converging flow model, on the other hand, collisions between the flows of low-density gas can lead to thermal instability to form a denser molecular cloud (see, e.g., Klessen & Glover 2016, and references therein).

Observations of molecular clouds attempted to reveal the relationship between the properties of molecular clouds, i.e., the size, mass, and internal velocity dispersion of the cloud. The empirical relations between these properties were first proposed by Larson (1981), and are referred to as the "Larson's relations":

$$\sigma = 1.1\mathcal{R}^{0.38}, \tag{1.1}$$

$$\sigma = 0.42M^{0.2}, \tag{1.2}$$

where $\mathcal{R}$ (pc), M ($M_\odot$), and σ (km s^{-1}) are the size, mass, and velocity dispersion of the molecular cloud, respectively. Similar power-law relations between the size of the cloud and its velocity dispersion were found for the lower-mass regions (Solomon et al. 1987), and are given as:

$$\sigma \propto \mathcal{R}^{0.5}. \tag{1.3}$$

The velocity dispersion in high-mass star-forming regions follows the relation (Caselli & Myers 1995):

$$\sigma \propto \mathcal{R}^{0.21}. \tag{1.4}$$

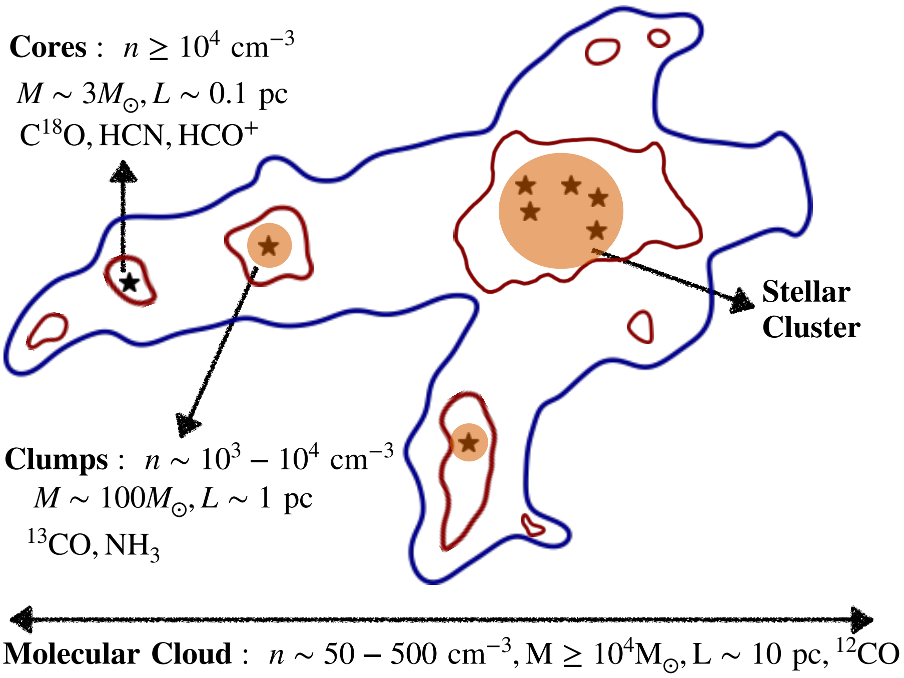

Figure 1.1: Cartoon of hierarchical structures within a molecular cloud with the information about their gas density, masses, sizes, and main tracers used for observations. The structures are not drawn to scale.

Turbulence is highly supersonic on scales of the GMCs and thus can inject energy into the cloud, causing fragmentation, and subsequent formation of dense structures on smaller scales. High-resolution far-infrared (far-IR) observations with *Herschel* (Pilbratt et al. 2010)) revealed hierarchical sub-structures within molecular clouds: filaments, clumps, and dense cores. Filamentary structures of the dense gas have lengths of a few up to ten pc and widths of ~0.1 to a few tenths parsecs (see e.g., André et al. 2010; Arzoumanian et al. 2011). Clumps are the dense ($n \sim 10^3 - 10^4$ cm^{-3}) sub-structures in the molecular cloud with the typical sizes of 0.1–3 pc and masses of 50–500 $M_\odot$, from which an assembly of stars (stellar cluster) can be formed (Bertoldi & McKee 1992). Dense cores have densities of $\sim 10^5$–10^6 cm^{-3}and sizes ranging from 0.01 to 0.1 pc; they are the sites of the formation of a single or multiple stars (Benson & Myers 1989). When there is no evidence of star formation in a core, the structure is referred to as a starless core, otherwise, it is called the prestellar core. Cores which already possess the embedded young stellar objects (YSOs) are referred as protostellar cores. The sub-structures of a molecular cloud are illustrated in Figure 1.1.

1.1.1 Collapse of dense cores

Inside cold regions of molecular clouds, gravitational instability can lead to the collapse of the densest structures and the formation of a new star. Jeans (1928) showed that a uniform isothermal core must have a minimum mass ($M_{\rm J}$) above which the internal thermal pressure can no longer support the material against gravity and the core can undergo the self-gravitational collapse. This critical value of mass is the so-called Jeans mass and is given as:

$$M_{\mathrm{J}} = \frac{4\pi c_{\mathrm{s}}^{3}}{3\sqrt{\rho G^{3}}}, \tag{1.5}$$

where ρ is the gas volume density, $c_{\mathrm{s}} = \sqrt{k_{\mathrm{B}}T/(\mu m_{\mathrm{H}})}$ is the isothermal sound speed of the gas corresponding to a uniform temperature T, k_{B} is the Boltzmann constant, μ is the mean molecular weight per hydrogen molecule, and m_{H} is the mass of a hydrogen atom. However, there are other internal factors providing support against the collapse. For example, magnetic fields (B-fields) provide magnetic pressure and turbulence can inject the non-thermal kinetic energy to destroy the over-dense regions. Radiative and mechanical feedback from external sources can also influence the gravitational collapse.

The dynamical state of a dense core can be analyzed using the virial theorem (Chandrasekhar & Fermi 1953). Assuming that the dense core is an isothermal sphere of a radius R, a gas volume density ρ, and a uniform temperature T, the core is in a state of virial equilibrium if the internal thermal (E_{th}), kinetic (E_{kin}), magnetic (E_{mag}), and gravitational potential (E_{grav}) energies within the core follow the relation:

$$2\left(E_{\mathrm{th}} + E_{\mathrm{kin}}\right) + E_{\mathrm{mag}} + E_{\mathrm{grav}} = 0. \tag{1.6}$$

The spherical core with a mass of $M = \frac{4}{3}\pi\rho R^{3}$ posses a gravitational potential energy of:

$$E_{\mathrm{grav}} = -\frac{3GM^{2}}{5R}. \tag{1.7}$$

The internal thermal and kinetic energy due to motions of the gas within the core can be expressed as:

$$E_{\mathrm{th}} + E_{\mathrm{kin}} = \frac{3M}{2}\left(\frac{k_{\mathrm{B}}T}{\mu m_{\mathrm{H}}} + \sigma^{2}{}_{\mathrm{NT}}\right) = \frac{3M}{2}\left(c_{s}^{2} + \sigma^{2}{}_{\mathrm{NT}}\right), \tag{1.8}$$

where σ_{NT} is the non-thermal velocity dispersion of the gas within the core, constituting the turbulence contribution. The B-fields with the strength of B will exert pressure of:

$$P_{\mathrm{mag}} = \frac{B^{2}}{8\pi}, \tag{1.9}$$

and are associated with the Alfvénic velocity given as:

$$v_{\mathrm{A}} = \frac{B}{\sqrt{4\pi\rho}}. \tag{1.10}$$

As a result, Eq. 1.6 can be written as:

$$3M\left(\frac{k_{\mathrm{B}}T}{\mu m_{\mathrm{H}}} + \sigma^{2}{}_{\mathrm{NT}}\right) - \frac{1}{R}\left(\frac{3}{5}GM^{2} - \frac{1}{3}B^{2}R^{4}\right) = 0 \tag{1.11}$$

If the left-hand side of Eq. 1.11 is negative, i.e., gravity is able to take over the total internal pressures within the core, the core will become gravitationally unstable and eventually undergo the self-gravitational collapse. Conversely, the core is gravitationally stable and might expand due to the dominant internal pressure if the term has a positive value. The virial mass is defined as the critical mass needed for the core to leave the equilibrium state:

$$M_{\mathrm{vir}} = \frac{5R}{G}\left(c_{s}^{2} + \sigma_{\mathrm{NT}}^{2} + \frac{v_{A}^{2}}{6}\right). \tag{1.12}$$

The virial parameter, which is the ratio between the virial and isothermal mass of the core

($M_{\rm iso}$), $\alpha_{\rm vir} = M_{\rm vir}/M_{\rm iso}$, can be used to characterize the gravitational stability of the cores. If a core exhibits $\alpha_{\rm vir} \lesssim 1$, then gravity overcomes the other factors and the core becomes gravitationally unbound and will collapse. Otherwise, the core is gravitationally bound and it will not collapse unless an additional factor changes the conditions in the core so that the contraction may occur.

1.1.2 Role of magnetic fields

Magnetic fields (B-fields) are believed to play an important role in the evolution of the molecular cloud and also in the star formation process, by supporting against the self-gravitational collapse (see e.g., Shu et al. 1987; Mouschovias 2001; Crutcher 2012; Hennebelle & Inutsuka 2019; Pattle & Fissel 2019; Pattle et al. 2022a). In Eq. 1.11, if we consider only gravity and B-fields support in the core, the critical mass for which the magnetic flux induced by B-fields ($\phi_B = B\pi R^2$) is still able to support against gravity, can be given by the mass-to-magnetic-flux ratio (Nakano & Nakamura 1978):

$$\left(\frac{M}{\phi_B}\right)_{\rm crit} = \frac{1}{2\pi\sqrt{G}}. \tag{1.13}$$

The relative importance of B-fields compared to gravity in the core can be quantified by the determination of the mass-to-magnetic-flux ratio, λ, which is in units of the above critical ratio $(M/\phi_B)_{\rm crit}$, introduced by Crutcher (2004):

$$\lambda = \frac{(M/\phi)_{\rm observed}}{(M/\phi)_{\rm crit}} = 7.6\times10^{-21}\frac{N({\rm H_2})}{B}, \tag{1.14}$$

where $N(\rm H_2)$ is $\rm H_2$ column density in units of cm^{-2} and B is in units of μG. If $\lambda > 1$, the core is magnetically super-critical, meaning that B-fields are not strong enough to prevent gravity; the collapse can generally occur in the dense core leading to the formation of protostars. Conversely, if λ<1 the core is then magnetically sub-critical and the B-fields are sufficient to support the matter against gravitational collapse. However, several mechanisms might enhance the mass-to-flux ratio in the strong B-fields region. In the magnetically dominated dense core with a typically low ionization fraction, neutral gas is well-coupled with the ion particles which are frozen into the B-field lines. The drifting of the neutral-ion particles along the B-field lines will slowly enhance the gas mass density in the core until the core itself reaches the critical mass-to-magnetic-flux ratio. Eventually, the collapse starts to occur in the core (ambipolar diffusion; see e.g., Mouschovias et al. 2006; Liu et al. 2022). In turbulent regions, on the other hand, the fast reconnection of turbulence might also reduce the magnetic energy, which increases the mass-to-magnetic-flux ratio. Eventually, the core will become magnetically super-critical and collapse (magnetic reconnection diffusion, Lazarian & Vishniac 1999).

B-fields are also believed to play an essential role during the formation of the protostellar system after the first collapse of the prestellar core, for which B-fields help transfer angular momentum from the envelope to the inner part of the system and aid in facilitating the growth of central stellar objects (Shu et al. 1987; Frank et al. 2014a). Particularly, strong B-fields in the core produce magnetic tension, acting on the matter from the surrounding envelope that is falling and rotating. This tension can create a strong magnetic torque able to remove the angular momentum in the collapsing fluids and transfer it out-ward via the bipolar energetic jets and outflows.

Since the discovery of starlight polarization (Hall 1949; Hiltner 1949), dust grains appear to have aspherical shapes and are aligned preferably with the B-field direction in the medium. Measuring and characterizing B-fields are challenging since the 3D structure and strengths of B-fields in molecular clouds are not completely observable. There are a few methods used to probe interstellar B-fields today. The strengths of B-field along the light-of-sight ($B_{\rm los}$) and projected on the plane-of-sky ($B_{\rm pos}$) can be directly measured via the Zeeman splitting of spectral lines for (for e.g., H I, OH, or CN, see Crutcher & Kemball 2019, for a review). However, this method is difficult to perform due to the calibration challenge and long time of observations. Faraday rotation and synchrotron polarization are two techniques used to probe B-fields but likely not relevant in star formation studies. Thermal dust emission polarization is useful to trace the morphology of B-fields on the plane-of-sky in diverse astrophysical environments, from the diffuse medium (for e.g., Planck Collaboration et al. 2015) to dense molecular clouds (for e.g., Fissel et al. 2016; Ward-Thompson et al. 2017; Chuss et al. 2019; Coudé et al. 2019; Arzoumanian et al. 2021; Kwon et al. 2022), dense cores (for e.g., Sadavoy et al. 2019; Pattle et al. 2021), and also in the extra-galactic regimes (Lopez-Rodriguez et al. 2021, 2022; Borlaff et al. 2023). Polarimetric instruments have been developed for decades, especially in the far-IR and (sub)mm regime, such as *Planck* satellite (Lamarre et al. 2010), BLASTPol (Galitzki et al. 2014), JCMT/POL-2 POL-2 polarimeter (Friberg et al. 2016), ALMA (Cortes et al. 2016), SMA (Primiani et al. 2016), SOFIA/HAWC+ (Harper et al. 2018) together with the optical and near-IR polarimeters; for e.g., AIMPOL on Sampurnanand telescope (Rautela et al. 2004), IRSF/SIRPOL (Kandori et al. 2006), and Mimir on the Perkins Telescope (Clemens et al. 2007).

It has been observed that the diffuse ISM are magnetically sub-critical where the B-fields are typically strong and able to support the matter against gravity. In contrast, the molecular clouds are more likely magnetically super-critical, and thus the B-fields cannot confront gravity. Observations of B-fields in various diffuse medium and dense molecular clouds have shown that the mean value of the strength of B-fields in the diffuse region remains constant with the gas number density $\rm n_H$ <300 $\rm cm^{-2}$, while it is seen to increase with gas density in the denser region with $\rm n_H$ >300 $\rm cm^{-2}$ (Crutcher et al. 2010). Crutcher et al. (2010) also showed that these B-field strengths in were proportional to $\rm n_H^{\it k}$ with the power-law index k is 0.65. On the other hand, theoretical studies have suggested that this power-law index k varies between weak (~2/3, Mestel 1966) and strong B-fields ($\lesssim$0.5, Mouschovias & Ciolek 1999). Thus, to understand in detail the role of B-fields on smaller scales, we need to use the observations with higher resolution (e.g., JCMT/POL-2, SOFIA/HAWC+, and ALMA) to probe B-fields in dense regions such as the dense cores.

1.2 Low-mass star formation

As shown in Eq. 1.11, once gravity dominates over the turbulence and B-fields in the dense core, the core will leave the hydrostatic equilibrium and start to collapse under its own gravity. The formation of a low-mass star can be then described by the following main phases.

During the so-called *prestellar phase*, the dense core starts to collapse under its own gravity. Larson (1969) first performed a numerical model of the collapse in cores.The collapse proceeds isothermally and the energy of the core produced by the gravitational contraction can be radiated away mainly via the thermal emission of dust, as a blackbody with T ~10–20 K. After ~4×10^5 years, the inner region of the core has densities of 10^{-13} g cm^{-3}. At this point, the dust in the core becomes completely optically thick and no longer freely radiate energy away. Consequently, the gas in the core center is heated up adiabatically, and the temperature of the core increases. As the collapse slows down, over the next few thousand years, the center of the core reaches its hydrostatic equilibrium, forming the first hydrostatic core. The core has a typical size of about 4 AU, a temperature of ~100–200 K, and a volume density of ~ 10^{-10} g cm^{-3}. The lifetime of the first hydrostatic core is short, about 10^3 years, which makes its observation statistically unfavorable. After the formation of the first hydrostatic core, the central core accretes material from the surrounding envelope, while the envelope collapses under self-gravity. The temperature of the core reaches 2000 K, at which point the dissociation of the molecular hydrogen (H_2) begins, leading to a second phase of collapse. Eventually, this ends up with the formation of the second hydrostatic core, which is a protostar with a size of 0.01 AU and a volume density of ~1 g cm^{-3}. The infalling gas becomes supersonic and the shock front forms in the outer edge of the protostellar core.

The protostellar core enters the *protostellar phase*, also called the *accretion phase* or *embedded phase* with a system consisting of a dusty envelope component with an accreting disk and a central hydrostatic object (protostar) which are embedded in the circumstellar envelope. Due to the angular momentum conservation in YSOs, the centrifugal force forms the rotating accretion disk of dust and gas. The B-fields provide magneto-centrifugal force which acts to reduce the angular momentum of the disk and thus launches the bipolar, collimated jets along the rotational axis.

The mass of a YSO is initially dominated by its envelope. The material is accreted onto the central object from the surrounding envelope at a high accretion rate. The material of the envelope is entrained by the powerful outflows, which carve out wide-angle cavities and partly dissipate the envelope. During the protostellar phase, YSOs are divided into Class 0 and I phases based on the relative mass of the envelope with respect to that of the central object (see details in Section 1.2.1).

After ~ 2×10^5 years, the envelope disappears, and the system reveals a star surrounded by a protoplanetary disk where planets can form. The star still accretes some mass from the disk; its mass dominates the mass of the YSO. At that point, the star already moves to the *pre-main sequence phase*. Such YSOs are divided into Class II and Class III based on the evidence of the accretion process.

After another 10^5 years, the central star accumulates most of its final mass and slowly undergoes further contraction and heating until it reaches a stable equilibrium at ~ 10^8 K. Then, the hydrogen fusion begins and the star enters the main sequence.

1.2.1 Evolutionary sequence of low-mass stars

YSOs are classified based on the shape of their spectral energy distributions (SEDs). Figure 1.2 illustrates the evolutionary sequence of a YSO from the pre-stellar phase to

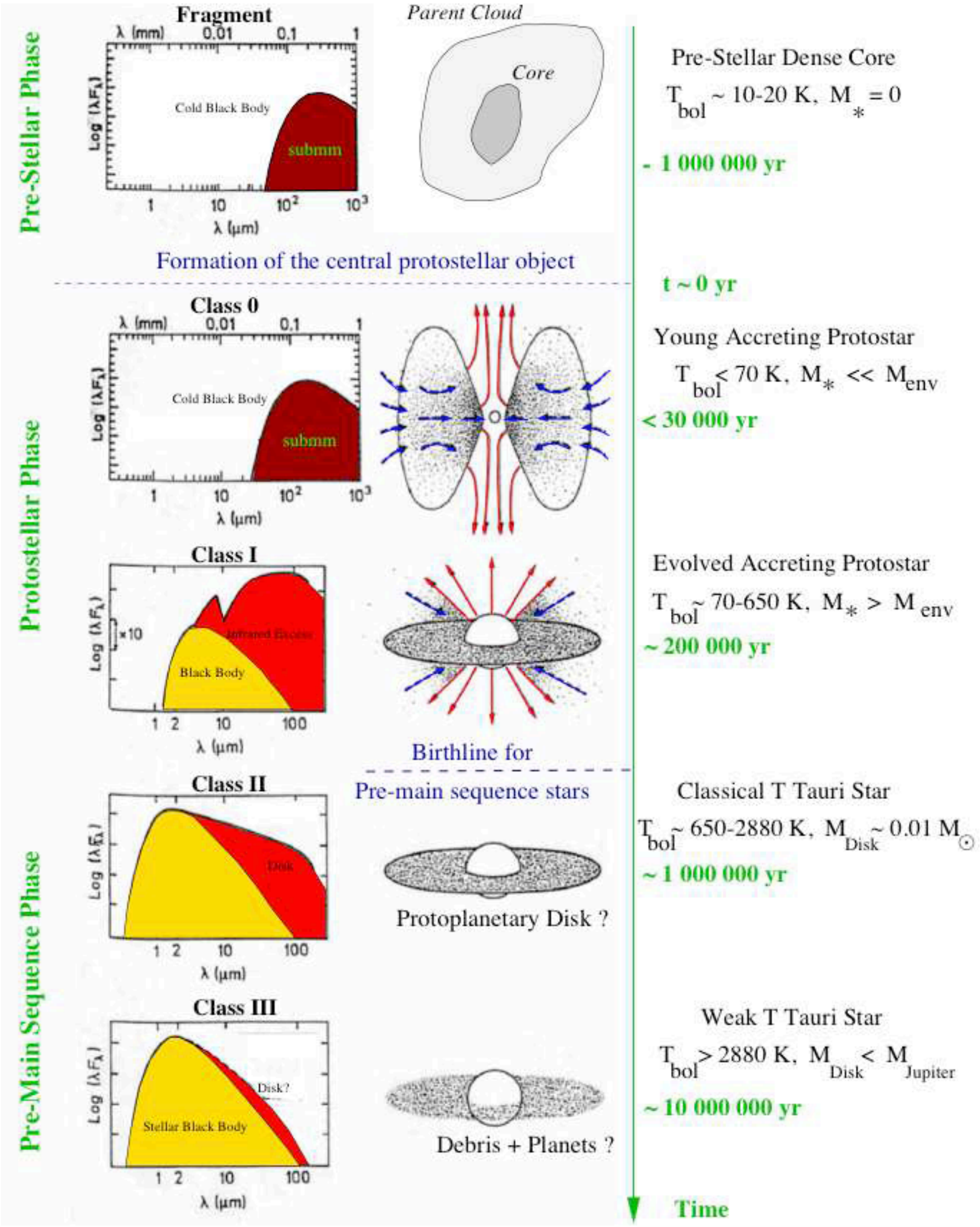

Figure 1.2: Schematic view of the evolution of a low-mass young stellar object with their corresponding SEDs. Adapted from André (2002).

pre-main sequence phase.

Class 0 object is the least evolved object formed when the prestellar core enters the protostellar phase (Andre et al. 2000). At this stage, the central object and the accretion disk are completely embedded in the dusty envelope. The mass of the envelope is much larger than that of the central object ($M_{\mathrm{env}} \gg M_{\star}$) and its bolometric luminosity is dominated by accretion luminosity. The YSO is invisible in the near and mid-IR range, with SED peaking at (sub)millimeter wavelengths, where most of the emission from the cold, dusty envelope is radiated away. The accretion of material is accompanied by the ejection of energetic bipolar jets and outflows along the rotational axis (Frank et al. 2014b). The system is characterized by a bolometric temperature $T_{\rm bol}$ <70 K. Its lifetime is approximately a few 10^4 years (Evans et al. 2009).

Class I object is associated with the evolved accretion phase. The material from the envelope has been mostly accreted onto the protostar and thus, the mass of the stellar object becomes larger than that of the envelope ($M_\star > M_{\rm env}$). The outflows become less collimated and less massive (Frank et al. 2014b).More and more radiation from the protostar can escape the system, and the SED shows evidence of the stellar radiation and excess IR emission from a massive, embedded disk. The Class I YSOs have typical $T_{\rm bol}$ in the range from 70 to 650 K and ages of the order of 10^5 years (Evans et al. 2009).

Class II object (or Classical T Tauri star) is optically visible since by the time the envelope has completely disappeared. The system is composed of a star and a protoplanetary disk forming planets (Testi et al. 2014). The peak of the SED is shifted toward the optical wavelengths and shows the excess IR emission from the disk with $M_{\rm disk}$ ~$0.01 M_\odot$. The central star still accumulates mass from the disk and starts to appear on the birthline of the Hertzsprung–Russell (HR) diagram. The object has $T_{\rm bol}$ in the range from ~650 to2880 K and a lifetime of about 1–4 Myrs (Lada 1999).

Class III object (or Weak T Tauri star) is the most evolved young star that approaches the Main Sequence. Its SED peaks in the optical wavelength and shows a very small IR excess due to the gas-poor debris disk. The source has a typical $T_{\rm bol}$>2880 K and lifetime of about 1-10 Myrs (Lada 1999).

1.2.2 Mass accretion

The bolometric luminosity of the protostellar system can be estimated as: $L_{\rm bol} = L_\star + L_{\rm acc}$, where $L_\star$ is the luminosity from the stellar object and $L_{\rm acc}$ is the accretion luminosity, the product of mass accretion onto the star-disk system. At the earliest stages of star formation, the bolometric luminosity is dominated by accretion, $L_{\rm bol} \approx L_{\rm acc}$. The $L_{\rm acc}$ can be converted into the mass accretion rate, $\dot{M}_{\rm acc}$, if the mass and radius of the stellar object are known (Gullbring et al. 1998; Hartmann 1998):

$$\dot{M}_{\rm acc} = \left(1 - \frac{R_\star}{R_{in}}\right)^{-1} \frac{R_\star}{GM_\star} L_{\rm acc} = 1.25 \frac{R_\star}{GM_\star} L_{\rm acc}, \tag{1.15}$$

where $R_\star$ and $M_\star$ are the stellar radius and mass, $\rm R_{in}$ is a truncated inner disk radius, assumed to be $\sim 5 \rm R_\star$ (Gullbring et al. 1998).

The magnetospheric accretion model is a current paradigm describing the mass accretion process in the YSOs (Uchida & Shibata 1985; Shu et al. 1994). The model predicts that the material from the vicinity of the inner disk can be channeled along the B-field lines and accumulated onto the central stellar object. The accretion shocks on the stellar surface can lead to the formation of hydrogen recombination and atomic lines (e.g., [O I], [Ca II]) (Muzerolle et al. 2003) along the accretion funnel flow. The experimental relationship between these emission lines and the accretion luminosity follows the relation (see e.g., Muzerolle et al. 1998; Calvet et al. 2004):

$$\log(L_{\rm acc}) = -0.7 + 0.9(\log(L_{\rm Br\gamma}) + 4), \tag{1.16}$$

$$\log(L_{\rm acc}) = 1.8 + 1.03 \log(L_{\rm Pa\beta}). \tag{1.17}$$

The accretion rates differ between stages of the evolution of the young stellar objects, and are the largest during the Class 0 phase, $\dot{M}_{\rm acc}\sim 10^{-6} - 10^{-5}\ M_\odot\ {\rm yr}^{-1}$ (Bontemps et al. 1996). During the Class II phase, the accretion rates are much lower ($\lesssim 10^{-7}\ M_\odot\ {\rm yr}^{-1}$) and there is no evidence of mass accretion in Class III sources (see e.g., Andre et al. 2000).

1.2.3 Jets and outflows

The gravitational collapse of dense cores is accompanied by the accretion of matter from the surrounding envelope onto the star-disk system. A fraction of accreted matter is ejected in the form of bipolar jets and wider-angle outflows in the direction parallel to the rotational axis of the disk. Such ejections alter the physical conditions and chemistry of the protostellar environment even on clump scales (Arce et al. 2007; Frank et al. 2014a).

Jets contain both atomic and molecular gas components and are characterized by velocities as high as $v \gtrsim 100$ km s^{-1}. Outflows, created by both jets and winds, are mostly molecular, slower, and less collimated.Jets and outflows interact with the surrounding medium creating non-dissociative shock waves (Kaufman & Neufeld 1996; Flower & Pineau des Forêts 2012), which heat up the gas up to typically ~300 K (Karska et al. 2018; Yang et al. 2018).Additionally, UV photons generated by the accretion in the central region of a YSO can contribute to the gas heating and influence the chemical composition of the envelopes of low- to high-mass protostars (Bruderer et al. 2009; Visser et al. 2012). The stronger the UV radiation fields, the larger post-shock temperature of the gas at a

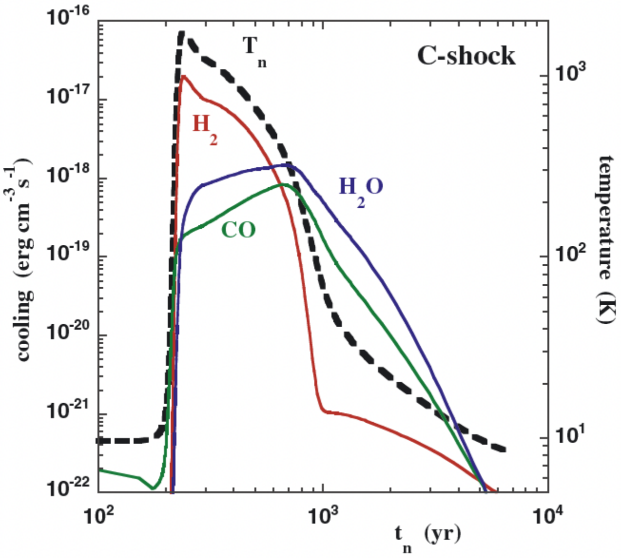

Figure 1.3: Time evolution of gas temperature (black dashed line) and cooling rates of the main molecular coolants: H_2(in red), H_2O (in blue), and CO (in green) assuming a non-dissociative C-shock propagating with velocity of v=20 km s^{-1}in the medium with pre-shock H_2 density of $n_{\rm H}=2\times10^4$ cm^{-3}. Adapted from Flower & Pineau Des Forêts (2010).

given shock velocity and gas density (Melnick & Kaufman 2015). This has a significant impact on the gas composition and molecular excitation.

A variety of tracers can be used to probe jets and outflows in the protostellar system. For instance, high J−CO transitions, SiO, H_2O, and shocks-excited H_2 lines are usually the proxies of warm gas in the molecular outflows (Fukui et al. 1993; Nisini et al. 2007, 2013, see also Figure1.3). Near-IR emission of atomic hydrogen lines or forbidden transitions of [S I], [O I], [O II], and [N II], as well as the emission of H_2 and [Fe II] are common tracers of atomic and ionized gas components of outflows (Garcia Lopez et al. 2010). Inner parts of the jets can be also studies in the radio continuum emission tracing free-free and even synchrotron emission(Rodríguez-Kamenetzky et al. 2016; Tychoniec et al. 2018b,a).

The cooling of the gas, which in the case of embedded objects is dominated by line emission in the far-IR and (sub)millimeter domains (for e.g., high J−CO, H_2O, OH, [O I], or [C II]), provides important constraints on the heating mechanisms. Observations of these cooling lines allow us to constrain gas temperatures, densities, and UV fields (Goldsmith & Langer 1978; Hollenbach & McKee 1989).

1.3 Star formation in the outer Galaxy

Star formation is ubiquitous in the Galaxy but may differ with physical and chemical conditions in various environments. Star formation in our Galaxy occurs mainly in giant molecular clouds (GMCs) and seems to be quite uniformly distributed in its inner parts

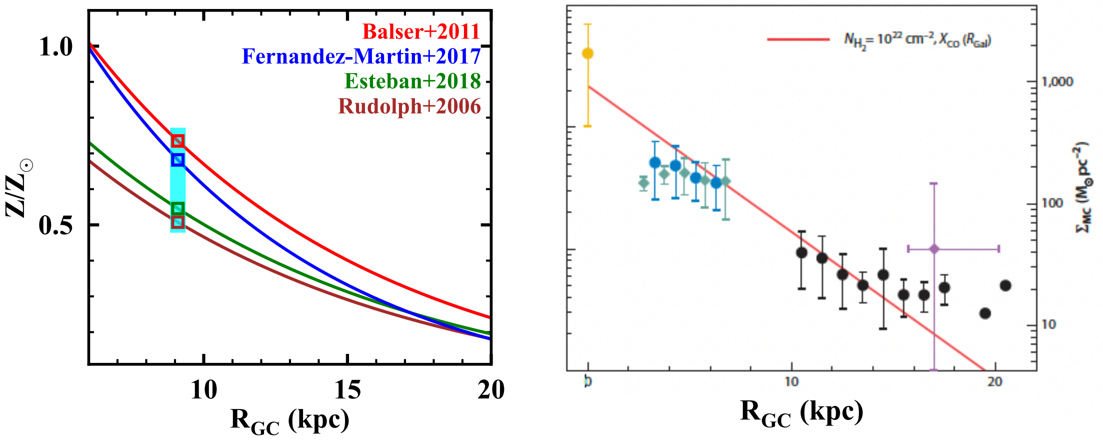

Figure 1.4: Trends of metallicity (Z) and the mass surface density (Σ_{MC}) of molecular clouds with respect to the Galactocentric radius (R_{GC}). *Left:* Metallicity as a function of Galactocentric radius, calculated using various relations of O/H gradients inferred from the H II regions. The small squares indicate the metallicity calculated in CMa-ℓ224 region using the relation of O/H gradients derived from the specific studies mentioned in the top right corner of the plot. The cyan box indicates the range of metallicity found in CMa-ℓ224 cloud, ~0.55–0.73 $Z_\odot$ derived among all the methods. *Right:* The mass surface density of molecular clouds as a function of the Galactocentric radius, adapted from Figure 8 in Heyer & Dame (2015).

despite the preferential formation of clouds in the spiral arms (Urquhart et al. 2021). Due to the negative-metallicity gradient, the Galactic surface mass density of molecular clouds, i.e., the abundances of dust and molecules decrease in the outer Galaxy (Sodroski et al. 1997; Heyer & Dame 2015, see also in Figure 1.4). The metallicity affects the gas and dust cooling budget of molecular clouds.

Despite the overall decreasing trend of the mass surface density of molecular clouds in the outer Galaxy (for a review, see Heyer & Dame 2015), some star-forming regions show significant star-formation activity. Additional environmental factors such as interstellar radiation field and cosmic-ray flux alter the physical conditions in clouds e.g., by decreasing gas and dust temperatures in distant clouds (Roman-Duval et al. 2010). All in all, the gas in the outer Galaxy is mostly atomic and the star formation seems to be rather sparse (Kennicutt & Evans 2012).

1.4 Star forming regions studied in this thesis

1.4.1 Oph–A

The Oph-A is located in the northern part of the L1688 active star-forming region in the ρ Ophiuchus dark cloud complex (Loren et al. 1990; Wilking et al. 2008; Esplin & Luhman 2020). The star formation activity in the L1688 is believed to be affected by the Sco OB2 association located at the western part of the cloud at a distance of ~145 pc (de Zeeuw et al. 1999). The Oph–A region was initially identified as a dense gas clump based on DCO^+ observations performed by Loren et al. (1990) among other clumps named from Oph–B to Oph–F. Oph–A has high extinction ($A_V \gtrsim 20$ mag) corresponding to the high H_2 column densities compared to other regions which are typically more quiescent (see left panel in Figure 1.5). Being one of the closest star-forming regions in our Galaxy, located at a distance of ~137 pc (Ortiz-León et al. 2017), the gas and dust content in Oph–A region has been studied extensively at almost every wavelength by both ground-based and space instruments for many years (see e.g., Wilking et al. 2008, for a review).

The Oph–A region hosts numerous starless, prestellar, and protostellar cores and protostars in various evolutionary stages (Motte et al. 1998; Pattle et al. 2015; Enoch et al. 2009; Ladjelate et al. 2020). Many YSOs in Oph–A show excess emission in the near-IR wavelength, indicating that Oph–A is a very young low-mass star-forming region with an age likely less than 1 Myr (Bontemps et al. 2001). The region also reveals some remarkable outflows from young stars seen by molecular tracers (e.g., CO 2–1 Andre et al. 1990).

The Oph–A molecular cloud is located in the vicinity of a high-mass B3/4 star (Brown & Zuckerman 1975; Mookerjea et al. 2018), Oph S1 or so-called S1, which has a mass of ~$8M_\odot$ (Hamaguchi et al. 2003). Also, the S1 star is surrounded by a compact H II region (Andre et al. 1988) and is believed to trigger the star formation activity in Oph–A, especially along the ridge of the dense cloud with indications of protostellar clumps (see Figure 2a in Motte et al. 1998). With the very short projected distance from the peak of H_2 column density to the S1 star of ~0.065 pc, material in Oph–A is heated mainly by the ionized radiation coming from the S1 star. However, the radiation cannot penetrate deeper toward the western side of the cloud due to the denser material surrounding the

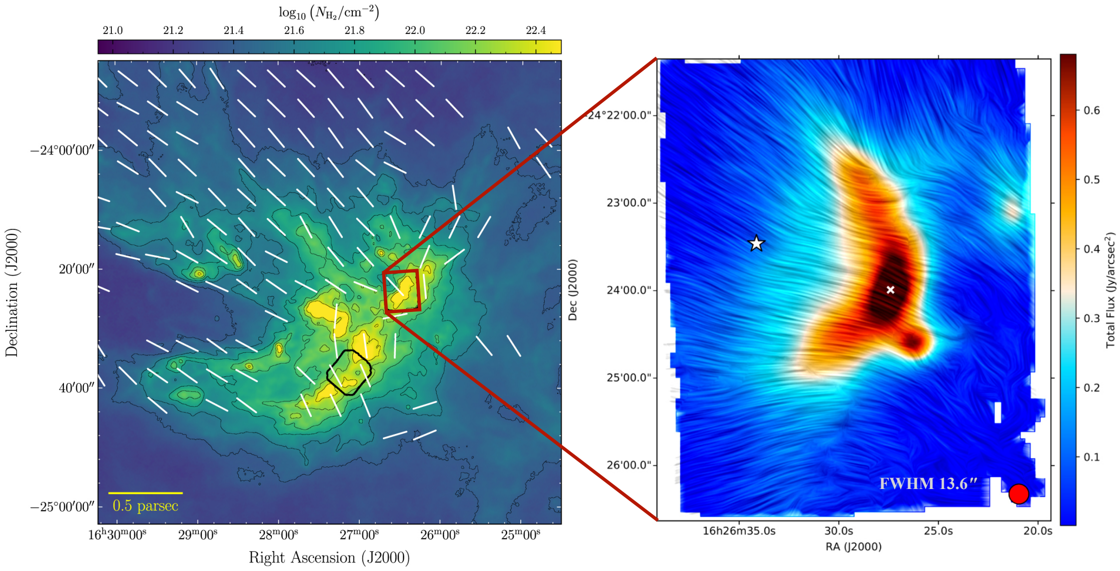

Figure 1.5: *Left:* Map the H_2 column density (N_{H_2}) in the L1688 active star-forming region hosting the Oph–A cloud with the white segments indicating the inferred B-field orientation observed with Planck at 353 GHz. Black contours are also the H_2 column density in units of $\log_{10}(N_{H_2})$ with the highest level at 22.4 and decreasing in steps of 0.2. Adapted from Lee et al. (2021). The red rectangle corresponds to the Oph–A cloud with its area zoomed in the right panel. *Right:* Continuum map of the Oph–A cloud observed with SOFIA/HAWC+ at 154 μm with the streams illustrating the inferred B-field orientation from SOFIA/HAWC+. The star and 'x' symbols show the position of the S1 high-mass star and the peak of (N_{H_2}) in Oph–A. Adapted from Santos et al. (2019).

cloud (see e.g., Figure 1 in Mookerjea et al. (2018)), resulting in a clumpy morphology of the cloud and a ridge structure(see right panel in Figure 1.5).

Figure 1.5 shows the map of the H_2 column density in the L1688 star-forming region which hosts the Oph-A dense molecular cloud (left panel, Lee et al. 2021) and a zoom-in view of the Oph–A region (right panel, Santos et al. 2019) representing the continuum emission at 154 μm superimposed by the inferred B-field orientation observed from SOFIA/HAWC+ toward Oph–A. The B-field orientation is generally well-ordered and likely bent perpendicularly to the ridge of the cloud toward the higher-density regime. Thus, this region provides an ideal isolated system to study the impact of the B-fields in the star-forming region and to investigate the interplay between the B-fields and the stellar radiation feedback onto the cloud. We will present our results of mapping the B-fields morphology and strengths toward the Oph–A cloud and the role of B-fields in star formation and evolution in Chapter 3.

1.4.2 CMa–ℓ224

The CMa-ℓ224 region, located at the longitude of ~224° at the northern part of the Canis Major (CMa) region, is the most prominent star-forming region within the third Galactic quadrant uncovered by The Warm Spitzer Exploration Science Program "GLIMPSE360:

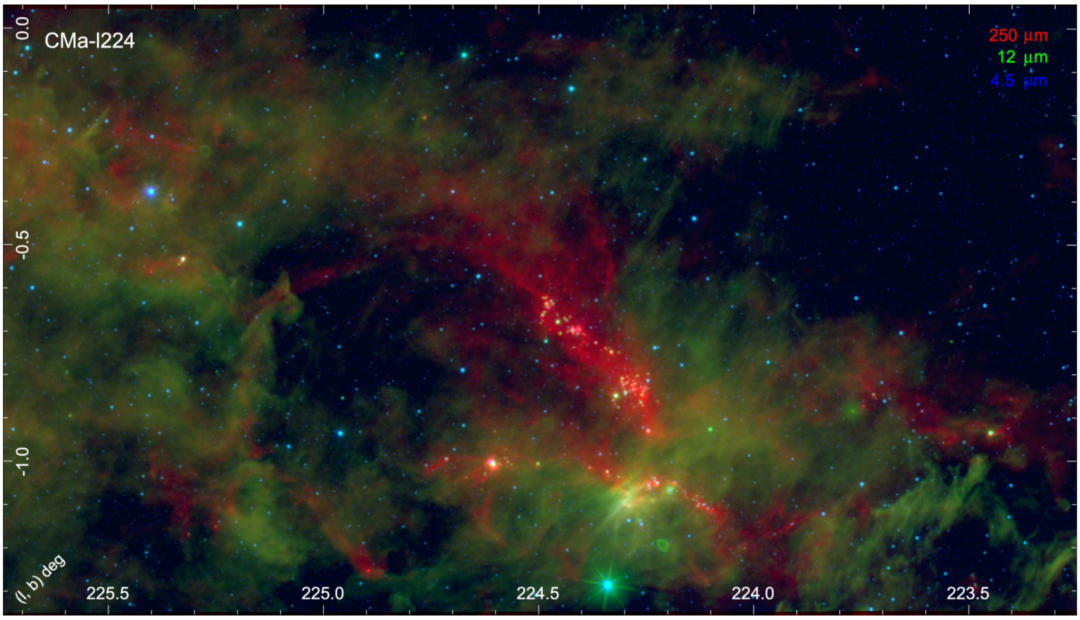

Figure 1.6: Three-color composite image of CMa-ℓ224 region combining the *Herschel*/Hi-GAL SPIRE 250 μm (red), WISE 12 μm (green), and *Spitzer*/GLIMIPSE360 IRAC 4.5 μm (blue) mosaics. Adapted from Sewiło et al. (2019).

Completing the Spitzer Galactic Plane Survey". The CMa-ℓ224 star-forming region lies in the boundary of the CMa OB1 association (Ruprecht 1966) and at the northern part of the very large H II region Sh 2-296 (Sharpless 1959) which belongs to the CMa R1 association, together with the other nearby H II regions (S293, S295, and S297; see e.g., Figure 1 in Sewiło et al. (2019) and references therein). The distance to CMa-ℓ224 is determined in the range of ~0.5–1.3 kpc, with a median value of ~0.92 kpc (Sewiło et al. 2019), corresponding to a Galactocentric distance of ~9.1 kpc (Claria 1974). The region is predicted to have a relatively low metalicity, of $\sim 0.55 - 0.73\ Z_{\odot}$ (Itrich et al. 2023; see also left panel in Figure 1.4).

The star formation activities in CMa-ℓ224 are believed to be triggered by the supernova explosion in the CMa OB1 association (Herbst & Assousa 1977; Nakano et al. 1984), revealed by a large-scale expanding ionized Hα gas emission shell. The CMa-ℓ224 region is seen especially bright in the 4.5 μm emission (see Figure 1.6), which most likely comes from the emission of the H_2 lines generated by the outflow shocks from early embedded protostars (see e.g., He et al. 2012; Cyganowski et al. 2013). Recently, large-scale outflow activities in CMa-ℓ224 are detected with the survey of CO spectral lines. These outflows predominantly lie along the main filaments (Olmi et al. 2016; Lin et al. 2021), indicating that this region harbors a large number of young stars at young evolutionary stages. The CMa-ℓ224 region also shows remarkably bright emission in the far-IR wavelengths (see Figure 1.6), as revealed by *Herschel*/Hi-GAL survey (Elia et al. 2013). Nearly 300 YSO candidates have been identified there and most of them is associated with the positions of filaments in CMa-ℓ224 (Fischer et al. 2016; Sewiło et al. 2019) with high H_2 column densities ($\gtrsim 4 \times 10^{21}$ cm^{-2}). There are also numerous studies on IRAS sources in the CMa-ℓ224 region showing strong evidence of star formation activities, e.g., the survey of the CS emission associated with dense star-forming regions by (Bronfman et al. 1996), observations of the H_2O maser (Valdettaro et al. 2001) and SiO emission (Harju et al. 1998) which are mainly the tracer of shocks.

Gy 3–7 is a deeply-embedded cluster (Soares & Bica 2002, 2003; Bica et al. 2003) located at $(\ell, b) \sim (224.6^\circ, -1^\circ)$ in the CMa-ℓ224 star-forming region, revealed by remarkable emission in 4.5 μm from *Spitzer*/IRAC and also in far-IR wavelengths observed with *Herschel*/Hi-GAL. The cluster appeared as a high-mass star-forming region and bright in CO emission(Wouterloot & Brand 1989; Lin et al. 2021). Figure 1.6 shows the CMa-ℓ224 star-forming region in the Outer Galaxy which is very bright in 4.5 μm emission (blue) associated with emission of H_2 jets/outflows and also in far-IR wavelength (red). Thus, CMa-ℓ224 is expected as an ideal laboratory to investigate the possible impact of the environment (e.g., metallicity) on star formation. An exceptionally bright spot toward the position of the Gy3–7 cluster is also revealed.

In Chapter 4, we will present our analysis of line cooling in far-IR toward the Gy 3–7 cluster. We will also present our results of the near-IR spectroscopic survey of 33 low- and intermediate-mass YSO candidates among ~300 sources in CMa-ℓ224 in Chapter 5.

1.5 Relevant instruments

During the earliest evolutionary stages, young stars are embedded in the dusty envelopes, which are characterized by high extinction. Protostars are therefore not visible in the UV and optical wavelengths and the only way to probe their physical components is to use the observations at longer wavelenthgs. In particular, near-IR spectroscopy is commonly used to study protoplanetary disks and accretion processes in more-evolved YSOs. Far-IR and (sub)mm spectroscopy reveals physical conditions and processes during the earliest, most embedded stages of YSO evolution.

1.5.1 SOFIA

The Stratospheric Observatory for Infrared Astronomy telescope (SOFIA[1], Temi et al. 2018) is a modified Boeing 747-SP aircraft carrying a 2.7–meter reflecting telescope with an effective aperture of 2.5 m. Operating at the stratosphere layer of the atmosphere at the height of 11.5–13.7 km, above 99% of the water vapor in the Earth's atmosphere, SOFIA was designed for observations of various astrophysical environments in the IR regimes (0.3–612 μm). SOFIA consists of six instruments which are specialized for spectroscopic, imaging, and polarimetric observations, covering a wide range of wavelength and spectral resolution: EXES (Echelon-Cross-Echelle Spectrograph), FORCAST (Faint Object InfraRed CAmera for the SOFIA Telescope), FIFI-LS (Field Imaging Far-Infrared Line Spectrometer), FPI+ (Focal Plane Imager), HAWC+ (High-resolution Airborne Wideband Camera), and GREAT (German Receiver for Astronomy at Terahertz Frequencies).

The atmospheric transmission of SOFIA is sufficient to probe star formation in the far-IR regime (~50-300 μm), as opposed to ground-based observatories such as ALMA (Figure 1.7). In this thesis, we use observations from the HAWC+ and FIFI-LS to study

---

[1] `https://www.sofia.usra.edu/about-sofia/sofia-overview`

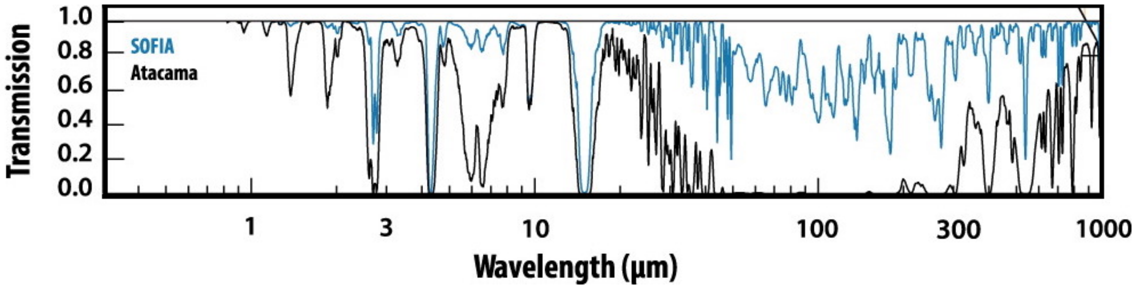

Figure 1.7: Comparison of the atmospheric transmission for SOFIA (blue) and ALMA (black) at the altitudes of ~12.5 km and 5 km, respectively. Adapted from Ennico et al. (2018).

magnetic fields in the Oph–A molecular cloud (Chapter 3) and far-infrared line cooling in the Gy 3-7 cluster in the CMa-ℓ224 star-forming region (Chapter 4, respectively).

FIFI–LS is an integral field unit consisting of two grating spectrometers with a spectral coverage ranging from 51 to 120 μm (blue) and from 115 to 200 μm (red), facilitating simultaneous observations of selected wavelength intervals (0.3-0.9 μm) in both channels (Fischer et al. 2018), see also SOFIA Observer's Handbook for Cycle 10[2]. The spectral resolution, R, ranges from ~500 to 2000, and increases with wavelength for a given grating order. The corresponding velocity resolution of ~150 to 600 km s^{-1} provides unresolved spectral profiles of all far-IR lines, including H_2O (Kristensen et al. 2012; Mottram et al. 2017), CO (Kristensen et al. 2017b), and [O I] (Kristensen et al. 2017a; Yang et al. 2022a). The FIFI-LS detector is composed of 5×5 spatial pixels (hereafter *spaxels*) with the centers offset by 10″, similar to the PACS spectrometer (Poglitsch et al. 2010) on *Herschel*. The spaxel size is 6″ × 6″ in the blue channel (field-of-view, FOV, of 30″ × 30″) and 12″ × 12″ in the red channel (FOV of 1′ × 1′), providing an improvement over PACS by matching the actual wavelength-dependent beam sizes.

HAWC+ is a far-IR camera and polarimeter which provides two observing modes, total intensity and polarimetry with four bandpasses (A, C, D, and E) from ~ 50 – 200 μm (Harper et al. 2018). Both these modes can be performed with the Node Match Chope and/or On the Fly mapping. The HAWC+ detectors are two Transmission Edge Sensor (TES) bolometric arrays that are able to detect the reflected (R array) and transmitted (T

---

[2] https://www-sofia.atlassian.net/wiki/spaces/OHFC1/overview

Table 1.2: Characteristics of the SOFIA/HAWC+ instrument. Table adopted from Observer's Handbook for Cycle 10[2].

Band name	Band center λ_0 (μm)	Bandwidth $\Delta\lambda$ (μm)	Pixel size (″)	Beam size FWHM (″)	FOV Polarimetry (′)	FOV Photometry (′)
A	53	8.7	2.55	4.85	1.4 × 1.7	2.8 × 1.7
C	89	17.0	4.02	7.80	2.1 × 2.7	4.2 × 2.7
D	154	34.0	6.90	13.60	3.7 × 4.6	7.2 × 4.6
E	214	44.0	9.37	18.20	4.2 × 6.2	8.4 × 6.2

array) far-IR radiation from the polarizing beam splitter. The R array consists of 64 × 40 pixels which are made up of two 32 × 40 pixels sub-arrays (R0 and R1 arrays) while the T array consists of only one sub-array made up of 32×40 pixels (T0 array). The observations of total intensity are done using the R0 and R1 arrays. The polarization observations are done using the R0 and T0 arrays. HAWC+ observations are diffraction-limited with a spatial resolution ranging from ∼5″ to 20″ and with the FOV in the range of ∼2′ to 10′. The characteristics of HAWC+ instrument in all four bandpasses are summarized in Table 1.2, including the band center wavelength, Full Width Half Maxiumum (FWHM), pixel size, beam size, and the FOV for photometry and polarimetry observations.

1.5.2 NASA IRTF

The NASA Infrared Telescope Facility[3] is the 3.2–meter telescope operated by NASA and commissioned for the infrared observations. It is mounted on the Mauna Kea, Hawai‘i. Its facility instruments include SpeX, MORIS (MIT Optical Rapid Imaging System), iSHELL, and Opihi.

In this thesis, we use near-IR spectroscopy from the NASA IRTF/SpeX instrument toward a sample of YSO candidates in the CMa-ℓ224 star-forming region (Chapter 5). SpeX is a medium-resolution 0.7–5.3 μm spectrograph (Rayner et al. 2003). It operates in the short-wavelength cross-dispersed mode (SXD) with the 0.3″ × 15″ slit and the 2024 × 2024 Aladin 3 InSb array.

1.6 This thesis

In this thesis, we aim to investigate the role of B-fields and metallicity on the star formation processes. As mentioned in Section 1.3, the physical and chemical conditions in star-forming sites likely differ between the inner to outer parts of our Galaxy. These differences might influence the physical processes associated with star formation activities, and have implications for the interpretation of star formation in external, low-metallicity galaxies. Additionally, B-fields are known to play a critical role in the formation and evolution of molecular clouds, as well as in the star formation processes, together with gravity, turbulence, and stellar feedback. With the advent of numerous new techniques and instruments, it is now possible to study the impact of metallicity and magnetic fields within our Galaxy, where high angular resolution allows us to spatially-resolve individual protostars or their clusters. We address the following questions:

1. What is the morphology of B-fields and the distribution of its strengths within a molecular cloud? What is the role of B-fields in regulating star formation and shaping the cloud?

2. What is the impact of reduced metallicity in the outer Galaxy on the far-IR line cooling from deeply-embedded clusters?

3. Are the mass accretion rates from YSOs in the outer Galaxy lower than in the Solar neighborhood?

---

[3] http://irtfweb.ifa.hawaii.edu/

Chapter 2 introduced the methodology used in the thesis, in particular the dust polarization as a tool to trace B-fields in molecular clouds and the Davis-Chandrasekhar-Fermi method to calculate the strength of B-fields projected onto the plane of the sky. We also describe the method to measure the temperature of the molecular gas, the so-called rotational diagram.

Chapter 3 shows the results of mapping the morphology and measuring the strengths of the B-fields toward the nearby molecular cloud in Ophiuchus, and of investigating the role of B-fields in the cloud's evolution and star formation processes.

Chapter 4 shows the analysis of line cooling in the far-IR in the embedded cluster Gy 3–7 located in the outer Galaxy. We investigate possible effects of metallicity, but also derive physical conditions and ultraviolet field strengths.

Chapter 5 shows the near-IR survey toward 33 YSO candidates located in the CMa-ℓ224 star-forming region to characterize their spectral types, extinctions, and to identify signatures of ongoing accretion. We look for the impact of metallicity on mass accretion rates by comparing our results with those of YSOs in the nearby star-forming regions.

Finally, Chapter 6 presents the summary of our main findings and a discussion of the future directions of this research.

Chapter 2

Methodology

2.1 Probing magnetic fields from magnetically aligned dust grains

Dust grains are known to be aspherical and aligned with respect to the direction of B-fields. As a result, B-field orientation in molecular clouds can be inferred either from the linear polarized starlight from aligned dust grains (Hall 1949; Hiltner 1949) or from dust polarized thermal emission (Hildebrand 1989). These techniques have been used to trace B-fields in diffuse and dense molecular clouds for many decades.

In general, dust grains have the axis of the maximum moment of inertial (also called the minor axis) aligned with the preferred direction in the medium, e.g., the B-field direction. This phenomenon can be explained by the Radiative Alignment Torques (RAT) mechanism. We refer the reader to the papers presenting this RATs mechanism in detail (Draine & Weingartner 1997; Lazarian & Hoang 2007). In the ISM, dust grains absorb or scatter the stellar radiation in UV, optical, or in near-IR range. However, dust grains tend to absorb/scatter more efficiently the electric field component of the stellar radiation coming along their major axis. This results in the starlight coming from the background stars being polarized parallel to their minor axis. Thus, the polarization of the starlight seen in the UV to optical or near-IR wavelength has the polarization angle parallel with the B-fields direction (see left panel in Figure 2.1). Aligned dust grains also re-emit the absorbing energy in the longer wavelength, this is so-called thermal dust emission. As absorbing more electric field components along their major axis, dust grain will tend to re-emit more electric energy components along this major axis than that at the minor axis. This makes the thermal emission of the aligned dust grains also polarized along the major axis. On the other hand, dust grain has their minor axis aligned with the B-field direction. This results in the linear polarized thermal emission of aligned dust grains being perpendicular to the B-field orientation. Thus, if the position angle of the polarized thermal dust emission is known, one can rotate by 90° to infer the position angle of the B-field vectors in the medium (see right panel in Figure 2.1).

The Davis-Chandrasekhar-Fermi (DCF) technique has been routinely used to measure the strengths of the B-field projected on the plane-of-sky, $B_{\rm pos}$(Davis & Greenstein 1949; Chandrasekhar & Fermi 1953). We first consider that a uniform magnetic field can produce the alfvénic waves that propagate along the B-field lines. The DCF method is based

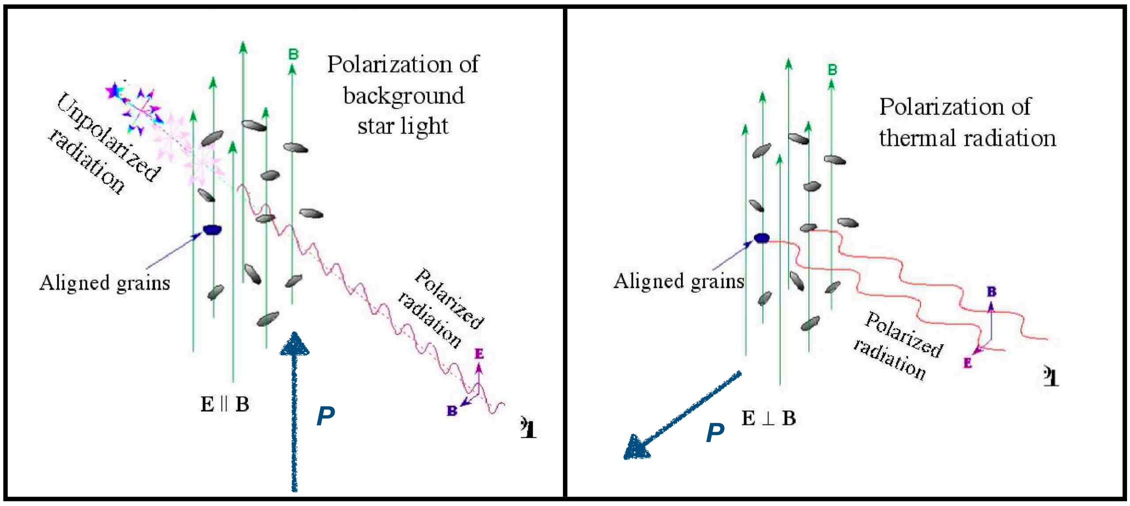

Figure 2.1: Illustrations of polarization of the starlight passing through the ISM with aligned dust grains (*left panel*) where the direction of polarization (P) is parallel to the plane-of-sky of the B-field direction (B) and of polarization of thermal emission of aligned dust grains (*right panel*) where P is perpendicular to B. Adapted from Lazarian (2007).

on the assumption that any perturbation of the B-field lines is associated with the turbulent motions of gas in the medium due to turbulence. Assuming that the non-thermal kinetic and magnetic energies are in equipartition, one can deduce the $B_{\rm pos}$ component of B-field strengths if the information of non-thermal velocity dispersion (related to strengths of turbulence), gas density, and the dispersion of polarization angle (related to the perturbation of B-fields) are known. Crutcher (2004) introduced a simple formula to estimate the $B_{\rm pos}$ strengths, given as:

$$B_{\rm pos} = \mathscr{Q}\sqrt{4\pi\rho}\,\frac{\sigma_{\rm NT}}{\sigma_\theta} \approx 9.3\,\sqrt{n({\rm H_2})}\,\frac{\Delta v_{\rm NT}}{\sigma_\theta}\ (\mu{\rm G})\,, \tag{2.1}$$

where $\mathscr{Q}$=0.5 is the correction factor applied for dense clouds where the polarization angle dispersion does not exceed 25° (Ostriker et al. 2001), $\rho = \mu m_{\rm H} n({\rm H_2})$ is the H_2 gas volume density in units of g cm^{-3} (μ=2.8 is the mean molecular weight per hydrogen molecule (Kauffmann et al. 2008), $m_{\rm H} = 1.67 \times 10^{-24}$ g is the mass of the hydrogen atom, $n({\rm H_2})$ is the volume density of the molecular hydrogen in units of cm^{-3}, $\sigma_{\rm NT} = \Delta v_{\rm NT}/\sqrt{8\ln 2}$ is the one-dimensional (1D) non-thermal velocity dispersion along the line-of-sight of the ideal gas species that traces the dense region as similar as by dust polarization emission in units of km s^{-1} ($\Delta v_{\rm NT}$ is non-thermal FWHM velocity dispersion, also measured in units of km s^{-1}), σ_θ is the polarization angle dispersion in degrees. The DCF method has been continuously modified and improved to better trace the strengths of B-fields in different astrophysical media at various scales (Hildebrand et al. 2009; Houde et al. 2011; Skalidis & Tassis 2021; Lazarian et al. 2022).

2.2 CO rotational diagram

In a molecular cloud, we consider the two-level system of the lower level l and upper u which are specified by the energy levels of the molecule. We assume that at the energy level i, the molecules have a population of N_i and have a state energy of E_i with the degeneracy of g_i. The Boltzmann distribution for the molecular populations of level l and level u at a temperature T can be written as:

$$\frac{N_u}{N_l} = \frac{g_u}{g_l} \exp\left(-\frac{E_u - E_l}{k_\mathrm{B} T}\right), \tag{2.2}$$

where k_B is the Boltzmann constant. If we call the total population of the molecules over all the levels N_tot, then we have:

$$\begin{aligned}
N_\mathrm{tot} &= N_0 + N_1 + N_2 + ... && (2.3)\\
&= \frac{N_0}{g_0}\left(g_0 + g_0\frac{N_1}{N_0} + g_0\frac{N_2}{N_0} + ...\right) && (2.4)\\
&= \frac{N_0}{g_0}\exp\left(\frac{E_0}{k_\mathrm{B}T}\right)\left\{g_0 \exp\left(\frac{-E_0}{k_\mathrm{B}T}\right) + g_1 \exp\left(\frac{-E_1}{k_\mathrm{B}T}\right) + g_2 \exp\left(\frac{-E_2}{k_\mathrm{B}T}\right) + ...\right\} && (2.5)\\
&= \frac{N_0}{g_0}\exp\left(\frac{E_0}{k_\mathrm{B}T}\right)Q(T)\,, && (2.6)
\end{aligned}$$

where $Q(T)$ is the partition function at the temperature T, defined as:

Thus, the population of the molecule in the upper level u can be written in terms of the total population of the molecule as:

$$N_u = N_\mathrm{tot}\frac{N_u}{N_\mathrm{tot}} = N_\mathrm{tot}\frac{\frac{g_u}{g_0}N_0 \exp\left(-\frac{E_u - E_0}{k_\mathrm{B}T}\right)}{\frac{N_0}{g_0}\exp\left(\frac{E_0}{k_\mathrm{B}T}\right)Q(T)} = g_u \frac{N_\mathrm{tot}}{Q(T)}\exp\left(-\frac{E_u}{k_\mathrm{B}T}\right). \tag{2.7}$$

In Local Thermodynamic Equilibrium (LTE) conditions and if the molecular emission line is optically thin, the temperature T is so-called the rotation temperature, $T \equiv T_\mathrm{rot}$. Eq. 2.7 can be re-written as:

$$\ln\frac{N_\mathrm{u}}{g_\mathrm{u}} = \ln\frac{N_\mathrm{tot}}{Q(T_\mathrm{rot})} - \frac{1}{T_\mathrm{rot}}\frac{E_\mathrm{u}}{k_\mathrm{B}}. \tag{2.8}$$

Clearly, Eq. 2.8 is a linear function of $\ln\frac{N_\mathrm{u}}{g_\mathrm{u}}$ and $\frac{E_\mathrm{u}}{k_\mathrm{B}}$, and also called the Boltzmann (or rotational) diagrams. The number of molecules in upper level N_u can be observationally measured from the line flux with respect to the transition of the molecules:

$$N_\mathrm{u} = \frac{4\pi d^2 \lambda F_\lambda}{Ahc} \tag{2.9}$$

where F_λ is the flux of the line at wavelength λ, d is the distance to the observing source, A is the Einstein coefficient, c is the speed of light, and h is the Planck's constant. If there is more than one transition is observed, one can perform a linear fit on the rotational diagram ($y = ax + b$). The T_rot and N_tot are then derived from the slope a and y-intercept b of the fit in Eq. 2.8. Figure 2.2 show an example of the rotational diagram of the CO molecule toward the high-mass YSO W51N-e1 where the observation of CO transitions

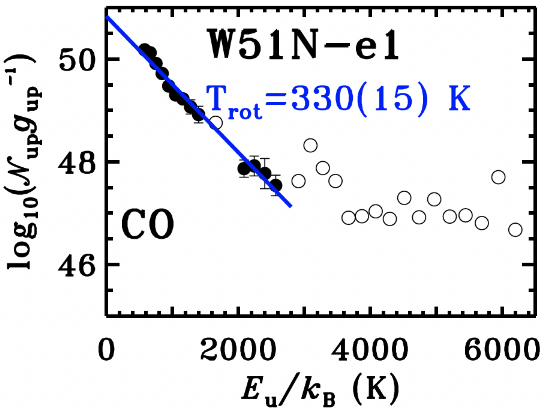

Figure 2.2: Rotational diagram of CO toward a high-mass protostar W51N-e1. The base-10 logarithm of the number of emitting molecules from a level u, N_u, divided by the degeneracy of the level, g_u, is shown as a function of the energy of the upper level in K, E_u. Adapted from Karska et al. (2014a).

with J_up=14–30 were done with *Herschel*/PACS (Karska et al. 2014a).

Chapter 3

Mapping and characterizing magnetic field in the Ophiuchus A Molecular Cloud with SOFIA/HAWC+

To be submitted to Astronomy & Astrophysics

3.1 Introduction

Stars like our Sun form in the cold and dense parts of molecular clouds, which consist of filaments, clumps, and cores (Lada & Lada 2003; Kennicutt & Evans 2012). The contraction of clouds into cores is controlled not only by gravity but also by magnetic fields, turbulence, and radiative and mechanical feedback from nearby stars (McKee & Ostriker 2007; Hennebelle & Falgarone 2012). Turbulence counteracts gravity and prevents the collapse in the dense core but can also generate shocks that compress the gas and trigger the formation of new stars.

Magnetic fields (B-fields) play an important role in the early stages of star formation by supporting the material in the cloud against self-gravitational collapse (see, e.g., Mouschovias 2001). The collapse generally occurs when the cloud is magnetically supercritical, with the ratio of mass to magnetic flux (known as mass-to-flux ratio) greater than one, i.e., B-fields are not strong enough to prevent the gravitational collapse; the contraction can occur in the cloud leading to the formation of protostars. Conversely, when the cloud exhibits a mass-to-flux ratio below one, the B-fields support the cloud against the cloud collapse. However, several mechanisms might enhance the mass-to-flux ratio in the interstellar medium (ISM). In the regions with a low-ionization fraction, the coupling between the neutral and charged particles causes a fast increase of density, leading to the cloud collapse (ambipolar diffusion; see e.g., Mouschovias et al. 2006; Liu et al. 2022). In the turbulent regions, on the other hand, the fast reconnection of turbulence might also dissipate the magnetic energy, increasing the cloud instability and aiding its contraction (magnetic reconnection diffusion, Lazarian & Vishniac 1999).

Feedback from massive (O– or B–type) stars might influence the properties of the parental molecular cloud and the star formation processes (e.g., Krumholz et al. 2014; Pabst et al. 2019, 2020). B-fields also influence ithe structure of a cloud, as suggested by both simulations (e.g., Henney et al. 2009; Mackey & Lim 2011) and observations (e.g., Soam et al. 2017, 2018; Pattle et al. 2018; Hwang et al. 2023). When the radiation field is parallel to the B-field vector, clouds are characterized by a flattened shape, whereas when its perpendicular, the cloud has a column-like or pillar structure.

Interstellar dust consists of aspherical, micron-size grains, which can be used to trace B-fields molecular clouds. The UV radiation from young stars irradiates the dust, which subsequently re-emits the excess energy in the IR and (sub)mm domains. According to the theory of thermal dust polarization, FIR polarized emission from dust grains is aligned with their major axis perpendicular to the orientation of the magnetic fields (see e.g., Lazarian & Hoang 2007; Andersson et al. 2015; Tram & Hoang 2022). Thus, the B-field vectors can be inferred by rotating the vectors of the polarization angle by 90°. The strength of the $B_{\rm pos}$ can be subsequently derived using the Davis-Chandrasekhar-Fermi method (DCF; Davis 1951; Chandrasekhar & Fermi 1953) assuming the kinetic energy of turbulent gas balances to that of turbulent magnetic fields. Another common method used to trace the morphology of B-fields in the ISM is based on the Goldreich-Kylafis effect (Goldreich & Kylafis 1981) where the splitting in the spectral line of molecules is due to the linear polarization radiation absorption or emission, this results polarization angle being either aligned or perpendicular to the ambient magnetic field direction on the plane-of-sky (see e.g, Crutcher 2012; Maury et al. 2022). Linear polarized dust emission has been routinely used to measure B-fields in environments of molecular clouds in the Milky Way (see, e.g., Ward-Thompson et al. 2017; Chuss et al. 2019; Pattle et al. 2022b) and extra-galactic regions (see, e.g., Lopez-Rodriguez et al. 2021, 2022; Borlaff et al. 2023).

Adopting the mean value of the field strength (i.e., strength estimated by the DCF over the observed clouds, regardless of the cloud's size and shape), Crutcher et al. (2010) showed the relationship between the B-field strengths and gas volume density in the diffuse and dense molecular clouds. For gas densities in excess of $\sim$300 cm^{-3}, the B-field strengths were proportional to n^k, where the power-law index k is 0.65, in agreement with follow-up observations (for e.g., see Figure 2 in Pattle & Fissel 2019). For lower volume densities, B-fields were predicted to have a uniform strength across the entire cloud (Crutcher et al. 2010). Theoretical studies, on the other hand, suggested that the power-law index k varies between weak ($\sim$2/3, Mestel 1966) and strong B-fields ($\lesssim$0.5, Mouschovias & Ciolek 1999).

The maps of the B-fields morphology and strength within the observed regions become essential to understanding the local role of the field. Indeed, other authors attempted to derive the map of the B-fields toward some well-known star-forming regions, including OMC–1 (Guerra et al. 2021, Hwang et al. 2021), and 30 Doradus (Tram et al. 2023). The authors showed a significant variation in the B-field morphology and strength across the clouds and demonstrated that the B-fields significantly influence the cloud's evolution and, thus, the star-formation activities. However, as both the OMC–1 and 30 Dor systems are complex, the effect of B-fields is challenging to disentangle. In this work, we focus on a simple system of ρ Ophiuchus-A (hereafter Oph–A) molecular cloud to study the effect of B-fields in star formation activities and in regulating the shape of this region.

The Oph-A is located in the northern part of the L1688 active star-forming region in the ρ Ophiuchus dark cloud complex (Loren et al. 1990; Wilking et al. 2008; Esplin & Luhman 2020). The Oph–A cloud is a low-mass star-forming region influenced by a nearby embedded early high-mass B star, Oph S1, which has a mass of ~8 $M_\odot$ (Hamaguchi et al. 2003) and is located in a distance of ~137 pc (Ortiz-León et al. 2017). The Oph–A region hosts numerous prestellar and protostellar cores identified by the Ground Belt Survey (Ladjelate et al. 2020) and protostars in the early stages (i.e., Class 0/I Young Stellar Objects (YSOs), Enoch et al. 2009). The star formation activity in the region is also believed to be affected by the Sco OB2 association located at the western part of the cloud at a distance of ~145 pc (de Zeeuw et al. 1999). B-fields in Oph–A were observed by JCMT/POL–2 and SOFIA/HAWC+. Kwon et al. (2018) estimated the B-fields strengths projected on the plane-of-sky ($B_{\rm pos}$) in Oph–A using the JCMT/POL–2 data at 850 μm toward the few densest parts of the cloud, yielding the $B_{\rm pos}$ in the range of ~0.5–5 mG. The highest strength was measured toward the densest part of the cloud associated with the starless core SM1. These strengths in Oph–A are comparable to what is found in the OMC–1 region (Hwang et al. 2021). They also found that the B-field direction in the cloud is generally perpendicular to the main shape of the cloud which is broadly seen in the dense core or the high-density structure of the molecular clouds. Thus, this region provides an ideal isolated system to study the impact of the magnetic fields in the star-forming region and to investigate the interplay between the magnetic fields and the stellar feedback into the molecular cloud.

In this Chapter, we aim to:

1. determine the magnetic field morphology and strengths in the entire Oph–A region using the SOFIA/HAWC+ observations;
2. investigate the role of the magnetic fields for the star formation activity in Oph–A;
3. quantify the combined effect of magnetic field and radiation from a nearby B star on the shape of Oph–A cloud.

The Chapter is organized as follows. We describe the set of archival data in Section 3.2. We present the results of mapping the B-field morphology and strength in Section 3.3 and discuss the roles of B-fields and radiation fields from the OB star in the cloud in Section 3.4. Finally, we summarize our results in Section 3.5.

3.2 Data

3.2.1 Polarimetric data

We use the FIR polarimetric observations toward Oph–A from the High-resolution Airborne Wideband Camera-plus (HAWC+; Harper et al. 2018) onboard the 2.7 m Stratospheric Observatory For Infrared Astronomy (SOFIA) telescope. The observations were done in two bands C and D, centered at 89 and 154 μm, respectively on 17 May 2017, under the proposal ID 70_0511 (PI: Darren Dowell). The observations and data reduction are described in Santos et al. (2019) where they analyzed the slope of polarization spectrum versus the H_2 column density, $N(H_2)$, and dust temperature, $T_{\rm dust}$. Here, we use the SOFIA/HAWC+ Level–4 data which is fully calibrated and can be directly downloaded from the SOFIA archive[1]. The final maps cover an area of ~ $4.5' \times 4.5'$ toward the central region in Oph–A with the angular resolution of $7.8''$ and $13.6''$ at 89 and 154 μm, respectively.

From the maps of the Stokes I, Q, U and their uncertainties $\sigma_{\rm I}$, $\sigma_{\rm Q}$, $\sigma_{\rm U}$ obtained from SOFIA/HAWC+ observations, the maps of polarization fraction p_0 and its uncertainty $\sigma_{\rm p}$ are calculated in units of percent (%). The de-biased polarization fraction, p, is calculated as $p^2 = p_0^2 - \sigma_{\rm p}^2$ to take into account the observational uncertainty. The map of polarization angle (θ) in degrees is also derived from the stokes Q and U: $\theta = 0.5 \arctan(U/Q)$.

To enhance the quality in measuring the maps of magnetic field orientation and strength in Oph–A, we apply some critical conditions in choosing vectors (pixels) in SOFIA/HAWC+ maps. We mask out from SOFIA/HAWC+ maps the pixels for which I/σ_I<54 and for band C and I/σ_I<214 for band D. In both two bands, we also remove the pixels for which p/σ_p<3 and p>50% from the maps (see Appendix 3.A).

3.2.2 Spectroscopic data

We quantify dense molecular gas in Oph–A using the map of HCO^+ 4−3 line at ~356.734 GHz obtained from the Heterodyne Array Receiver Program (HARP; Buckle et al. 2009) mounted on the 15–m James Clerk Maxwell Telescope (JCMT). The observations were done during June and July 2011 (Proposal ID: M11AU13), covering the Oph–A region with a beam size (or FWHM) of ~$14''$. We use the reduced spectral map of HCO^+4−3 directly downloaded from the JCMT science archive[2]. For comparison to the HCO^+ 4−3 data, we also use the observations of N_2H^+ 3−2 line at ~279.515 GHz obtained from the APEX–2 instrument on the 12–m Atacama Pathfinder EXperiment telescope (APEX; Güsten et al. 2006). We use the back-end data with a spectral resolution of 0.082 km s^{-1}. The reduced spectral map covering the Oph–A region has a beam size of ~$22''$ (for details, see Liseau et al. 2015).

3.2.3 Dust temperature and column density maps

We adopt the maps of $T_{\rm dust}$ and $N(H_2)$ from Santos et al. (2019) to infer the non-thermal velocity dispersion and to investigate the roles of magnetic fields together with thermal and non-thermal kinetic energy on star formation activity and energy balance in Oph–A. These maps were obtained from the fitting of a modified black-body to the spectral energy distribution (SED) using the continuum flux maps from *Herschel*/PACS (Poglitsch et al. 2010) at 70, 100, and 160 μm and have the FWHM of $11.4''$ (for details, see Section 3.2 in Santos et al. 2019).

3.3 Magnetic fields in Oph–A

In this Section, We use the SOFIA/HAWC+ polarimetric data to infer the maps of the magnetic field morphology and strengths projected on the plane-of-sky in Oph–A, $B_{\rm pos}$,

---

[1] https://irsa.ipac.caltech.edu/Missions/sofia.html

[2] https://www.cadc-ccda.hia-iha.nrc-cnrc.gc.ca/en/jcmt/

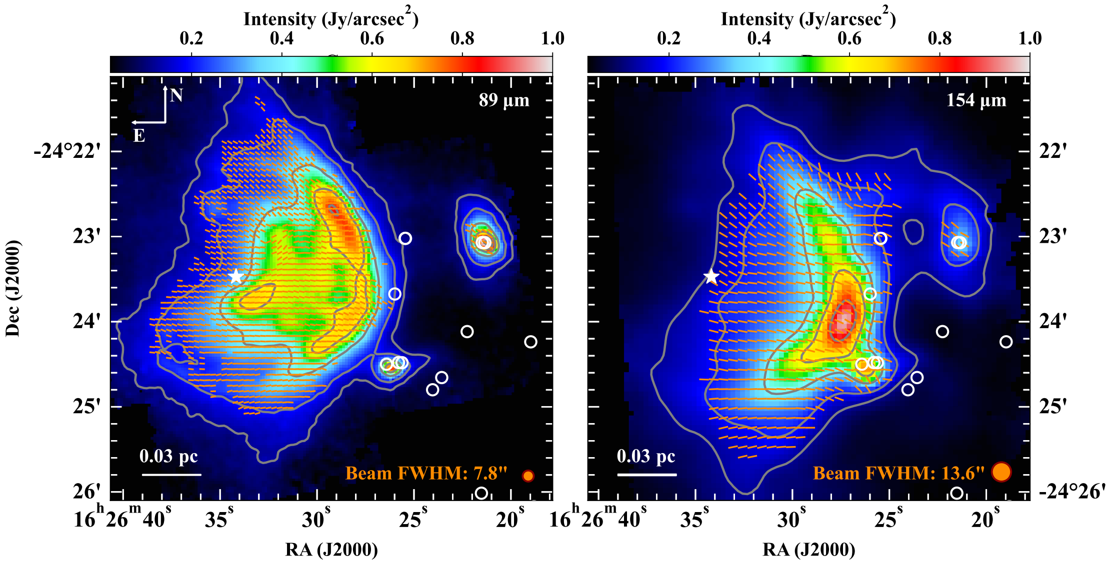

Figure 3.1: Maps of the B-field orientation (orange vectors) on top of the total intensity (Stokes–I, color maps) toward Oph–A, observed with SOFIA/HAWC+ in band C (*left panel*) and band D (*right panel*), centered at 89 and 154 μm, respectively. The gray contours in each map show the total intensity at the corresponding wavelength, with the contour levels at 0.12, 0.2, 0.4, 0.6, and 0.8 Jy/arcsec^2. The B-field half-vectors are inferred by rotating the polarization half-vectors by 90°. White star marks the position of the B S1 star. Small white circles indicate the positions of YSOs identified from Enoch et al. (2009); Evans et al. (2009); Connelley & Greene (2010). The orange circles show the beam size of each color map.

and to investigate the role of the magnetic fields in Oph–A.

3.3.1 Magnetic fields morphology

We construct the map of B-field morphology by rotating by 90° from the polarization angle maps observed with SOFIA/HAWC+. Figure 3.1 shows the maps of B-fields orientation (half-vectors) inferred from the maps of polarization angle in bands C (left panel) and D (right panel), and centered at 89 and 154 μm, respectively. The background color maps show the Stokes–I intensity at the respective wavelength. Here, the position angle of B-fields is measured east to north, which is in the range from 0° to 180°. The polarimetric data at both wavelengths are able to trace the B-fields toward Oph–A where the intensity I>0.12 Jy/arcsec^2 (the area inside the lowest contour in each map). The data at the higher wavelength (154 μm) can well resolve the B-fields morphology toward a small region extended to the north side of the map, while the data at 89 μm represents the B-fields in the warmer dust region closer to the S1 star.

The B-field vectors in Oph–A are generally well-ordered and follow the flow of material in the low- to the intermediate-intensity regime (Figure 3.1). B-field vectors tend to be bent toward the higher-density region in the center of the map, resulting in the hourglass shape located perpendicular to the ridge of the cloud. On the eastern side of the map, the orientation of B-vectors tends to vary in the counter-clockwise direction from North to South. In the North-East part of the map, B-field vectors run along the North-East to South-West direction with a median position angle of ~56° and 49° at 89 and 154 μm, respectively. This feature is also seen in a small area in the North-West part of the map. On the other hand, in the East and South-East regions, B-field vectors orient consistently to the East-West and South-East to Norht-West direction, with the median position angles of ~83° and 92° at 89 μm, and ~75° and 85° at 154 μm, respectively. Interestingly, the data at 154 μm shows B-field vectors running nearly vertically, i.e., along the North-South (direction toward a small area at the North part of the map, which is not seen in the data at 89 μm.

In addition, there are two outstanding components of B-fields toward the regions characterized by the highest H_2 column densities: one component associated with the peak of continuum emission at 154 μm runs along North-East to South-West direction with the median B-field direction of ~70°; the other is located at the North of the first component and associated with the peak of continuum emission at 89 μm, which exhibits the B-field vectors along the East-West direction with a median position angle of ~88° and 81° at 89 and 154 μm, respectively. We will further discuss the B-field morphology together with the field strengths in Section 3.4.

3.3.2 Magnetic fields strength

We apply the DCF method to calculate the strength of the B-field projected on the plane-of-sky ($B_{\rm pos}$) in the entire region of the Oph–A cloud. We follow the formula introduced in Crutcher (2004):

$$B_{\rm pos} = \mathcal{Q}\sqrt{4\pi\rho}\frac{\sigma_{\rm NT}}{\sigma_\theta} \approx 9.3\sqrt{n({\rm H_2})}\frac{\Delta v_{\rm NT}}{\sigma_\theta}\ (\mu{\rm G})\,, \tag{3.1}$$

where $\mathcal{Q}$=0.5 is the correction factor applied for dense clouds where the polarization angle dispersion does not exceed 25° (Ostriker et al. 2001), $\rho = \mu m_{\rm H} n({\rm H_2})$ is the H_2 gas volume density in units of g cm^{-3} (μ=2.8 is the mean molecular weight per hydrogen molecule (Kauffmann et al. 2008), $m_{\rm H} = 1.67 \times 10^{-24}$ g is the mass of the hydrogen atom, $n({\rm H_2})$ is the volume density of the molecular hydrogen in units of cm^{-3}, $\sigma_{\rm NT} = \Delta v_{\rm NT}/\sqrt{8\ln 2}$ is the one-dimensional (1D) non-thermal velocity dispersion along the line-of-sight of the ideal gas species that traces the dense region as similar as by dust polarization emission in units of km s^{-1} ($\Delta v_{\rm NT}$ is non-thermal FWHM velocity dispersion, also measured in units of km s^{-1}), σ_θ is the polarization angle dispersion in degrees.

3.3.2.1 Polarization angle dispersion maps

It is essential to see how the magnetic fields flow the field lines locally. To do that, we calculate the dispersion in the polarization angle distribution (σ_θ) across the Oph–A region. We use the method presented in Hwang et al. (2021) for which the σ_θ is calculated pixel-by-pixel throughout the map of Oph–A. We summarize the procedure of calculating the polarization angle dispersion toward each pixel $i^{\rm th}$ in the map as follows:

1. We generate a small box covering the pixel $i^{\rm th}$ with a size of 9×9 pixels, corresponding to 2 beam sizes of the SOFIA/HAWC+ observations (i.e., 15.6″ and 36.4″ in

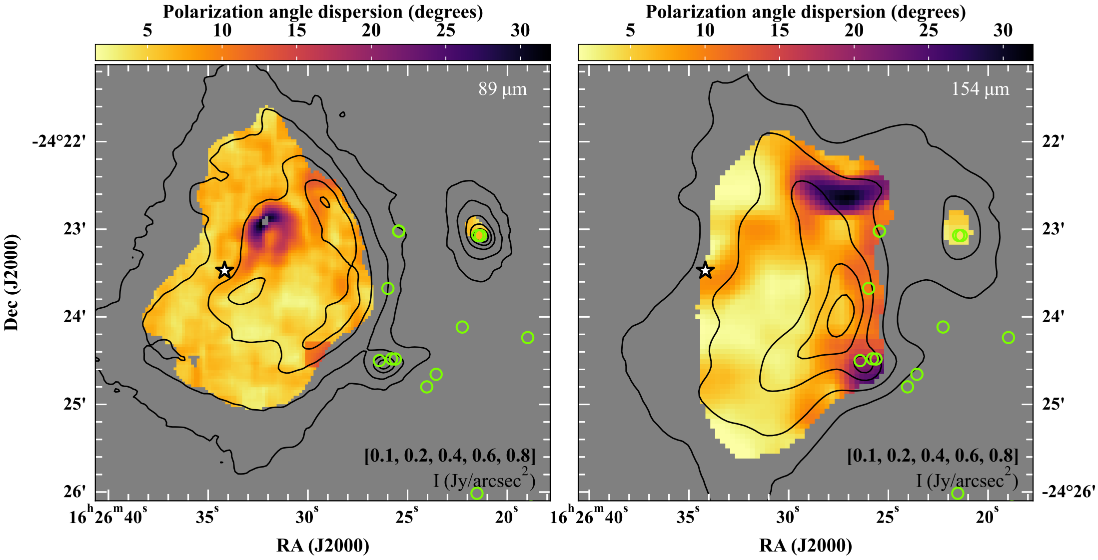

Figure 3.2: Polarization angle dispersion maps in Oph–A using data in band C (*left panel*) and band D (*right panel*). The black contours are from the total intensity map at the corresponding wavelength, contour levels are indicated at the bottom right corner of each map. The other notations are similar as in Figure 3.1.

bands C and D, respectively).

2. We calculate the mean value of polarization angles within the small box, $\bar{\theta}_{\rm i}$, which implies the local mean polarized angle toward the pixel $i^{\rm th}$.

3. For each pixel within the small box, we calculate the difference between the observed polarized angle and the mean value. We compute the root mean square (RMS) of the distribution of angle differences in the box. This RMS value indicates the polarization angle dispersion calculated toward the pixel $i^{\rm th}$.

4. The uncertainty of the polarization angle dispersion toward the pixel $i^{\rm th}$ is propagated from the uncertainty of polarization angles in the small box.

By repeating the process for all of the pixels in the entire region, we obtain the map of polarization angle dispersion in Oph–A. We note that if there are more than 50% of pixels with NaN value in the computing box, the result of polarization angle dispersion calculation toward pixel $i^{\rm th}$ is expelled. We apply this criterion to gain the estimation quality of the σ_θ. It is also necessary to de-bias the polarization angle dispersion due to the uncertainty of the observed polarized angle.

Figure 3.2 shows the maps of polarization angle dispersion toward Oph–A using HAWC+ data in two bands C (left panel) and D (right panel), centered at 89 and 154 μm, respectively. The polarization angle dispersion calculated using data in bands C and D are in ranges 1.3°– 31.5° and 2.3°– 31.2°, which both correspond to the median value of ~5.7°.

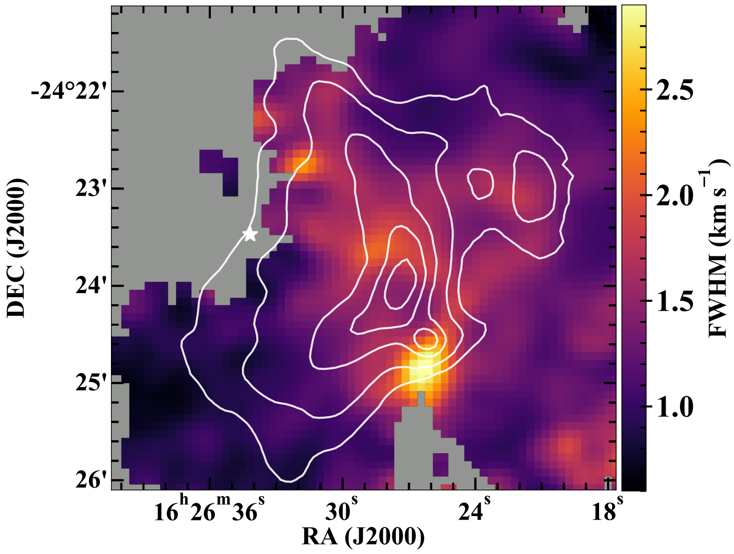

Figure 3.3: Distribution of the non-thermal FWHM of the HCO$^+$ 4−3 molecular line toward Oph–A. White star marks the position of the S1 star. White contours show the continuum emission (Stokes–I) at 154 μm, with contours levels at 0.12, 0.2, 0.4, 0.6, and 0.8 Jy/arcsec^2.

3.3.2.2 Velocity dispersion map

We use the HCO$^+$ 4−3 molecular data observed from JCMT/HARP to estimate the total velocity dispersion, σ_v. This molecular line has a critical density of ~10^6 cm^{-3} and thus is considered as a good probe of the dense region in the Oph–A cloud. The HCO$^+$ 4−3 emission is well-represented by a single Gaussian profile. Thus, in each pixel we fit the line with a single Gaussian. The central velocity across Oph–A covers the range of 2.25–3.76 km s^{-1} with a median value of 3.12 km s^{-1}, which is in agreement with the systemic velocity of Oph–A of ~3.44 km s^{-1} (André et al. 2007). We use the line width of the Gaussian as the measure of total velocity dispersion toward each pixel.

To construct the map of the 1D non-thermal velocity dispersion ($\sigma_{\rm NT}$), we subtract the thermal velocity dispersion component ($\sigma_{v,\rm th}$) from the map of the total velocity dispersion, given by:

$$\sigma_{\rm NT} = \sqrt{\sigma_v^2 - \sigma_{v,\rm th}^2} = \sqrt{\sigma_v^2 - \frac{k_{\rm B} T_{\rm gas}}{m_{\rm mol}}} \left(\text{km s}^{-1}\right), \tag{3.2}$$

where $m_{\rm mol}$=29 amu is the mass of the HCO$^+$ molecule, $k_{\rm B}$ is the Boltzmann constant, and $T_{\rm gas}$ is the kinetic temperature of the gas. Here, we assume that the gas is in the local thermodynamical equilibrium (LTE) and well-coupled with the dust in the cloud. Thus, the gas kinetic temperature is equal to the excitation temperature in all levels ($T_{\rm ex}$) and equal to the dust temperature: $T_{\rm gas} = T_{\rm ex} = T_{\rm dust}$. We convolve the map of $T_{\rm dust}$ to the lower resolution of the molecular line map (14″) to obtain the same pixel size on both maps. We convert the velocity dispersion of the non-thermal component into the FWHM velocity dispersion, given as $\Delta v_{\rm NT} = \sigma_{\rm NT}\sqrt{8\ln 2}$. The uncertainty of the FWHM is propagated from the uncertainty of the line width obtained from the Gaussian fit.

Figure 3.3 shows the map of the 1D non-thermal FWHM of the HCO$^+$ molecular

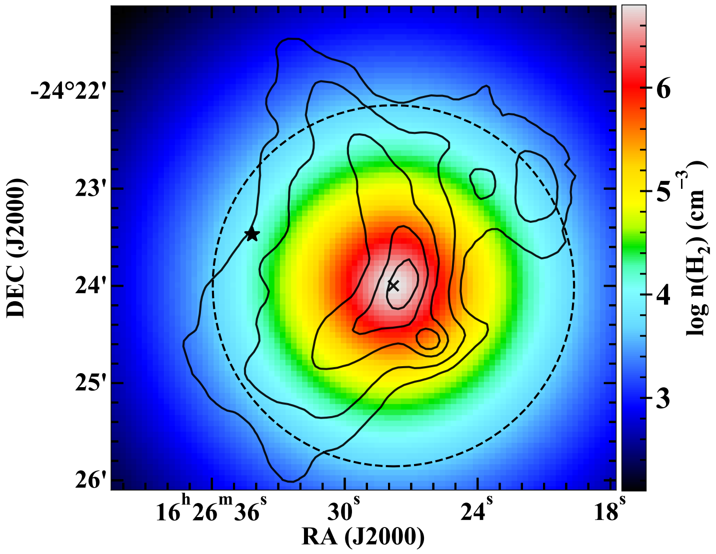

Figure 3.4: Map of the H_2 gas volume density in Oph–A generated based on the Plummer sphere model. The black "×" symbol indicates the peak of the dust temperature map. The black star marks the position of the Oph S1 star. The dashed circle in black color with radius R=0.074 pc. The overlaid contours in black colors are from the continuum emission at 154 μm with the levels similar as shown in Figure 3.3.

line toward Oph–A. The non-thermal FWHM velocity dispersion ranges from 0.62 to 2.98 km s^{-1} with a median value of 1.19 km s^{-1}. We find a good agreement between our result obtained with HCO^+ and those from other line tracers, i.e., 0.95 km s^{-1} using N_2H^+ 3–2 from APEX and 1.5 km s^{-1} using $C^{18}O$ 3–2 from JCMT/HARP (see Appendix 3.B for details). Thus, it is plausible to use the results from the HCO^+ 4–3 line in the following analysis.

3.3.2.3 Gas volume density map

We generate the map of the H_2 volume density, $n(H_2)$, assuming the Oph–A cloud is a Plummer sphere (Santos et al. 2019). This model is typically used to describe the globular molecular cores, filaments, or stellar clusters (Plummer 1911). The distribution of the H_2 volume density is defined as:

$$n(r) = n_0 \left(1 + \frac{r^2}{R_P^2}\right)^{-5/2} \left(\mathrm{cm}^{-3}\right), \tag{3.3}$$

where n_0 is the is the H_2 volume density at the center of the Plummer sphere and R_P is the Plummer's radius. We adopt n_0=6.4×10^6 cm^{-3} estimated at the peak position of $N(H_2)$ map, located at (RA, Dec)= ($16^h26^m27^s.8$, −24°24′00″.0) and R_P=0.018 pc as results from simulation based on *Herschel* data presented in Santos et al. (2019). Figure 3.4 shows the map of the H_2 volume density and the continuum emission at 154 μm (Stokes–I) from SOFIA/HAWC+. The map angular resolution is set by the Stokes–I map and equals 13.6″. We also generate another map of the $n(H_2)$, with the resolution of 7.8″, to calculate

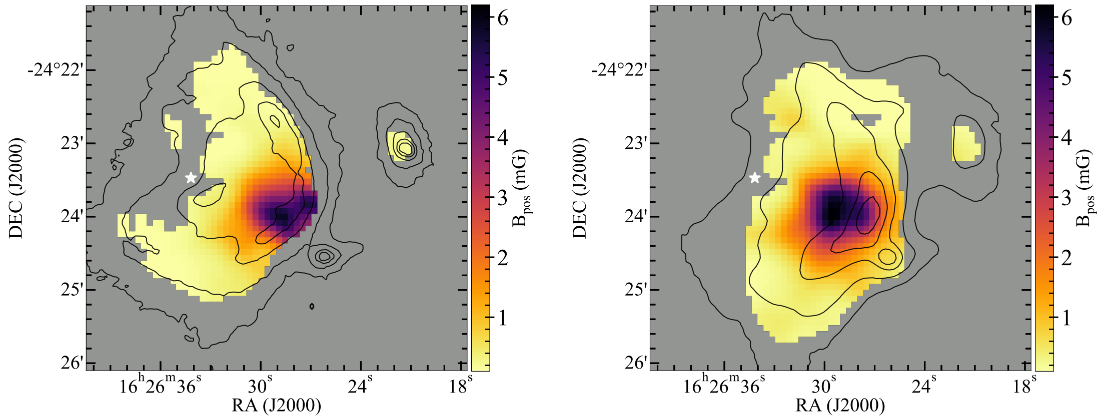

Figure 3.5: Maps of magnetic field strengths projected on the plane-of-sky (B_{pos}) in Oph–A using data at 89 μm (*left panel*) and 154 μm (*right panel*), respectively. The contours in each map are similar as in Figure 3.1. The star symbol marks the position of the S1 star.

the map of B_{pos} at 89 μm.

3.3.2.4 Inferred magnetic field strength maps

We use the maps of polarization angle dispersion, FWHM of the molecular gas, and the H_2 volume density to measure the B_{pos} strengths in the entire region of Oph–A. All three input maps are convolved to the angular resolution of 14″, corresponding to those of non-thermal FWHM map. We then calculate the B_{pos} strength toward Oph–A using Eq. 3.1.

Figure 3.5 shows the maps of the B_{pos} strengths toward Oph–A, inferred from the HAWC+ data at 89 μm (left panel) and 154 μm (right panel). B-field strengths vary from 0.1 to 5.8 mG and from 0.1 to 6.21 mG for data at 89 and 154 μm, respectively. The highest strength is found at the center of the cloud, associated with the emission peak at 154 μm and the position of the SM1 core. The median B-field strengths there are 0.34 and 0.46 mG, as measured using 89 and 154 μm data, respectively. The uncertainty of the magnetic field strength is propagated based on the uncertainty of the velocity dispersion of the gas and polarization angle dispersion. Since we generate the $n(H_2)$ map based on the model of the Plummer sphere where the Plummer radius and the central gas volume density are taken from the result of complex simulation (see Santos et al. 2019), we do not take into account the uncertainty of the gas volume density in the total uncertainty of the B-field strengths. For this reason, the uncertainty of B_{pos} might be underestimated.

The strength of the B-field along the light-of-sight, B_{los}, of ~10 μG was measured toward a dense region in the L1688 star-forming region covering the Oph–A cloud with a volume density of ~1.6×10^3 cm^{-3} using the OH Zeeman effect observations (Troland et al. 1996). This value is much smaller than the B_{pos} measured across the Oph–A region with gas densities up to 10^6 cm^{-3}. Thus, hereafter we scale the total magnetic field strengths (B) by the B_{pos} component only: $B \equiv B_{tot} = B_{pos} + B_{los} \approx B_{pos}$. For the following analysis, we will employ only the B-field strength map inferred from the polarimetric data at 154 μm since it covers a larger area of the higher-density region in Oph–A than that from the data at 89 μm.

3.3.3 Mass-to-flux ratio

To examine the relative importance of B-fields and gravity in Oph–A, we calculate the map of the mass-to-flux ratio (λ), which is proportional to the ratio between the H_2 column density and magnetic field strengths (Crutcher 2004):

$$\lambda = 7.6 \times 10^{-21} \frac{N(H_2)}{B}, \tag{3.4}$$

where $N(H_2)$ is in units of cm^{-2} and B is in units of μG.

The top panel in Figure 3.6 shows the spatial distribution of the mass-to-flux ratio in the Oph–A cloud. It reveals an increasing gradient of λ from the central and eastern parts of the clump to the outer regions, spanning from 0.02 to 10.64, with a median value of 0.43. The region exhibiting the lowest values of $\lambda \ll 1$ is close to the S1 star, suggesting that the region is strongly magnetically sub-critical, i.e., B-field is strong enough to prevent the gravitational collapse. This can be explained by the influence of the strong winds and radiation fields from the S1 star pushing the material away to the vicinity. The mass-to-flux ratio increases toward the outer regions, where the gas volume density is $\lesssim 10^4$ cm^{-3}. These regions are magnetically super-critical and so, the self-gravitational collapse might occur there. Indeed, several protostars and a single protostellar core are detected toward this part of Oph–A (Enoch et al. 2009; Evans et al. 2009; Connelley & Greene 2010).

3.3.4 Alfvénic Mach number

To investigate the interplay between B-field and turbulence due to the non-thermal motion of the gas in Oph–A, we calculate the map of Alfvénic Mach number, given as:

$$\mathscr{M}_A = \sqrt{3}\frac{\sigma_{NT}}{v_A}, \tag{3.5}$$

where σ_{NT} stands for the 1D non-thermal velocity dispersion driven by the turbulence and v_A is the Alfvénic velocity driven by the magnetic fields ($v_A = B/\sqrt{4\pi\rho}$), both in units of km s^{-1}. The factor $\sqrt{3}$ in Eq. 3.5 assumes that turbulence is isotropic, and allows the calculation of the 3D Alfvénic Mach numbers.

The middle panel in Figure 3.6 shows the map of $\mathscr{M}_A$ toward Oph–A using results of polarimetric data at 154 μm and HCO$^+$ as a gas tracer. The $\mathscr{M}_A$ values are in the range from 0.09 to 1.61 across the cloud, with a median value of 0.37. Most of Oph–A shows $\mathscr{M}_A$ <1 (magnetically sub-Alfvénic), except the small region close to the emission peak at 89 μm , and the position of the protostar VLA–1623 at the South-West part of the map. The spatial distribution of $\mathscr{M}_A$ suggests that B-field dominates over turbulence in the cloud. The regions exhibiting the highest values of $\mathscr{M}_A$ indicate strong Alfvénic motions of the gas. The same regions are also associated with the positions of a few prestellar and protostellar cores, and YSO candidates (Enoch et al. 2009; Evans et al. 2009; Connelley & Greene 2010).

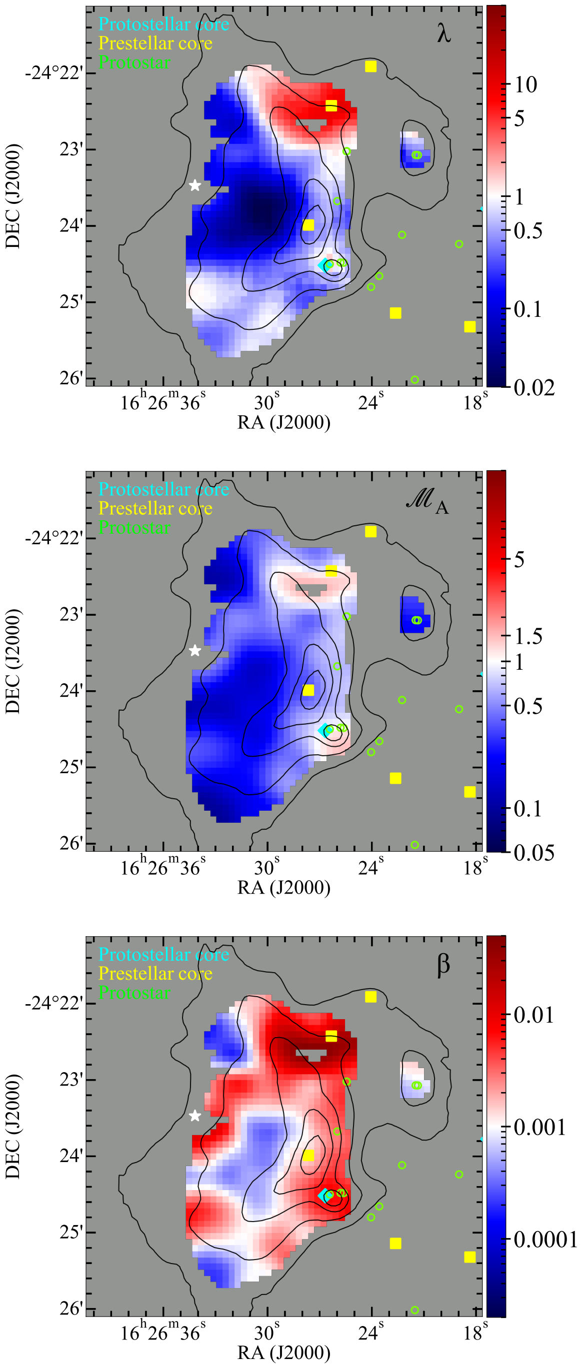

Figure 3.6: Maps of the mass-to-flux ratio (*top panel*), Alfvén Mach number (*middle panel*), and plasma β parameter (*bottom panel*) in Oph–A. In each map, the yellow squares and cyan diamonds indicate the positions of prestellar and protostellar cores, respectively, identified in the *Herschel* Gould Belt Survey (Ladjelate et al. 2020). Green circles indicate the positions of embedded protostars (Enoch et al. 2009; Evans et al. 2009; Connelley & Greene 2010), several of which were observed with ALMA (Sadavoy et al. 2019). Black contours show the continuum emission at 154 μm, similar to Figure 3.3.

3.3.5 Plasma beta parameter

To compare the magnetic (P_{mag} and thermal plasma (P_{th}) pressures in Oph–A, we construct the map of the plasma beta parameter (β), given as:

$$\beta = \frac{P_{\mathrm{th}}}{P_{\mathrm{mag}}} = 2\left(\frac{c_{\mathrm{s}}}{v_{\mathrm{A}}}\right)^2, \tag{3.6}$$

where $c_{\mathrm{s}} = \sqrt{k_{\mathrm{B}}T_{\mathrm{gas}}/\left(\mu_{\mathrm{H_2}}m_{\mathrm{H}}\right)}$ is the thermal sound speed measured in units of km s^{-1}, assuming T_{gas}=T_{dust} (see Section 3.3.2.2).

The bottom panel in Figure 3.6 shows the map of the β parameter toward Oph–A. We obtain $\beta \ll 1$ across the cloud, implying that the cloud is confined by the strong magnetic pressure, much greater than the one induced by thermal motions of the gas.

3.3.6 Virial mass analysis

To probe the dynamical state of the Oph–A cloud, we calculate the virial parameter (α_{vir}), which is the ratio of the virial mass (M_{vir}) and the isothermal mass (M_{iso}) of the cloud. The virial mass of a uniform spherical cloud, determined from B-fields, thermal, and non-thermal kinetic energies, is defined as (see e.g., Pillai et al. 2011; Devaraj et al. 2021):

$$M_{\mathrm{vir}} = \frac{3R_{\mathrm{eff}}}{G}\frac{5-2i}{3-i}\left(c_{\mathrm{s}}^2 + \sigma_{\mathrm{NT}}^2 + \frac{v_{\mathrm{A}}^2}{6}\right), \tag{3.7}$$

where R_{eff} is the effective surface radius of the cloud, i=5 is the power index of the gas volume density profile, $n(r) = n_0 r^{-i}$, and G is the gravitational constant. The isothermal mass is obtained assuming the self-gravity of the cloud, denoted as:

$$M_{\mathrm{iso}} = \frac{4}{3}\pi\rho R_{\mathrm{eff}}^3. \tag{3.8}$$

We estimate the effective radius, R_{eff} by identifying an ellipse covering the area where the B-field strengths can be measured in Oph–A. This ellipse is centered at (RA, Dec) = ($16^{h}26^{m}28\overset{\mathrm{s}}{.}78$, $-24^\circ23'34\overset{''}{.}97$) with the semi-major and semi-minor axes are a=144″ and b=100″, respectively. The R_{eff} is then determined as $R_{\mathrm{eff}} = \sqrt{ab}$ = 120″ (~0.08 pc assuming the distance to Oph–A of 137 pc). We use the mean values of the velocities, non-thermal velocity dispersion, and the gas volume density to calculate M_{vir} and M_{iso} in Eqs. 3.7 and 3.8, yielding $\alpha_{\mathrm{vir}} = M_{\mathrm{vir}}/M_{\mathrm{iso}} \approx 10$. This implies that even with the high gas density ($n(\mathrm{H_2}) \gtrsim 10^4$ cm^{-3}), the cloud is able to act against the gravitational collapse, mostly due to the strong B-fields and turbulence. Our rough estimation is in agreement with Pattle et al. (2015), who concluded that most of the cores identified in the cloud are starless, i.e. gravitationally unbound. In order to study smaller scales across the clump, a better spatial resolution of the polarimetric observations would be required.

3.4 Discussion

3.4.1 Morphology and strengths of B-fields in Oph–A

The B-field direction in Oph–A is well-ordered and shows an hourglass shape, which is almost perpendicular to the ridge of the dense cloud (Section 3.3.1). The feature is illustrated most clearly by the data at the longer wavelength (154 μm). The data at 89 μm better traces warmer dust in the lower-density region of Oph–A.

The SOFIA/HAWC+ data are qualitatively consistent with previous measurements of the B-field directions in Oph–A obtained at 850 μm using JCMT/POL–2 Kwon et al. (2018). In this dataset, Oph–A was divided into 10 subregions, identified based on their position angle of B-fields and the polarization degree, covering the entire extent of SOFIA/HAWC+ maps. The highest density region is characterized by the average B-field direction of 50°, which is also consistent with the near-IR data toward the L1688 main cloud (Kwon et al. 2015). Table 3.1 shows the median B-field position angle in each subregion which has been covered also by the FIR and sub-mm observations. The median position angles from the 89, 154, and 850 μm datasets are in rather good agreement, with the angles ranging from 3° to 19° (≤30%). The differences could be explained by the fact that the sub-mm data probe colder dust layers of the cloud, while the FIR data trace warmer layers. Indeed, such foreground layers were identified through the detection of the self-absorption features in the spectra of the [O I] line at 63 μm (Liseau et al. 2006) and the [C II] at 158 μm (Mookerjea et al. 2018). Another reason for the discrepancy in B-field position angles might be the difference in spatial resolution among the measurements in the FIR and sub-mm regimes, i.e., 7.6″, 13.6″, and 14.1″at 89, 154, and 850 μm, respectively.

Kwon et al. (2018) calculated $B_{\rm pos}$ in three subregions associated with the densest parts of Oph–A using non-thermal velocity dispersion from the N_2H^+ 1–0 line (André et al. 2007) and the sub-mm data at 850 μm. In our study, we calculate pixel-by-pixel $B_{\rm pos}$ in the entire region of Oph–A. To facilitate comparisons with the results obtained from the sub-mm data, we calculate the mean value of $B_{\rm pos}$ in two out of these three subregions,

Table 3.1: B-field direction (X) and strength in subregions for the dataset at 89, 154, and 850 μm.

Subregion[a]	X_{89} (deg)	X_{154} (deg)	X_{850} (deg)	$X_{89,850}$ Diff.[b] (%)	$X_{154,850}$ Diff.[b] (%)	$B_{\rm pos}$ (mG)		
a	73.9 ± 3.1	70.8 ± 3.2	54.4 ± 1.5	36	30	4.45	2.12	5.0
b	56.3 ± 2.7	48.7 ± 0.6	39.7 ± 4.4	42	23	0.13	0.21	–
e	87.9 ± 2.4	80.6 ± 3.4	99.6 ± 2.7	12	19	0.68	0.25	0.8
f	60.1 ± 1.5	55.0 ± 1.2	76.2 ± 4.7	21	28	0.22	0.28	–
g	82.9 ± 4.2	75.4 ± 1.4	66.3 ± 3.3	25	14	0.50	0.68	–
i	92.0 ± 4.3	84.9 ± 1.6	75.0 ± 3.0	23	13	0.39	0.47	–

Notes: (a) The subregions are named as in Kwon et al. (2018). (b) The relative difference in $X_{\lambda,850}$ is taken as $|1 - X_\lambda/X_{850}| \times 100$, where X_λ is the B-field direction at wavelength λ=[89, 154] (μm).

covered by the HAWC+ data (see Table 3.1). B_{pos} seems to be weaker than the ones obtained with the sub-mm data, which traces colder dust layers in the cloud characterized also by the higher-densities. The HAWC+ data, on the other hand, essentially traces the warmer layers in the lower-density region. Also, Kwon et al. (2018) adopted values of the polarization angle dispersion as the standard deviation of the polarization angles, which are much smaller than those using the spread of the dust polarization angles (see Section 3.3.2.1). As a consequence, the B_{pos} is expected to be stronger than the one obtained with sub-mm data.

The hourglass morphology of B-fields is a common characteristic of star-forming regions such as OMC–1 in Orion A (Ward-Thompson et al. 2017; Chuss et al. 2019; Hwang et al. 2021), Serpens South (Pillai et al. 2020), M17 (Hoang et al. 2022), NGC 6334 (Tahani et al. 2023), and even in pre-stellar cores (CB 54; Pattle et al. 2022b). This phenomenon can be explained by the motion of the high-density material during the self-gravitational collapse. When the contraction occurs, the material becomes denser and compressed, which could cause the B-field lines to be re-configured. Eventually, the B-field lines are dragged and reshaped to become more uniform and perpendicular to the high-density structure of the field. To investigate what is the relative orientation of the B-fields with respect to the gas structure in Oph–A, we quantify the projected offset angle between the orientations of B-field vectors projected on the plane-of-sky and the main structure associated with the ridge of the cloud, given as: $\Delta X = X_B - X_{\text{ridge}}$, where X_B and X_{ridge} are the position angles of the B-fields and the ridge, respectively. We identify the shape of the ridge using the Python package `RadFil`[3] (Zucker & Chen 2018, see appendix 3.C).

Figure 3.7 shows the map of the offset angles (ΔX) in Oph–A, overlaid with white contours showing the continuum emission at 154 μm. Clearly, the offset angle appears to increase when moving from the lower-density regions to the denser regions, indicating that the relative orientation of B-fields with respect to the main cloud structure turns from parallel to perpendicular toward the high-density region. This is in agreement with *Planck* polarization observations at 353 GHz (850 μm) toward nearby Gould belt molecular clouds, where the relative orientation of B-fields with respect to the gas structure changes gradually from parallel in the low-density region to perpendicular toward the higher-density region (i.e., $\log N_{\text{H}} \gtrsim 21.7$ or $A_V \gtrsim 2.7$; see Planck Collaboration et al. 2016). Figure 3.8 shows the offset angles between the orientation of B-fields and the main cloud structure as a function of the visual extinction A_V. We convert A_V from $N(\text{H}_2)$ using the relation: $N(\text{H}_2)/A_V = 0.94\times10^{21}$ molecules cm^{-2} mag^{-1} (Frerking et al. 1982). The HAWC+ data traces B-fields in the dense region with A_V ranging from ~3 up to ~260 mag. Clearly, the offset angle drops nearly to 0°at $A_V \sim 20$–30 mag. We find this change in the relative orientation of B-field from perpendicular to parallel in Oph–A similar to what is found in the dense filament in the Serpens South (Pillai et al. 2020). We note, however, the offset angle then progressively increases with $A_V>60$, indicating the relative orientation of B-field changes back from parallel to perpendicular, which was not seen in the Serpens South filamentary cloud but occurs in the other denser region with very high A_V (see e.g, Serpens Main Kwon et al. 2022).

We also compare our B_{pos} strengths calculation with that measured in other molecular

---

[3] `https://github.com/catherinezucker/radfil`

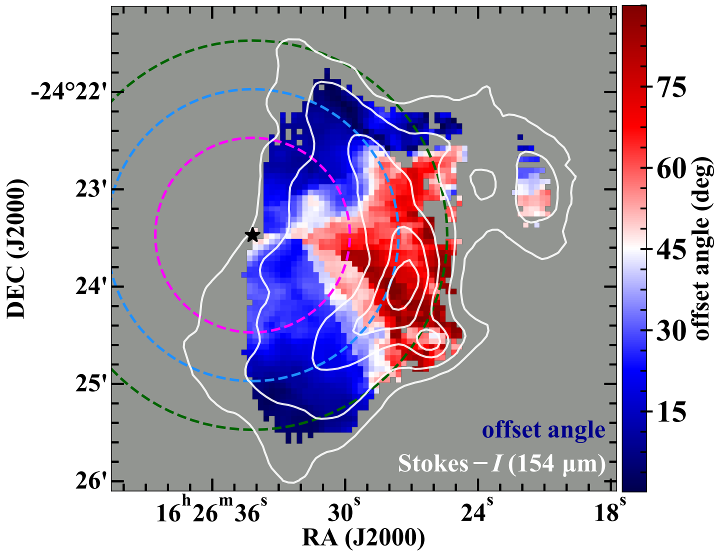

Figure 3.7: Map of the offset angle between orientations of B-fields and main cloud structure in Oph–A. White contours show the continuum emission at 154 μm with similar levels as in Figure 3.3. The dashed circles centered at the position of the S1 star have a radius of 60″ (magenta), 90″ (blue), and 120″ (green), corresponding to the levels of A_V of ~6, 30, and 200 mag. The star symbol indicates the position of the S1 star.

clouds. The B-field strengths in Oph–A are higher than those in most clouds, where it ranges from 50 to 400 μG (Coudé et al. 2019; Pattle et al. 2021; Ward-Thompson et al. 2023). Noteworthy, B-fields in Oph–A are similar to those OMC–1 cloud in Orion A region, where B_{pos} of a few mG was measured (Pattle et al. 2017; Hwang et al. 2021).

Magnetic field strength B_{tot} (or B) can be expressed as a function of n_{H} (or n): $B \propto n^k$. Theoretical models predict k ~2/3 in the weak B-field regions (Mestel 1966) and k ≲0.5 in the strong B-field regions where magnetic energy dominates over the gravity (Mouschovias & Ciolek 1999). Consequently, in the later case, it suggests that the gas density would increase faster than the B-field strength if there is any collapse in the dense cloud. Here, we test the relation $B - n$ within the Oph–A cloud. Figure 3.9 shows the B-field strength as a function of gas volume density, n, in Oph–A. We find a strong correlation between the B-field strength and the gas density, characterized by the Pearson coefficient of ~0.8, corresponding to ~24σ. We perform the power-law fit toward the dataset using the `curve_fit` function in Python ($B = a \times n^k$). We find a power-law index of $k = 0.51 \pm 0.01$, which is similar to the theoretical prediction for strong B-fields (Mouschovias & Ciolek 1999). This is also consistent with $\beta \ll 1$, representing strong B-fields in Oph–A (see bottom panel in Figure 3.6 and Section 3.3.5). Crutcher et al. (2010) implemented the fit for a large sample of diffuse and dense molecular clouds and found a higher power-law index, k ≈0.65, which suggests a faster increase of B-field strength with density than that expected from theoretical predictions (see Figure 3.9). We note, however, that this result was based on the mean values of B and n in the molecular cloud, where the conditions of gas density and B-field might differ locally.

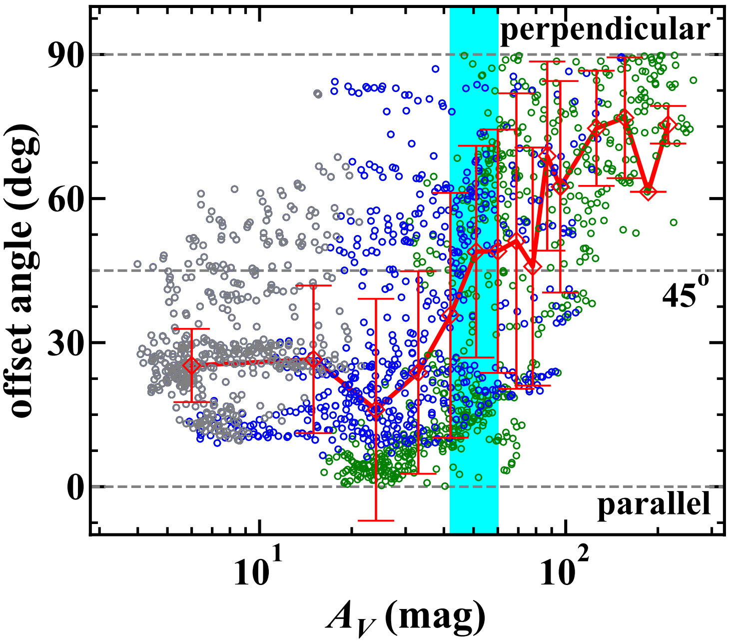

Figure 3.8: Distribution of the offset angles between the orientations of B-fields and the ridge in Oph–A, as a function of A_V (circle symbols). The data in gray color represent the offset angle collected within the magenta circle centered at the position of the S1 star with a radius of 60″ in Figure 3.7. The data in blue and green additionally represent the offset angle collected within the two rings "II" and "III" in Figure 3.7, respectively. The red diamonds represent the median value of the offset angles in each interval of A_V=3. The number of red diamonds is reduced to improve the clarity of the figure. The red curve connecting all the red diamonds shows the trend of the offset angles vs. A_V in Oph–A. The cyan box indicates the range of A_V= 42–60 where relative orientation between B-fields and the ridge changes from parallel to perpendicular. The gray horizontal dashed lines indicate perpendicular, 45°, and parallel relative orientations of B-fields with respect to the ridge.

3.4.2 Magnetic fields versus stellar feedback

High-mass stars irradiate and heat up the surrounding gas and create the H II regions (see e.g., Zinnecker & Yorke 2007). The ionized, hot gas expands and interacts with the environment. The radiation pressure can drive strong shock winds that can sweep up all material away into the denser region. The lower-density matter in the outer regions are more exposed to the ionization source and pushed away faster than the higher-density matter. This results in dust and gas being driven away, compressed and forming the dense shell structure at the edge of the cloud. Here, we investigate a possible impact of the radiation field from the high-mass star S1 on the Oph–A cloud. The Oph–A molecular cloud is directly exposed to the strong UV radiation field emitted by the S1 star from the East. Figure 3.10 shows the map of the continuum emission at 154 μm from SOFIA/HAWC+, superimposed by the white contours showing the $N(H_2)$ column density.

We calculate the external radiation pressure the S1 star acting on the densest part of

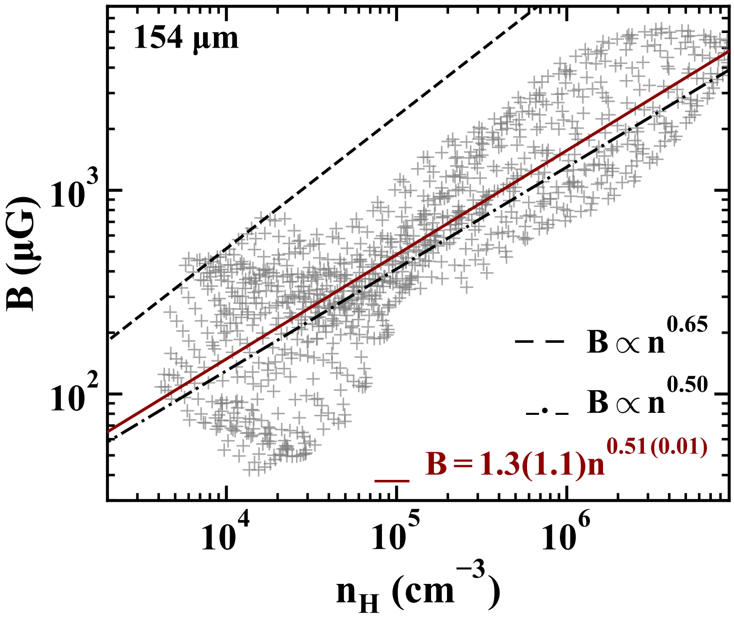

Figure 3.9: Correlation between B-field strengths and gas volume density in Oph–A. $B_{\rm pos}$ is calculated using data in band D centered at 154 μm. The black dash-dotted line indicates the critical power-law $B \propto n^{0.5}$ for strong B-fields predicted from the theoretical models (Mouschovias & Ciolek 1999). The black dashed line indicates the relation found by Crutcher et al. (2010) using the Zeeman observational data. The red solid line shows the power-law fit toward our data in Oph–A, the values in the bracket stand for the uncertainty of the parameters derived from the power-law fit.

the cloud, given by:

$$P_{\rm ext,rad} = \frac{L_{\rm bol}}{4\pi\mathcal{R}^2 c}, \tag{3.9}$$

where $L_{\rm bol}$=1100 $L_\odot$ is the luminosity of the S1 star adopted from Lada & Wilking (1984) and $\mathcal{R} \approx 0.06$ pc is the projected distance to the S1 star. We obtain $P_{\rm ext,rad}/k_{\rm B} \approx 2.4 \times 10^6$ K cm^{-3}, which is in agreement with the result calculated from the ionizing photons emitted by the S1 star (~2×10^6 K cm^{-3}, Pattle et al. 2015).

To compare with the external radiation pressure, we calculate the internal thermal pressure due to the hot gas in Oph–A, $P_{\rm th} = nk_{\rm B}T_{\rm gas}$ where n is the gas density. We consider the hot gas within the densest part of Oph–A where I>0.4 Jy/arcsec^2 at 154 μm only, which corresponds to the area inside the third contour shown in Figure 3.4. Within this region, we adopt $n = n_{\rm H}$ in the range of 10^4–10^6 cm^{-3} and the average temperature of the hot gas $T_{\rm gas} \approx T_{\rm dust} \approx$20 K, which yields $P_{\rm th}/k_{\rm B}$ in the range of (0.2–20)×10^6 K cm^{-3}. The highest internal thermal pressure of ~2×10^7 K cm^{-3} is seen toward the densest part of the cloud, associated with the position of the SM1 core. This suggests that the internal thermal pressure is strong enough to help the material refrain from external pressure. We note that, however, in the vicinity region away from the center (for e.g., the tails of the ridge shown in Figure 3.10), the internal thermal pressure is weaker, at least 1 order of magnitude less than the external one. In this case, the radiation pressure from the S1 star on the east side is dominant and able to push away all the matter into the surrounding envi-

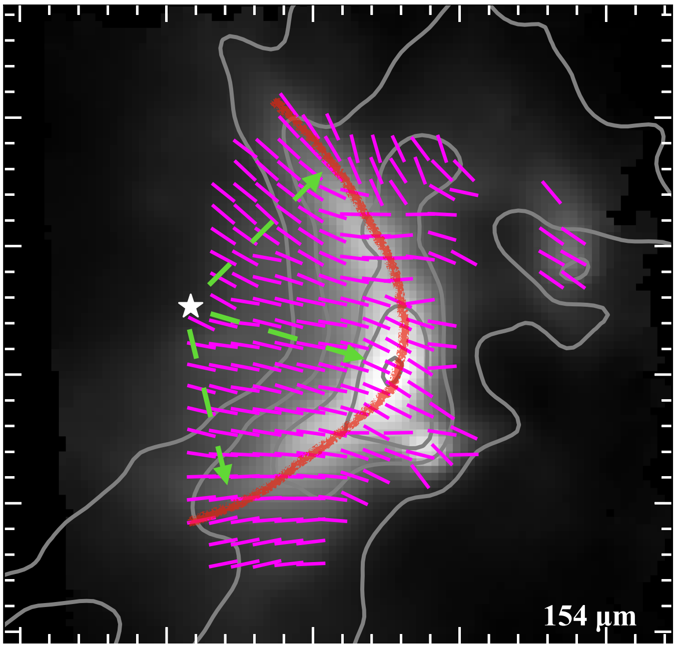

Figure 3.10: Image of the continuum emission at 154 μm toward Oph−A. B-field vectors obtained from SOFIA/HAWC+ at 154 μm are shown in magenta solid segments. The green dashed arrows indicate the radiation directions from the S1 star toward the cloud. White star marks the position of the S1 star. The red curve illustrates the elongated shape of the ridge in the dense cloud. The gray contours are the $N(H_2)$ column density, with contour levels at (1, 2, 5, 10, 20)$\times 10^{22}$ cm^{-2}.

ronment toward the west side. However, it is observed that the material in the low-density region still survives, despite owning a low internal thermal pressure (see Figure 3.10), indicating that there must be another mechanism is engaged in. This is likely due to the presence of the B-field in Oph–A with the strength of a few mG. We estimate roughly the magnetic pressure ($P_{\rm mag} = B^2/(8\pi)$) to be in the range of 10^8–10^9 K cm^{-3} for B-field strengths between 1–5 mG. This indicates that the magnetic pressure is at least two orders of magnitude higher than the external pressure of $\sim 10^6$ K cm^{-3}, Thus, the magnetic pressure is sufficient to support the matter against the external pressure along with the gas thermal pressure.

We investigate how the interplay between the strong B-field and radiation direction on the evolution of the cloud. We determine the mean radiation direction from the S1 star toward the densest region in the cloud, associated with the position of the starless core SM1 by connecting the S1 star and SM1 core positions. We find that the main radiation direction of 70°, measured east to north. We also estimate the main B-field orientation in the densest region of Oph–A of ~74°, almost along the radiation field. The strong radiation pressure from the S1 star pushes all the material away and creates a dense shell toward the west side. To prevent this compression of dust and gas in the dense region, the B-fields exert a magnetic pressure perpendicular to the B-field orientation, which is also seen perpendicular to the direction of the radiation pressure. This suggests that the magnetic pressure does not help the matter resist the external pressure, but also tends to stretch the structure out along the NW-SE direction, resulting in an elongated shape of the dense shell. When moving toward the vicinity in the west side, the external thermal pressure is blocked by the gas thermal pressure due to the high-density material. This results in the ridge shape in the cloud with very high densities. These results are consistent with what found by the 3D magnetohydrodynamic (MHD) simulation presented by Henney et al. (2009). They predicted that if the B-field orientation in the cloud is parallel or along with the radiation direction, the tends to have a flattened shape. We note that, however, toward the north-east and south-east regions the offset position angles between the B-field vectors and radiation field become larger, i.e., the B-field orientation becomes perpendicular to the radiation direction. In this such case, the magnetic pressure and tension induced by B-fields run parallel with the radiation pressure, suggesting magnetic pressure plays a positive role to support the matter against the radiative compression and prevent the sweeping dust and gas away. This results in bending the material structure and finally, an umbrella-like shape in the dense ridge is formed. Interestingly, in the case study of Oph–A the ionization source is very close to the cloud (<0.1 pc) and the offset position angle between the radiation and magnetic fields is not homogeneous but varies from parallel to orthogonal. This allows to examine widely how the interplay between the B-fields and radiation fields could influence the material structure of the cloud.

In conclusion, the strong B-fields in Oph–A is found to be important in supporting the material prevent the radiative compression, but also in regulating the material structure in the dense cloud together with the radiation fields.

3.5 Summary

In this Chapter, we presented the analysis using the SOFIA/HAWC+ polarimetric observations toward the Oph–A molecular cloud in the L1688 active star-forming region of the Ophiuchus dark cloud complex. Our main results are as follows:

- Using the map dust polarization at 89 and 154 μm, we derive the map of the map of B-field morphology in Oph–A. We found that the B-field in Oph–A is are generally well-ordered and tend to be bent perpendicular perpendicular to the ridge of the cloud toward the higher-density regime. We measured the $B_{\rm pos}$ in the entire region of Oph–A using the DCF method, ranging from 0.1 to 6 mG at 89 and 154 μm. The $B_{\rm pos}$ is seen strongest toward the densest region of the cloud associated with the starless core SM1, and decrease toward the outskirt. This is the first time we manage to estimate the distribution of the B-field strengths in Oph–A, which is important to understand how the B-fields vary across the entire region. Our derived B-fields morphology and strengths are in good agreement with the previous measurements using the sub-mm data.

- We calculated the distribution of the mass-to-flux ratio, Alfvénic Mach, and plasma β toward Oph–A using the inferred $B_{\rm pos}$ from SOFIA/HAWC+ data at 154μm. We found that the cloud is magnetically sub-critical and sub-alfvénic where B-field dominates over the gravity and turbulence in Oph–A. We obtained $\beta \ll 1$ in Oph–A, suggesting the cloud is confined by the strong magnetic pressure and much greater than the thermal gas pressure. Our Virial analysis in the entire cloud shows the Virial parameter $\alpha_{\rm vir} \sim 10$, suggesting that the cloud is gravitationally unbound and able to against the self-gravitational collapse. However, our rough estimation is applied for the entire cloud; whereas Oph–A is known as one of the densest part of the active star-forming region L1688 hosting a few pre- and proto-stellar cores and embedded protostars. The higher spatial resolution observations toward the smaller scale region in the cloud will be necessary to investigate in detail the dynamical state of the cloud.

- We examined the role of B-fields in supporting the cloud against the external pressure due to the ionization radiation from the nearby high-mass star S1. We found that at the center part of the cloud, the magnetic pressure indeed does not play a role in helping the material prevent radiative compression. However, toward the northeast and southeast regions of the cloud the magnetic pressure positively supports the cloud to prevent the radiative pressure together with the gas thermal pressure.

Appendix

3.A Histogram of SOFIA/HAWC+ dataset

Figure 3.A.1 and 3.A.2 show the histogram of Stokes–I, σ_I, SNR$_I$, p, σ_p, and SNR$_p$ of the SOFIA/HAWC+ data in band C and band D. Table 3.A.1 shows the summary of the mean and RMS of the distribution of Stokes–I, p, their uncertainties and SNRs.

Table 3.A.1: Summary of the mean and RMS of I, P, and their SNR.

Wavelength	I (Jy/arcsec^2)		σ_I (Jy/arcsec^2)		SNR$_I$	
	Mean	RMS	Mean	RMS	Mean	RMS
89 μm	0.163	0.166	0.00488	0.004409	44.825	52.879
154 μm	0.143	0.142	0.00122	0.000713	177.478	214.099

Wavelength	p (%)		σ_P (%)		SNR$_P$	
	Mean	RMS	Mean	RMS	Mean	RMS
89 μm	8.272	9.229	6.284	7.784	3.189	3.486
154 μm	5.702	4.135	1.245	1.527	10.333	9.909

3.B Velocity dispersion traced by other molecular lines

To test whether the FWHM map of HCO$^+$4–3 line is the good choice, we further use the N$_2$H$^+$ 3−2 molecular data observed from APEX to estimate the total velocity dispersion, σ_v. The majority of the Oph–A cloud exhibits the N$_2$H$^+$ 3−2 emission showing 3 single Gaussian profiles; the middle peak is much stronger compared with the other two components. This strongest hyperfine line indicates the central velocity which is in the range of 2.54–3.97 km s^{-1}, with an average velocity of 3.42 km s^{-1}, in agreement with the systemic velocity of Oph–A of ~3.44 km s^{-1} estimated by André et al. (2007). To each pixel we fit the spectrum with the sum of 3 single Gaussian profiles and then use the line width of the primary peak as the total velocity dispersion toward the computing pixel. We construct the map of the FWHM velocity dispersion, following the procedure presented in Section 3.3.2.2 for the case of the HCO$^+$ molecular line.

Figure 3.B.1 shows the map of the non-thermal FWHM of the N$_2$H$^+$ 3−2 molecular line toward Oph–A. The FWHM ranges from 0.18 to 1.73 km s^{-1} with a median value of 0.95 km s^{-1}, in good agreement with those obtained by HCO$^+$ line. We note, however, that the spatial extent of the HCO$^+$4–3 emission line is large than that of the N$_2$H$^+$ 3−2. Thus, we use the map of FWHM of the HCO$^+$ line to calculate the $B_{\rm pos}$ strengths in Oph–A. Similarly, White et al. (2015) reported a mean FWHM velocity dispersion of 1.5 km s^{-1} using the ^{18}O 3−2 data from JCMT/HARP in overall entire ρ Ophiuchus cloud. Using the N$_2$H$^+$ 1−0 data from IRAM, André et al. (2007) estimated an average value of the one-dimensional nonthermal velocity dispersion toward Oph–A, $\sigma_{\rm NT}$=0.2 km s^{-1}, corresponding to $\Delta v_{\rm NT}$ ~0.47 km s^{-1}. Observations of the NH$_3$ hyperfine emission from the Green Bank telescope (GBT) also returned the similar 1D velocity dispersion with the

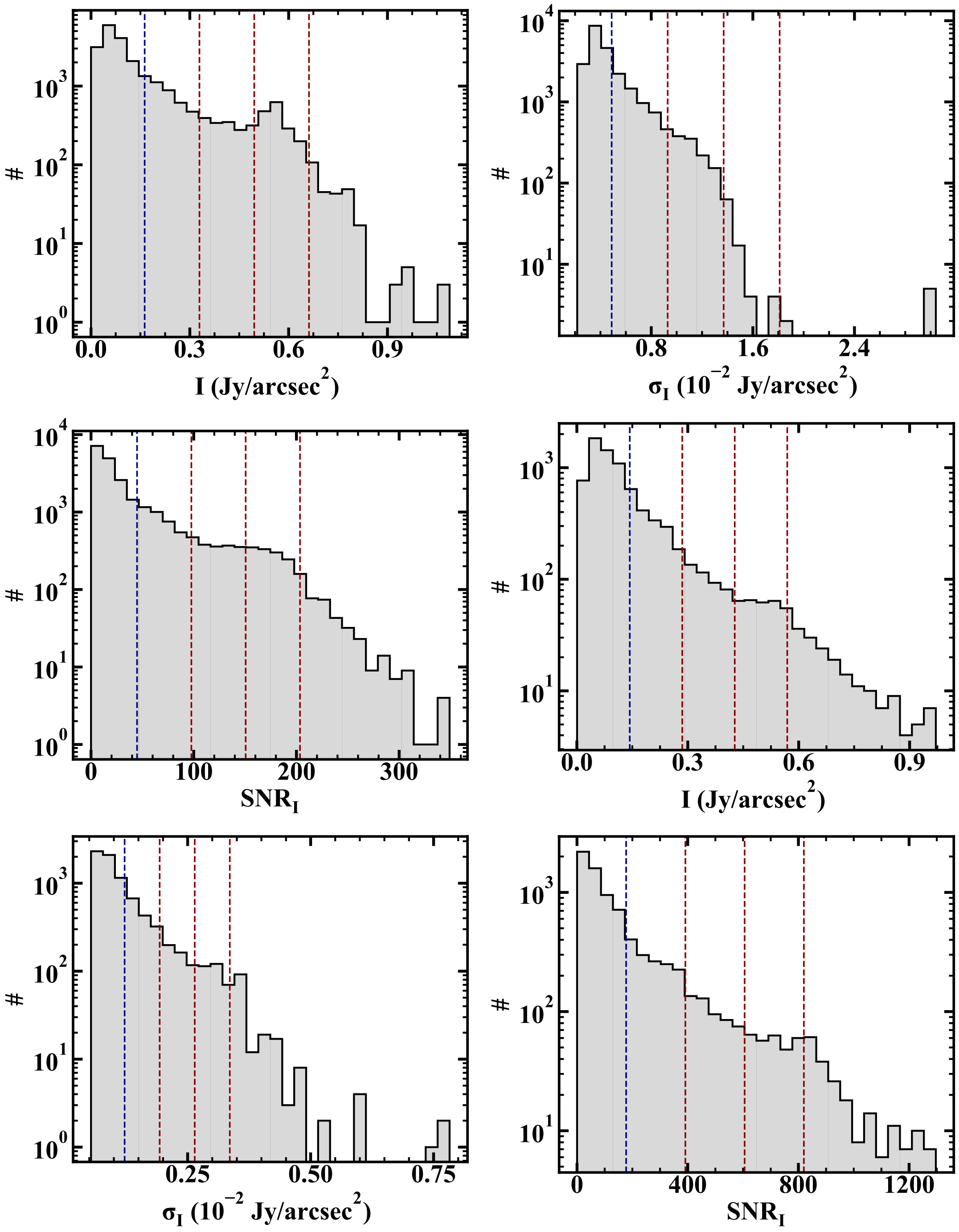

Figure 3.A.1: Histograms of Stokes–I (left panels), σ_I (middle panels), and SNR_I (right panels) of the SOFIA/HAWC+ data. Top panels represent data in band C at 89 μm and bottom panels represent data in band D at 154 μm. The blue vertical dashed lines in each panel represent the mean value of the distribution. The red vertical dashed lines show the position of mean value plus 1σ, 2σ, and 3σ of the distribution from left to right, respectively.

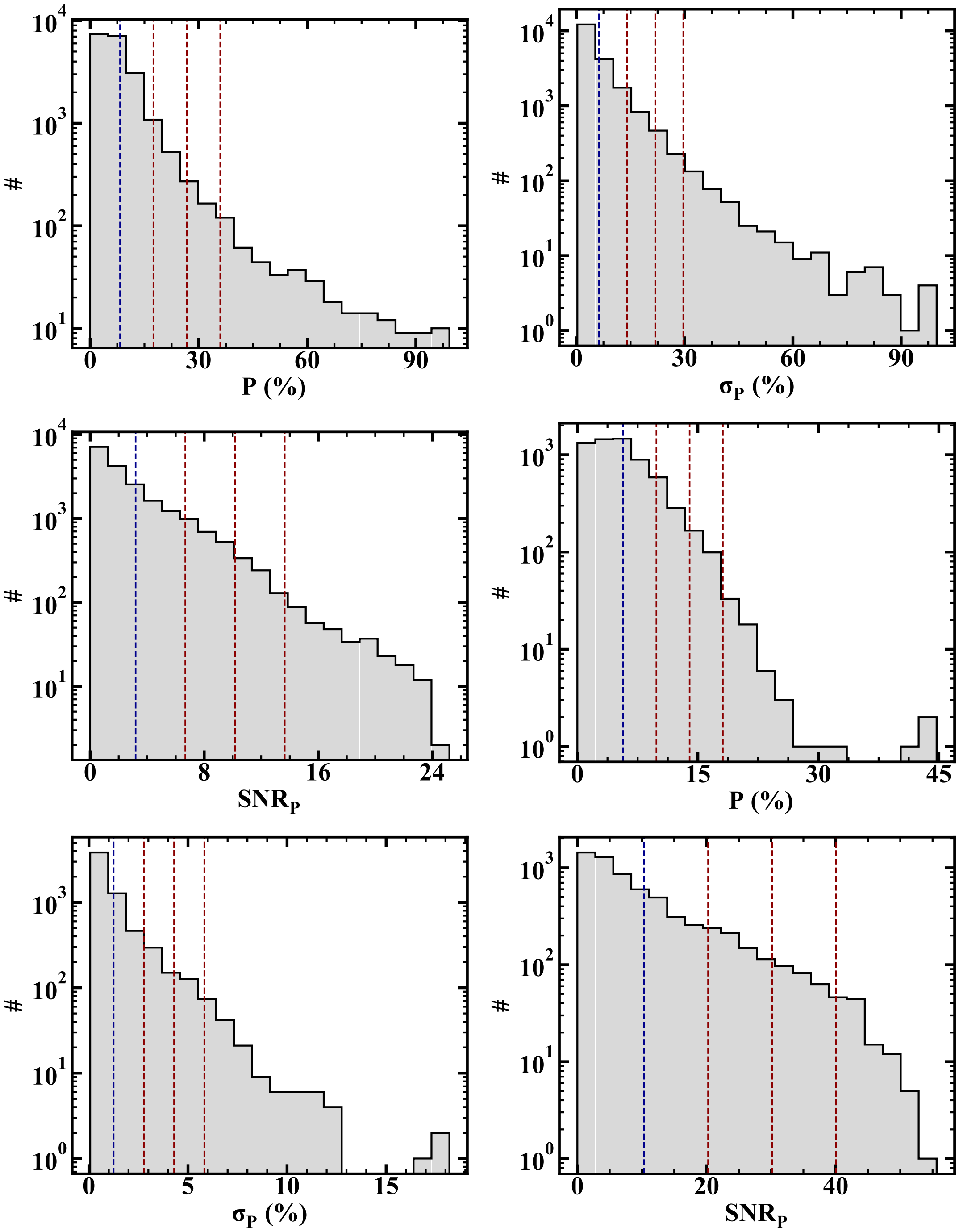

Figure 3.A.2: Histograms of p (left panels), σ_p (middle panels), and SNR$_p$ (right panels) of the SOFIA/HAWC+ data. Top panels represent data in band C at 89 μm and bottom panels represent data in band D at 154 μm. The blue vertical dashed lines in each panel represent the mean value of the distribution. The red vertical dashed lines show the position of mean value plus 1σ, 2σ, and 3σ of the distribution from left to right, respectively.

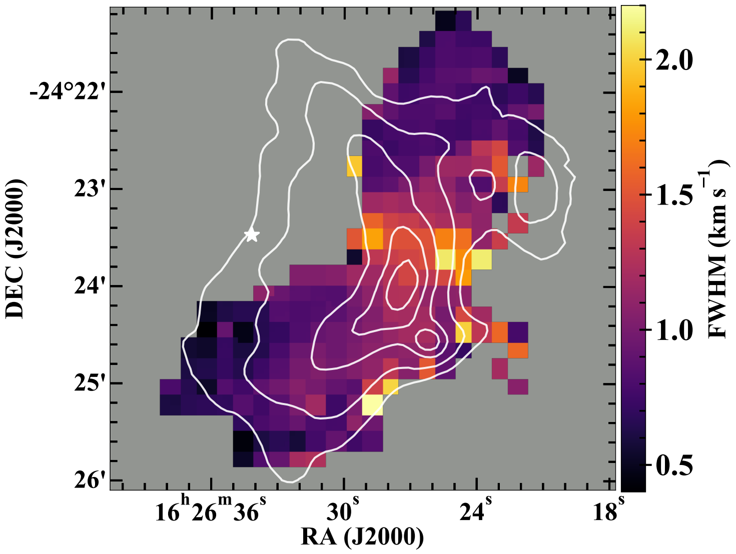

Figure 3.B.1: Distribution of the non-thermal FWHM of the N_2H^+ 3−2 molecular line toward Oph–A. White star marks the position of the S1 star. White contours show the continuum emission (Stokes–I) at 154 μm, with contours levels at 0.12, 0.2, 0.4, 0.6, and 0.8 Jy/arcsec^2.

average value of 0.3 km s^{-1}, corresponding to an average of FWHM of 0.65 km s^{-1} (Chen et al. 2019).

3.C Main structure of the ridge identification

We identify the elongated shape of the ridge in the densest region of Oph–A using the Python package `RadFil`. We first apply a threshold of I ≥0.5 Jy/arcsec^2 in the map of Stokes–I at 154 μm to build a mask for the main shape of the densest region. The spine of the ridge is identified by using the Python package `FilFinder`[4] from Koch & Rosolowsky (2015). We then smooth the spine of the ridge and define a tangent line at every position on the ridge, from that the orientation of the ridge at every position is identified. Figure 3.C.1 shows the schematic view of the ridge and the perpendicular cuts at each position on the ridge. The position angle of the tangent line at each position located on the ridge is defined as the orientation of the ridge at that position, measured east to north and ranges from 0°to 180°.

---

[4] `https://github.com/e-koch/FilFinder`

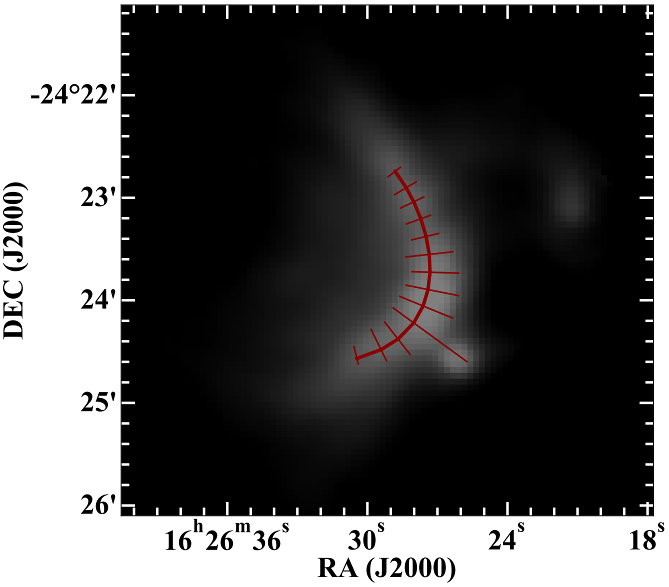

Figure 3.C.1: Schematic view of the ridge in the Oph–A. The background color map shows the Stokes–I intensity at 154 μm. The thick red line indicates the main shape of the ridge. Thin red lines show the lines perpendicular to the tangent line at each position on the ridge.

Chapter 4

Far-infrared line emission from the outer Galaxy cluster Gy 3–7 with SOFIA FIFI-LS: Physical conditions and UV fields

Based on N. Lê et al. (2023), Astronomy & Astrophysics, 674, 64

4.1 Introduction

During the earliest stages of star formation, the gravitational collapse of dense cores is accompanied by the ejection of bipolar jets originating from the resulting protostars, which may alter physical conditions and chemistry of their environment, even on clump scales (Arce et al. 2007; Frank et al. 2014a). Non-dissociative shock waves develop as the jets (and winds) interact with the surrounding medium (Kaufman & Neufeld 1996; Flower & Pineau des Forêts 2012), and heat up the gas up to typically ~300 K (Karska et al. 2018; Yang et al. 2018). Additionally, ultraviolet (UV) photons contribute to the gas heating and influence the chemical composition of the low- to high-mass protostars' envelopes (Bruderer et al. 2009; Visser et al. 2012). Similar to some pc-scale outflows, UV photons may operate over a significant fraction of low-mass star-forming clumps and clusters (Mirocha et al. 2021). The cooling of the gas, which in the case of embedded objects is dominated by line emission in the far infrared (far-IR) and (sub)millimeter domains, provides important constraints on the heating mechanisms and observations of these cooling lines allow us to constrain gas temperatures, densities, and UV fields (Goldsmith & Langer 1978; Hollenbach & McKee 1989).

Recent observations with the *Herschel* Space Observatory (Pilbratt et al. 2010)[1] targeted the main gas cooling lines toward a significant sample of protostars spanning a broad range of masses (van Dishoeck et al. 2021). In particular, the Photodetector Array Camera and Spectrometer (PACS; Poglitsch et al. 2010) provided detections of high−J

---

[1] *Herschel* was an ESA space observatory with science instruments provided by European-led Principal Investigator consortia and with important participation from NASA.

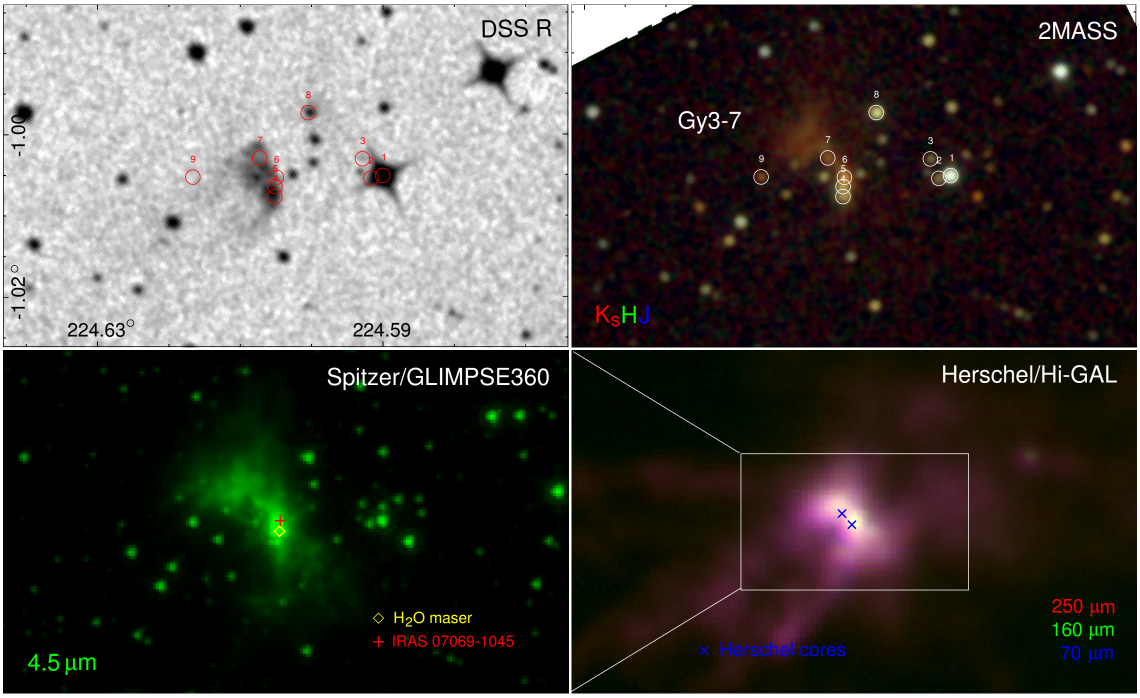

Figure 4.1: Digital Sky Survey (DSS) R (top left), 2MASS composite image using the J, H and K_s filters (top right), *Spitzer*/GLIMPSE360 4.5 μm (Sewiło et al. 2019; bottom left), and *Herschel*/Hi-GAL composite image at 70, 160, and 250 μm (Elia et al. 2013; bottom right) of the Gy 3–7 cluster. The circles in top panels show the positions of YSO candidates from Tapia et al. (1997). The yellow diamond and red cross in the bottom left panel show the position of the H_2O maser (Urquhart et al. 2011) and the IRAS source at the south-west side (IRAS 07069–1045), respectively. The blue " × " symbols in the bottom right panel show the positions of dense cores as traced by the H_2 column density (Elia et al. 2013); the dense core in the west corresponds to IRAS 07069–1045.

CO ($J_{\rm up}$ ≥14), H_2O, and OH lines, and forbidden transitions of [O I] and [C II], all of them being important diagnostic tools in molecular clouds. Among the key findings with PACS are the following: (i) the presence of ubiquitous ‘warm’ gas (~300 K) associated with low- to high-mass protostars (Green et al. 2013; Manoj et al. 2013; Karska et al. 2013, 2014a; Matuszak et al. 2015); (ii) the detection of a plethora of high$-J$ CO (up to $49-48$; $E_{\rm u}$ ~6700 K) and H_2O (up to $E_{\rm u}$ ~1500 K) lines tracing the ‘hot’ gas component (Herczeg et al. 2012; Goicoechea et al. 2012), with a median temperature of ~720 K (Karska et al. 2018); (iii) the identification of the origin of the far-IR line emission in UV-irradiated non-dissociative shocks extending along the outflows (Karska et al. 2014b; Benz et al. 2016; Kristensen et al. 2017b; Karska et al. 2018); (iv) the recognition of the dominant role of CO and H_2O in the gas cooling budget of low-mass (LM) protostars (Karska et al. 2013, 2018), and CO and [O I] as coolants of high-mass (HM) protostars (Karska et al. 2014a). The above observations provided a surprisingly uniform picture of the far-IR line emission from deeply-embedded protostars, but targeted only relatively nearby regions (d<450 pc in case of LM objects van Dishoeck et al. 2021).

Observations of the Large and Small Magellanic Clouds (LMC and SMC) with *Her-*

schel shed some light on the far-IR line cooling from protostars in a significantly different, low-metallicity environment (Z of 0.2–0.5 $Z_\odot$; Russell & Dopita 1992). The Spectral and Photometric Imaging Receiver (SPIRE, Griffin et al. 2010) and PACS provided detections of CO (up to J=14-13), H_2O, OH, and [O I], and [C II] lines, facilitating comparisons with Galactic sources (Oliveira et al. 2019). The CO emission toward 15 sources in the LMC showed two relatively cool gas components, with temperatures of ~40 and ~120 K, consistent with Galactic measurements using SPIRE (White et al. 2010; Jiménez-Donaire et al. 2017; Yang et al. 2018). The line cooling budget of protostars in the Magellanic Clouds is dominated by [O I] and [C II] emission, with an increasing contribution of CO as the metallicity increases from the SMC to LMC, and to the Galactic young stellar objects (YSOs, Karska et al. 2014a; Oliveira et al. 2019). The low fraction of CO line cooling is interpreted as a metallicity effect: the combined result of a reduced carbon abundance and higher grain temperatures due to a lower shielding from UV photons (Oliveira et al. 2019).

The outer parts of our Galaxy provide an alternative site for testing the impact of metallicity on the far-IR gas properties of protostars. Due to the negative-metallicity gradient, the abundances of dust and molecules decrease in the outer Galaxy (Sodroski et al. 1997). The metallicity affects the gas and dust cooling budget of molecular clouds and results in lower CO rotational temperatures, T_rot (Roman-Duval et al. 2010). Despite the overall decreasing trend of the mass surface density of molecular clouds in the outer Galaxy (for a review, see Heyer & Dame 2015), some star-forming regions show a significant star-formation activity. For example, the CMa–l224 star-forming region at Galactocentric radius, R_GC, of 9.1 kpc, consists of ~290 Class I/II YSOs, as identified by Sewiło et al. (2019) using data from 'GLIMPSE360: Completing the Spitzer Galactic Plane Survey' (PI: B. Whitney) and the 'Herschel infrared Galactic Plane Survey' (Hi-GAL; Molinari et al. 2010a, see also Elia et al. 2013). The expected metallicity of this region is ~0.55-0.73 $Z_\odot$, depending on the adopted O/H Galactocentric radial gradient (Balser et al. 2011; Fernández-Martín et al. 2017; Esteban & García-Rojas 2018).

Gy 3–7 is a deeply-embedded cluster with exceptionally bright far-IR continuum emission, located at the second most-massive filament in the CMa–l224 region (Sewiło et al. 2019) at a distance of ~1 kpc (e.g, Lombardi et al. 2011). It is associated with IRAS 07069–1045 that was early on recognized as a star-forming region driving a CO outflow, with the bolometric luminosity (L_bol) of 980 $L_\odot$ (assuming a distance of 1.4 kpc; Wouterloot & Brand 1989). The source was considered as a candidate HM star-forming region based on its position on the IRAS color-color diagrams and the presence of dense gas traced by CS $2-1$ (Wood & Churchwell 1989; Bronfman et al. 1996). However, several attempts failed to detect the CH_3OH maser emission, which is a common signature of HM protostars (Menten et al. 1992; Szymczak et al. 2000). Instead, H_2O maser and thermal NH_3 emission was detected as part of the Red MSX Survey (RMS; Urquhart et al. 2011, see Figure 4.1).

Recent far-IR observations with *Herschel*/Hi-GAL spatially resolved two dense cores in Gy 3–7 with L_bol of 75.9 and 324.2 $L_\odot$, the latter corresponding to IRAS 07069–1045 (Elia et al. 2013, 2021, see Figure 4.1). Near-IR observations revealed an extended H_2 emission, which may arise from the jets from protostars (Navarete et al. 2015). Gy 3–7 contains several more evolved YSOs, with spectral types ranging from B1 to B5 (Gyulbudaghian 2012; Tapia et al. 1997), and is cataloged as a young stellar cluster (Soares & Bica 2002, 2003; Bica et al. 2003).

In this Chapter, we investigate the far-IR line emission toward Gy 3–7 obtained using the Stratospheric Observatory for Infrared Astronomy (SOFIA) observations with the Field-Imaging Far-Infrared Line Spectrometer (FIFI-LS; Klein et al. 2014; Fischer et al. 2018). We also consider the gas densities and UV radiation fields in Gy 3–7, and the stellar content of the cluster. We examine whether the rotational temperatures and the ratio of CO and [O I] line luminosities in Gy 3–7 are consistent with the picture of star formation in the inner Galaxy and/or the low-metallicity environment of the Magellanic Clouds. Finally, we also present the results of our search for water masers with the Toruń 32-m radio telescope (RT4).

This Chapter is organized as follows. Section 4.2 describes the observations with SOFIA/ FIFI-LS and RT4. In Section 4.3, we present line and continuum maps, and the line profiles at selected positions of interest. Section 4.4 shows the analysis of the results and Section 4.5 provides the discussion of the results in the context of previous studies. We provide the summary and conclusions in Section 4.6.

4.2 Observations

4.2.1 SOFIA FIFI-LS

SOFIA/FIFI-LS observations were collected in November 2019 as part of the SOFIA Cycle 7 (Project ID 07_0157, PI: M. Kaźmierczak-Barthel). FIFI-LS is an integral field unit consisting of two grating spectrometers with a spectral coverage ranging from 51 to 120 μm (blue) and from 115 to 200 μm (red), facilitating simultaneous observations of selected wavelength intervals (0.3-0.9 μm) in both channels (SOFIA Observer's Handbook for Cycle 10[2]). The spectral resolution, R, ranges from ~500 to 2000, and increases with wavelength for a given grating order. The corresponding velocity resolution of ~150 to 600 km s^{-1} provides unresolved spectral profiles of all far-IR lines, including H_2O (Kristensen et al. 2012; Mottram et al. 2017), CO (Kristensen et al. 2017b), and [O I] (Kristensen et al. 2017a; Yang et al. 2022a).

The FIFI-LS detector is composed of 5×5 spatial pixels (hereafter *spaxels*) with the centers offset by 10″, similar to the PACS spectrometer on *Herschel*. The spaxel size is $6'' \times 6''$ in the blue channel (field-of-view, FOV, of $30'' \times 30''$) and $12'' \times 12''$ in the red channel (FOV of $1' \times 1'$), providing an improvement over PACS by matching the actual wavelength-dependent beam sizes. The far-IR sky background was subtracted by symmetric chopping around the telescope's optical axis with a matched telescope nod. The 300″ throw in the east-west direction was chosen to avoid contaminated regions.

Table 4.1 shows the full catalog of lines targeted with FIFI-LS. The maps of the [O I] line at 63.2 μm and the [C II] line at 157.7 μm were obtained simultaneously as 2×2 mosaics, with a FOV of $60'' \times 60''$ in the blue channel, and $90'' \times 90''$ in the red channel, during the wall-clock time of 51 minutes. The maps of the remaining lines were collected as a single FOV with dithering. The total observing time was 239 minutes (~4 hours).

---

[2] `https://www-sofia.atlassian.net/wiki/spaces/OHFC1/overview`

Table 4.1: Catalog of lines observed with FIFI-LS toward Gy 3–7

Line	Transition	E_u/k_B (K)	A_u (s^{-1})	g_u	λ_{lab} (μm)	Map size (″×″)	Beam (″)
CO	14 – 13	580.5	2.7(-4)	29	185.99	60×60	18.3
CO	16 – 15	751.7	4.1(-4)	33	162.81	60×60	16.1
CO	17 – 16	845.6	4.8(-4)	35	153.27	60×60	15.2
CO	22 – 21	1397.4	1.0(-3)	45	118.58	30×30	11.9
CO	30 – 29	2564.9	2.3(-3)	61	87.19	30×30	8.6
CO[a]	31-30	2735.3	2.5(-3)	63	84.41	30×30	8.3
OH[b]	$\frac{1}{2},\frac{1}{2}-\frac{3}{2},\frac{1}{2}$	270.1	6.5(-2)	4	163.12	60×60	16.1
OH[c]	$\frac{1}{2},\frac{1}{2}-\frac{3}{2},\frac{3}{2}$	181.7	2.9(-2)	3	79.18	30×30	7.9
OH[a]	$\frac{7}{2},\frac{3}{2}-\frac{5}{2},\frac{3}{2}$	290.5	5.1(-1)	9	84.42	30×30	8.3
[O I]	$^3P_0$–$^3P_2$	227.7	8.9(-5)	3	63.18	60×60	7.1
[O I]	$^3P_1$–$^3P_2$	326.6	1.8(-5)	1	145.52	60×60	14.4
[C II]	$^2P_{3/2}$–$^2P_{1/2}$	91.2	2.4(-6)	5	157.74	90×90	15.6

Notes: Molecular data adopted from the Leiden Atomic and Molecular Database (LAMDA, Schöier et al. 2005) and the JPL database (Pickett et al. 1998). [a] CO 31-30 and OH line at 84.42 μm are blended. [b] OH line at 163.12 μm is non-detected [c] The 79.18 μm is detected at the band edge, and its line fluxes cannot be securely measured due to the lack of baseline.

The data was reduced with the SOFIA FIFI-LS pipeline (Vacca et al. 2020), which contains all the necessary calibrations and flat-field corrections. For the telluric correction in the pipeline reduction we used water vapor values obtained with the method described in Fischer et al. (2021) and Iserlohe et al. (2021). Then, the IDL-based software FLUXER v.2.78[3] was used to produce the continuum and line emission maps. The continuum was fitted as a 0th order polynomial in spectral areas free of line emission and the spectral line was fitted with a Gaussian. The selection of channels for the baseline subtraction, the observed wavelength of the targetted line and its width were obtained over the area with strong line detections, separately for each species. Subsequently, these values were adopted for the entire datacube to obtain the integrated line fluxes for the entire map. Further processing of the maps was performed with Python.

The overall calibration accuracy can be assumed to be within 20%, including a 10% calibration accuracy of the instrument, and the additional uncertainty due to telluric effect, which is assumed to be well under 10%. For the [O I] line at 63.2 μm, which is located close to the water absorption line, the water vapor overburden was determined between 3.5 and 3.7 μm. With an error of 10% on this water vapor range, this results in a transmission at the line location of 78-83%.

---

[3] `http://ciserlohe.de/fluxer/fluxer.html`

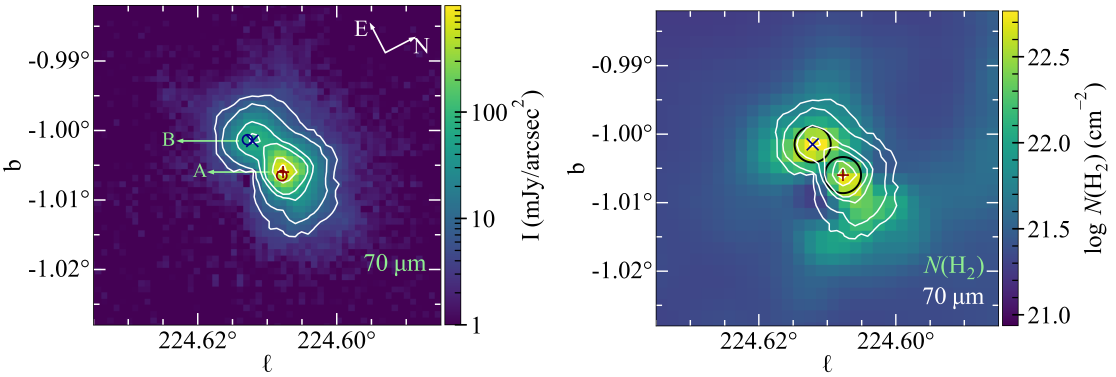

Figure 4.2: The distribution of dust continuum emission toward Gy 3–7. Left: Continuum map of Gy 3–7 at 70 μm observed with *Herschel*/PACS. Red " + " and blue " × " symbols refer to the 70 μm continuum peaks, which are adopted as the positions for the dense cores A and B in the subsequent analysis. Circles show the positions of HIGALBM224.6079–1.0065 and HIGALBM224.6128–1.0013 cores from the *Herschel*/Hi-GAL catalog (Elia et al. 2021). Right: The map of the H$_2$ column density (N_{H_2}). The black circles with the beam size of 20″ indicate the extract regions of the SOFIA FIFI-LS spectra toward the two dense cores A and B (see more in Section 4.3.1). The white contours in each map show the continuum at 70 μm, with contour levels at 5, 10, 40, 80, 400, and 800 mJy/arcsec^2.

4.2.2 *Herschel*/PACS

We use the *Herschel*/PACS 70 μm continuum map to verify the positions of the dense cores in Gy 3–7 listed in the *Herschel*/Hi-GAL compact source catalogue[4] (Elia et al. 2021). Figure 4.2 shows the 70 μm continuum map and the H$_2$ column density, N(H$_2$), map obtained using the `ppmap` tool with the *Herschel*/Hi-GAL survey (Marsh et al. 2017). Overall, there is a good agreement between the catalog positions and the peaks in the continuum at 70 μm and N(H$_2$). In the subsequent analysis, we adopt the coordinates of the 70 μm peaks as the dense core coordinates. We refer to the core at (RA, Dec) = ($7^h09^m20\overset{s}{.}4$, $-10^\circ50'28\overset{''}{.}4$) as A and to that at ($7^h09^m21\overset{s}{.}9$, $-10^\circ50'35''$) as B; they correspond to the *Herschel*/Hi-GAL catalog sources HIGALBM224.6079–1.0065 and HIGALBM224.6128–1.0013, respectively (Elia et al. 2021).

4.2.3 RT4

We conducted a survey at 22 GHz using the Toruń 32-m radio telescope (RT4) toward the entire CMa–l224 region. The full-beam width at half maximum of the antenna at 22 GHz is ~106″, with a pointing error of ≲12″ (Lew 2018).

Two series of observations were performed from 2019 April to 2020 January and from 2020 January to May 2020 in which a total of 205 positions were observed. We used the correlator with 2×4096 channels and 8 MHz bandwidth operating in the frequency–

---

[4] https://vialactea.iaps.inaf.it/vialactea/public/HiGAL_360_clump_catalogue.tar.gz

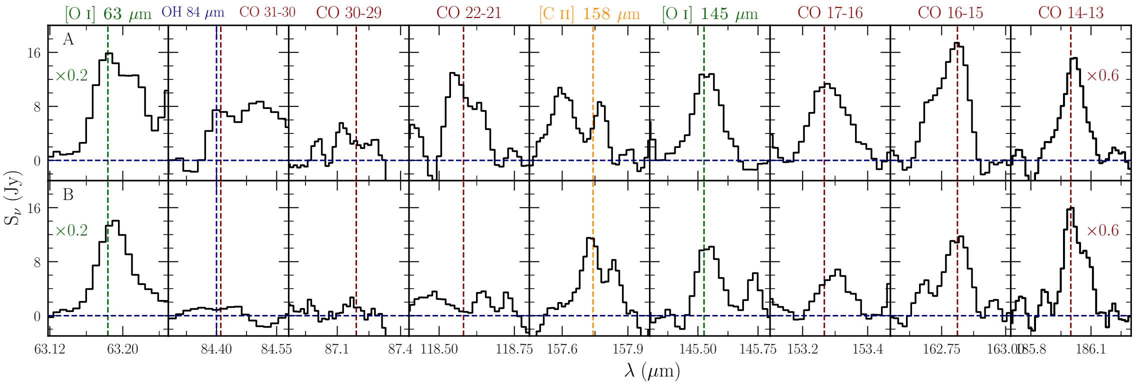

Figure 4.3: SOFIA/FIFI-LS continuum-subtracted spectra toward the two dense cores in Gy 3–7: HIGALBM224.6079–1.0065 (source "A") and HIGALBM224.6128–1.0013 (source "B"). The emission is extracted within a beam size of 20″ indicated by black circles in the right panel of Figure 4.2. Vertical lines show the laboratory wavelengths of the detected lines. The spectra of [O I] line at 63 μm are multiplied by a factor of 0.2 and those of the CO 14 – 13 line by a factor of 0.6 to better illustrate line detections.

switching mode, which provided a local standard of rest velocity coverage from −11.9 to 41.9 km s^{-1}. The spectral resolution of the observations is 0.03 km s^{-1}. The observations were calibrated by the chopper wheel method and corrected for the gain elevation effect. The system temperature varied from ∼120 K during winter to ∼200 K in summer. Overall, the 3σ detection limit was between ∼3.8 and ∼7.5 Jy per 0.03 km s^{-1} channel. The telescope pointing was checked every ∼2 hrs by observing a nearby bright, point source.

We successfully detected a variable water maser emission at (RA, Dec) = ($7^h09^m21\overset{s}{.}05$, $-10^\circ50'05\overset{''}{.}4$), in direct vicinity of Gy 3-7, and at (RA, Dec) = ($7^h09^m22\overset{s}{.}66$, $-10^\circ30'45\overset{''}{.}6$), associated with IRAS 07069-1026 (see Appendix 4.A).

4.3 Results

Near-IR images of Gy 3–7 reveal an extended nebulosity associated with the two Hi-GAL dense cores and several YSO candidates (see Figure 4.1). Spatially-resolved far-IR line emission data obtained with FIFI-LS allows us to study key gas cooling lines at ∼10 000 au scales and identify regions where processes responsible for the gas heating are at play.

4.3.1 Line detections

Figure 4.3 shows the far-IR line emission toward the two Hi-GAL dense cores in Gy 3–7 (see Section 4.2.2); for the full list of targeted lines see Table 4.1. All lines are spectrally-unresolved with FIFI-LS and can be represented by single Gaussian profiles (Section 4.2.1).

The spectra show strong line emission in the [O I] lines at 63 μm and 145 μm, as well as in the high−J CO lines: the CO 14 – 13 line at 186.0 μm, the CO 16 – 15 line at

162.8 μm, and the CO 17 − 16 line at 152.3 μm. Core A shows also a detection of the CO 22 − 21 line at 118.6 μm (E_u of ∼1400 K) and a tentative detection of CO 30 − 29 line at 87.2 μm (E_u of ~2600 K). The CO 31 − 30 line at 84.41 μm is blended with the OH line at 84.42 μm, and due to the lack of baseline covering the OH 84.6 μm line from the doublet, its emission cannot be quantified. The OH doublet at ∼79.2 μm seems to be tentatively detected toward both cores, but is severely affected by the rise of the baseline on its left side and its flux cannot be properly measured (Appendix 4.B). The OH doublet at 163.12 and 163.18 μm, located next to the CO 16-15 line, is not detected in neither of the two cores.

The [O I] line at 63.18 μm sits on the edge of a telluric water feature, and the low transmission at $\lambda \gtrsim 63.24$ μm increases the noise on the continuum. Since the transmission at the spectral line location is well known and the S/N is very high, there is no relevant effect on the uncertainty of the line flux. Possible self-absorption of this [O I] line cannot be identified at the spectral resolution of FIFI-LS. The higher-resolution spectra collected toward other YSOs using the German REceiver for Astronomy at Terahertz Frequencies (GREAT; Risacher et al. 2018) show that self-absorption could decrease the integrated emission of the line by a factor of 2–3 (Leurini et al. 2015; Mookerjea et al. 2021).

Similarly, self-absorption in the [C II] line at 157.7 μm might affect the FIFI-LS spectra. Strong self-absorption unresolved by FIFI-LS may result in a non-detection of this line toward core A. In contrast, the line is clearly detected toward core-B. Decreases of the flux of [C II] line due to self-absorption as high as a factor of 20 have been estimated toward photodissociation regions (Guevara et al. 2020).

To summarize, FIFI-LS spectra provide detections of key far-IR cooling lines toward two dense cores in Gy 3–7: the high−J CO, [O I], and [C II]. Due to the atmospheric absorption, the H_2O emission could not be targeted; the OH emission suffers from line blending and poor baselines. In Section 4.3.2, we show the distribution of line emission in various species toward the entire cluster.

4.3.2 Spatial extent of far-IR line emission

The far-IR range contains several important diagnostic lines, which inform about the physical conditions and processes that strongly contribute to the gas cooling (Goldsmith & Langer 1978; Kaufman & Neufeld 1996). The analysis of spatial extent of various far-IR species pin-points the presence of shocks and/or UV radiation associated with star formation.

Figures 4.4 and 4.5 show the spatial extent of the far-IR lines detected toward Gy 3–7 (Section 4.3.1). The line emission is compared to the far-IR dust continuum emission at 70 or 160 μm from *Herschel*/PACS (Figure 4.4), and the 4.5 μm continuum tracing warmer dust from *Spitzer*/IRAC (Figure 4.5). Bright rotationally excited H_2 emission associated with shocks might also contribute to the flux in the 4.5 μm IRAC band (Cyganowski et al. 2008, 2011). Appendix 4.B shows additional maps of Gy 3–7 for lines from various species.

The high−J CO emission distribution is elongated in the same direction as the IR continuum, but its peaks are offset from the continuum peaks at wavelengths similar to those of the respective CO lines. A similar pattern of emission is also seen for the [O I]

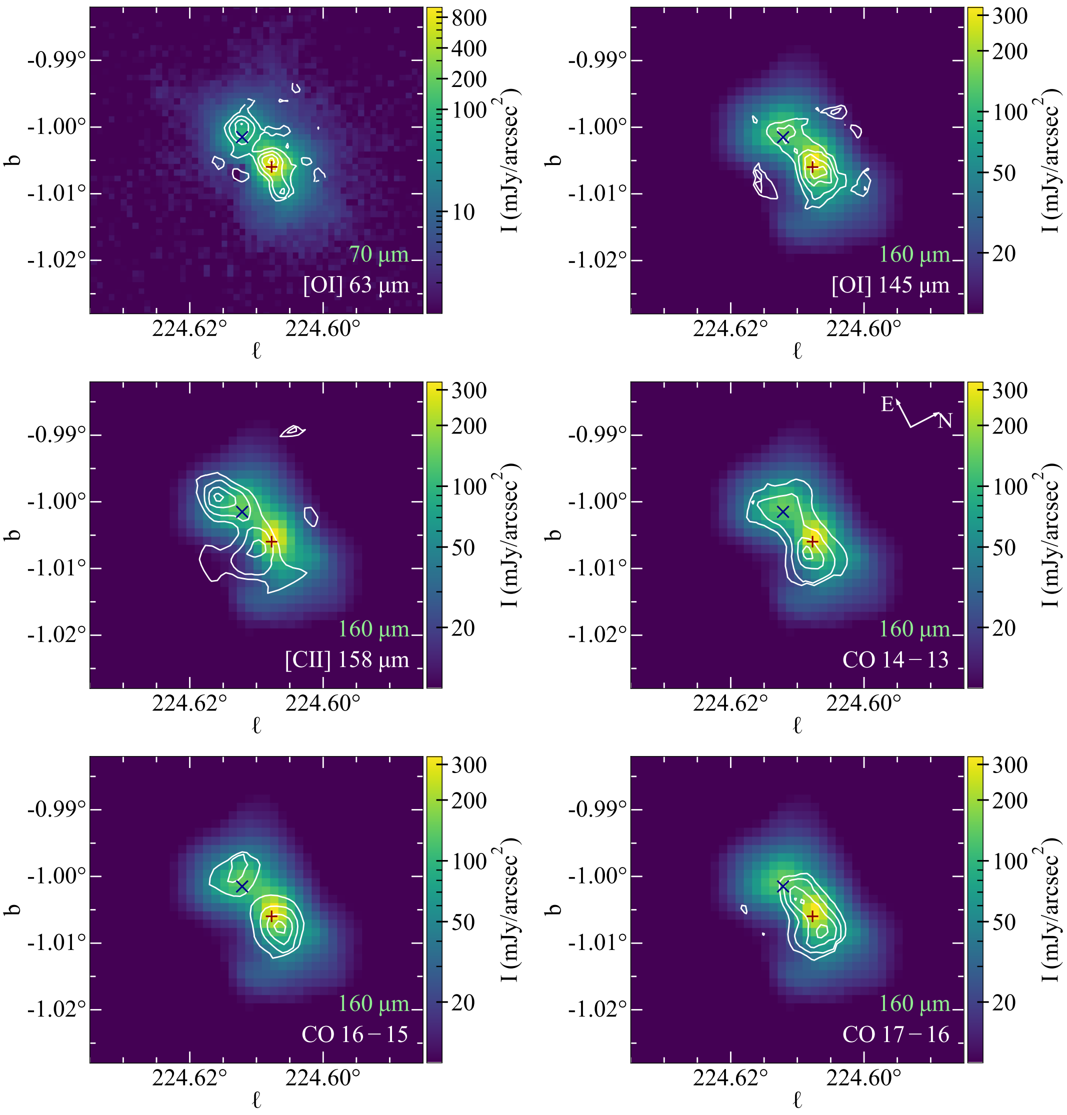

Figure 4.4: FIFI-LS contour maps of the [O I] lines at 63.2 and 145.5 μm, the [C II] line at 157.7 μm, the CO lines with $J_{\rm up}$ = 14, 16, 17 at 186, 163, and 153 μm respectively (white contours) on top of the continuum emission at 160 μm (at 70 μm for the [O I] line at 63.2 μm) from *Herschel*/PACS. The white contours show line emission at 25%, 50%, 75%, and 95% of the corresponding line emission peak. The " + " and " × " signs show the positions of the dense cores A and B.

63 μm and 145 μm lines; yet, the peak of the [O I] lines are almost co-spatial with the core positions, which is not the case for the CO lines. Nevertheless, both the CO and the [O I] extend beyond the core positions along the E–W direction. Such elongated high−J CO morphologies have been commonly interpreted as arising in shocked outflows from LM and IM protostars (Goicoechea et al. 2012; He et al. 2012; Kristensen et al. 2012; Karska et al. 2013; Matuszak et al. 2015; Green et al. 2016; Tobin et al. 2016; Kristensen et al. 2017b). Similarly, extended [O I] emission has been associated with embedded, atomic outflows (Karska et al. 2013; Nisini et al. 2015), as recently confirmed by detections of

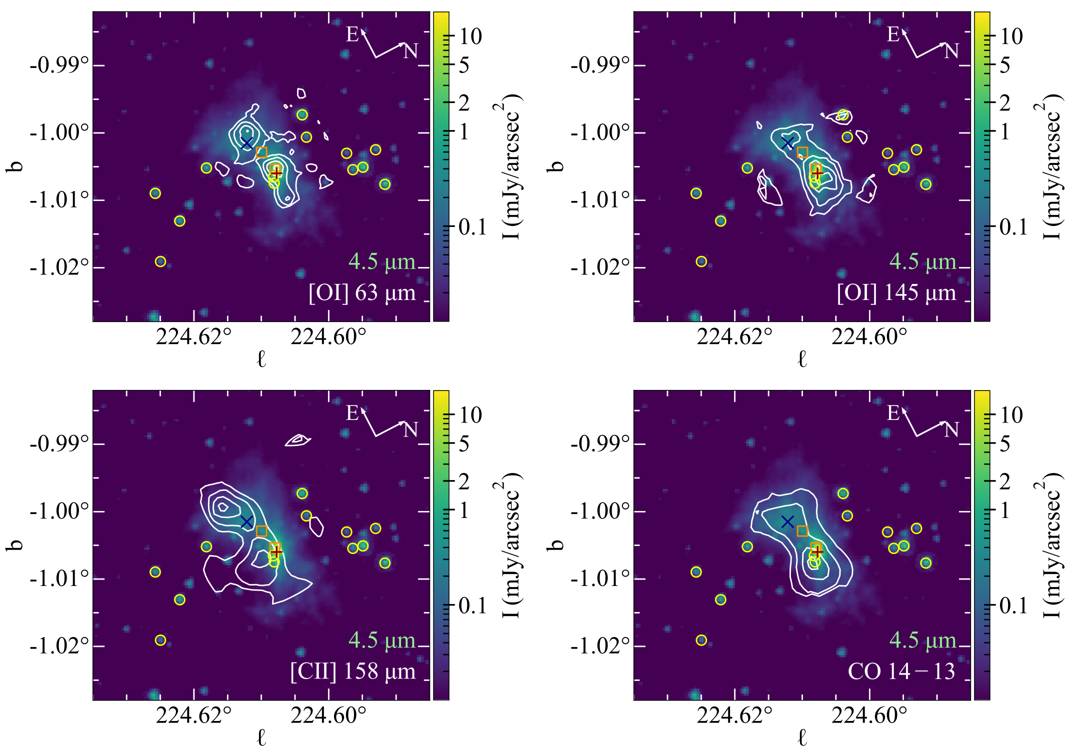

Figure 4.5: FIFI-LS contour maps of the [O I] lines at 63.2 and 145.5 μm, the [C II] line at 157.7 μm, and the CO 14 – 13 line at 186 μm (white contours) on top of the continuum emission at 4.5 μm from *Spitzer*/IRAC. The contours show line emission at 25%, 50%, 75%, and 95% of the corresponding line emission peak. The '+' and '×' signs show the positions of the dense cores A and B, respectively. The orange squares show the positions of two YSO candidates with envelopes, and the yellow circles show the positions of the remaining YSOs (Section 4.4.5).

broad line wings in the 63 μm line with SOFIA/GREAT (Leurini et al. 2015; Kristensen et al. 2017a; Yang et al. 2022a). Thus, the high$-J$ CO and [O I] emission toward Gy 3–7 might also arise from outflows, where shocks and UV radiation both contribute to gas cooling (see Section 4.5).

The [C II] emission also follows the pattern of the continuum emission, but its two emission peaks are offset by ~11″ in different directions from the corresponding [O I] 63 μm peaks. These differences are illustrated further in Figure 4.6, in which emission in various species is directly compared. Clearly, the [C II] emission traces different regions of Gy 3–7 than the high$-J$ CO and [O I] lines, which is at least partly due to its lower critical density, $n_{\rm crit}$ ~(3.7–4.5)×10^3 cm^{-3} for $T_{\rm kin}$ of 300-100 K (assuming collisions with H$_2$, Wiesenfeld & Goldsmith 2014). As a result, [C II] is excited in lower density regions and likely exposed to external UV radiation creating a photodissociation region (Hollenbach & Tielens 1997). To some extent, the pattern of [C II] emission might be also affected by self-absorption, which is spectrally-unresolved in the FIFI-LS data (Section 4.3.1).

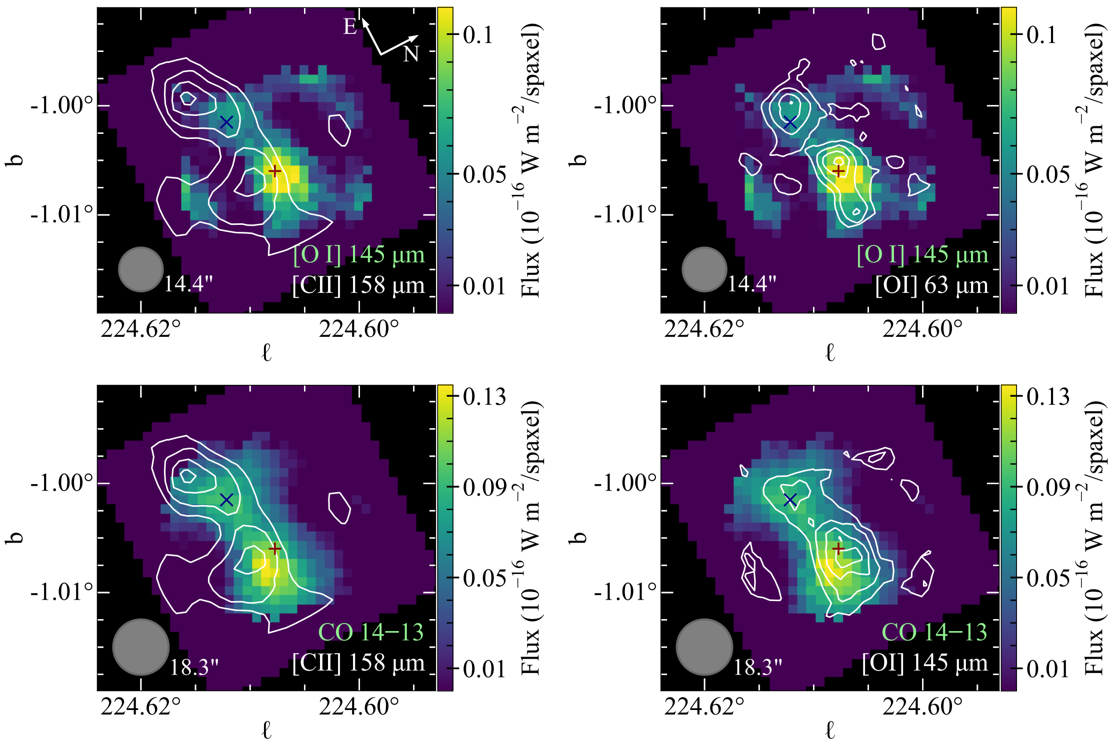

Figure 4.6: Integrated intensity maps of selected pairs of far-IR lines from FIFI-LS with the top line shown in colors, and the bottom line in white contours. The contour levels are 25%, 50%, 75%, and 95% of the corresponding line emission peak. The '+' and 'x' signs show the positions of the dense cores A and B, respectively. The spaxel size in the emission map of the [O I] line at 63 μm is $6'' \times 6''$ (blue channel) and in the map of other lines (CO 14 − 13, [O I] at 145 μm, and [C II] at 157.7 μm) is $12'' \times 12''$ (red channel). Gray circles show the beam size for each color map.

4.4 Analysis

The high−J CO emission allows us to measure the CO rotational temperature of the warm molecular gas and to estimate the total line cooling by the far-IR CO lines. The mapping capabilities of FIFI-LS provide information about the spatial distribution of the temperature and gas cooling across the entire clump.

4.4.1 CO rotational temperatures

We use Boltzmann (or rotational) diagrams to calculate the CO rotational temperature toward the two dense cores in Gy 3–7 as a proxy of gas kinetic temperature. Assuming that all these lines are optically thin and thermalized, their upper level column densities, N_u, are estimated using Eq. 4.1 following Goldsmith & Langer (1999):

$$\ln \frac{N_u}{g_u} = \ln \frac{N_{tot}}{Q(T_{rot})} - \frac{E_u}{k_B T_{rot}}, \tag{4.1}$$

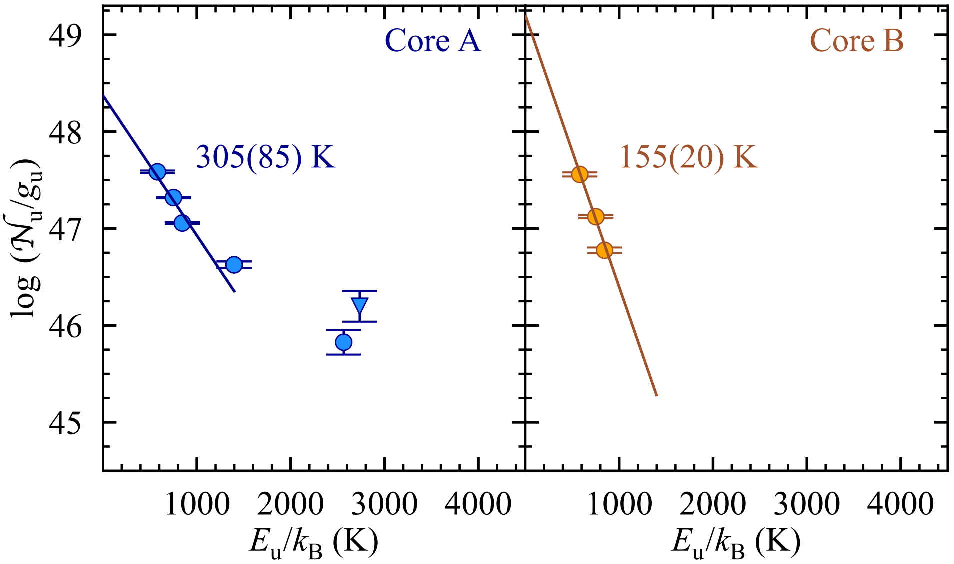

Figure 4.7: CO rotational diagrams toward core A (*left*, in blue) and B (*right*, in orange). Circles refer to values based on line detections and the triangle shows the measurement using the upper limit of the CO 31-30 line, which is blended with OH. Solid lines show fits using transitions belonging to the 'warm' gas component; the CO 30 – 29 line at 87.19 μm is therefore not included. The CO rotational temperature $T_{\rm rot}$ derived from the rotational diagram is labeled in each panel and the value in parenthesis indicates its uncertainty.

where g_u is the degeneracy of the upper level, $Q(T_{\rm rot})$ is the rotational partition function at a temperature $T_{\rm rot}$, $N_{\rm tot}$ is the total column density, and k_B is the Boltzmann constant (see Table 4.1).

Due to the low spatial resolution of FIFI-LS, the emitting region of the highly-excited gas is unresolved and thus we calculate instead the number of emitting molecules, $\mathcal{N}_u$, for each transition (see e.g., Herczeg et al. 2012; Karska et al. 2013):

$$\mathcal{N}_u = \frac{4\pi d^2 \lambda F_\lambda}{Ahc} \tag{4.2}$$

where F_λ is the flux of the line at wavelength λ, d is the distance to Gy 3–7, A is the Einstein coefficient, c is the speed of light, and h is the Planck's constant. Consequently, the total number of emitting molecules $\mathcal{N}_{\rm tot}$ is derived instead of the $N_{\rm tot}$ from Eq. 4.1. To measure $T_{\rm rot}$ over the same physical scales, we convolve the CO emission maps down to the lowest spatial resolution corresponding to CO 14 – 13 observation (18.3″, see Table 4.1) and resample the maps to the same pixel size. The flux of CO lines toward cores A and B is calculated within a beam of 20″ (see Table 4.B.1). We perform a linear fit on the rotational diagram using the `curve_fit` function in Python ($y = ax + b$). The $T_{\rm rot}$ and $\mathcal{N}_{\rm tot}$ are derived from the slope a and y-intercept b of the fit (Eq. 4.1).

Figure 4.7 shows the CO Boltzmann diagrams toward the two cores in Gy 3–7. We obtain rotational temperatures of 305 ± 85 K and 155 ± 20 K toward dense cores A and B, respectively, using CO lines with $J_{\rm up}$ of 14 – 22 (see Table 4.2). The same transitions have been associated with the "warm" component detected on CO diagrams toward protostars

Table 4.2: CO rotational temperature, the number of emitting molecules, and total line luminosities of CO and [O I] lines toward dense cores in Gy 3–7 and IM YSOs from Matuszak et al. (2015)

Source	$T_{\rm rot}{}^a$ (K)	$\log\mathcal{N}_{\rm tot}{}^a$	$L_{\rm CO}$(warm)^b	$L_{\rm [O\,I]63\mu m}$ ($10^{-3}L_\odot$)	$L_{\rm [O\,I]145\mu m}$
Dense cores in Gy 3–7					
Core A	305 ± 85	50.41 ± 0.34	73.31 ± 19.69	92.69 ± 5.01	8.38 ± 0.29
Core B	155 ± 20	50.96 ± 0.24	30.47 ± 6.10	76.17 ± 5.37	6.15 ± 0.37
IM YSOs in the inner Milky Way					
AFGL 490^c	255 ± 25	51.11 ± 0.13	225.17 ± 19.85	336.65 ± 1.47	29.56 ± 0.24
L1641	270 ± 35	50.06 ± 0.17	24.31 ± 2.74	14.69 ± 0.14	1.20 ± 0.05
NGC 2071	295 ± 20	51.23 ± 0.10	425.38 ± 26.11	312.72 ± 0.91	21.59 ± 0.13
Vela 17	215 ± 25	51.08 ± 0.17	125.56 ± 15.44	369.84 ± 1.33	77.85 ± 0.21
Vela 19	255 ± 20	50.66 ± 0.10	86.00 ± 9.27	130.69 ± 0.70	13.60 ± 0.09
NGC 7129	295 ± 35	50.84 ± 0.14	187.26 ± 19.16	66.03 ± 0.78	3.13 ± 0.88

Notes: ^{a} $T_{\rm rot}$ and $\mathcal{N}_{\rm tot}$ calculated using only CO 14 – 13, CO 16 – 15, CO 18 – 17, and CO 22 – 21 transitions for more direct comparisons with the cores in Gy 3–7. ^{b} The CO line luminosity in the 'warm' component is obtained using all transitions reported in Matuszak et al. (2015) with $J_{\rm up}$ from 14 to 24 (see Section 4.4.2). ^{c} We adopt the new distance of 0.97 kpc toward this source when calculating $T_{\rm rot}$, $\mathcal{N}_{\rm tot}$, and luminositiy of CO and [O I] lines (see Table 4.D.2 and references therein).

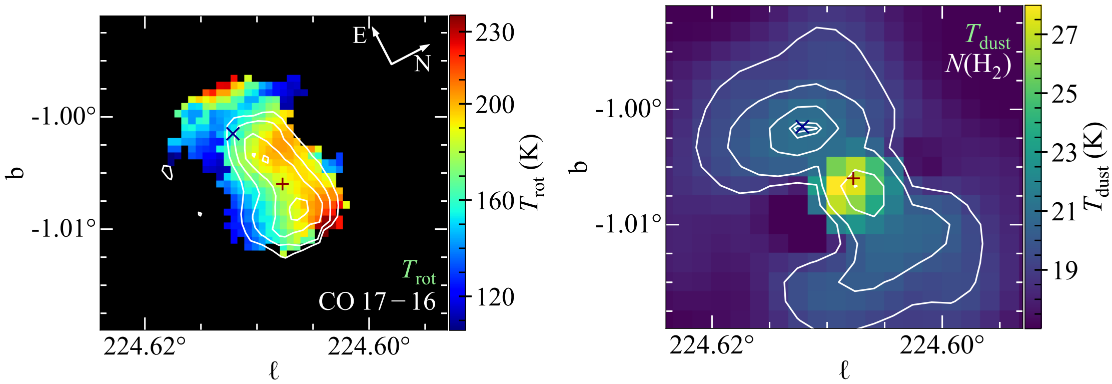

Figure 4.8: Gas and dust temperatures toward Gy 3–7. *Left:* CO rotational temperature map obtained using Boltzmann diagrams. The white contour map shows the CO 17 – 16 emission at 25%, 50%, 75%, and 95% of the emission peak. *Right:* H_2 column density contour map overlaid on the dust temperature map derived from the `ppmap` tool with the *Herschel*/Hi-GAL survey (Marsh et al. 2017). The contour levels of the $N(H_2)$ are at (5, 10, 30, 50, 55)×10^{21} cm^{-2}.

in the inner Galaxy and corresponding to the widely found $T_{\rm rot}$ of 300 K (Karska et al. 2013; Manoj et al. 2013; Green et al. 2013). The CO 30 – 29 and CO 31 – 30 data at 87.2 and 84.4 μm, respectively, indicate the presence of the "hot" component toward core A (Karska et al. 2013). However, the 84.4 μm line is blended with OH, which clearly affects

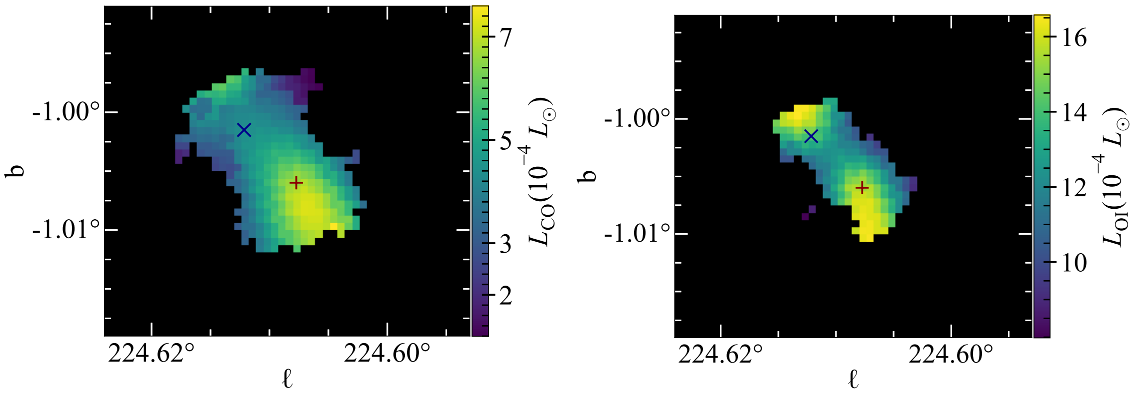

Figure 4.9: Spatial extent of far-IR line luminosities of CO (*left*) and [O I] (*right*) toward Gy 3–7. The calculation procedure is described in Section 4.4.2.

the CO line flux (see Figure 4.3). Consequently, we are not able to constrain the "hot" component using only the CO 30-29 line.

The spatial distribution of the "warm" component's CO rotational temperature toward the entire Gy 3–7 clump is shown in the left panel of Figure 4.8. Here, we calculate T_{rot} using the three lowest transitions (J_{up} of 14 – 17), which are detected in a large part of the map, except for the map edges where even CO 17 – 16 is not detected (Figure 4.4). The resulting T_{rot} values range from 105 to 230 K across the map, with a median value of 170(15) ± 30 K[5]. The CO rotational temperatures are the highest in the vicinity of the CO 17 – 16 emission peaks, which are offset by ~17″ from core A to the west (Figure 4.4). The morphology of the T_{rot} distribution suggests the origin of high−J CO in a bipolar outflow driven by core A. Significantly lower CO temperatures, $\lesssim$150 K, are measured in the surroundings of core B, without a clear outflow signatures from this object. The temperatures around 200 K at the eastern edge of the map are likely caused by higher gas densities in this region rather than higher gas kinetic temperatures.

The spatial distribution of dust temperatures T_{dust} toward Gy 3–7, adopted from the *Herschel*/Hi-GAL survey, is also shown in the right panel of Figure 4.8. The morphology of regions with elevated temperatures is similar to the extent of $N(H_2)$, and shows two peaks at 27 and 21 K toward core A and B, respectively. The pattern differs significantly from the distribution of warm, ~300 K gas, traced by CO lines, favoring the origin of the CO emission in a bipolar outflow driven by core A. Nevertheless, the lowest−J CO transitions observed with FIFI-LS might partly trace the extended continuum emission, e.g., on the eastern part of Gy 3–7. We will discuss this issue further in Section 4.5.1.

4.4.2 Far-IR line cooling

The far-IR line cooling budget in LM protostars is sensitive to a source's evolutionary stage and L_{bol}, and its contributions provide important information on the shock origin of the far-IR emission (Karska et al. 2013, 2018). Here, we quantify the luminosity of the

---

[5] The temperature in the bracket shows the mean error of the T_{rot} distribution and ± 30 refers to the standard deviation of the T_{rot} values.

far-IR CO and [O I] lines toward the two cores in Gy 3–7 and a sample of IM protostars observed with *Herschel*/PACS (Matuszak et al. 2015).

4.4.2.1 Calculation procedure

We calculate the line cooling following procedures developed for *Herschel*/PACS observations in the same wavelength range (Karska et al. 2018). Briefly, we determine the line luminosity of CO lines in the 'warm' component, $L_{\rm CO}$(warm), from the sum of the individual line fluxes with $J_{\rm up}$ from 14 to 24, corresponding to $E_{\rm u}/k_{\rm B}$=580–1800 K. Since not all CO transitions are observed, we use linear fits from the Boltzmann diagram to the 'warm' component to recover the fluxes of the transitions not covered by FIFI-LS or PACS observations. The flux uncertainties of those transitions are propagated from the parameters of the linear fit and their uncertainty. The same procedure cannot be applied to the 'hot' component toward Gy 3–7 cores due to the lack of data on a sufficient number of high−J CO transitions. As a result, we do not calculate the total far-IR CO cooling i.e., do not account for transitions with $E_{\rm u}$>1800 K. The advantage of this approach is that we avoid significant source-to-source variations in $L_{\rm CO}$(hot), which is reflected by the broad range of rotational temperatures measured using the highest−J CO lines (see Figure 6 in Karska et al. 2018). The total line luminosity of [O I], $L_{\rm [O\,I]}$, is calculated by the addition of the fluxes of the [O I] 63 and 145 μm lines. Table 4.2 shows the far-IR line luminosities obtained for Gy 3–7, as well as for six IM YSOs from Matuszak et al. (2015).

Figure 4.9 shows the spatial distribution of the far-IR line luminosity of CO and [O I] toward Gy 3–7. Most of the CO luminosity orginates in a region west of core A, suggesting an outflow origin (see also Section 4.3.2). A similar region is characterized also by a high [O I] luminosity, which typically follows the pattern of high−J CO emission around LM protostars (Karska et al. 2013; Nisini et al. 2015; van Dishoeck et al. 2021). Additionally, a high [O I] luminosity is measured to the east from core B, toward the direction of the [C II] peak (see Figures. 4.5 and 4.6). The lack of enhancement of CO line luminosity in this region could suggest an origin of the [O I] emission in the PDR. We explore this scenario further in Section 4.4.3.

4.4.2.2 Flux correlations

We compare the far-IR line emission in Gy 3–7 with the data based on *Herschel*/PACS measurements toward LM Class 0 and Class I (Karska et al. 2018), IM (Matuszak et al. 2015), and HM YSOs (Karska et al. 2014a). CO luminosities are consistently calculated for the 'warm'component on Boltzmann diagrams. The correlations between luminosities of the two [O I] lines, and the [O I] and CO lines are shown in Figure 4.10.

A strong power-law correlation is found between the [O I] line luminosities for all low- and intermediate-mass sources including the two cores in Gy 3–7 (the Pearson coefficient of the correlation is r = 0.996, which corresponds to a significance of 8.2σ). The observed ratios of the [O I] 63 μm/145 μm lines span a range from 4 to 38 with a median value of ~12. These results are quantitatively similar to those shown in Figure 11 of Karska et al. (2013) for a sub-sample of 18 LM YSOs.

The HM YSOs follow a similar trend, however, several sources show a flux deficit in the [O I] 63 μm line, which is likely caused by line-of-sight contamination and optical

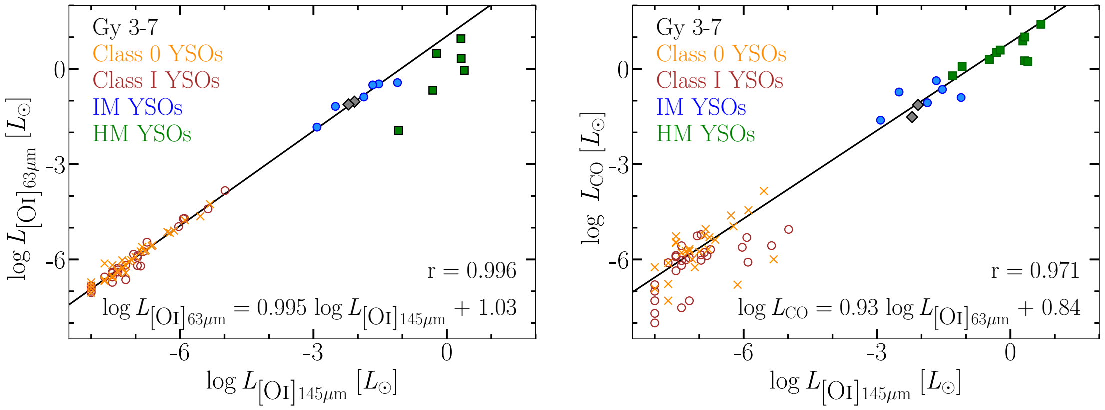

Figure 4.10: Correlation between luminosities of far-IR CO and [O i] lines. *Left:* correlation between the luminosities of the 63 and 145 μm [O i] lines from LM to HM YSOs. Cores A and B in Gy 3–7 are marked as grey diamonds, Class 0 and Class I YSOs as orange '×' signs and red circles (Karska et al. 2018), respectively, IM YSOs as blue circles (Matuszak et al. 2015), and HM YSOs as green squares, respectively (Karska et al. 2014a). The black solid line is the linear fit to all sources except for the HM YSOs, showing a strong correlation between the two [O i] line luminosities. *Right:* Correlation between luminosities of the CO lines and the [O i] line at 145 μm. The black solid line shows the linear fit to all sources including the HM YSOs.

depth effects (see, e.g., Liseau et al. 1992; Leurini et al. 2015). A power-law fit to the sample including HM YSOs shows a shallower slope (b = 0.91 versus b = 0.99, when only LM and IM YSOs are considered). The correlation strength is comparable to the one for LM and IM sources alone, with a Pearson coefficient of 0.991 corresponding to 8.5σ.

The CO line luminosity in the 'warm' component shows a strong correlation with the 145 μm [O i] line luminosity. A power–law fit to the entire sample returns a slope of b ~0.93 and the Pearson coefficient of 0.971, corresponding to $\sim 8.2\sigma$ (Figure 4.10). Clearly, the line luminosity of the [O i] 145 μm line shows a smaller scatter for the HM YSOs with respect to the 63 μm line. In case of LM YSOs, a significant scatter in the ratio of CO and [O i] line luminosities is likely linked to their different evolutionary stages. The ratio of CO line luminosity over L_{bol} is ~2.3 larger for Class 0 than Class I sources, whereas the [O i] luminosities are similar for both groups (Karska et al. 2018). Thus, the molecular-to-atomic line cooling is expected to be higher in Class 0 objects. Indeed, the linear fit using only Class 0 sources results in a shallower slope, but do not affect the general conclusions.

In summary, we find a strong correlation between the line luminosities of the [O i] and CO lines for YSOs in a broad mass range, consistent with previous results for LM YSOs (Karska et al. 2013). Combined with the similar spatial extent of the [O i] and CO lines (Section 4.3.2), the correlations suggest a similar physical origin of the two species.

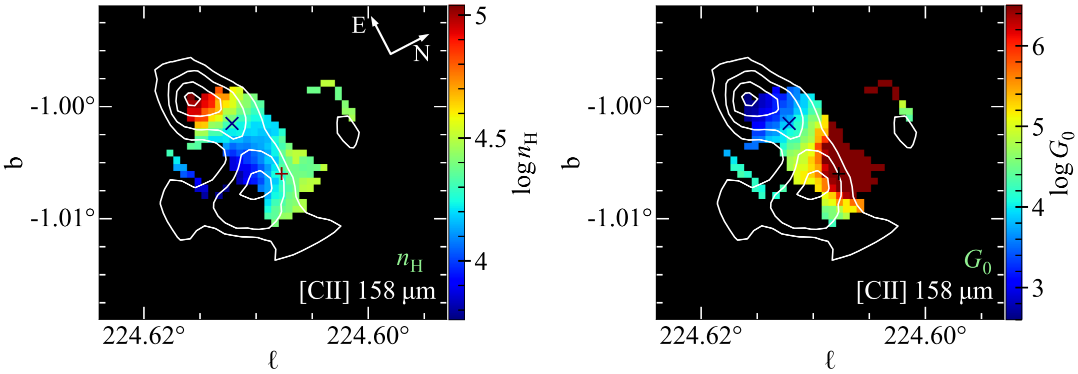

Figure 4.11: The spatial distribution of hydrogen nucleus number density, n_H (*left*), and the UV radiation field strength, G_0 (*right*) toward Gy 3–7. The assumption that the emission from the [O I] and the [C II] lines arises from a PDR holds only in the eastern part of the clump (see Section 4.4.3). The white contours show the emission of the 158 μm [C II] line, at 25%, 50%, 75%, and 95% of the emission peak.

4.4.3 Properties of a possible photodissociation region

Assuming that the [O I] and [C II] lines predominately arise from a photodissociation region (PDR), the UV field strengths, G_0, and hydrogen nucleus number densities, n_H, across Gy 3–7 can be obtained from their ratios. These assumptions might be justified in case of the eastern part of Gy 3–7 with relatively weak CO line luminosities (see Section 4.4.2). On the contrary, the [O I] line luminosity in the surrounding of core A closely follows the high−J CO emission associated with outflow shocks.

We determine the physical properties of the PDR using the PDR Toolbox 2.1.1[6] (Pound & Wolfire 2011) based on the PDR models provided by Kaufman et al. (2006). We use three line ratios involving the [O I] lines at 63.2 μm and 145.5 μm, and [C II] line at 157.7 μm, and run the code at each spaxel of the FIFI-LS maps.

Figure 4.11 shows the spatial extent of n_H and G_0 toward Gy 3–7, only the results for the eastern part of the clump, where [C II] is detected, could be considered trustworthy. We obtain gas densities of 10^4–10^5 cm^{-3} and UV field strengths of the order of 10^3-10^6 times the average interstellar UV radiation field (Habing 1968). These physical conditions are typical for dense, star-forming clumps associated with HM YSOs (Ossenkopf et al. 2010; Benz et al. 2016; Mirocha et al. 2021). However, given that Gy 3–7 is associated with IM YSOs (see Section 4.4.5), UV radiation fields of 10^3 or higher are unlikely (e.g., Karska et al. 2018).

The similar spatial extent of the [O I] and high−J CO emission (Section 4.3.2) and the strong line luminosity correlation between the two species (Section 4.4.2) favor the origin of the bulk of [O I] in the outflow shocks rather than in the photodissociation region. We consider this scenario in Section 4.4.4.

---

[6] `https://dustem.astro.umd.edu/`

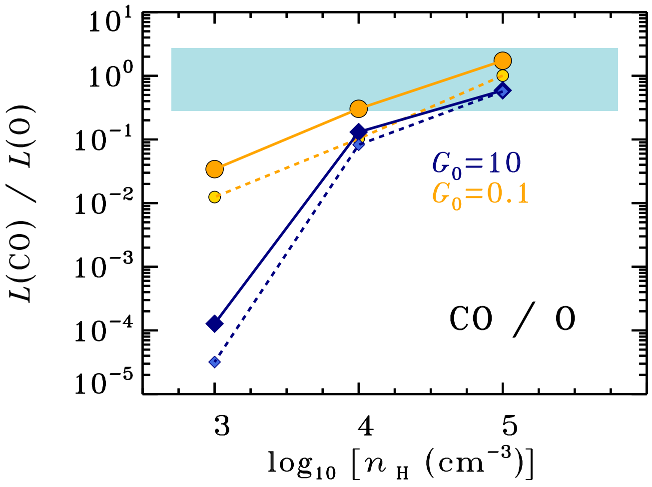

Figure 4.12: Ratio of the CO and [O I] luminosities as a function of pre-shock density for UV irradiated $C-$shock models and observations of Gy 3–7 cores and IM YSOs from Matuszak et al. (2015) (light blue box). All models correspond to UV fields parameterized by G_0 of 10 (in blue) and 0.1 (in orange). Solid lines connect models with shock velocities υ_s of 20 km s^{-1}, and dashed lines – the models with υ_s of 10 km s^{-1}.

4.4.4 Comparisons with UV-irradiated shocks

Bright far-IR emission detected toward LM YSOs has been interpreted in the context of continuous ($C-$type) shocks irradiated by UV photons (Karska et al. 2014b, 2018; Kristensen et al. 2017b). Figure 4.12 shows a comparison of the far-IR observations toward IM YSOs, including two cores in Gy 3–7, and the UV-irradiated shock models from Melnick & Kaufman (2015) and Karska et al. (2018).

The predictions of shock models have been calculated for high$-J$ CO lines covered by *Herschel*/PACS; here, we show predictions for UV field strengths, G_0, of 0.1 and 10, and shock velocities of 10 and 20 km s^{-1} (see also Figure 14 in Karska et al. 2018). For the sake of comparison, we calculated the total far-IR line luminosity of CO using the transitions in the 'warm' component (Section 4.4.2.1) as well as high$-J$ CO lines, both for Gy 3–7 and for IM YSOs (Matuszak et al. 2015). The [O I] line luminosity is calculated from the sum of the two fine-structure [O I] lines.

The models show a good match with observations for pre-shock H_2 number densities of 10^5 cm^{-3} and the entire range of the considered UV radiation field strengths. For shock velocities υ_s of 20 km s^{-1}, a possible match is also found for pre-shock densities of 10^4 cm^{-3} and G_0 of 0.1. The compression factor >10 is expected in $C-$type shocks (Karska et al. 2013), so the gas densities are of the order of 10^5-10^6 cm^{-3}, in agreement with those of LM YSOs (e.g., Kristensen et al. 2012; Mottram et al. 2017).

Due to the lack of H_2O observations from FIFI-LS and non-detections of OH, we are limited to comparisons between CO and [O I] lines. Some of the [O I] emission might arise in the PDR (Section 4.4.3), which would increase the observed line luminosity ratio; however, the strong correlation of [O I] and high$-J$ CO tracing outflow shocks does not

Table 4.3: Best-fit models of SED using the Robitaille (2017) classification

Model Set	# of sources	Components	Group
s−−−s−i	4	star	–
sp−−s−i	2	star + passive disk; $R_{\text{inner}} = R_{\text{sub}}$	*d*
sp−−h−i	4	star + passive disk; variable R_{inner}	*d*
s−pbhmi	1	star + power-law env. + cavity + medium; variable R_{inner}	*e*
spubsmi	1	star + passive disk + Ulrich env. + cavity + medium; $R_{\text{inner}} = R_{\text{sub}}$	$d + e$

Notes: Seven characters in the model set names indicate which component is present; they are (in order): s: star; p: passive disk, p or u: power-law or Ulrich envelope; b: bipolar cavities; h: inner hole; m: ambient medium; and i: interstellar dust. A dash (−) is used when a component is absent. R_{inner} is the inner radius for the disk, envelope, and the ambient medium - when one or more of these components are present. R_{sub} is the dust sublimation radius.

support this scenario.

4.4.5 Spectral energy distribution analysis

We investigate the physical properties of 15 individual YSO candidates from Tapia et al. (1997) and Sewiło et al. (2019) in Gy 3–7 to understand their possible impact on the far-IR and submillimeter line emission. Spectral energy distribution (SED) models of YSOs from Robitaille (2017) are fitted to the multi-wavelength photometry of YSOs using a dedicated fitting tool (Robitaille et al. 2007). Multi-wavelength photometry spanning from near- to mid-IR range of YSO candidates in the IRAS field is presented in Appendix 4.C.

We follow the procedures described in detail in Karska et al. (2022). We use 18 sets of model SEDs including various physical components of a YSO: star, disc, in-falling envelope, bipolar cavities, and an ambient medium (Robitaille 2017). We use the PARSEC evolutionary tracks produced by the revised Padova code (Bressan et al. 2012; Chen et al. 2014, 2015; Tang et al. 2014) to quantify the results of SED model fitting. Models producing YSO parameters outside of the PARSEC pre-main sequence (PMS) tracks are excluded. YSOs with models in line with the PARSEC tracks are illustrated on the Hertzsprung-Russell diagram in Appendix 4.C. For those YSOs, we calculate the stellar luminosity from the Stefan-Boltzmann law, using the stellar radius and effective temperature from the SED fitting. The masses and ages are determined from the closest PMS track; however, we only provide the stellar masses and ages that are consistent with the SED fitting results (i.e., the evolutionary stage) and YSO lifetimes from Dunham et al. (2015), respectively (see Section 3.7 in Karska et al. 2022).

Table 4.3 shows the best-fit SED models for 12 YSOs in Gy 3–7. SEDs of two sources require an envelope contribution which is typical for deeply-embedded Class 0/I YSOs (see Figure 4.13), six sources are successfully modeled with a passive disk, and four are normal stars (see Appendix 4.C). The resulting physical parameters determined from SED models are shown in Table 4.4.

The two YSOs with envelopes, No. 10 and 12 in Table 4.4, are located in the center

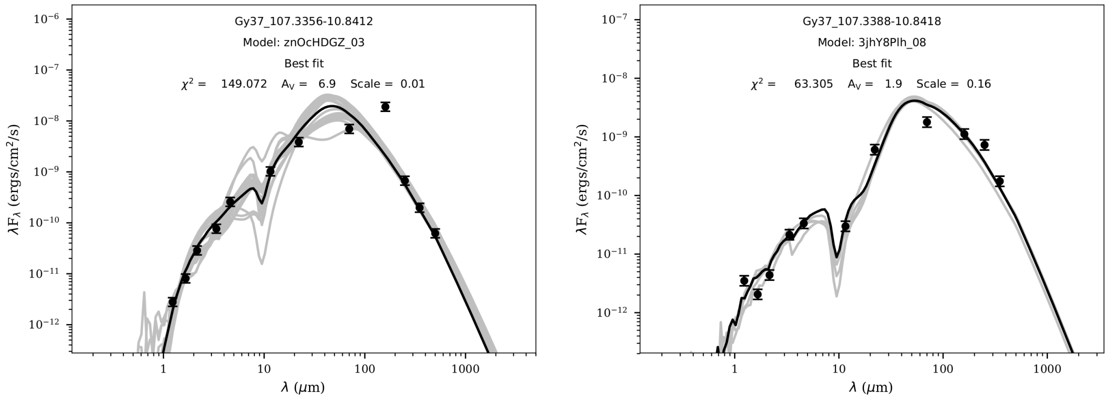

Figure 4.13: SEDs of YSOs in Gy 3–7 well-fitted with Robitaille (2017) models with envelopes. The best fit model is indicated with the black solid line and gray lines show the YSO models with χ^2 between $\chi^2_{\rm best}$ and $\chi^2_{\rm best}+ F \times n$, where n is the number of data points and F is a threshold parameter which we set to 3 (Sewiło et al. 2019). Filled black circles are valid flux values with uncertainties. The values of a reduced χ^2 and interstellar visual extinction for the best-fit model are indicated in the plots. Appendix 4.C shows the SEDs for the remaining YSOs in Gy 3–7.

of Gy 3–7 (see Figures 4.1 and 4.5), and their strong IR excess has already been noted by Tapia et al. (1997). The Class 0 YSO is co-spatial with the IRAS source and the dense core A (Elia et al. 2021), and might be the source of the outflow responsible for the far-IR emission. Both objects are in the IM regime based on their luminosities obtained from SEDs. The four objects that are modeled as stars with foreground extinction have photometry only from 1 to 5 μm. In this range, it is difficult to distinguish between stars with foreground extinction and stars with disks, so we do not rule out the latter explanation.

4.5 Discussion

Far-IR observations from FIFI-LS confirm the status of Gy 3–7 as a deeply-embedded cluster, as originally proposed by Tapia et al. (1997). Here, we will discuss the likely origin of far-IR emission in Gy 3–7 and search for any effects of metallicity by comparison with YSOs from the inner Galaxy.

4.5.1 Origin of far-IR emission in Gy 3–7

A strong correlation of high$-J$ CO and [O I] luminosities and their spatial extent in Gy 3–7 provides a strong support toward the common origin of the two species. Modeling of envelopes of HM YSOs showed that emission from shocks is necessary to reproduce line fluxes of high$-J$ CO lines (Karska et al. 2014a). The same is certainly also the case for LM and IM YSOs, which are characterized by lower envelope densities and temperatures. On the other hand, the [O I] emission could be associated with a photodissociation region (Kaufman & Neufeld 1996; Hollenbach & Tielens 1997) or outflow shocks (Karska et al. 2013; Nisini et al. 2015). Recent velocity-resolved profiles of the [O I] line at 63 μm with SOFIA/GREAT support the later scenario for LM YSOs, which does not suffer from

Table 4.4: Physical parameters for a subset of YSO candidates with at least 5 photometric data points

ID	Model set[a]	Class	R_* ($R_\odot$)	T_* (K)	L_* ($L_\odot$)	M_*^b ($M_\odot$)	Age[b] (Myr)	Note[c]
1	sp–s-i	II/III	5.2	3592	4.0	...	...	
2	sp–s-i	II/III	2.6	6791	13.2	...	...	TP01
4	s—s-i	star	1.2	2955	0.1	...	...	
5	s—s-i	star	1.0	3388	0.1	...	...	
6	s—s-i	star	1.0	5120	0.6	...	...	TP03
9	sp–h-i	II/III	3.3	3359	1.2	...	...	
10	s-pbhmi	0	25.8	6214	892.1	8.0	0.06	TP06
11	s—s-i	star	1.2	2955	0.1	...	...	
12	spubsmi	I	23.0	6194	702.1	...	...	TP07
13	sp–h-i	II/III	2.6	6112	8.4	...	...	TP09
14	sp–h-i	II/III	3.6	3736	2.2	...	...	
15	sp–h-i	II/III	10.3	7101	244.9	...	...	TP08

[a] See Table 4.3 footnotes for the description of the model set names.
[b] We provide stellar masses (M_*) and ages only for sources with reliable estimation of these parameters (see text for details).
[c] IDs of the YSO candidates in Gy 3–7 identified by Tapia et al. (1997), see Figure 4.1.

strong self-absorption (Kristensen et al. 2017a; Yang et al. 2022a). Therefore, we assume that the entire high−J CO and [O I] emission originates from outflow shocks. As shown in Section 4.4.4, the line luminosity ratio of CO and [O I] is consistent with C−type shocks irradiated by UV fields of 0.1–10 times the average interstellar radiation field and pre-shock densities of 10^4–10^5 cm^{-3} (see also, Melnick & Kaufman 2015; Karska et al. 2018). The detection of variable H_2O maser further confirms the outflow activity in the region (Furuya et al. 2003), see Appendix 4.A.

The physical conditions in Gy 3–7 are also constrained by CO rotational temperatures, which provide a good proxy of gas kinetic temperatures (Karska et al. 2013; van Dishoeck et al. 2021). The high−J transitions are likely optically thin and thermalized at gas densities >10^5 cm^{-3} routinely measured for LM and IM YSOs (e.g., Kristensen et al. 2012; Mottram et al. 2017). The top panel in Figure 4.14 shows that $T_{\rm rot,CO}$ associated with the two dense cores in Gy 3–7 is either fully consistent (core A) or at the low-end of other IM YSOs (core B), for which the median value from the literature is 320(33) ± 35 K (Matuszak et al. 2015). Similar rotational temperatures have been measured for LM and HM YSOs (Karska et al. 2013, 2014a, 2018; Green et al. 2013, 2016; Manoj et al. 2013; Yang et al. 2018), with average values of 328(33)±63 K (Karska et al. 2018) and 300(23)±60 K (Karska et al. 2014a), respectively.

Some differences between the dense core B in Gy 3–7 and the other YSOs studied in the literature might result from a smaller number of transitions probed by FIFI-LS. The curvature seen in the rotational diagrams causes the rotational temperature to be underestimated if high−J CO transitions are not observed. Therefore, we re-calculated all

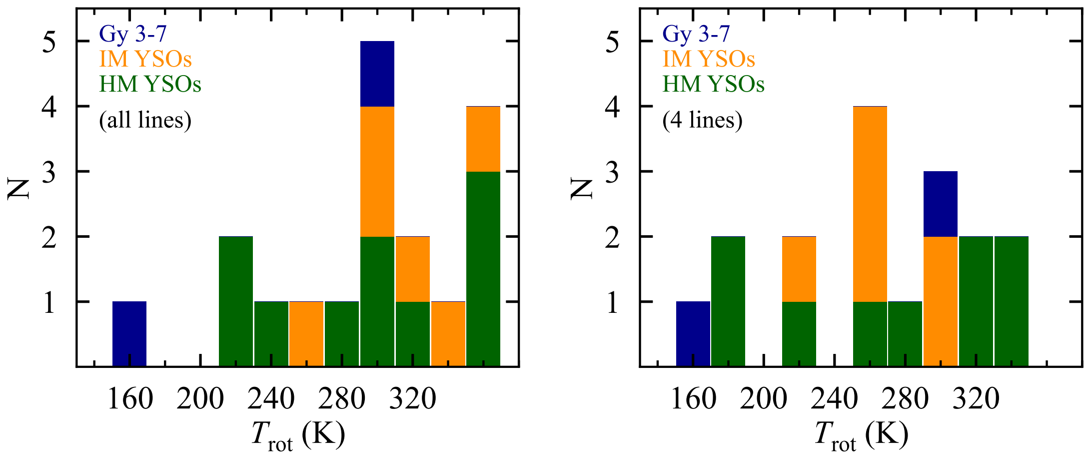

Figure 4.14: CO rotational temperatures for dense cores in Gy 3–7 and intermediate- and high-mass YSOs from the literature (Karska et al. 2014a; Matuszak et al. 2015). *Left:* A straightforward comparison with the literature values. *Right:* A comparison accounting for the number of observed CO lines considered in the rotational diagrams.

literature measurements of $T_{\rm rot}$ for IM and HM YSOs using the same or similar transitions as obtained for Gy 3–7 (Table 4.2 and Appendix 4.D). As expected, CO rotational temperatures for IM and HM YSOs are now lower than reported in the literature, and consistent even with core B (see bottom panel of Figure 4.14).

4.5.2 Possible impact of metallicity on far-IR line emission in the outer Galaxy

Far-IR observations of HM YSOs in the low-metallicity environments of the SMC and LMC show a lower fraction of molecular-to-atomic emission with respect to Galactic YSOs (Oliveira et al. 2019). Here, we investigate the impact of bolometric luminosity, $L_{\rm bol}$, and source Galactocentric radius, $R_{\rm GC}$, on the ratio of CO and [O I] line luminosity.

Figure 4.15 shows the molecular-to-atomic ratio toward Gy 3–7 cores and other Galactic IM and HM YSOs as a function of $L_{\rm bol}$. The values of $L_{\rm bol}$ for the two cores in Gy 3–7 are adopted from Elia et al. (2021), and are equal to 75.9 and 324.2 $L_{\odot}$, respectively. The correlation is characterized by a Pearson coefficient of 0.19, corresponding to 1.6σ. Since the number of LM YSOs exceeds by far the number of IM and HM sources, we also search for trends in the binned datasets. We bin sources in equal intervals of $\log L_{\rm bol}$=1, and adopt a 1σ variance of the distribution as the uncertainty inside the bin. As a result, we confirm a weak correlation between the ratio of line luminosity and $L_{\rm bol}$ (r ~0.59, corresponding to 1.5σ). Thus, our large sample of YSOs starts to reveal a relationship between the mass of YSOs and the fraction of molecular-to-atomic cooling. This has not been possible with a sample of 18 LM YSOs and 10 HM YSOs analysed in Karska et al. (2014a), where a ratio of ~4 was reported for YSOs in the entire mass regime. We note, however, that the *Herschel*/PACS measurements from the literature benefited from additional detections of H_2O and OH, which were included in the molecular far-IR cooling.

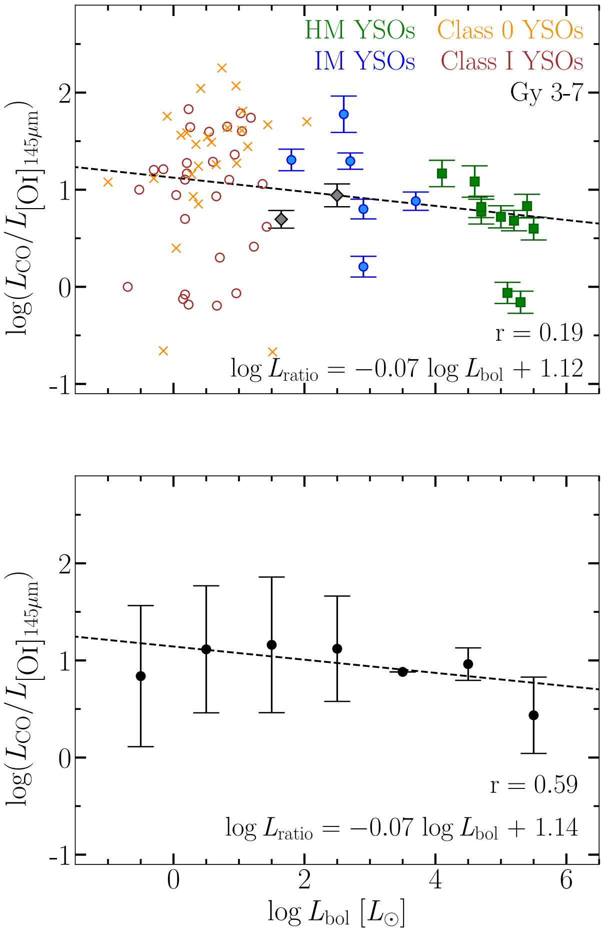

Figure 4.15: Correlations between the ratio of CO and [O I] line luminosities and bolometric luminosity of YSOs in the two cores in Gy 3–7 (gray diamonds), Class 0 and Class I YSOs (orange '×' signs and red circles, respectively; Karska et al. 2018), IM YSOs (blue circles; Matuszak et al. 2015), and HM YSOs (green squares; Karska et al. 2014a). The bolometric luminosities for Gy 3–7 cores are adopted from Elia et al. (2021). The top panel shows a power-law fit to all individual data points, and the bottom panel shows the fit to the data bins (both shown as black dashed line).

Figure 4.16 shows the molecular-to-atomic ratio as a function of Galactocentric radius. In addition, Figure 4.17 shows the same ratio as a function of metallicity, Z, estimated assuming elemental abundance gradients derived from H II regions (Balser et al. 2011). Appendix 4.D provides heliocentric distances, Galactocentric radii, and metallicities of Galactic sources, as well the measurements of CO and [O I] for YSOs in both the Milky Way and the Magellanic Clouds.

The molecular-to-atomic ratio decreases very weakly with the Galactocentric radius (Figure 4.16), but the Pearson coefficient is too small to confirm the correlation (r = 0.08, corresponding to 0.7σ). Additional observations of YSOs in the outer Galaxy would be necessary to constrain the molecular-to-atomic ratio, in particular in the gap between 10 and 12 kpc. Due to the lack of such observations, we search for trends as a function of

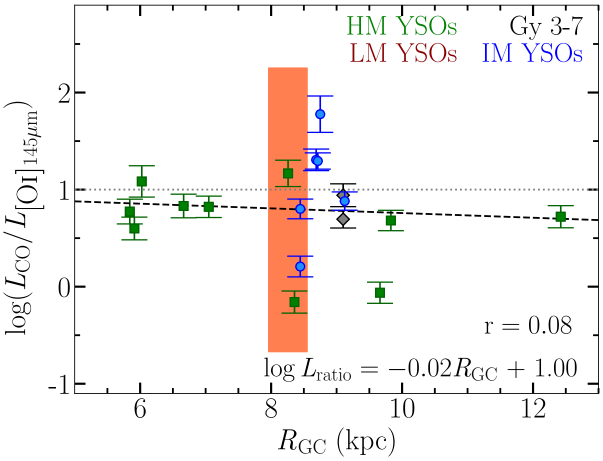

Figure 4.16: The ratio of molecular to atomic line luminosities as a function of the Galactocentric radius. The light coral box indicates the range of the line luminosity ratio and the Galactocentric radius for LM YSOs in the nearby clouds, which are excluded from the power-law fit to the remaining YSOs (dashed black line). The gray dotted horizontal line indicates where the molecular luminosity is equal to the atomic luminosity.

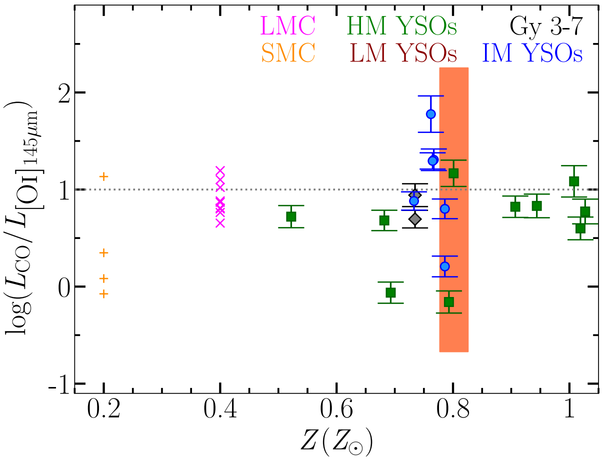

Figure 4.17: The ratio of molecular to atomic line luminosities as a function of metallicity, Z. HM YSOs in the SMC and LMC are shown with cross and '×' symbols in orange and purple colors, respectively. The light coral box indicates the range of the line luminosity ratio and the metallicity for LM YSOs in the nearby clouds, which are excluded from the power-law fit to the remaining YSOs (dashed black line). The gray dotted horizontal line indicates where the molecular luminosity is equal to the atomic luminosity.

metallicity by including YSOs in the Magellanic Clouds (Figure 4.17). We note, however, that the [O I] line at 145 μm was not observed toward sources in the Magellanic Clouds, and the ratio of the two [O I] lines calculated for LM YSOs from Karska et al. (2018) was adopted to estimate its fluxes (Oliveira et al. 2019). As seen in Figure 4.10, this ratio may differ for HM YSOs due to self-absorption or optical depth effects in the [O I] 63 μm line. Additionally, the total CO luminosity of YSOs in the SMC and LMC was estimated using the detections in SPIRE and the conversion factor from Yang et al. (2018), based also on LM YSOs.

In conclusion, Gy 3–7 follows closely the correlations set by YSOs observed in the Milky Way and the Magellanic Clouds. The ratio of molecular-to-atomic line emission is dominated by source bolometric luminosities, and only a very weak decreasing trend with the Galactocentric radius is detected.

4.6 Conclusions

We investigated the SOFIA/FIFI-LS maps of the CO transitions from $J = 14 - 13$ to $J = 31 - 30$, the [O I] lines at 63.2 μm and 145.5 μm, and the [C II] 158 μm line toward the outer Galaxy cluster Gy 3–7. The spatial information about the far-IR emission enables to quantify physical parameters such as temperatures, densities, and UV radiation fields, and associate them with identified YSOs. The conclusions are as follows:

- The CO $J = 14 - 13$ to $J = 16 - 15$ emission lines are detected in a significant part of Gy 3–7, where *Herschel*/PACS 160 μm continuum emission is also strong. Higher$-J$ CO lines up to $31 - 30$ are clearly detected only toward the dense core A.

- The spatial extent of the [O I] emission at 63 and 145 μm is similar to that of CO 14−13 and the 70 and 160 μm continuum emission. The [C II] emission is also extended, but shows systematic shifts in the emission peaks away from the far-IR continuum, tracing lower density gas.

- The CO rotational diagrams show the warm components toward two cores with $T_{\rm rot}$ of 305 and 155 K, and a range of $T_{\rm rot}$ from ~105 to 230 K throughout the cluster, where only three high$-J$ CO lines are unambiguously detected. Similar rotational temperatures have been detected toward IM and HM YSOs in the inner Milky Way calculated using the same or similar CO transitions.

- Strong correlation of the CO and [O I] line luminosities and their similar spatial extent point at the common origin in the outflow shocks. The CO / [O I] line luminosity ratio of Gy 3–7 cores and other intermediate-mass YSOs is consistent with C-type shocks propagating at pre-shock densities of $10^4 - 10^5$ cm^{-3} and UV fields of 0.1-10 times the average interstellar radiation field.

- Physical parameters for 15 YSO candidates in the Gy 3–7 cluster are obtained from a YSO SED model fitting (Robitaille 2017). Two sources, corresponding to Hi-GAL dense cores from Elia et al. (2021), are well-fitted with YSO models including the envelope, confirming their early evolutionary stage (Class 0/I). The location of the Class 0 source at the center of Gy 3–7 cluster suggests that it might be the driving source of the outflow revealed by far-IR emission.

- The ratio of warm CO and [O I] at 145 μm line luminosities from protostellar envelopes shows a weak decreasing trend with the bolometric luminosity and Galactocentric radius. We do not identify any significant dependence of the line cooling in Gy 3–7 on metallicity.

High-resolution submillimeter observations would be necessary to unambiguously associate far-IR emission from FIFI-LS with candidate YSOs and their outflows. Alternatively, efficient imaging of Gy 3-7 with the Mid-Infrared Instrument on board James Webb Space Telescope in F560W and/or F770 W filters tracing H_2 emission would unveil the details in the outflows (Yang et al. 2022b).

Appendix

4.A Water masers in CMa–ℓ224

4.A.1 Survey results

Water masers are important signposts of both low- and high-mass star formation; they are collisionally excited, tracing warm molecular gas behind shock waves in the environment of YSOs and H II regions (e.g., Litvak 1969; Elitzur et al. 1989; Furuya et al. 2003; Ladeyschikov et al. 2022 and references therein). Figure 4.A.1 shows the pointings of our 22 GHz water maser survey of the CMa−l224 star-forming region with the 32-m radio telescope in Toruń (RT4; a half-power beam width, HPBW∼106″, corresponding to ∼0.5 pc at 1 kpc; see Section 4.2.3), overlaid on the CO 1–0 integrated intensity image from the Forgotten Quadrant Survey (FQS, Benedettini et al. 2020; HPBW∼55″ at 115 GHz). The RT4 water maser survey targeted the fields harboring YSO candidates identified by Sewiło et al. (2019). Out of 205 observed fields, (185, 18, 2) were observed in (2, 3, 6) epochs. Water masers were detected toward two fields, one centered on Gy 3–7 and the other on source IRAS 07069−1026 in the main filament in CMa−l224. The very low detection rate is likely the result of the low sensitivity of our observations and the variability of the maser emission (see Section 4.2.3).

The detection of the water maser toward IRAS 07069−1026 constitutes the first maser detection toward this source, while the detection toward Gy 3–7 has previously been reported in the literature. Urquhart et al. (2011) detected the 22 GHz water maser emission toward Gy 3–7 (their source G224.6075−01.0063) with the 100-m Green Bank Telescope (GBT; HPBW∼30″). Water masers were detected toward two other locations in CMa−l224 by Valdettaro et al. (2001) with the Medicina 32-m radio telescope (a similar angular resolution as for RT4), toward IRAS 07077−1026 and IRAS 07054−1039 (see Figure 4.A.1).

Table 4.A.1: Parameters of the 22 GHz H_2O maser lines detected toward CMa−l224 with RT4

Obs. date	V_p (km s^{-1})	S_p (Jy)	FWHM (km s^{-1})	$\int S\,dV$ (Jy km s^{-1})
Gy 3–7				
2019 Dec 11	1.76 ± 0.01	117.33 ± 0.43	0.79±0.003	41.65 ± 0.32
2020 Feb 21	2.28 ± 0.03	7.27 ± 0.25	1.42 ± 0.06	4.67 ± 0.33
2020 Feb 25	2.30 ± 0.04	5.87 ± 0.35	1.36 ± 0.09	3.61 ± 0.45
2020 Feb 27	2.23 ± 0.08	4.41 ± 0.43	1.59 ± 0.18	3.16 ± 0.66
2020 Mar 21	2.53 ± 0.06	5.87 ± 0.33	1.90 ± 0.12	5.04 ± 0.60
2020 May 15	3.94 ± 0.01	23.80 ± 0.33	1.11 ± 0.02	11.93 ± 0.35
IRAS 07069−1026				
2020 May 21	15.73 ± 0.02	12.15 ± 0.40	0.80 ± 0.03	4.38 ± 0.31

The water maser spectra for Gy 3–7 and IRAS 07069–1026 for all epochs of the RT4 observations are shown in Figure 4.A.2 and Figure 4.A.3, respectively. Gy 3–7 was observed with RT4 six times over five months with the time interval between subsequent epochs ranging from 2 days to over 2 months (see Table 4.A.1 for observing dates). The water maser emission was detected in all epochs. IRAS 07069−1026 was observed in two epochs separated by about six months (see Table 4.A.1). The water maser emission toward IRAS 07069−1026 was only detected in the second epoch, illustrating a high variability of the water maser phenomenon. The RT4 spectra of Gy 3–7 also show clear evidence for a variable nature of the maser emission in this region. Both the peak flux density and central velocity of the maser spots varied significantly between April 2019 and May 2020, covering the flux density and velocity ranges of 4.4–117.2 Jy and 1.8–3.9 km s^{-1}, respectively.

The Gauss functions were fitted to the 22 GHz water maser lines observed towards Gy 3–7 and IRAS 07069−1026. The Gauss fitting results are shown Table 4.A.1: the central velocities (V_p) of the water maser lines, their peak flux densities (S_p), full-widths at half maximum (FWHM), and the integrated flux densities ($\int S\,dV$). The measured flux densities are likely underestimated by 10–20% due to the atmospheric conditions at the observatory site; no correction for atmospheric attenuation was applied.

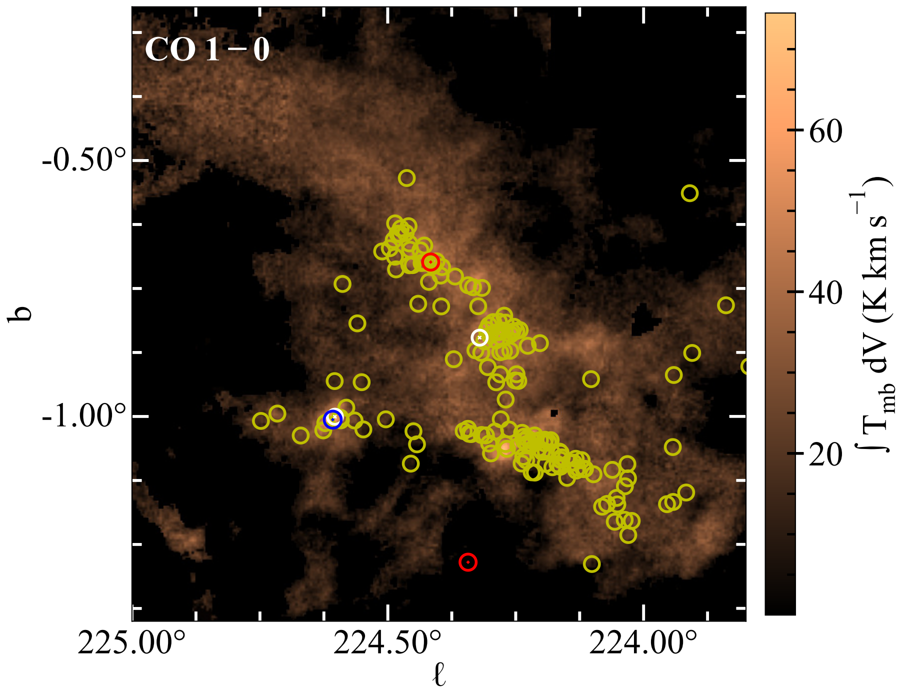

Figure 4.A.1: CO 1 − 0 integrated intensity map of CMa−l224. Yellow circles show all RT4 pointings, while white circles indicate those with the 22 GHz water maser detections: toward Gy 3–7 and source IRAS 07069−1026 in the main filament. Blue and red circles indicate the positions of water masers detected toward CMa−l224 with the GBT (Urquhart et al. 2011) and the Medicina telescope (Valdettaro et al. 2001), respectively (see text for details).

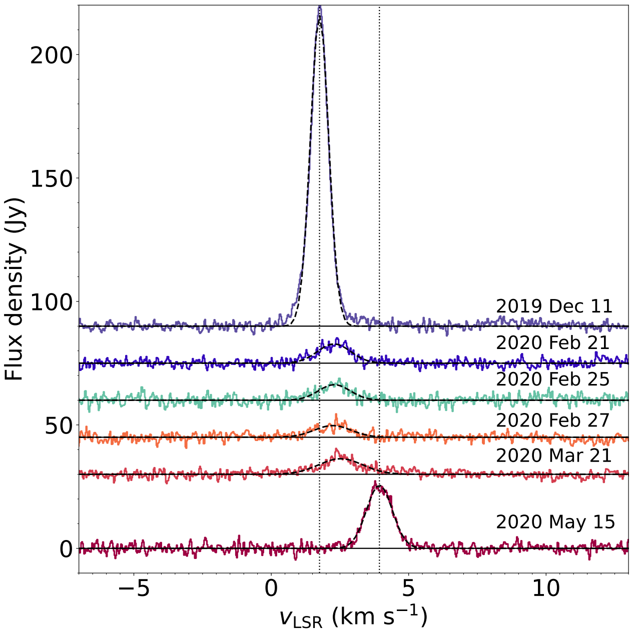

Figure 4.A.2: The 22 GHz H_2O maser spectra obtained toward Gy 3–7 with the 32-m radio telescope in Toruń from December 2019 to May 2020. The date of observations is indicated above each spectrum. Except for the spectrum corresponding to the observation on May 15, 2020, spectra are shifted vertically by 30 Jy (for the observation on March 21, 2020) and 15 Jy (for the remaining observations) to improve the clarity of the figure. Dashed vertical lines show the central velocities of the lines detected in the latest (May 15, 2020) and earliest (December 11, 2019) of the six epochs of observations (see also Table 4.A.1).

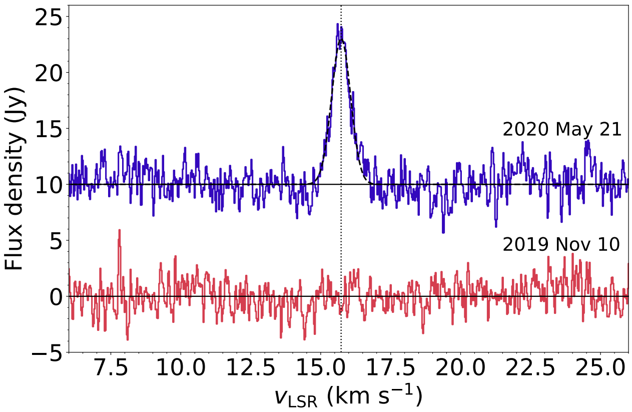

Figure 4.A.3: The 22 GHz H_2O maser emission detected toward IRAS 07069−1026 (see also Table 4.A.1). The H_2O maser was detected only in one of the two observing epochs. The spectrum observed on May 21, 2020 is shifted vertically by 10 Jy to improve the clarity of the figure.

4.A.2 Water maser emission in Gy 3–7

Urquhart et al. (2011) reported the detection of a single water maser spot toward Gy 3–7 (G224.6075−01.0063) with the peak flux density of 2.57 Jy and velocity of 28.7 km s^{-1} (~25 km s^{-1} higher than the emission detected with RT4). However, the inspection of the spectrum provided by Urquhart et al. (2011) reveals a second, much fainter and broader water maser line centered at the velocity of ~0 km s^{-1}, only ~2–4 km s^{-1} lower than the peak velocities of the lines detected in our observations. No water maser emission at higher velocities was detected in any of the six RT4 epochs.

The systemic velocity of Gy 3–7 is 16.7 km s^{-1} based on the NH_3 observations of Urquhart et al. (2011), in a very good agreement with the CO 1–0 velocity of ~16 km s^{-1} (Benedettini et al. 2020), indicating that NH_3 and CO trace the same molecular gas. The water maser emission toward Gy 3–7 is blueshifted (this study) and redshifted (Urquhart et al. 2011) with respect to the systemic velocity. The blueshifted emission has the similar velocity offset (~13–16 km s^{-1}) from the systemic velocity as the redshifted emission (12 km s^{-1}), extending the velocity range over which the maser spots are found toward Gy 3–7 from ~2 km s^{-1} reported in Urquhart et al. (2011) to ~30 km s^{-1}.

About 60% of the sources from the Urquhart et al. (2011) sample have total velocity ranges of the water maser emission of $\lesssim$20 km s^{-1}. The mean/median velocity range of the entire sample is 24.7/15.2 km s^{-1}. Six sources have velocity ranges of >100 km s^{-1}. The Gy 3–7's water maser velocity range of ~30 km s^{-1} is larger than the velocity ranges of the majority of the sources from the Urquhart et al. (2011) sample, but it is well within the observed values.

The water maser data currently available for Gy 3–7 show that the blueshifted water maser spots are brighter than the redshitfed ones (and thus detected more often), in agreement with the results obtained by Urquhart et al. (2011) for a large sample of ~300 YSOs and H ii regions. The higher relative velocities of blueshifted masers also agree with the Urquhart et al. (2011)' results.

The difference of ~12–16 km s^{-1} between the systemic velocity of Gy 3–7 and the velocities of maser spots is small enough to assume that there is the physical association between the molecular gas traced by NH_3 and CO and the maser emission (possibly originating in outflow shocks); it is less likely that the maser emission is arising from a different region located along the same line of sight. The mean difference between the maser and systemic velocities for the Urquhart et al. (2011) sample of YSOs and H ii regions is −3.8 km s^{-1}, but with the large standard deviation (~20 km s^{-1}). It is possible that the water maser emission with smaller offsets from the systemic velocity of Gy 3–7 exists, but remained undetected due to the maser variability and/or limited sensitivity of the observations.

The spatial resolution of the existing water maser observations of Gy 3–7 is too low to accurately pinpoint the location of the maser spots in the region. Higher-resolution observations are needed to investigate the distribution of the maser spots toward Gy 3–7 and the origin of the maser emission. Systematic monitoring of the water maser activity at high angular resolution would be necessary to constrain any periodicity in the maser line intensity in one or more velocity components (Szymczak et al. 2016).

4.B Spatial extent of far-IR line emission

Figures 4.B.1 and 4.B.2 show the spatial extent of the [O I] lines at 63 and 145 μm, the [C II] line at 157 μm, the CO lines with $J_{\rm up} = 14 - 31$, and the OH line at 79.2 μm. We calculate the flux of these emission line toward the two dense cores A and B, within a beam size of 20″ (Table 4.B.1). Since all lines are spectrally-unresolved, the line fluxes are obtained using Gaussian fits and their uncertainties are estimated as 1σ of the distribution of 10 000 Gaussian profiles generated based on the parameters of the Gaussian fit and their uncertainty.

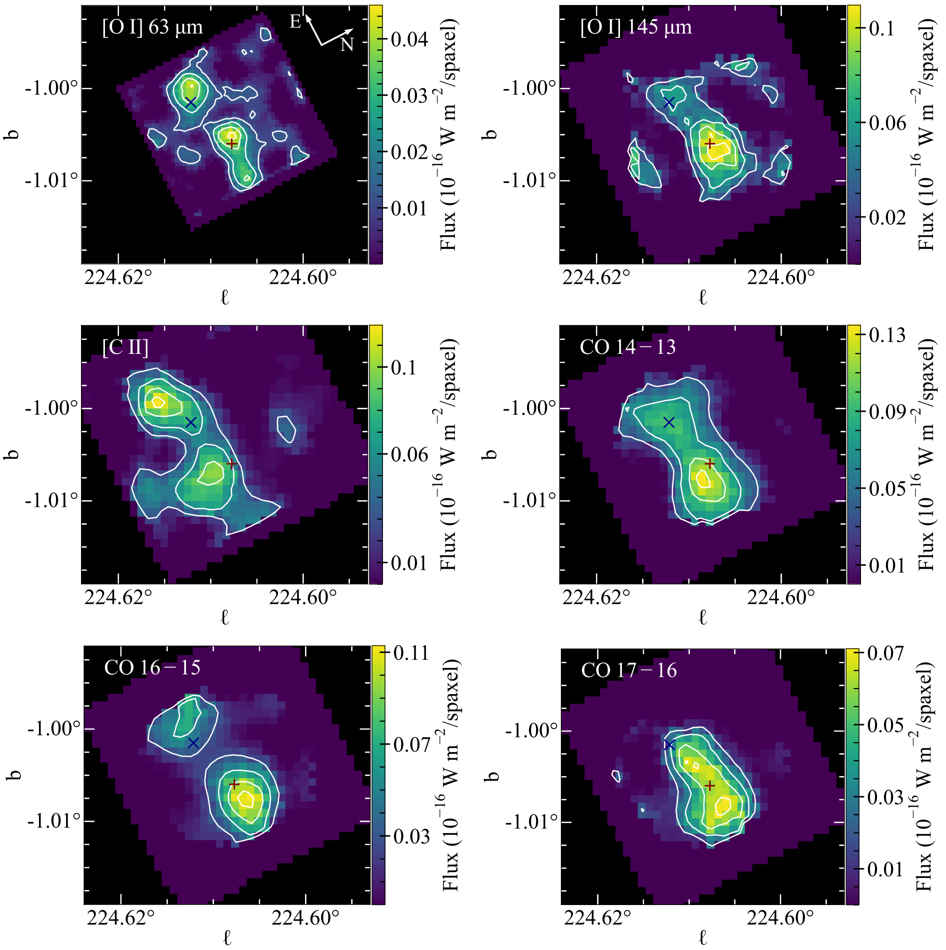

Figure 4.B.1: FIFI-LS integrated intensity maps of the [O I] lines at 63.2 and 145.5 μm, the [C II] line at 157.7 μm, the CO lines $J = 14 - 13$, $16 - 15$, $17 - 16$ at 186, 162.8, 153.3 μm, respectively. The white contours show line emission at 25%, 50%, 75%, and 95% of the corresponding line emission peak. The '+' and 'x' signs show the positions of the dense cores A and B, respectively.

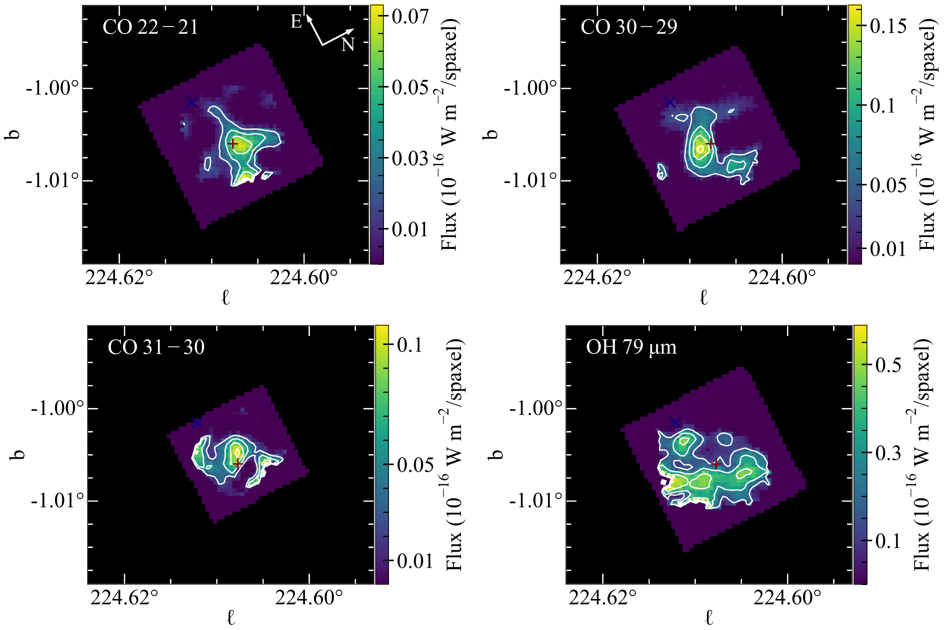

Figure 4.B.2: Similar as Figure 4.B.1 but for the CO 22 − 21, CO 30 − 29 , and CO 31 − 30 transitions at 118, 84, and 87 μm, respectively, and the OH line at 79.2 μm.

4.C Multi-wavelength photometry and SED fitting results

Table 4.C.1 shows the multi-wavelength photometry for 15 YSO candidates in Gy 3–7. Figure 4.C.1 shows the SEDs of YSO candidates in Gy 3–7 with the best-fit Robitaille (2017) models. Figure 4.C.2 shows the Hertzsprung-Russell diagram with the positions of the YSOs obtained from the SED modeling in line with the PMS tracks.

We note that sources No. 3 – 8 and source No. 11, lack continuum measurements > 4.5 μm, which limits the SED modeling. The best-fit models for sources No. 4 – 6 and 11 are stars (Table 4.4), since the envelope emission could not be traced. Near-IR observations show some IR excess toward source No. 6 (Tapia et al. 1997), but the

Table 4.B.1: Flux SOFIA FIFI-LS toward the two dense cores within a beam size of 20″.

λ (μm)	Flux (10^{-16} W m^{-2})	
	core A	core B
63.18	29.65 ± 1.60	24.37 ± 1.72
84.41	4.93 ± 1.80	–
87.19	1.81 ± 0.53	–
118.58	2.68 ± 0.21	–
157.74	1.15 ± 0.07	1.90 ± 0.09
145.53	2.68 ± 0.09	1.97 ± 0.12
153.27	2.09 ± 0.05	1.09 ± 0.07
162.81	2.84 ± 0.05	1.80 ± 0.07
186.00	2.73 ± 0.08	2.56 ± 0.13

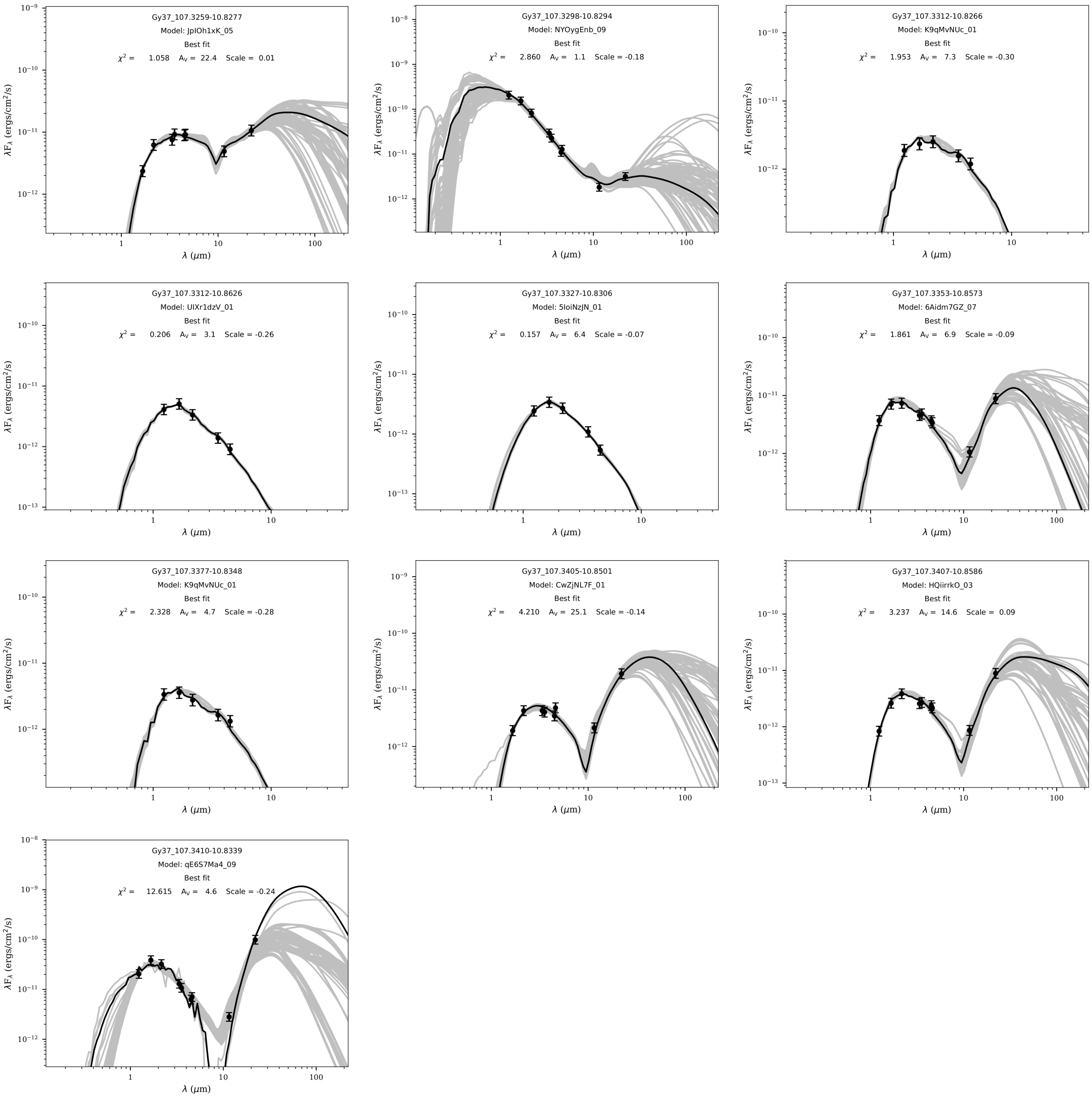

Figure 4.C.1: SEDs of YSO candidates with well-fitted Robitaille (2017) YSO models. The best-fit model is indicated with the black solid line; gray lines show the YSO models with χ^2 between $\chi^2_{\rm best}$ and $\chi^2_{\rm best}$+ $F \times n$, where n is the number of data points and F is a threshold parameter which we set to 3 (Sewiło et al. 2019). Filled circles and triangles are valid flux values and flux upper limits, respectively. The values of a reduced χ^2 and interstellar visual extinction for the best-fit model are indicated in the plots.

confirmation of its YSO status would require additional observations, which are outside of the scope of this paper.

Table 4.C.1: Multi-wavelength photometry of YSO candidates in the IRAS field. The columns represent the 2MASS *JHK*$_s$, *Spitzer* IRAC 3.6 and 4.5 μm, AllWISE, *Herschel* PACS and SPIRE

ID	RA (deg)	Dec (deg)	S_J (mJy)	S_H (mJy)	S_K (mJy)	$S_{3.6}$ (mJy)	$S_{4.5}$ (mJy)	$S_{\rm W1}$ (mJy)	$S_{\rm W2}$ (mJy)
1	107.32592	-10.82772	...	1.33 ± 0.06	4.56 ± 0.13	11.11 ± 0.43	13.57 ± 0.30	8.59 ± 0.18	14.28 ± 0.27
2	107.32975	-10.82944	86.55 ± 2.07	86.28 ± 2.07	60.13 ± 1.27	27.44 ± 1.05	16.67 ± 0.57	33.60 ± 0.72	20.02 ± 0.43
3	107.33013	-10.83094	...	2.33 ± 0.33	3.15 ± 0.26	2.61 ± 0.10	2.63 ± 0.07	...	...
4	107.33121	-10.82658	0.79 ± 0.07	1.33 ± 0.07	1.85 ± 0.12	1.89 ± 0.08	1.82 ± 0.05	...	...
5	107.33121	-10.86256	1.72 ± 0.06	2.86 ± 0.12	2.45 ± 0.13	1.67 ± 0.06	1.38 ± 0.04	...	...
6	107.33275	-10.83064	1.02 ± 0.06	1.92 ± 0.09	1.98 ± 0.12	1.31 ± 0.06	0.82 ± 0.04	...	...
7	107.33379	-10.84222	2.33 ± 0.24	14.68 ± 1.47	23.61 ± 2.36	...	...	...	...
8	107.33467	-10.84192	2.59 ± 0.35	16.75 ± 1.67	32.03 ± 3.20	...	...	...	...
9	107.33529	-10.85725	1.55 ± 0.08	4.01 ± 0.11	5.40 ± 0.19	5.79 ± 0.21	5.58 ± 0.16	5.16 ± 0.12	5.31 ± 0.11
10	107.33563	-10.84117	1.17 ± 0.16	4.57 ± 0.65	21.06 ± 1.46	...	...	87.24 ± 1.79	403.08 ± 7.87
11	107.33771	-10.83483	1.41 ± 0.07	2.02 ± 0.07	2.03 ± 0.10	1.98 ± 0.07	2.02 ± 0.07	...	...
12	107.33879	-10.84178	1.47 ± 0.15	1.16 ± 0.20	3.22 ± 0.30	...	...	24.38 ± 2.28	52.26 ± 1.41
13	107.34054	-10.85011	...	1.08 ± 0.07	3.15 ± 0.10	4.89 ± 0.21	5.30 ± 0.11	4.91 ± 0.10	7.53 ± 0.10
14	107.34071	-10.85858	0.35 ± 0.05	1.48 ± 0.09	2.82 ± 0.13	3.25 ± 0.12	3.62 ± 0.14	2.93 ± 0.06	3.38 ± 0.07
15	107.34100	-10.83386	8.58 ± 0.29	21.79 ± 0.60	23.65 ± 0.50	12.97 ± 0.61	9.56 ± 0.36	14.79 ± 0.27	11.00 ± 0.18

ID	RA (deg)	Dec (deg)	$S_{\rm W3}$ (mJy)	$S_{\rm W4}$ (mJy)	S_{70} (Jy)	S_{160} (Jy)	S_{250} (Jy)	S_{350} (Jy)	S_{500} (Jy)
1	107.32592	-10.82772	19.26 ± 0.41	79.72 ± 2.92	...	...	...	...	...
2	107.32975	-10.82944	7.16 ± 0.28	23.74 ± 1.56	...	...	...	...	...
3	107.33013	-10.83094	...	...	...	...	...	...	...
4	107.33121	-10.82658	...	...	...	...	...	...	...
5	107.33121	-10.86256	...	...	...	...	...	...	...
6	107.33275	-10.83064	...	...	...	...	...	...	...
7	107.33379	-10.84222	...	...	...	...	...	...	...
8	107.33467	-10.84192	...	...	...	...	...	...	...
9	107.33529	-10.85725	4.18 ± 0.19	66.19 ± 2.99	...	...	...	...	...
10	107.33563	-10.84117	4017.01 ± 33.44	28890.97 ± 160.10	165.8 ± 0.5	1030.6 ± 0.4	57.0 ± 0.5	23.5 ± 0.1	10.6 ± 0.1
11	107.33771	-10.83483	...	...	...	...	...	...	...
12	107.33879	-10.84178	117.25 ± 2.62	4541.11 ± 46.24	42.5 ± 0.2	60.8 ± 0.2	62.0 ± 0.6	20.8 ± 0.1	...
13	107.34054	-10.85011	8.38 ± 0.17	144.66 ± 1.34	...	...	...	...	...
14	107.34071	-10.85858	3.38 ± 0.20	66.43 ± 2.62	...	...	...	...	...
15	107.34100	-10.83386	11.04 ± 0.14	743.98 ± 1.37	...	...	...	...	...

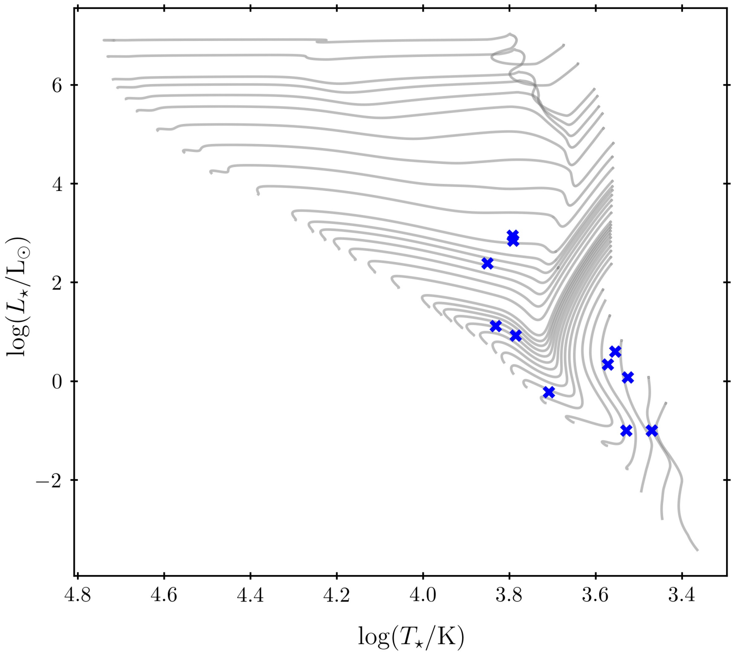

Figure 4.C.2: HR diagram with YSOs in Gy 3–7 (blue '×' symbols) and the PARSEC evolutionary tracks (Bressan et al. 2012; Chen et al. 2014, 2015; Tang et al. 2014).

4.D CO rotational temperature of the intermediate-to high-mass YSOs in the Milky Way

We compare the rotational temperatures towards the two dense cores to the results found in the samples of the IM and HM YSOs in the Milky Way. There are 6 IM and 10 HM YSOs presented in Karska et al. (2014a) and Matuszak et al. (2015), respectively using the data from *Herschel*/PACS. To be consistent with our SOFIA/FIFI-LS data, we re-calculate the rotational temperatures derived by fitting the rotational diagram using 4 CO transitions with J_{up} = (14, 16, 18, 22) and (14, 16, 17, 22) for the IM and HM YSOs, respectively.

We check the new results with the ones presented in the aforementioned studies and find that using only 4 CO transitions returns a lower T_{rot} than the case of using all the observable CO transitions. The relative difference is in between 4-27% with a median of 5% for the HM YSOs. The comparison of these differences is shown in Table 4.D.1.

Table 4.D.2 shows heliocentric distances, Galactocentric radii, metallicities, and luminosities of the sources in the Milky Way and Magellanic Clouds. We used heliocentric distances together with source coordinates to calculate Galactocentric radii, assuming a distance from the Sun to the Galactic center of 8.34 kpc. We estimated the metallicity toward the Milky Way sources using the O/H galactocentric radial gradient based on H II regions in the Galactic disk (Balser et al. 2011).

Table 4.D.1: CO rotational temperature and number of emitting molecules for HM YSOs, derived by fitting the rotational diagram of CO using all and only four available CO transitions.

Source	$T_{\rm rot,4}{}^{a}$ (K)	$T_{\rm rot,all}{}^{b}$ (K)	$T_{\rm rot}$ Diff.^{c} (%)
G327-0.6	275 ± 60	265 ± 30	4
W51N-e1	270 ± 15	260 ± 15	4
DR21OH	225 ± 25	235 ± 15	4
W33A	135 ± 5	185 ± 25	27
G34.26+0.15	330 ± 60	320 ± 25	3
NGC6334-I	320 ± 55	300 ± 25	7
NGC7538-I1	175 ± 25	185 ± 15	5
AFGL2591	175 ± 10	195 ± 15	10
W3IRS5	335 ± 40	320 ± 15	5
G5.89-0.39	345 ± 40	285 ± 15	21

Notes: ^{a} Rotational temperatures calculated using 4 CO transitions with $J_{\rm up} = (14, 16, 17, 22)$. $^{(b)}$ Rotational temperatures calculated using all detected CO transitions, data is adopted from Karska et al. (2014a). $^{(c)}$ The relative difference of $T_{\rm rot}$ is taken as $|1 - T_{\rm rot,4}/T_{\rm rot,all}| \times 100$.

Table 4.D.2: Far-IR line cooling luminosity of the sample in the Milky Way (MW), LMC, and SMC used to compare with results of this study

Source	D (kpc)	D Ref.	$R_{GC}{}^{a}$ (kpc)	Z^{b} ($Z_\odot$)	$\log(L_{bol}/L_\odot)$	L_{bol} Ref.	$L_{CO}{}^{c}$ ($10^{-2}L_\odot$)	$L_{[O\,I]}{}^{d}$ ($10^{-2}L_\odot$)	$L_{CO}/L_{[O\,I]}$	L_{lines} Ref.
LMC YSOs										
IRAS04514−6931	50.0 ± 1.1	1	—	0.4	4.8	16	5.3	8.8	0.605	16
N113 YSO3	50.0 ± 1.1	1	—	0.4	5.4	16	29.5	57.8	0.511	16
SAGE045400.9−691151.6	50.0 ± 1.1	1	—	0.4	5.1	16	14.6	29.2	0.5	16
SAGE051351.5−672721.9	50.0 ± 1.1	1	—	0.4	5.1	16	5.5	15.4	0.357	16
SAGE052202.7−674702.1	50.0 ± 1.1	1	—	0.4	4.5	16	4.3	9.4	0.459	16
SAGE052212.6−675832.4	50.0 ± 1.1	1	—	0.4	5.5	16	14.9	25.4	0.585	16
SAGE053054.2−683428.3	50.0 ± 1.1	1	—	0.4	4.9	16	6.8	5.4	1.24	16
ST01	50.0 ± 1.1	1	—	0.4	4.6	16	7 .1	8.5	0.833	16
N113 YSO1	50.0 ± 1.1	1	—	0.4	5.4	16	47.5	47.5	1	16
SMC YSOs										
IRAS00464−7322	62.1 ± 2.0	2	—	0.2	4.1	16	3.0	2.8	1.077	16
IRAS00430−7326	62.1 ± 2.0	2	—	0.2	4.9	16	1.9	10.9	0.176	16
N81	62.1 ± 2.0	2	—	0.2	4.7	16	2. 4	36.4	0.067	16
SMC012407-730904	62.1 ± 2.0	2	—	0.2	5.3	16	6.8	71.2	0.096	16
MW IM YSOs										
AFGL 490	0.97 ± 0.40	3	9.12	0.7	3.7	17	24.7 ± 2.5	36.6 ± 0.2	0.7 ± 0.1	32
L 1641	0.428 ± 0.010	4	8.69	0.8	1.8	18	2.7 ± 0.4	1.6 ± 0.1	1.7 ± 0.3	32
NGC 2071	0.422 ± 0.050	4	8.71	0.8	2.7	19	44.8 ± 4.3	33.4 ± 0.1	1.3 ± 0.1	32
Vela 17	0.7	5	8.44	0.8	2.9	20	13.2 *pm* 2.0	44.8 ± 0.1	0.3 ± 0.1	32
Vela 19	0.7	5	8.45	0.8	2.9	5	9.7 ± 2.0	14.4 ± 0.1	0.7 ± 0.1	32
NGC 7129	1.25	6	8.75	0.8	2.6	21	20.9 ± 3.0	6.9 ± 0.1	3.0 ± 0.4	32
MW HM YSOs										
G327-0.6	3.3	7	5.84	1.0	4.7	22	180 ± 60	30 ± 10	6.0 ± 2.8	33
W51N-e1	5.1 ± 2.2	8	12.42	0.5	5.0	23	2530 ± 680	760 ± 180	3.3 ± 1.2	33
DR21(OH)	1.50 ± 0.08	9	8.26	0.8	4.1	24	120 ± 30	9 ± 3	13.3 ± 5.6	33
W33A	2.40 ± 0.16	10	6.02	1.0	4.6	25	60 ± 20	5 ± 2	12.0 ± 6.2	33
G34.26+0.15	3.30	11	5.91	1.0	5.5	26	770 ± 240	190 ± 50	4.1 ± 1.7	33
NGC6334I	1.7 ± 0.3	12	6.66	0.9	5.4	27	340 ± 100	4 ± 3	85.0 ± 68.5	33
NGC7538-IRS1	2.7 ± 0.1	13	9.66	0.7	5.1	28	280 ± 50	1100 ± 250	0.2 ± 0.1	33
AFGL2591	3.3 ± 0.08	9	8.36	0.9	5.3	29	160 ± 50	340 ± 90	0.5 ± 0.2	33
W3-IRS5	2.00 ± 0.07	14	9.83	0.7	5.2	30	1050 ± 250	420 ± 10	2.5 ± 0.8	33
G5.89-0.39	1.30 ± 0.09	15	7.05	0.9	4.7	31	390 ± 90	370 ± 90	1.1 ± 0.4	33

References: (1) Pietrzyński et al. (2013), (2) Graczyk et al. (2014)), (3) Purser et al. (2021), (4) Wilson et al. (2005), (5) Liseau et al. (1992),(6) Shevchenko & Yakubov (1989), (7) Minier et al. (2009), (8) Xu et al. (2009), (9) Rygl et al. (2012) , (10) Immer et al. (2013), (11) Kuchar & Bania (1994), (12) Neckel (1978), (13) Moscadelli et al. (2009), (14) Hachisuka et al. (2006), (15) Motogi et al. (2011), (16) Oliveira et al. (2019),(17) Navarete et al. (2015), (18) Stanke et al. (2000) , (19) Butner et al. (1990), (20) Giannini et al. (2005), (21)Johnstone et al. (2010), (22) Urquhart et al. (2012), (23) van Dishoeck et al. (2011),(24) Jakob et al. (2007), (25) Faúndez et al. (2004), (26) Hatchell & van der Tak (2003), (27) Sandell (2000), (28) Sandell & Sievers (2004), (29) van der Tak et al. (1999), (30) Ladd et al. (1993), (31) van der Tak (2012), (32) Matuszak et al. (2015), (33) Karska et al. (2014a).

[a] Galactocentric radius toward the sources in the Milky Way is calculated using the information from their coordinate and distance to the Sun, assuming the distance from the Sun to the Galactic center is 8.34 kpc.

[b] Metallicity towards the sources in the Milky Way is calculated using the relation of O/H gradients inferred from the H II regions: $12 + \log(O/H) = -0.0446R_{GC} + 8.962$ (Balser et al. 2011).

[c] Total far-IR luminosity of CO derived from the rotational diagram fitting.

[d] Total far-IR luminosity of [O I] calculated by summing the luminosity of [O I] lines at 63 and 145 μm.

Chapter 5

Near-infrared spectroscopy of young stellar objects in the CMa–ℓ224 star-forming region: spectral types, extinction, and mass accretion

To be submitted to Astronomy & Astrophysics

5.1 Introduction

Star formation in our Galaxy occurs mainly in giant molecular clouds and seems to be quite uniformly distributed in its inner parts despite the preferential formation of clouds in the spiral arms (Urquhart et al. 2021). Globally, the Galactic surface mass density of molecular clouds decreases steeply with Galactocentric radius, at least partly due to the negative metallicity gradient lowering molecular and dust abundances (Heyer & Dame 2015). Additional environmental factors such as interstellar radiation field and cosmic-ray flux alter the physical conditions in clouds e.g., by decreasing gas and dust temperatures in distant clouds (Roman-Duval et al. 2010). All in all, the gas in the outer Galaxy is mostly atomic and the star formation seems to be rather sparse (Kennicutt & Evans 2012).

Recent large-scale IR and ongoing submm surveys probe star formation in the outer Galaxy with unprecedented sensitivity and offer the opportunity to verify its efficiency and impact on the environment. In particular, the largely uncharted, third quadrant of the Galaxy around the longitude of 224° has been surveyed as part of the Warm *Spitzer* Exploration Science Program "GLIMPSE360: Completing the Spitzer Galactic Plane Survey" (PI: M. Meade) and the Open Time Key Project "Herschel infrared Galactic Plane Survey" (Hi-GAL, Molinari et al. 2010b). These surveys, combined with CO mapping, revealed a significant star formation activity along the most massive filaments in CMa-ℓ224 molecular cloud (Elia et al. 2013; Schisano et al. 2014) and provided a catalog of star-forming clumps, cores, and their physical properties (Olmi et al. 2016).

Candidates of YSO and their clusters have been identified using color-color diagrams with the multi-wavelength photometry, and verified with models of spectral energy distributions (Fischer et al. 2016; Sewiło et al. 2019). The most significant star formation activ-

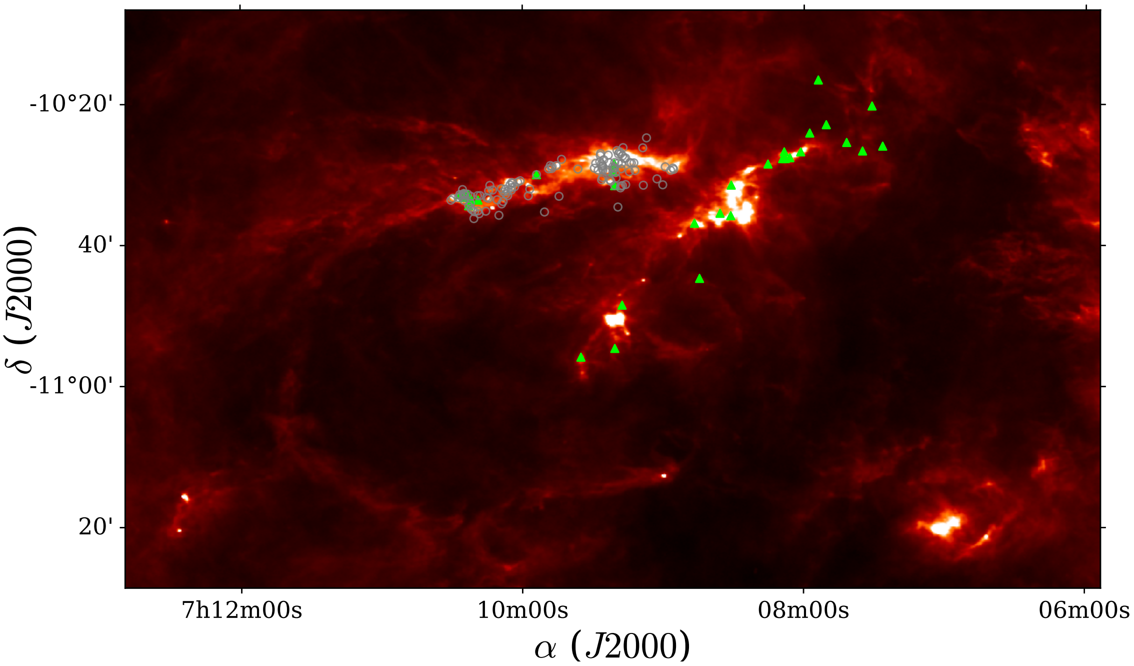

Figure 5.1: Continuum emission map at 250 μm toward the CMa-ℓ224 region. The gray circles and green triangles indicate the positions of YSO candidates, observed by the VLT/KMOS (Itrich et al. 2023) and NASA IRTF/SpeX (this thesis), respectively.

ity in the third quadrant, measured by the concentration of YSO candidates, is contained within the 2.5° × 1.4° region centered at $(\ell, b) = (224.5°, -0.65°)$ and referred as CMa-ℓ224 (Sewiło et al. 2019). Among 293 YSO candidates, many are expected to belong to the Class 0/I protostars, based on the presence of bright, extended 4.5 μm emission likely related to H_2 jets (Sewiło et al. 2019) and the CO outflows revealed with a single-dish survey in the Purple Mountain Observatory (Lin et al. 2021). Nevertheless, high-angular resolution spectroscopic observations are necessary to confirm the YSO identification and evolutionary stages.

The NASA IRTF/SpeX spectra contain, among others, the hydrogen H Brγ line at 2.17 μm which is a well-established tracer of accretion luminosity, and a number of diagnostic photospheric lines (Connelley & Greene 2010). The higher-sensitivity VLT/KMOS spectra provide information about the spatial extent of line and continuum emission in K-band for 8 sources observed also with SpeX. A separate analysis of VLT/KMOS spectral maps focusing on the links between accretion and ejection of ~120 YSO candidates in CMa-ℓ224 is presented in Itrich et al. (2023). Figure 5.1 shows the *Herschel*/SPIRE map of the CMa-ℓ224 star-forming region at 250 μm with the positions of YSO candidates observed with both instruments.

In this Chapter, we present the near-IR survey of 33 sources located in the CMa-ℓ224 star-forming region with the aim to characterize their spectral types and signatures of ongoing accretion. The near-IR spectroscopy presented here is used to address the following questions:

1. What are the stellar spectral types and extinction toward YSO candidates in CMa-ℓ224?

2. Do the sources show signatures of ongoing accretion?
3. To what extent do the mass accretion rates in CMa-ℓ224 compare to those of YSOs located in the nearby star-forming regions in the Gould Belt?

In Section 5.2 we describe our sample selection, observations, and data reduction. In Section 5.3 we show the statistics of line detections and compare the sources in common to the VLT/KMOS survey results. Section 5.4 shows the calculations of extinction, spectral types, excess continuum emission, and mass accretion rates. Section 5.5 discusses the results obtained in previous sections and Section 5.6 presents the summary and conclusions.

5.2 Observation and data reduction

5.2.1 SpeX

We used the IR spectrograph SpeX (Rayner et al. 2003) at the 3.2–m NASA InfraRed Telescope Facility (IRTF) to observe 33 sources in the CMa-ℓ224 region (proposal numbers 2015B082 and 2019A096, PI: W. Fischer). The sources were selected from the catalogs of Fischer et al. (2016) and Sewiło et al. (2019) based on their K-band brightness and positions outside of the two KMOS patrol fields (see below), with the exception of 8 sources from the first observing run which were observed with the two instruments. Table 5.1 shows coordinates and source properties, including physical characteristics from Sewiło et al. (2019). Hereinafter, only the first part of the IRAC name, including the galactic longitude of the source, is used for referencing the targets.

The A0 V star HD 56525 was also observed for telluric correction and flux calibration purposes. The data were reduced using the `Spextool`, an IDL-based data reduction package for SpeX (Cushing et al. 2004). The steps included the dark frame subtraction and flat fielding, extraction of the spectrum, and wavelength calibration. The telluric absorption was corrected using the IDL routine `xtellcor` (Vacca et al. 2003).

To obtain the shape of the continuum, we adopted the following procedure. The spectrum for each source was divided into sub-ranges (I, Y, J, H, and K band-passes), smoothed, and the residuals between the original data and the smoothed spectral bands were calculated. Data points with flux densities above 1σ of the residual distribution were removed. The smoothing was repeated until the standard deviation of residual distribution was less than 10% compared to the previous loop. The remaining data points were fitted with a low-order polynomial, which describes the shape of the continuum.

The continuum was subtracted from the observed spectrum to analyze the emission/absorption features. The line identification was done with the help of the HITRAN[1] database and the high-resolution spectral atlas provided by Hinkle et al. (1995). Since most lines are spectrally unresolved and the S/N of the spectra is often relatively low, we calculated the line fluxes using Gaussian fits. For most atomic lines and their doublets, we used single or double Gaussians with fixed line widths corresponding to the instrumental values calculated based on the spectral resolution of SpeX at a given wavelength. For all

---

[1] `https://hitran.org/`

Table 5.1: Properties of YSO candidates in the CMa-ℓ224 star-forming region

No.	IRAC name	RA J2000	DEC J2000	J[b]	H[b]	K[b]	Class[c]	Other names	
	SSTGLMA	(°)	(°)	(mag)	(mag)	(mag)		2MASS	WISEA
1	G224.0300-01.2317	106.860468	−10.432493	12.251	11.650	11.10	II	286316409	J070726.50-102557.0
2	G224.1368-01.0903	107.038035	−10.462196	15.177	13.614	12.59	II	286373991	J070809.14-102743.8
3	G224.2337-01.0397	107.129153	−10.524914	–	14.709	12.32	II	286388979	J070830.99-103129.5
4	G224.3005-00.8417[a]	107.339159	−10.492918	13.044	11.631	10.52	II	286433619	J070921.39-102934.2
5	G224.3285-00.8597[a]	107.336023	−10.526146	13.263	12.182	11.71	II	286433738	J070920.64-103133.8
6	G224.4649-00.6415[a]	107.596975	−10.546402	–	13.924	12.08	II	286504944	J071023.27-103247.1
7	G224.4664-00.6346[a]	107.603906	−10.544595	15.293	13.065	11.85	II	286504951	J071024.94-103241.3
8	G224.1291-01.1006	107.025231	−10.460084	14.886	13.209	12.03	II	286373982	J070806.04-102736.2
9	G224.2833-00.8353B	107.336914	−10.474753	16.001	13.473	11.97	I	286433562	J070920.82-102828.9
10	G224.3019-01.0531	107.149012	−10.591564	15.041	13.537	12.49	II	286388739	J070835.75-103529.5
11	G224.4688-00.6638	107.578710	−10.560110	12.665	12.269	12.22	–	286491861	J071018.88-103336.3
12	G224.4721-00.6296[a]	107.611051	−10.547358	15.517	13.092	11.52	II	286504937	J071026.64-103250.4
13	G224.4735-00.6529	107.59069	−10.559280	14.267	13.027	12.52	–	286491858	J071021.75-103333.3
14	G224.4883-00.6555[a]	107.595338	−10.573611	–	14.279	12.67	II	286491898	J071022.88-103424.9
15	G224.6701-01.0373	107.335878	−10.911046	13.010	12.015	11.39	II	286435238	J070920.60-105439.6
16	G224.0304-01.1210	106.960647	−10.381908	14.161	13.220	12.59	II	286331305	J070750.55-102254.7
17	G224.0612-01.1045	106.989901	−10.401638	13.853	12.972	12.45	II	286373769	J070757.57-102405.6
18	G224.1080-01.1110	107.005962	−10.446119	15.271	13.040	11.67	II	286373929	J070801.41-102646.6
19	G224.1212-01.0855	107.035171	−10.446143	14.663	13.061	12.06	II	286373928	J070808.44-102646.0
20	G224.1346-01.0945	107.033291	−10.462148	15.518	13.533	12.54	II	286373990	J070807.98-102743.9
21	G224.2833-00.8353A	107.336914	−10.474753	16.001	13.473	11.97	I	286433562	J070920.82-102828.9
22	G224.2983-01.0722	107.130020	−10.597202	16.052	13.630	12.26	II	286388722	J070831.20-103549.9
23	G224.3433-01.0242	107.194466	−10.615052	–	13.884	11.65	II	286388677	J070846.66-103654.1
24	G224.3684-00.7267[a]	107.474793	−10.500157	13.899	12.159	11.05	II	286491650	J070953.95-103000.5
25	G224.4549-01.0923	107.185324	−10.745472	13.357	12.410	11.87	II	286388115	J070844.47-104443.6
26	G224.4751-00.6383[a]	107.604575	−10.553973	13.766	12.612	12.11	II	286504916	J071025.08-103313.6
27	G224.7156-00.9944	107.396055	−10.931703	11.861	10.820	10.12	II	286445288	J070935.05-105554.1
28	G224.0513-01.1719	106.924401	−10.423878	15.110	13.721	12.76	II	286331137	J070741.85-102525.8
29	G224.0564-01.2058	106.896195	−10.443964	13.780	12.677	12.06	II	286331066	J070735.08-102638.2
30	G224.1599-01.0736	107.063971	−10.474973	16.043	13.980	12.91	II	286374049	J070815.36-102829.8
31	G224.5733-01.0014	107.322918	−10.808675	15.511	14.052	12.63	I	286434824	J070917.49-104831.1
32	G223.9430-01.0600	106.974817	−10.276177	13.019	12.394	12.09	II	286331713	J070753.94-101634.2
33	G223.9543-01.1714	106.879488	−10.337524	14.568	13.158	12.38	II	286331476	J070731.07-102015.0

Notes: [a] Sources observed with VLT/KMOS (Itrich et al. 2023). [b] The J, H and K photometry taken from the 2MASS catalogue (Skrutskie et al. 2006). [c] The classification of YSO candidates, taken from Sewiło et al. (2019), is identified based on the results of the SED fitting using YSO models in Robitaille et al. (2007).

other lines except H Brγ and CO bandhead, the line shapes resemble Gaussians but their widths are broader than the instrumental value. Thus, we adopted the line widths which are the average of the widths of the lines with the highest S/N for all lines. The line flux uncertainties are taken as the 1σ of the distribution of 1000 Gaussian profiles generated based on the parameters of the Gaussian fit and its uncertainty. For H Brγ and the CO bandhead, the line fluxes (and EWs) are calculated by integrating the line profile. The uncertainty was taken as the $\sqrt{2N_{\rm pixels}}\times$dispersion$\times\sigma_{\rm cont}$). The spectral ranges chosen for those integrations are adopted from Ramirez et al. (1997). The upper limit of line flux is estimated as $3\times RMS\times\lambda_0/R$, where RMS is the root mean square of the observed flux, λ_0

is the laboratory wavelength of the line, and R is the resolving power at this wavelength.

5.2.2 KMOS

Eight sources from the SpeX sample were also observed with KMOS on VLT as part of the survey of ~120 YSOs in the CMa-ℓ224 (proposal ID: 0102.C-0914(A), PI: A. Karska). The full sample is presented in Itrich et al. (2023).

KMOS is a multi-object, integral-field spectrograph with 24 configurable arms operating within a patrol field of 7.2′ in diameter (Sharples et al. 2013). Each of the 24 IFUs has a field of view of 2.8″ × 2.8″, with a spaxel size of 0.2″ × 0.2″. Each source was observed in Node-to-Sky mode with a total exposure time of 1300 seconds. KMOS data was obtained solely in the K-band, with a resolution of ~2.8 Å corresponding to a velocity resolution of ~39.7 kms^{-1}.

KMOS data were reduced using `EsoRex` – the ESO Recipe Execution Tool for flat-fielding, dark frame and background subtraction, wavelength and fluxes calibration, and the reconstruction of science datacubes (see Davies et al. 2013). The continuum was obtained by fitting the 7th-order Chebyshev polynomial to the spectrum in each spaxel (spatial pixel) in each datacube. Similarly, the line fluxes were calculated separately for each spaxel by fitting a Gaussian function to the emission line; random input parameters were generated 50 times and the fit with the lowest relative error was chosen. A detailed description of observations and data reduction is presented in Itrich et al. (2023). The KMOS continuum maps at 2.12 μm for all eight sources and the line fluxes calculated using the central 9 spaxels from the KMOS spectral cubes are shown in Appendix 5.A.

5.3 Results

Spectra from SpeX cover a broad range from 0.8 to 2.45 μm, which encompasses the H Paβ and H Brγ lines at 1.28 and 2.17 μm, the H_2 ro-vibrational lines including the 1-0 S(1) line at 2.12 μm, the CO vibrational overtone lines at ~2.3 μm (the CO bandhead), the He I line at 1.08 μm, and the Na I and Ca I doublets at 2.21 and 2.27 μm. Spectra of all 33 sources observed with SpeX are presented in Appendix 5.B. Figure 5.2 shows example K-band spectra with line identifications of 8 sources observed both from SpeX and KMOS. Table 5.2 shows the summary of the line detections, line profiles, and spatial extent for all the sources.

5.3.1 Line detections

The majority of sources (all but G224.5733) show well-established near-IR signatures of the YSO, including the presence of H Brγ and/or CO bandhead in their spectra and other characteristic lines in emission (see Figures 5.2 and 5.3). We divided them into four groups based on the detections of H Brγ and CO bandhead to facilitate forthcoming analysis.

Group 1 shows detections of both H Brγ and CO bandhead. The CO lines are seen in absorption, and the H Brγ is in emission except in the two sources G224.3005 and G224.4649 with H Brγ in absorption. Four out of seven sources observed with KMOS

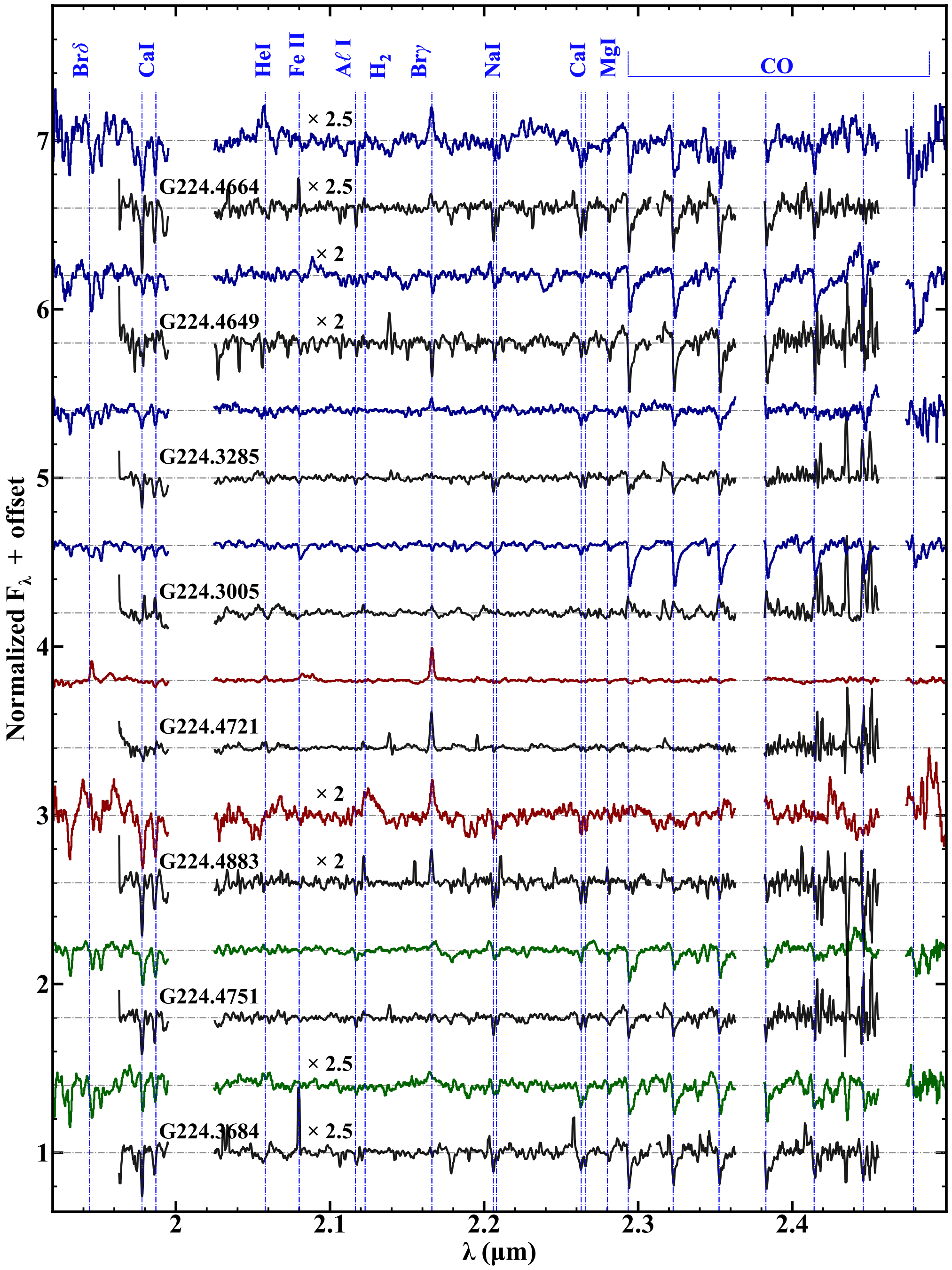

Figure 5.2: NASA IRTF/SpeX continuum-normalized spectra of YSO candidates observed also with VLT/KMOS (Itrich et al. 2023). Sources representing Groups 1, 2, and 3 are shown in blue, red, and green colors, respectively (see Section 5.3). The KMOS spectra are shown in black. Spectral ranges near to 2 μm, 2.37 μm, and 2.48 μm are strongly affected by telluric lines and not shown. The offsets are applied for clarity.

show also the H_2 emission (Itrich et al. 2023). The objects in this group are classified as Class II YSOs based on SED modeling (Table 5.1), but their near-IR spectra suggest that at least those with H_2 detections may be in fact Class I objects.

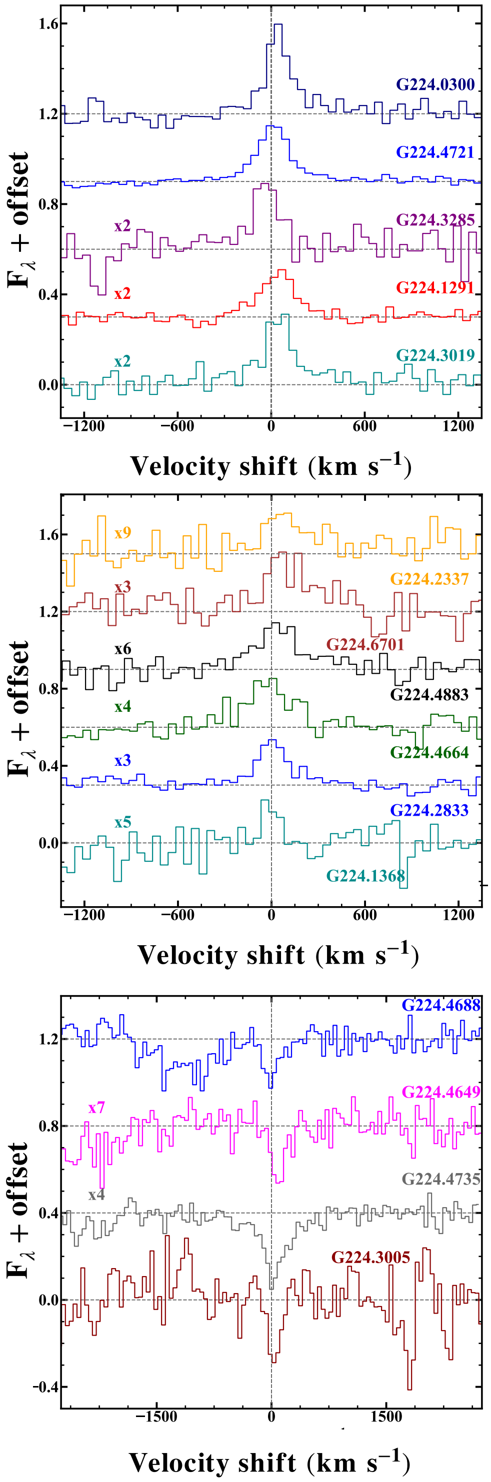

Figure 5.3: Line profiles of the H Brγ line at 2.17 μm detected with SpeX. Flux is in units of 10^{-15} erg s^{-1} cm^{-2} Å^{-1}. The scaling factors are shown in the figure.

Group 2 shows H Brγ lines typically in emission (6 our of 8 sources), but no CO bandhead. Similarly to sources from Group 1, the two objects observed with KMOS

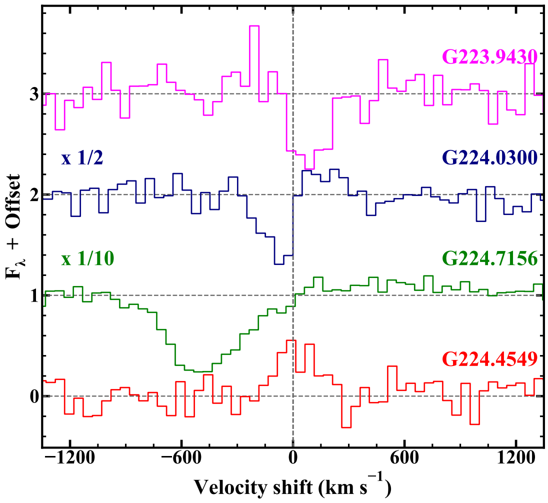

Figure 5.4: Similar to Figure 5.3, but for the He I line at 1.08 μm.

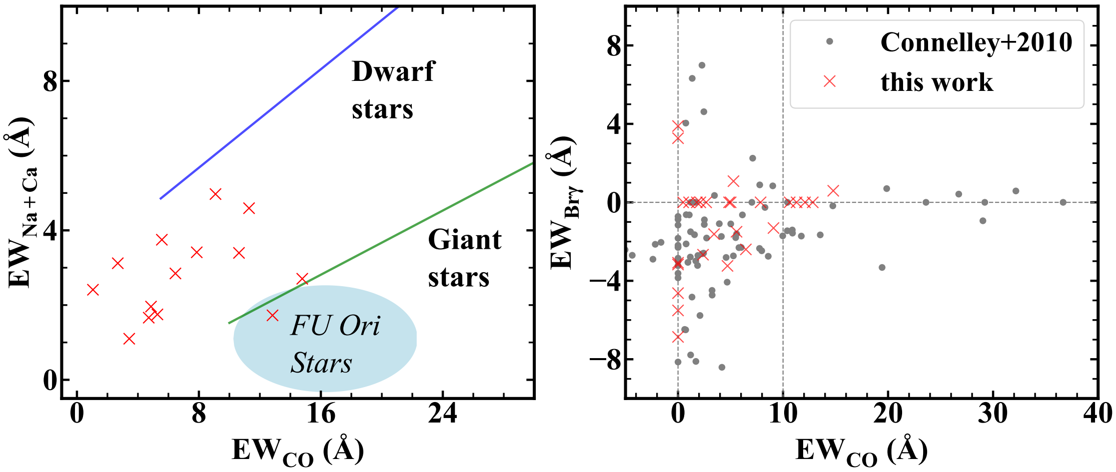

Figure 5.5: Comparison of the EWs of the CO bandhead, Na I and Ca I doublets, and of H Brγ line. *Left:* EW of the Na I and Ca I doublets at 2.21 and 2.26 μm versus the CO bandhead at 2.29 μm. Solid lines show the positions of dwarf (luminosity Class V, in blue) and giant (luminosity Class III, in green) stars from the SpeX spectral library, following Connelley & Greene (2010). The two objects with the deepest CO absorptions are G224.7156 and G224.3005. *Right:* EW of the H Brγ line at 2.17 μm versus the CO bandhead of YSOs in the CMa-ℓ224 region (red crosses) and of Class I protostars in nearby star-forming regions(grey dots; Connelley & Greene 2010). The sources with the highest EWs of CO are G224.3005 (with H Brγ detection), and G224.4751, G224.7156, G224.4549, and G224.1346 (due to the lack of H Brγ detection).

show H_2 emission, which is not detected with SpeX. All sources except G224.4688 show at least one emission line, and are likely Class II YSOs (Table 5.1). G224.2833B is the only source in this group classified as Class I based on its SED, but its mid- and far-IR photometry includes also G224.2833A.

Group 3 contains sources with CO bandhead in absorption and the lack of H Brγ de-

Table 5.2: Catalog of line detections

No.	Source	H Brγ	CO	H_2	H Paβ	Emis. lines[a]	Metal lines[b]	He I	TiO	Remarks
Group 1: YSOs with H Brγ and CO bandhead										
1	G224.0300	Y	Y	N	Y	Y	Y	Y	N	He I in abs.
2	G224.1368	Y	Y	N	N	Y	Y	N	N	
3	G224.2337	Y	Y	N	N	Y	N	N	N	no *J*-band
4	G224.3005	Y	Y	Y	N	N	Y	N	N	KMOS: extended H_2, non det. in SpeX; CO, H Brγ, and Fe II in abs; CO in emis. in KMOS
5	G224.3285	Y	Y	Y	Y	Y	Y	N	N	KMOS: compact H_2, non det. in SpeX; CO in abs.
6	G224.4649	Y	Y	Y	N	N	Y	N	N	KMOS: compact H_2, non det. in SpeX; CO, H Brγ , and Fe II in abs.
7	G224.4664	Y	Y	Y	N	Y	Y	N	N	KMOS: compact H_2, non det. in SpeX; CO and Fe II in abs.
Group 2: YSOs with H Brγ and no CO bandhead										
8	G224.1291	Y	N	N	Y	Y	N	N	N	
9	G224.2833B	Y	N	N	N	Y	N	N	N	no *J*-band
10	G224.3019	Y	N	N	Y	Y	Y	N	N	
11	G224.4688	Y	N	N	Y	N	Y	N	Y	H Brγ in abs.
12	G224.4721	Y	N	Y	Y	Y	Y	N	N	KMOS: compact H_2
13	G224.4735	Y	N	N	Y	Y	Y	N	Y	H Brγ and Fe II in abs.
14	G224.4883	Y	N	Y	N	Y	Y	N	N	KMOS: extended H_2, non det. in SpeX
15	G224.6701	Y	N	N	Y	Y	Y	N	N	
Group 3: YSOs with CO bandhead and no H Brγ										
16	G224.0304	N	Y	N	N	Y	Y	N	N	
17	G224.0612	N	Y	N	N	Y	Y	N	N	
18	G224.1080	N	Y	N	N	N	Y	N	N	
19	G224.1212	N	Y	N	N	Y	Y	N	N	
20	G224.1346	N	Y	N	N	N	Y	N	N	
21	G224.2833A	N	Y	N	N	N	Y	N	N	
22	G224.2983	N	Y	N	N	N	Y	N	N	no *J*-band
23	G224.3433	N	Y	Y	N	Y	Y	N	N	no *J*-band; H_2 in SpeX
24	G224.3684	N	Y	Y	Y	Y	Y	N	N	KMOS: compact H_2, non det. in SpeX; CO in abs.
25	G224.4549	N	Y	N	Y	Y	Y	Y	N	He I in emis.
26	G224.4751	N	Y	Y	N	Y	Y	N	N	KMOS: compact H_2, non det. in SpeX;COin abs.
27	G224.7156	N	Y	N	Y	N	Y	Y	N	H Paβ in abs., He I in abs. with strong blue shift
Group 4: YSOs with non-detections of H Brγ and CO bandhead										
28	G224.0513	N	N	Y	N	Y	Y	N	N	H_2 in SpeX
29	G224.0564	N	N	N	N	N	Y	N	N	
30	G224.1599	N	N	N	N	Y	Y	N	N	no *J*-band
31	G224.5733	N	N	N	N	N	N	N	N	
32	G223.9430	N	N	N	N	Y	Y	Y	N	He I and Fe II in abs.
33	G223.9543	N	N	N	N	N	Y	N	N	Fe II in abs

Notes: [a] Refers to any species detected in emission. [b] Refers to photospheric lines of metals, e.g. Na I and Ca I doublets.

tection. The group contains three sources with H Paβ and three sources with the H_2 detection, with G224.3684 showing both features. G224.2833A shows the H_2 2.12 μm line in the SpeX spectrum, which is consistent with the Class I classification from its SED. The majority of the sources show lines in emission (7 out of 12 sources), but the YSO status of the remaining sources is not clear and requires follow-up observations.

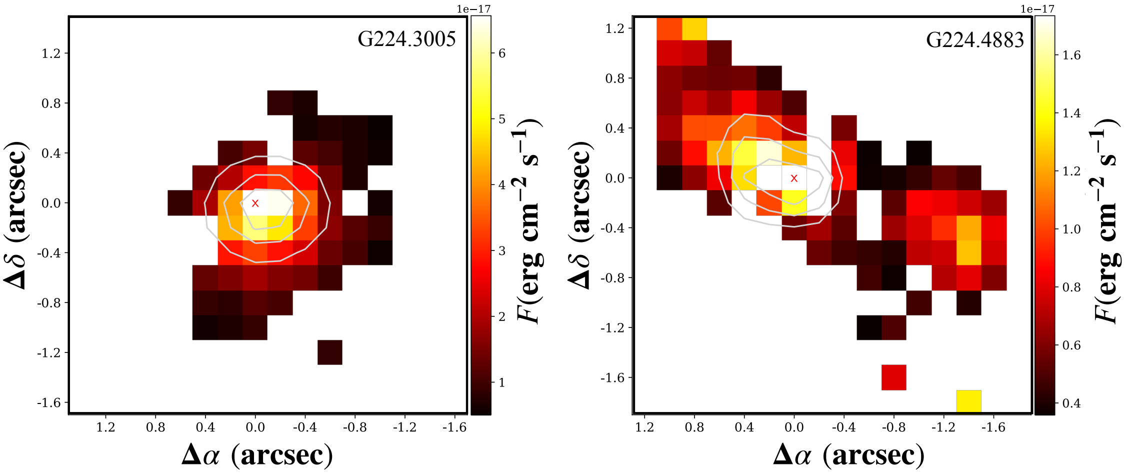

Figure 5.6: Emission maps of the H_2 line at 2.12 μm toward 2 out of 8 sources observed with VLT/KMOS. The contours show the continuum emission (see also Figure 5.A.1) and the colors show the H_2 emission above 3σ.

Finally, Group 4 shows a lack of detection of H Brγ and CO bandhead. Emission lines are present in 3 our of 6 sources. G224.0513 shows the detection of the H_2 2.12 μm line in the SpeX spectrum. G244.5733 is the only source with a featureless spectrum, and also the only Class I source classified using SED in the entire sample, with the exception of the mid-IR binary G244.2833.

Apart from the most commonly detected lines, four sources representing Groups 1, 3 (two sources), and 4 show the He I line at 1.08 μm (see Figure 5.4). The line is detected in absorption except 1 source G224.4549, and shows a clear red-shift in velocity with respect to the rest of the lines in two sources. A remarkable blueshift of about 600 km s^{-1} in G224.7156 is well spectrally-resolved even at the spectral resolution of SpeX and indicates the presence of a fast wind (Edwards et al. 2006; Kwan et al. 2007). Six sources show the detection of the Fe II line at 1.64 μm, which emission is a signature of dissociative shocks (Hollenbach & McKee 1989). Yet, the line is detected solely in absorption, pointing at the photospheric origins.

Figure 5.5 shows a comparison of the EW of the CO lines with those of Na I and Ca I doublets, and H Brγ, respectively. The former is a probe of the stellar gravity, and shows that the majority of the studied sources are the dwarf star (Connelley & Greene 2010). Two sources are located in the region occupied by giant stars or, alternatively, FU Orionis stars. The latter scenario is consistent with the location of these sources on the far-right part of the H Brγ versus CO diagram. According to Connelley & Greene (2010), the CO bandhead's EW in excess of 10Å is another signature of FU Ori stars and cannot be accounted for by the photospheric absorption from stars with spectral types below M4. Such sources are also expected to show little to no H Brγ emission, which is indeed the case for 5 sources in our sample (see right panel in Figure 5.5). The CO absorption in the remaining sources is consistent with photospheric absorption from dwarf stars.

To summarize, the overview of the near-IR spectra of the YSO candidates in the CMa-ℓ224 qualitatively confirm their initial identification based on photometric surveys (Sewiło et al. 2019). The estimate of extinction, stellar types, and accretion is necessary to fully characterize the sources (see Section 5.4).

5.3.2 Spatial extent of line emission

Gas ejections are likely presented in all sources with the detection of ro-vibrational H_2 lines, which requires high gas temperatures and densities for excitation. The pattern of the spatial extent of H_2 emission toward G224.3005 and G224.4883 (see Figure 5.6) resembles H_2 jets commonly seen in Class 0/I protostars in the Gould Belt (Davis et al. 2008). A generally poor statistics of H_2 detections in the SpeX sample is due to a lower sensitivity of NASA IRTF with respect to VLT (see Figure 5.2).

5.4 Analysis

5.4.1 Extinction and spectral types

We use several methods to determine the stellar parameters (extinction and spectral type) to our sources, based on the available photometry, line fluxes (or EWs), and continuum shapes. Extinction provides a necessary correction for line fluxes used in the analysis and informs how embedded YSOs are in the sample. The derived extinction values and spectral type of our sources using these methods are summarized in Table 5.3.

Firstly, we calculate visual extinction (A_V) to our sources using the 2MASS J-, H-, and K-band photometry, defined as (Cooper et al. 2013):

$$A_V = \frac{m_1 - m_2 + x_{\mathrm{int}}}{0.55^{1.75}(\lambda_1^{-1.75} - \lambda_2^{-1.75})} , \qquad (5.1)$$

where m_1 and m_2 refer to either J and H, or H and K magnitudes, and x_{int} is the intrinsic colour of a B0 type star equal 0.12 and 0.05 mag for $J - H$ and $H - Ks$, respectively.

The median extinction of our sources in J-and H-bands, $A_V(JH)$, is 12.2 mag and using H-and K-bands, $A_V(HKs)$, is 19.9 mag. The difference between these two quantities is related to the dust scattering at J-band and dust excess at K-band, and provides the lower and upper limits to the extinction (Porter et al. 1998; Cooper et al. 2013). Among the four groups of sources, the highest $A_V(\mathrm{HK_S})$ is determined toward sources in Groups 1 and 2 (21.5 and 21.4, respectively). The two sources with the highest extinction, $A_V(HKs)$>40, are G224.2337 (Group 1) and G224.3433 (Group 3), for which J band observations with SpeX are also not available.

Secondly, we use the ratio of H Paβ and H Brγ line fluxes to calculate the relative extinction, A_{rel}, between the wavelengths of the two hydrogen lines (see e.g., Reiter et al. 2019):

$$A_{\mathrm{rel}} = -2.5\frac{\log(\mathrm{Pa}\beta/\mathrm{Br}\gamma)_{\mathrm{obs}}}{\log(\mathrm{Pa}\beta/\mathrm{Br}\gamma)_{\mathrm{exp}}} . \qquad (5.2)$$

The subscripts refer to the observed ratios (“obs”), and the ratios expected (“exp”) for case B recombination, where the intrinsic flux ratio of H Paβ and H Brγ is 5.75 ± 0.15 and is appropriate for electron densities, $n_e \sim 10^2 - 10^4$ cm^{-3} and electron temperatures, $T_e \sim 5 \times 10^3 - 10^4$ K (Storey & Hummer 1995). Both lines are detected in 8/33 sources belonging to Groups 1 and 2 (see Table 5.2), but in two sources (G224.4688 and G224.4735) these lines appear in absorption and are not used to calculate the extinction, A_V(HI). The median value of A_{rel}(HI) for 6 sources with hydrogen recombination lines is 1.18 mag. We obtain the absolute value of extinction using the relation:

$$A_V(HI) = A_{rel}(k_{\lambda_1} - k_{\lambda_2})^{-1} , \tag{5.3}$$

where k_{λ_1} and k_{λ_2} are the ratios of extinction A_λ at the wavelengths of the H Paβ and H Brγ lines, and the A_V, and are calculated based on the extinction curve from (Cardelli et al. 1989):

$$k_\lambda = \frac{A_\lambda}{A_V} = a_x + b_x R_V , \tag{5.4}$$

assuming R_V=3.1, a_x=0.574$\lambda^{-1.61}$, and b_x=0.527$\lambda^{-1.61}$. The H Paβ/ H Brγ flux ratio and extinction values for 6 sources using this method are listed in Table 5.3.

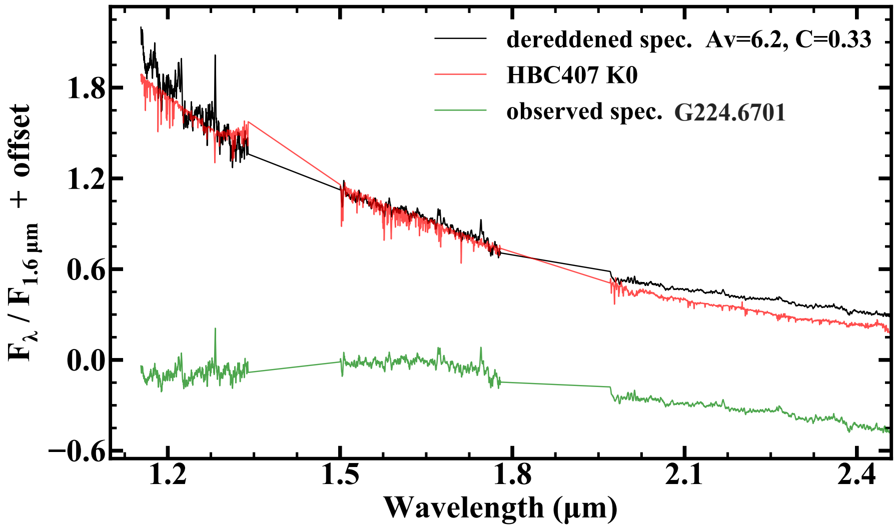

Figure 5.7: SpeX spectrum of G224.6701 and a best-fit stellar template of the K0 star HBC407 from Alcalá et al. (2014). Original YSO spectrum is shown in green, the dereddened spectrum in black, and the stellar template in red. The excess emission of the YSO in the *K*-band is due to accretion (see text).

Lastly, we determine extinction from the fit of the entire SpeX spectrum to the templates of non-accreting Class III YSOs with spectral types from G5 to M9.5 (Manara et al. 2013, 2017). We vary the template and extinction to match the shape of the YSO spectrum in *J*- and *H*-bands, which are less affected by disk extinction, following the procedures described in Alcalá et al. (2014) and Fiorellino et al. (2021). Figure 5.7 shows an example de-redenning and fitting of the template to the SpeX spectrum of source G224.670, normalized at a window of 0.02 μm around 1.6 μm, where no spectral features are present. In several cases, multiple spectral types and extinctions provided a satisfactory solution. Table 5.3 lists the ranges of A_V(SpT) and spectral types to our sources determined using this method (SpT(cont)).

The spectral types of young stars can be also inferred from some prominent spectral features e.g., Ca I line at 0.866 μm, Al I line at 1.31 μm, Mg I at 1.771 μm, or Na I line at 2.21 μm (see e.g., Rayner et al. 2009, and references therein). Here, we use the EWs of Na I line to estimate the spectral types of our sources based on the comparison to a large catalog of dwarf stars from Rayner et al. (2009), see Figure 5.8. The resulting

Table 5.3: Extinction and spectral types to YSOs

No.	Source	$A_V(JH)$	$A_V(HKs)$	Paβ/Brγ	A_V(HI)	A_V(SpT)	SpT(cont)	SpT(NaI)
Group 1: YSOs with H Brγ and CO bandhead								
1	G224.0300	7.3	11	4.79	1.2	–	–	F5
2	G224.1368	12.6	19.9	–	–	9.2	K6	M2
3	G224.2337	–	44.9	–	–	24.8-25.6	M0-M0.5	F5
4	G224.3005	13.5	21.5	–	–	28	K1	G8
5	G224.3285	6.4	9.6	2.21	6.1	5.8-4.6	K0.5-M2	K0
6	G224.4649	–	34.9	–	–	24.6	M0-M1	G3
7	G224.4664	14.6	23.4	–	–	14.0-10.6	K2-M3.5	G6
Group 2: YSOs with H Brγ and no CO bandhead								
8	G224.1291	14.2	22.7	1.64	8	8.4 - 10.6	K2-K7	G0
9	G224.2833B	17.8	28.7	–	–	12.2-17.4	K3-K7	G1.5
10	G224.3019	12.7	20.1	1.71	7.7	7.8-5.2	K2-M3	–
11	G224.4688	1.9	1.8	abs. [a]	–	–	K0	F6
12	G224.4721	18.5	30	0.72	13.2	13.8-13.4	K7-M0.5	F7
13	G224.4735	6.9	10.4	abs. [a]	–	–	K0	F6
14	G224.4883	–	30.5	–	–	17.4-20.2	K6-M0.5	G9
15	G224.6701	8.1	12.4	2.7	4.8	6.0 - 7.4	K0-K4	G1.5
Group 3: YSOs with CO bandhead and no H Brγ								
16	G224.0304	8.2	12.5	–	–	5.8-7.0	K1-K4	F9
17	G224.0612	7.1	10.6	–	–	3.6	K7	G4
18	G224.1080	16.3	26.2	–	–	14.8	M1	G0
19	G224.1212	12.2	19.3	–	–	11.8-9.8	G8-K6	F7
20	G224.1346	12.2	19.2	–	–	9.2-11.4	K6-M0	K1-K2
21	G224.2833A	17.8	28.7	–	–	14.6-17.4	K6-K7	K1
22	G224.2983	16.3	26.2	–	–	14-15.6	K7-M1	K1-K2
23	G224.3433	–	42.1	–	–	25-27	K3-M3	G3-G4
24	G224.3684	13.5	21.4	–	–	11.6	K3	F6
25	G224.4549	7.2	10.9	–	–	5.0-5.2	G5-K3	G1.5
26	G224.4751	6.8	10.2	–	–	3.4-4.8	K1-M3	K2
27	G224.7156	8.9	13.7	–	–	10	M3	F5
Group 4: YSOs with non-detections of H Brγ and CO bandhead								
28	G224.0513	11.8	18.6	–	–	5.2-6.8	M0-M4	K2
29	G224.0564	8.1	12.3	–	–	7.6 - 7.8	G8-G9	G9
20	G224.1599	13	20.6	–	–	5.6	M4.5	K2
31	G224.5733	16.9	27.2	–	–	–	–	–
32	G223.9430	4.7	6.6	–	–	0.5	M2	G9-K1
33	G223.9543	9.8	15.2	–	–	8.4-6.4	K0.5-K6	K1-K2

Notes: [a] The 'abs.' refers to sources with both H Brγ and H Paβ lines detected in absorption, for which the ratio was not calculated.

spectral types are generally comparable to those obtained from fitting stellar templates (Table 5.3); yet, for several sources the difference is quite substantial, illustrating the difficulty in obtaining the spectral types of YSOs.

5.4.2 Continuum excess due to accretion

A comparison between the spectra of the template young stars and the objects in the CMa-ℓ224 region shows an excess continuum emission after extinction correction, referred as veiling, which is dominant in the K-band. Proper determination of the excess spectrum

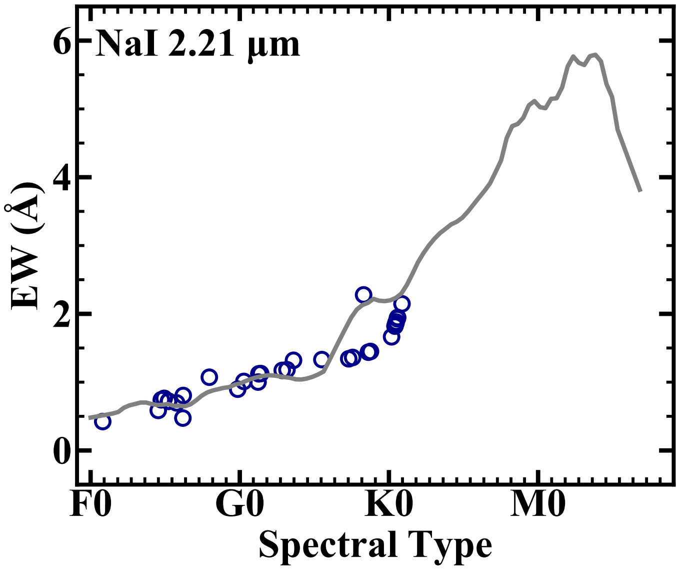

Figure 5.8: EW the Na I line feature as a function of the spectral type. The gray solid line represents the trend of EW vesus spectral type of dwarf stars from the SpeX spectral library (Rayner et al. 2009). Blue circles show our sources.

provides information about the ongoing accretion, and the source properties.

To calculate the excess emission spectra, E_λ, we adopt the procedure presented in Fischer et al. (2011), which is illustrated in Figure 5.9. The line veiling, r_λ, informs about the decrease of the EW of the absorption lines due to the presence of extra continuum emission, calculated as:

$$r_\lambda = \frac{E_\lambda}{P_\lambda} = \frac{\mathrm{EW_{ref}}}{\mathrm{EW_{obs}}} - 1. \tag{5.5}$$

where P_λ is an intrinsic photosphere of the star, $\mathrm{EW_{ref}}$ and $\mathrm{EW_{obs}}$ are the EW of the spectral line in the template spectrum (T_λ) and the observed SpeX spectrum (O_λ), respectively. We assume that the observed SpeX spectrum, O_λ, is the reddened sum of the photosphere and excess continuum:

$$O_\lambda = (P_\lambda + E_\lambda)\,10^{-0.4A_V} \tag{5.6}$$

The extinction to the computing source is calculated from the slope of the linear fit of the form:

$$2.5\log[T_\lambda/O_\lambda(1 + r_\lambda)] = k_\lambda\,(A_V - A_{V,T}) - 2.5\log C \tag{5.7}$$

assuming that $A_{V,T}$, the extinction to the template spectrum, is known. C is a normalization constant corresponding to the intercept of the fit, by which we multiply the template spectrum and subtract it from the de-reddened source. This way, we obtain the excess continuum λE_λ. The veiling spectrum is then computed by dividing E_λ by the scaled photospheric template P_λ.

Table 5.4 shows the extinction estimates obtained for 6 sources with sufficient veiling lines in the SpeX spectra. The extinction is the highest for G224.3005 and G224.3285 from Group 1, and G224.1346 from Group 3. In fact, the excess continuum method by Fischer et al. (2011) results in somewhat higher extinctions than obtained with the Manara et al. (2017) method. The results for all sources are, however, consistent within

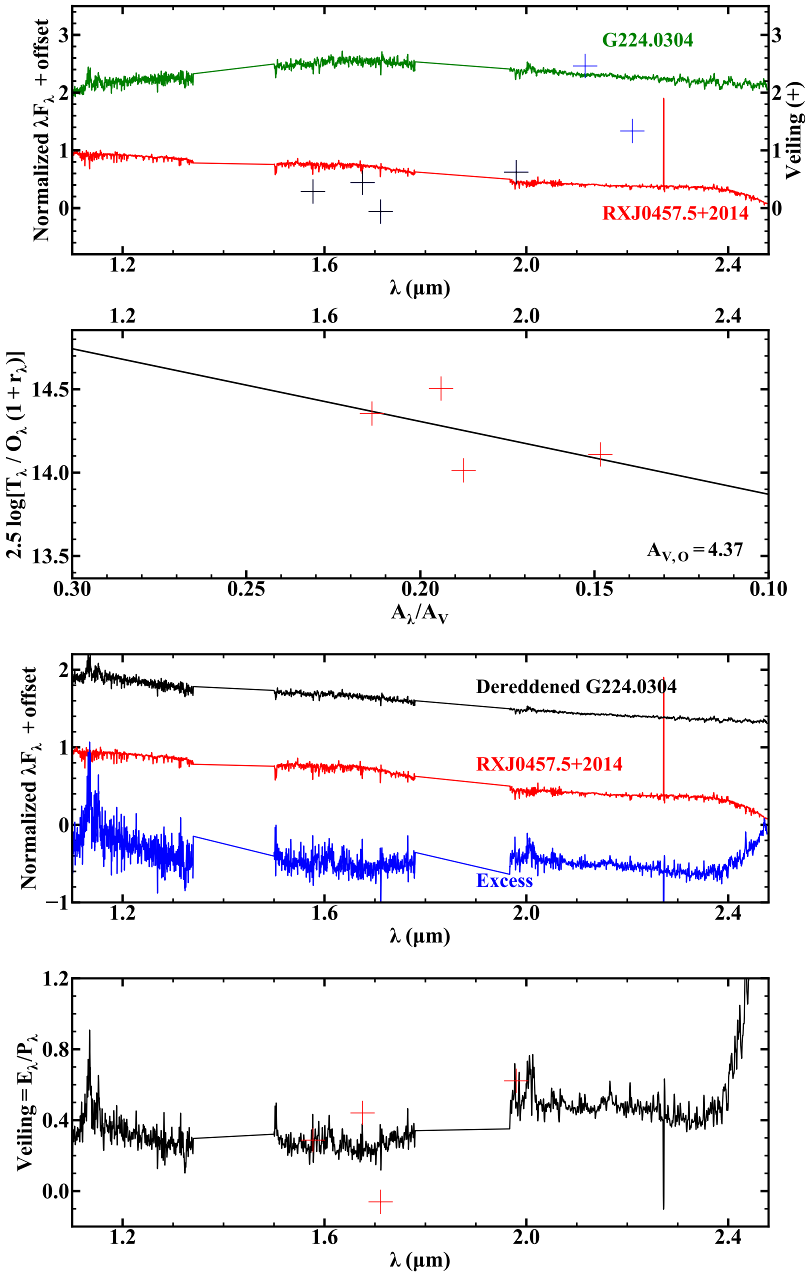

Figure 5.9: Determination of extinction A_V, excess emission spectrum E_λ, and the continuum veiling V_λ with SpeX toward G224.0304 following Fischer et al. (2011). *Top panel:* Observed spectra of a target YSO (green) and the template K2 dwarf star RXJ0457.5+2014 (red), and the SpeX line veilings r_λ for G224.0304 (plus signs). *Second panel:* Logarithm of the template-to-object flux ratio at each wavelength with a measured r_λ (veiling-corrected) versus the ratio of A_λ and A_V for the adopted reddening law (see text). *Third panel:* De-reddened spectrum of G224.0304 (black), the template spectrum (red), and the excess emission spectrum (blue). *Bottom panel:* The veiling spectrum V_λ (black) is obtained by dividing E_λ by the template. Plus signs are the line veilings, r_λ.

the uncertainties, which can be as high as 10 mag (Itrich et al. 2023, and Table 5.3).

Table 5.4: Extinction toward selected YSO candidates using the Fischer et al. (2011) and Manara et al. (2017) methods

No.	Source	A_V(excess) (mag)	A_V(SpT) (mag)
4	G224.3005	37.5	28
5	G224.3285	10.0	4.6-5.8
15	G224.6701	3.8	6.0-7.4
16	G224.0304	4.4	5.8-7.0
20	G224.1346	12.8	9.2-11.4
24	G224.3684	3.9	11.6

5.4.3 Mass accretion rates

Following previous near-IR surveys of YSOs, we use the extinction-corrected Brγ or Paβ luminosities as the proxy for accretion luminosities using the empirical relations (Muzerolle et al. 1998; Calvet et al. 2004):

$$\log(L_{\rm acc}) = -0.7 + 0.9\left(\log(L_{\rm Br\gamma}) + 4\right), \tag{5.8}$$

$$\log(L_{\rm acc}) = 1.8 + 1.03\log\left(L_{\rm Pa\beta}\right). \tag{5.9}$$

Table 5.5 shows the $L_{\rm acc}$ for 11 sources where H Brγ line is detected (see Section 5.3), representing Groups 1 and 2; and for 7 sources having the H Paβ line, representing in Group 1, 2, and 3. The line fluxes were corrected for extinction using the HI lines ratio method for sources having both H Paβ and H Brγ lines and the A_V(HK$_S$) for sources which do not have the H Paβ line detection. We find that the $L_{\rm acc}$(Paβ) is always higher than $L_{\rm acc}$(Brγ) in sources both two lines are detected (see Table 5.5). Average accretion luminosities $L_{\rm acc}$(Brγ) are comparable for the two groups, and equal $1.3\pm2.0\ L_\odot$ for Group 1 and $0.8 \pm 0.7\ L_\odot$ for Group 2, respectively. We obtained a similar result for the average accretion luminosities $L_{\rm acc}$(Paβ) in these two groups, $0.4\pm0.1\ L_\odot$ for Group 1 and $0.7\pm0.6\ L_\odot$ for Group 2, respectively (see Table 5.5).

The mass accretion rate $\dot{M}_{\rm acc}$ can be estimated using the relation from Gullbring et al. (1998):

$$\dot{M}_{\rm acc} = \left(1 - \frac{R_\star}{R_{\rm in}}\right)^{-1} \frac{R_\star}{GM_\star} L_{\rm acc} = \frac{R_\star}{0.8GM_\star} L_{\rm acc}, \tag{5.10}$$

where $R_\star$ and $M_\star$ are the stellar radius and mass, $R_{\rm in}$ is truncated inner disk radius ($R_{\rm in} \sim 5R_\star$, Hartmann 1998). We calculate $\dot{M}_{\rm acc}$ for 3 sources having H Brγ and/or H Paβ line with available $R_\star$ and $M_\star$ values, shown in Table 5.5. Except for source G224.2337 with the highest $\dot{M}_{\rm acc} \sim 2.3 \times 10^{-7} M_\odot$ yr^{-1}, two sources G224.6701 and G224.4549 have the comparable $\dot{M}_{\rm acc}$ values, $\sim 1.8 \times 10^{-8} M_\odot$ yr^{-1} and $2 \times 10^{-8} M_\odot$ yr^{-1}, respectively.

Table 5.5: Accretion rates using HI lines

ID	Source	$F_{\mathrm{Br}\gamma}$	$F_{\mathrm{Pa}\beta}$	$L_{\mathrm{acc}}(\mathrm{Br}\gamma)$	$L_{\mathrm{acc}}(\mathrm{Pa}\beta)$	$\dot{M}_{\mathrm{acc}}$
		(10^{-15} ergs s^{-1} cm^{-2})		($L_{\odot}$)	($L_{\odot}$)	(10^{-9} $M_{\odot}$ yr^{-1})
Group 1: YSOs with H Brγ and CO bandhead						
1	G224.0300	5.28 ± 0.54	25.3 ± 0.77	0.31 ± 0.06	0.47 ± 0.10	–
2	G224.1368	0.41 ± 0.23	–	0.22 ± 0.12	–	–
3	G224.2337	0.65 ± 0.17	–	4.90 ± 1.40	–	234.1
4	G224.3005	abs.[a]	–	–	–	–
5	G224.3285	2.24 ± 0.68	4.94 ± 0.80	0.24 ± 0.08	0.36 ± 0.09	–
6	G224.4649	abs.[a]	–	–	–	–
7	G224.4664	1.52 ± 0.29	–	1.10 ± 0.26	–	–
Group 2: YSOs with H Brγ and no CO bandhead						
1	G224.1291	2.02 ± 0.23	3.32 ± 0.22	0.27 ± 0.06	0.40 ± 0.09	–
2	G224.2833B	1.36 ± 0.17	–	1.70 ± 0.36	–	–
3	G224.3019	2.59 ± 0.34	4.43 ± 0.42	0.32 ± 0.07	0.50 ± 0.11	–
4	G224.4688	abs.[a]	abs.[a]	–	–	–
5	G224.4721	4.68 ± 0.20	3.38 ± 0.15	0.99 ± 0.18	1.80 ± 0.38	–
6	G224.4735	abs.[a]	abs.[a]	–	–	–
7	G224.4883	0.98 ± 0.16	–	1.50 ± 0.35	–	–
8	G224.6701	2.57 ± 0.59	6.93 ± 0.59	0.24 ± 0.27	0.35 ± 0.08	12.7/18.5
Group 3: YSOs with CO bandhead and no H Brγ						
1	G224.0304	<0.42	–	–	–	–
2	G224.0612	<0.92	–	–	–	–
3	G224.1080	<0.37	–	–	–	–
4	G224.1212	<0.37	–	–	–	–
5	G224.1346	<0.48	–	–	–	–
6	G224.2833A	<0.31	–	–	–	–
7	G224.2983	<0.44	–	–	–	–
8	G224.3433	<0.41	–	–	–	–
9	G224.3684	<0.88	abs.[a]	–	–	–
10	G224.4549	<0.61	2.03 ± 0.42	–	0.20 ± 0.06	20.5
11	G224.4751	<0.54	–	–	–	–
12	G224.7156	<12.78	abs.[a]	–	–	–
Group 4: YSOs with non-detections of H Brγ and CO bandhead						
1	G224.0513	<0.48	–	–	–	–
2	G224.0564	<0.70	–	–	–	–
3	G224.1599	<0.66	–	–	–	–
4	G224.5733	<0.44	–	–	–	–
5	G223.9430	<0.72	–	–	–	–
6	G223.9543	<0.80	–	–	–	–

Note: [a] The 'abs.' refers to sources with H Brγ or H Paβ in absorption, for which the flux was not calculated. The fluxes of the H Brγ lines are not corrected for extinction.

5.5 Discussion

5.5.1 YSO candidates in CMa-ℓ224

The origin of star formation in the CMa-ℓ224 region is believed to be triggered by the supernova event, with the evidence of an expanding dense shell of H α emission (Reynolds & Ogden 1978). The region reveals strong emission at 4.5 μm, which is commonly associated with the H_2 emission produced by the outflow shocks from the embedded young stars (Cyganowski et al. 2013). Almost 300 low- to intermediate-mass YSO candidates have been identified in CMa-ℓ224 region using the multi-wavelength photometric data and SED modeling (Fischer et al. 2016; Sewiło et al. 2019). The majority of those candidates is located along two filaments in the CMa-ℓ224 region (Fig. 5.1), characterized by high H_2 column densities ($\gtrsim 4 \times 10^{21}$ cm^{-2}). In this thesis, we analyzed the near-IR spectroscopy toward 33 sources with the highest K-band fluxes to confirm their status as YSOs and to derive their extinction, spectral types, and accretion properties.

NASA IRTF/SpeX spectra in JHK bands allowed us to identify spectral features typical for YSOs. Twenty-seven out of 33 sources show a detection of H Brγ line and/or CO bandhead, suggesting their young nature (see Section 5.3.1). The detection of H Brγ emission in 15 out of 33 sources provides a clear evidence of on-going mass accretion. The He I detected toward 4 sources likely originate in fast wind (Ward et al. 2015). Absorption lines detected in the SpeX spectra e.g., Na I and Ca I doublets, provide additional information about the central stars. Among sources with detections of the doublets and in the CO bandhead, twelve are likely dwarfs and two belong to giants and/or FU Ori stars, which are eruptive Class II YSOs (Section 5.3.1). Indeed, large surveys of YSOs suggest that most stars in Class I objects are dwarfs (Connelley & Greene 2010; Connelley & Reipurth 2018).

SpeX spectra allowed us to apply various methods to estimate the extinction toward YSOs in CMa-ℓ224 (see Section 5.4.1), which is critical to determine both stellar and accretion properties. The extinction derived from the hydrogen recombination lines is likely most accurate, but requires the detection of H Paβ line in the H-band. The method using templates of non-accreting class III YSOs by Manara et al. (2017) has the advantage of being easily used for a large sample of sources. This is not the case for the excess continuum emission method by Fischer et al. (2011), which requires detections of several key lines to obtain an accurate estimate of extinction and veiling. Each method is subject to uncertainties, e.g., in matching the best stellar template or the assumed extinction law, as discussed in Fischer et al. (2011), but are consistent within 10 mag or less, similar or better to extinction values obtained from the SED modeling (Itrich et al. 2023).

5.5.2 Accretion rates of YSOs in CMa-ℓ224 and other clouds

Accretion luminosities and mass accretion rates determined toward YSOs in CMa-ℓ224 (Section 5.4.3) can be compared to those of YSOs in other environments to investigate e.g., a possible impact of metallicity on mass accretion, which was proposed by previous studies (Ward et al. 2015, 2016). In all cases, the rates are derived based on the experimental relation with HI lines, which was found to hold for YSOs spanning a broad range of masses (Calvet et al. 2004). In addition, the relation is not expected to be affected by metallicity, as the Brγ emission is mostly a measure of the number of ionizing photons (Kudritzki 2002; Ward et al. 2015).

Median accretion luminosity of YSOs in the CMa-ℓ224 region obtained using SpeX spectra is 0.32 $L_\odot$ (Section 5.4.3). All but one source show $L_{\rm acc}$ consistent with the range from 0.003 to 4.0 $L_\odot$ obtained using VLT/KMOS (Itrich et al. 2023). G224.2337 has a somewhat higher accretion luminosity of 4.9±1.4 $L_\odot$, which is also consistent within uncertainties with the KMOS results. Similarly, the mass accretion rates obtained toward

3 sources with SpeX of ~1.8–23×10^{-8} M$_\odot$ yr^{-1}, are consistent with the KMOS survey range from 4×10^{-9} to 1×10^{-7} M$_\odot$ yr^{-1}. Due to the small number statistics of sources with mass accretion measurements, we will focus the remaining discussion on the accretion luminosities.

Figure 5.10 shows the distribution of accretion luminosity of low- and intermediate-mass YSOs located in the CMa-ℓ224 and other, more nearby star-forming regions: NGC 1333, Serpens, Lupus, and L1641. The median $\log(L_{\rm acc}) = -0.82^{+0.80}_{-0.82}$ $L_\odot$ toward CMa-l224 from the KMOS survey and the distribution of $L_{\rm acc}$ from SpeX (Fig. 5.10) are generally in agreement with the rates measured toward YSOs in other clouds (Caratti o Garatti et al. 2012; Antoniucci et al. 2014; Fiorellino et al. 2021). They are most similar to YSOs in the L1641 clouds forming many intermediate-mass stars, which show $L_{\rm acc}$ in the range from $\lesssim$0.1 to to 60 $L_\odot$ (Caratti o Garatti et al. 2012).

We investigate the relation of mass accretion rates and the stellar luminosity in Figure 5.11. A strong power-law correlation exists for low- and intermediate mass protostars (Pearson coefficient r of 0.87) and for low- to high-mass YSOs (r of 0.90). The YSOs in L1641 are indeed characterized by similar stellar luminosities to the sources studied in this thesis. Noteworthy, the correlation is also supported by observations of YSOs in the Orion molecular cloud and the Small Magellanic Cloud (Itrich et al. 2023).

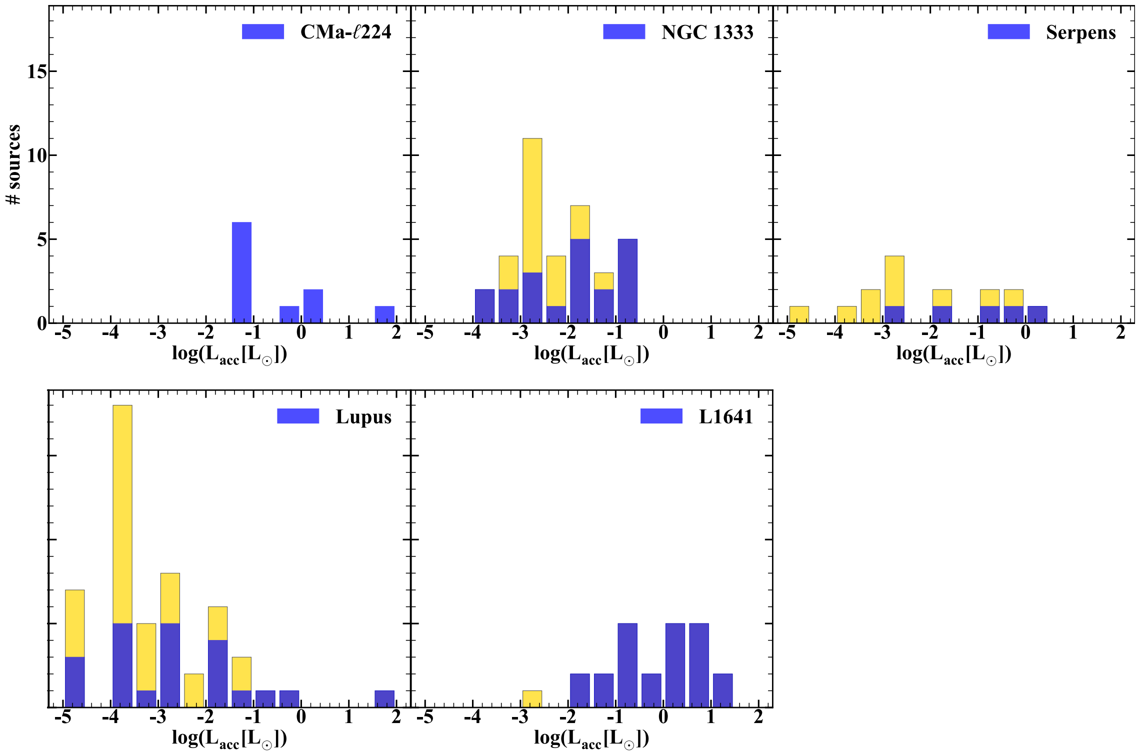

Figure 5.10: Histograms of accretion luminosity of YSOs in the CMa-ℓ224 and star-forming regions in the inner Galaxy. Blue bars show measurements based on detections and yellow bars – the ones based on upper limits. The rates for YSOs located in the NGC 1333 cluster in Perseus are taken from Fiorellino et al. (2021), in Serpens and Lupus from Antoniucci et al. (2014), and in L1641 from Caratti o Garatti et al. (2012).

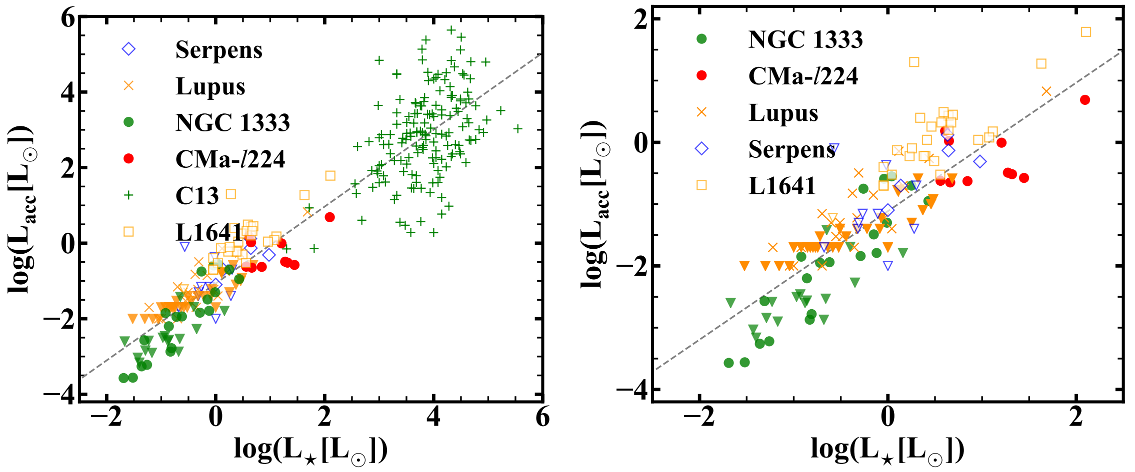

Figure 5.11: Accretion luminosity of YSOs versus stellar luminosity. *Left:* Comparison for low-mass YSOs in Serpens and Lupus (blue diamonds and orange crosses, respectively Antoniucci et al. 2014) and in NGC 1333 (green dots Fiorellino et al. 2021), for low- and intermediate mass YSOs in CMa-ℓ224 (this thesis; red squares) and L1641 (orange squares Caratti o Garatti et al. 2012), and for high-mass YSOs (green plus signs Cooper et al. 2013). The triangle symbols represent the upper limits. The dashed line shows a power-law fit to all YSOs. *Right:* Similar to the left panel, but without high-mass YSOs from Cooper et al. (2013).

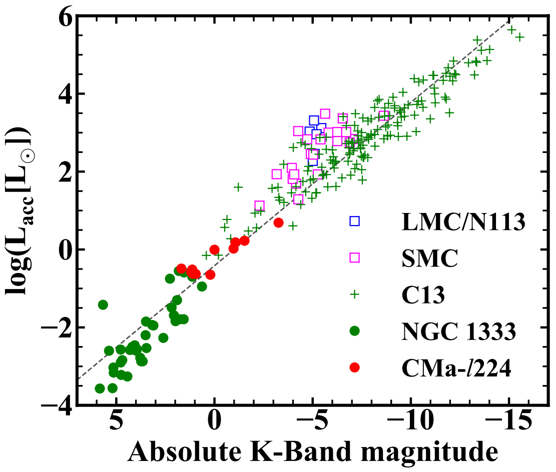

Figure 5.12: Accretion luminosity as a function of absolute K-band magnitude for low- and intermediate-mass YSOs in CMa-ℓ224, low-mass YSOs in NGC 1333 cluster in Perseus (Fiorellino et al. 2021), high-mass YSOs (Cooper et al. 2013), high-mass YSOs in the Large and Small Magellanic Clouds (Ward et al. 2015, 2016). The symbols are the same as in Fig. 5.11. The dashed line shows a power-law fit to the YSOs in NGC 1333 and high-mass YSOs.

Cooper et al. (2013) proposed to use *K*-band magnitudes instead of bolometric luminosities, which could be poorly-constrained for YSOs in the Magellanic Clouds, for comparisons of accretion luminosities between the galactic and extragalactic YSOs. Figure 5.12 shows such a comparison for low- and intermediate-mass YSOs located in the CMa-ℓ224 and NGC 1333 (Fiorellino et al. 2021), and for high-mass YSOs in the Milky Way (Cooper et al. 2013) and in the Small and Large Magellanic Clouds (Ward et al. 2015, 2016). The power-law fit to YSOs in NGC 1333 and the high-mass YSOs in the Milky Way (r of 0.97) shows that i) there are indeed no systematic differences between accretion rates in the CMa-l224 and other Galactic YSOs, ii) YSOs in the Magellanic Clouds are systematically offset toward higher accretion rates with respect to YSOs in the Milky Way.

The similarity between YSOs in the CMa-ℓ224 region and other Galactic YSOs indicates the lack of impact of reduced metallicity on accretion luminosities (or mass accretion rates). These conclusions are supported by the VLT/KMOS study of CMa-ℓ224 by Itrich et al. (2023) as well as by the SALT spectroscopy of the even lower metallicity region of the outer Galaxy, Sh 2-284 (Kalari & Vink 2015), and suggest that star formation operates in a similar manner across environments with significantly different metallicities.

The differences in accretion luminosities between YSOs in the Milky Way and the Magellanic Clouds are most likely caused by observational biases (Kalari & Vink 2015). Moreover, the differences disappear when the actual stellar luminosities of YSOs in the Magellanic Clouds are used in comparisons (Itrich et al. 2023). In conclusion, there is no solid observational evidence for the impact of reduced metallicities on accretion properties of YSOs.

5.6 Conclusions

In this Chapter, we presented the NASA IRTF/SpeX near-IR spectroscopy of 33 YSO candidates in the CMa-ℓ224 star-forming region in the outer Galaxy. Eight sources were also observed with VLT/KMOS in K-band. Our main findings are listed as follows:

- We detect H Brγ, H Paβ, and/or CO bandhead in 27 out of 33 YSO candidates observed with SpeX. The KMOS spectra also show these features, but also reveal the emission of the H_2 line at 2.21 μm. Two sources observed by both instruments show extended bipolar H_2 jets characteristic of Class 0/I protostars. Among 14 sources with Na I , Ca I, and CO bandhead detections, 12 are dwarfs and 2 are candidate FU Orionis stars.

- We estimated spectral types of stars and extinction toward our targets using various methods, which are consistent within uncertainties. The continuum emission in the K-band shows the evidence of excess emission due to accretion toward 6 sources.

- Extinction-corrected line fluxes of atomic hydrogen lines were used to calculate the accretion luminosity using the relation from Calvet et al. (2004). Median accretion luminosity of 0.32 $L_\odot$ obtained with SpeX is consistent with the survey with VLT/KMOS toward the other filament in the CMa-ℓ224 region (Itrich et al. 2023). It is also comparable to YSOs in the Solar neighborhood, in particular L1641 where YSOs are characterized by similar stellar luminosities as those in the CMa-ℓ224 region. Accretion luminosities of YSOs increase as a function of stellar luminosity and K-band magnitude.

- The observations obtained with both SpeX and KMOS (Itrich et al. 2023) does not support the earlier suggestions that accretion properties might be affected by metallicity of the environment (Ward et al. 2015, 2016). Similar to other study in the outer Galaxy (Kalari & Vink 2015), we find no evidence for the impact of metallicy on mass accretion onto YSOs.

Appendix

5.A *K*-band continuum maps with VLT/KMOS

Figure 5.A.1 shows the *K*-band (2.12 μm) continuum emission maps toward eight YSOs observed by both NASA IRTF/SpeX (Section 5.3.2) and VLT/KMOS (Itrich et al. 2023). The sources are all compact, well-pointed, and fully covered by the KMOS maps. G224.3005 and G224.4883 are associated with H_2 emission which extends beyond the continuum emission (Section 5.3.2).

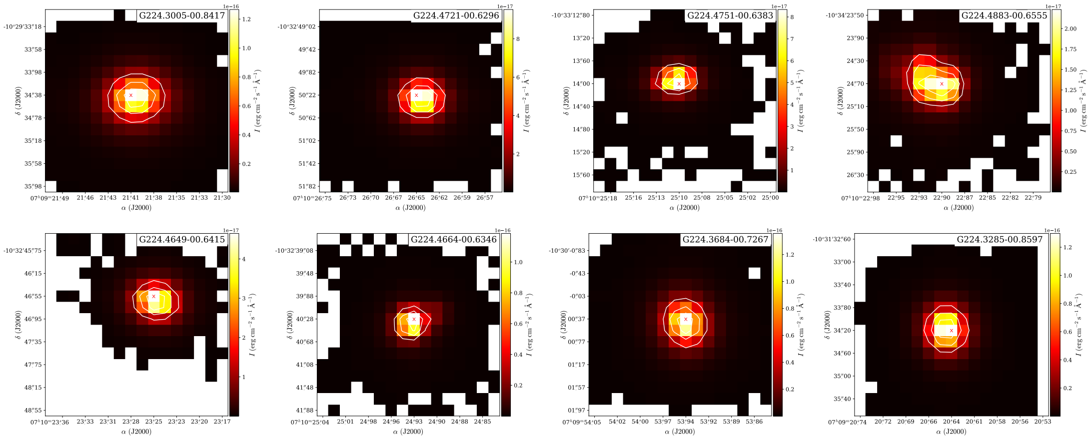

Figure 5.A.1: Continuum maps of YSOs in CMa-ℓ224 obtained with VLT/KMOS (see also Itrich et al. 2023). The contours show 25%, 50%, and 75% of the peak continuum, and the colors show spaxels with continuum flux above 3σ. Red crosses show the source positions.

5.B SpeX near-IR spectra

Near-IR spectra of all 33 YSO candidates observed with NASA IRTF/SpeX are presented in Figures 5.B.1–5.B.6. The sources are divided into 4 groups based on the detections of H Brγ and CO bandhead (see Table 5.2). The *IYJ* band spectra are presented in Figures 5.B.1 and 5.B.2, the *H* band spectra in Figures 5.B.3 and 5.B.4, and the *K* band spectra in Figures 5.B.5 and 5.B.6. All spectra are normalized to the near-IR continuum spectrum for each source.

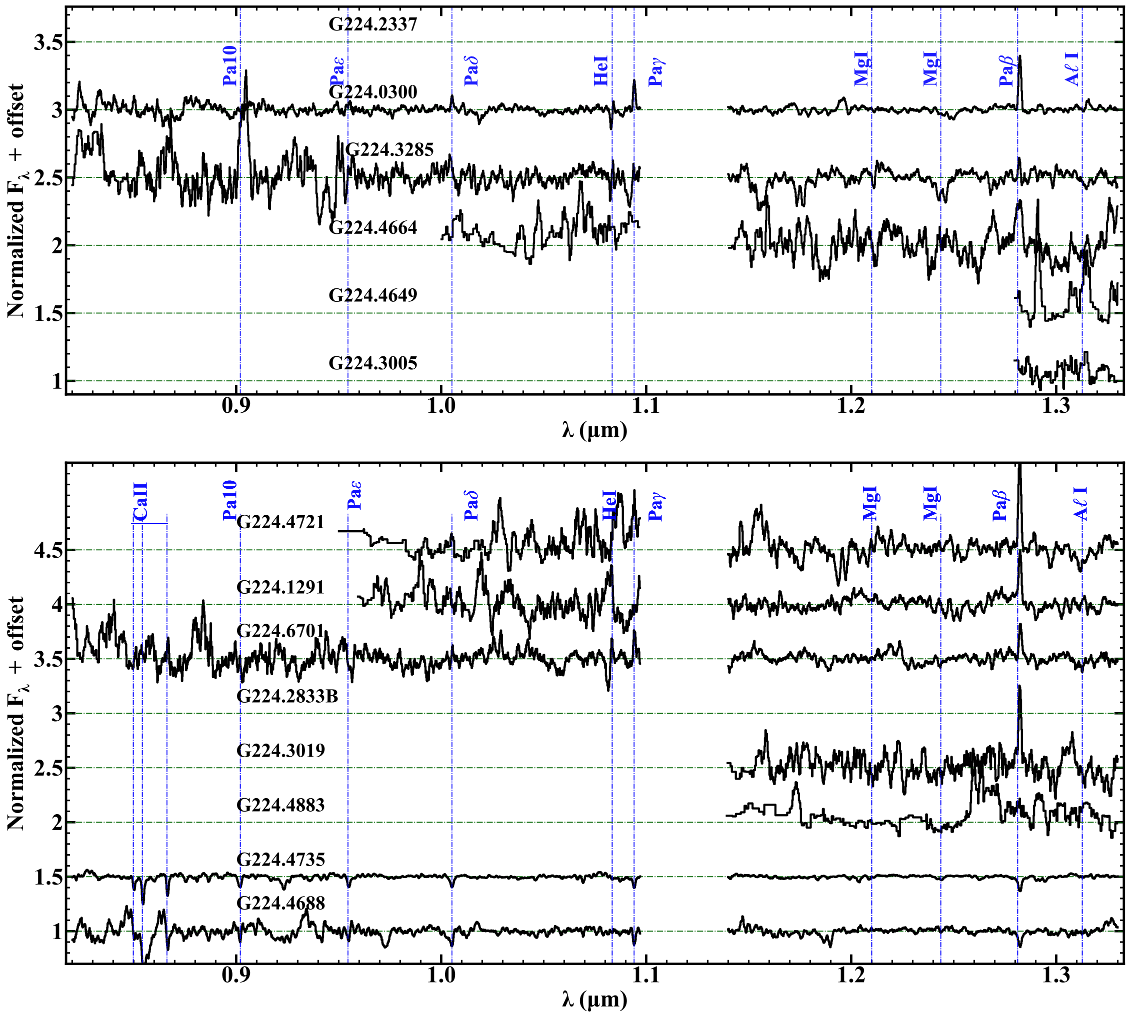

Figure 5.B.1: SpeX *IYJ*-band continuum-normalized spectra of YSO candidates from Group 1 (*top*) and 2 (*bottom*). The spectral range around 1.12 μm is strongly affected by telluric lines and not shown. The offsets are applied for clarity.

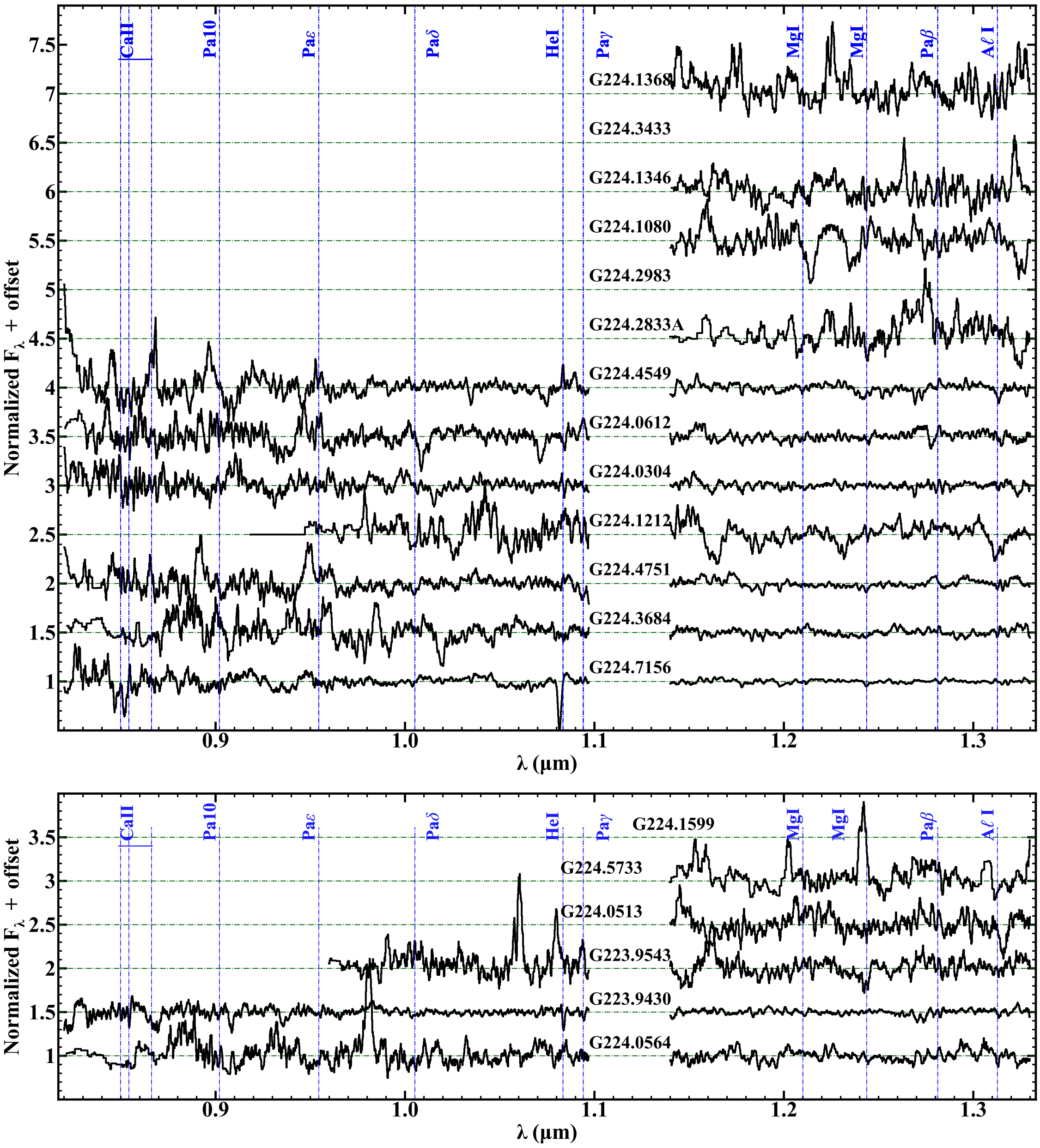

Figure 5.B.2: *IYJ*-band spectra of YSOs from Groups 3 (*top*) and 4 (*bottom*). Other notations are similar as in Figure 5.B.1.

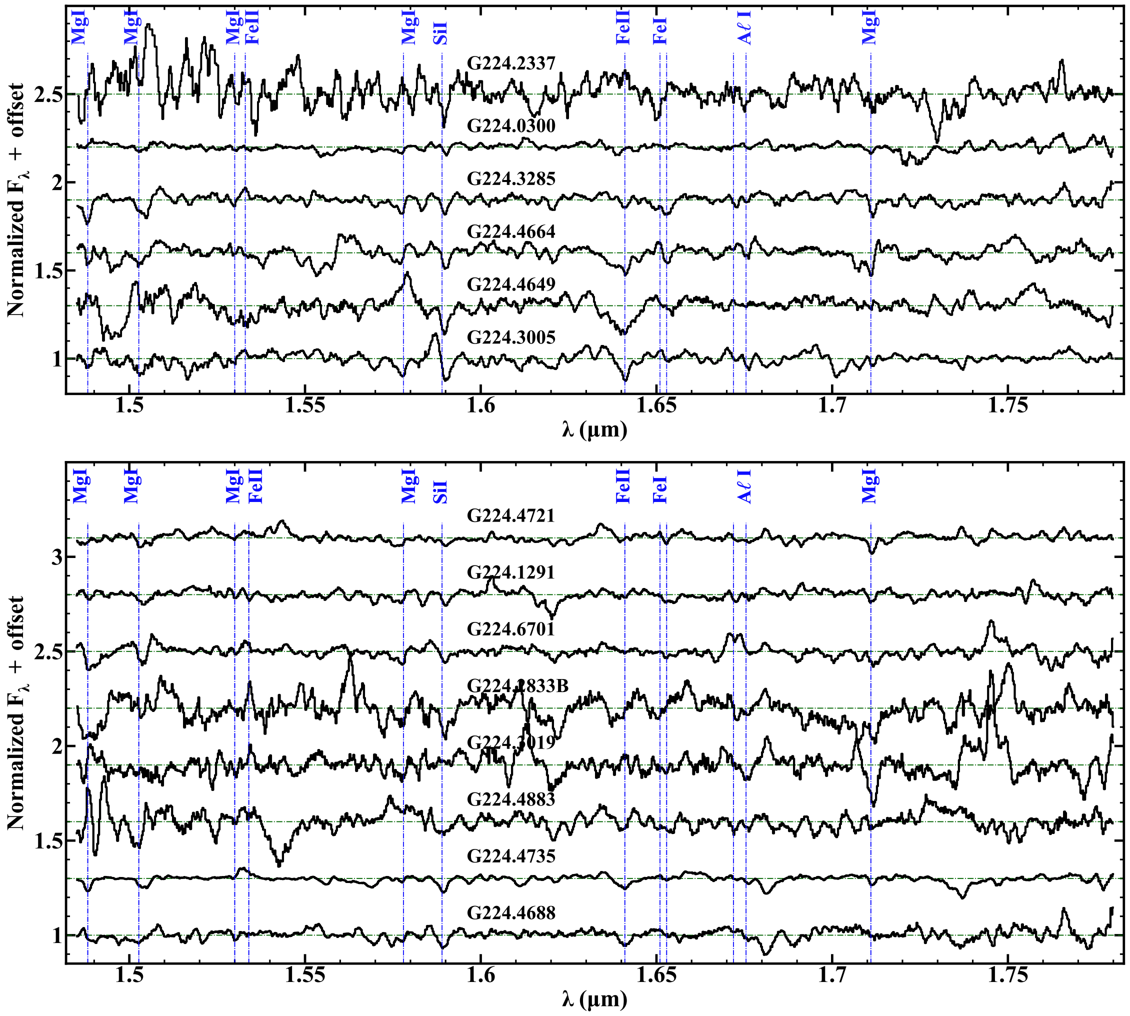

Figure 5.B.3: *H*-band spectra of YSO candidates from Group 1 (*top*) and 2 (*bottom*). The offsets are applied for clarity.

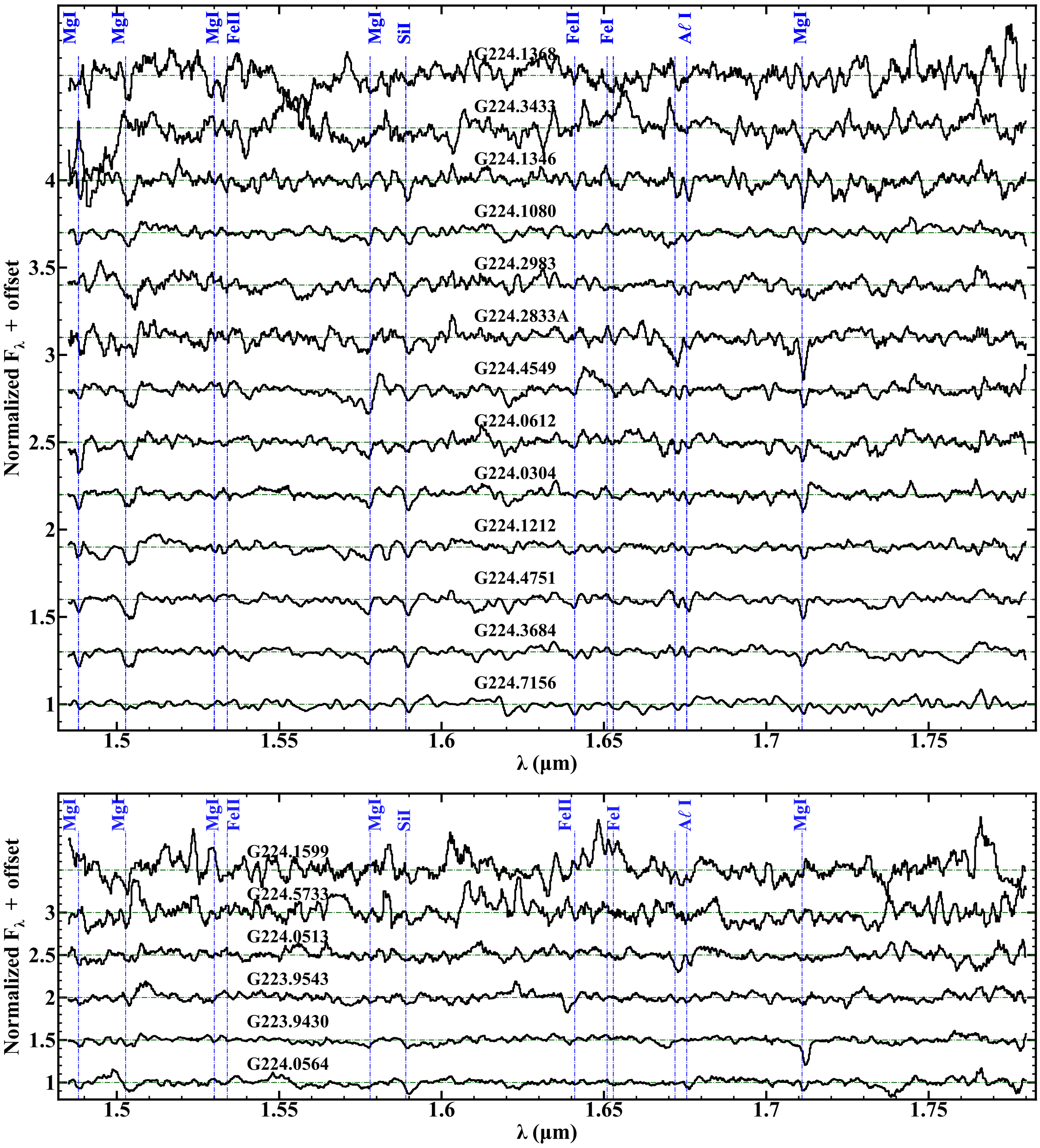

Figure 5.B.4: *H*-band spectra of YSOs from Groups 3 (*top*) and 4 (*bottom*). The offsets are applied for clarity.

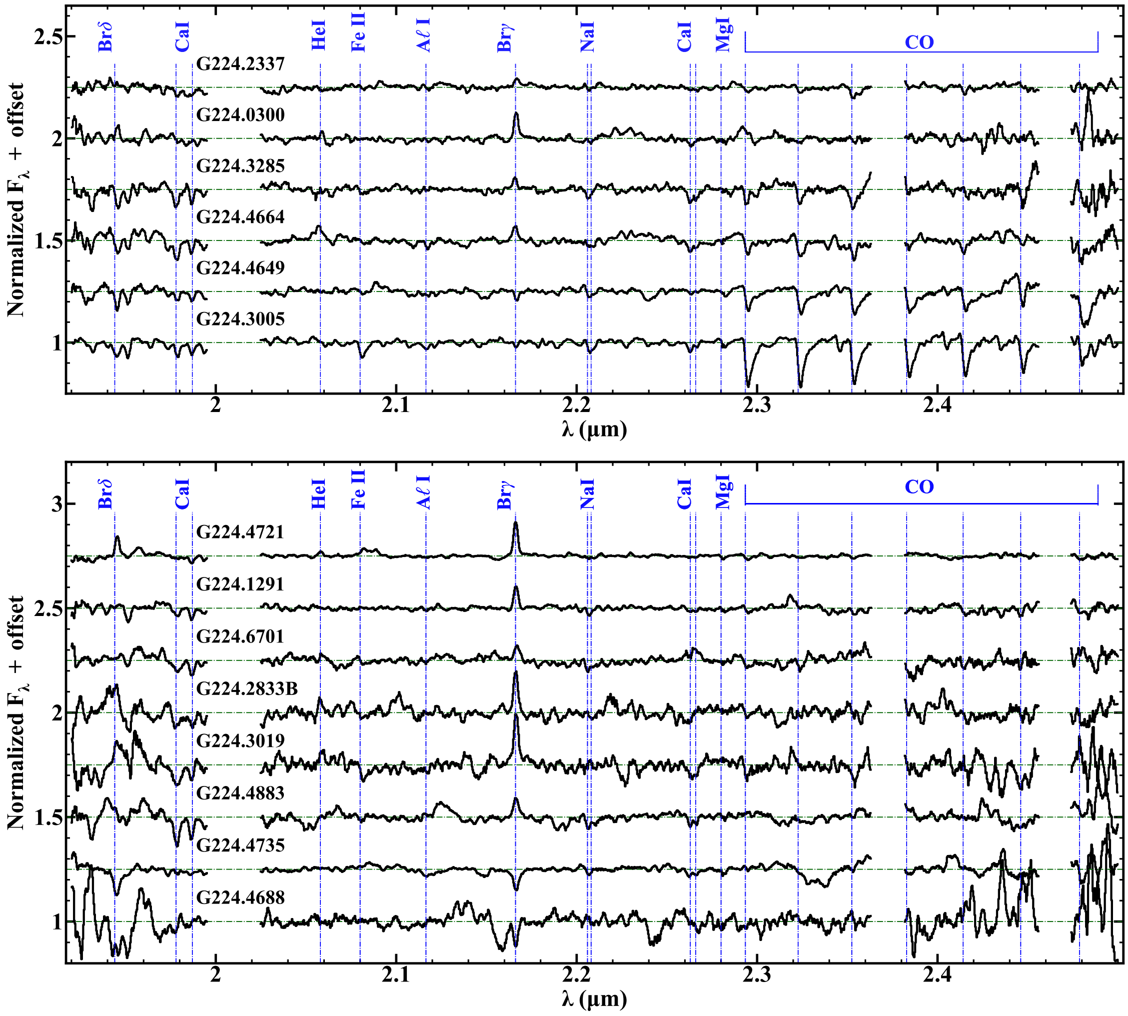

Figure 5.B.5: *K*-band spectra of YSO candidates from Group 1 (*top*) and 2 (*bottom*). Spectral ranges at 2 μm, 2.37 μm, and 2.48 μm are strongly affected by telluric lines and not shown. The offsets are applied for clarity.

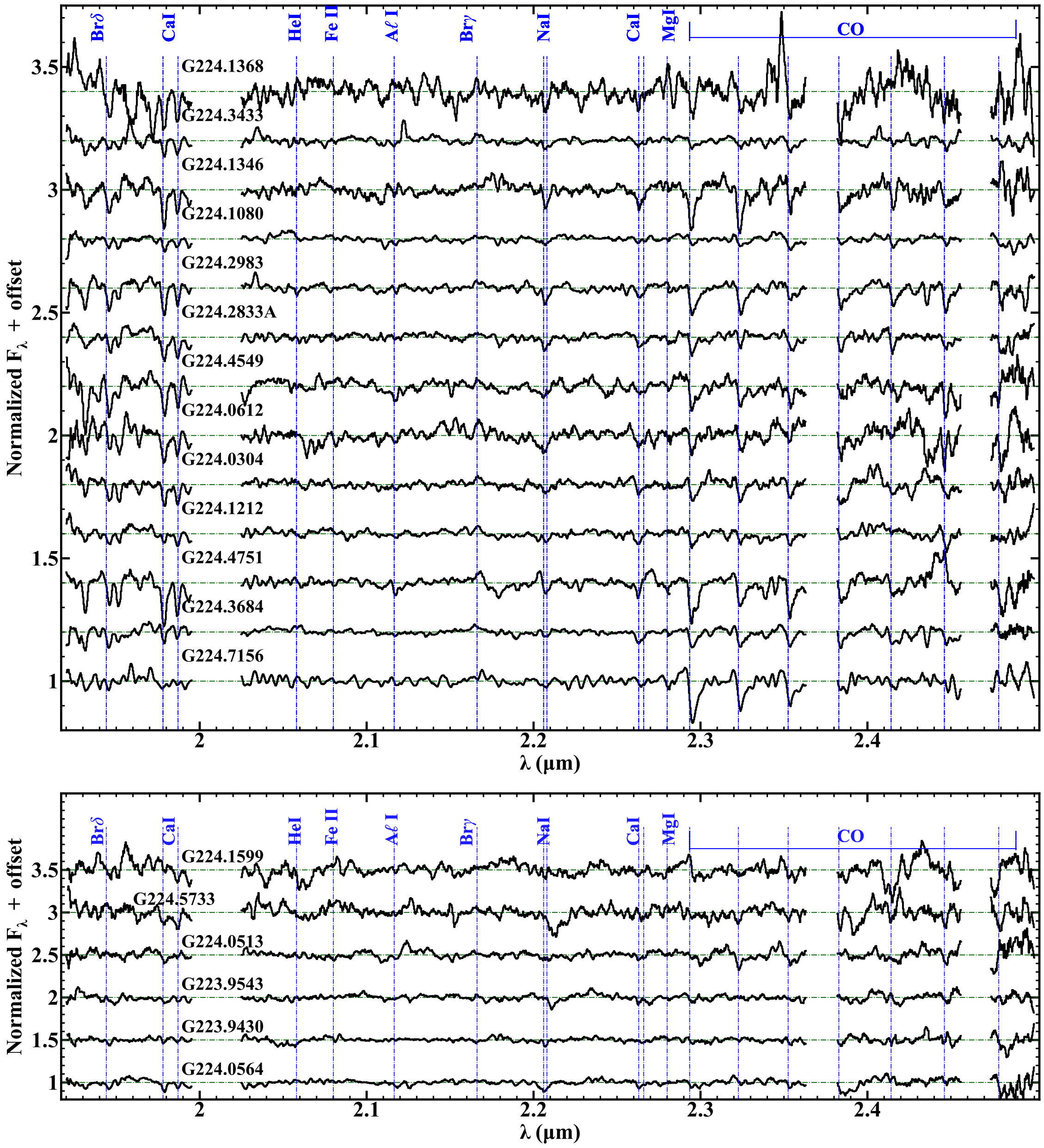

Figure 5.B.6: *K*-band spectra of YSO candidates from Group 3 (*top*) and 4 (*bottom*). Other notations are similar as in Figure 5.B.5.

Chapter 6

Summary and outlook

In this thesis, we presented a comprehensive analysis of multi-wavelength observations, from near-IR to radio wavelengths, of star-forming regions in our Galaxy. Polarimetric observations from SOFIA/HAWC+ were used to trace magnetic fields in Oph-A cloud and their role in local star formation. Spectroscopy from SOFIA/FIFI-LS and NASA IRTF/SpeX allowed us to determine the physical conditions (temperature, density, UV fields) and constrain accretion rates in sites of star formation with reduced metallicity. Our main results are summarized as follows.

Chapter 3: B-fields in Oph–A are typically well-ordered and tend to be bent perpendicular to the ridge of the cloud toward the higher-density regime. The strengths of B-fields, measured in the entire cloud using the Davis-Chandrasekhar-Fermi method, range from 0.1 to 6 mG and are the strongest in the densest parts of the cloud. The measurements of the B-field strengths in Oph–A are important to understand how the field varies across the entire region and as a function of gas number density, and how it affects the star formation activity. We found out that the Oph-A cloud is magnetically sub-critical and sub-alfvénic, supported by strong magnetic pressure, which dominates over turbulent and thermal pressures. The virial analysis shows that the cloud is gravitationally unbound. The strong B-fields in Oph–A help to support material against collapse due to gravity and the radiation compression from the external stellar source, and regulate the morphology of matter in the cloud.

Chapter 4: The spatial extent of high$-J$ CO emission in Gy 3–7 resembles that of the elongated 160 μm continuum emission detected with *Herschel*, but its peaks are offset from the positions of the dense cores. The [O I] lines at 63.2 μm and 145.5 μm follow a similar pattern, but their peaks are found closer to the positions of the dense cores. CO transitions from $J = 14 - 13$ to $J = 16 - 15$ were detected throughout the cluster and constrained the gas temperature across Gy 3–7, with a median at 170±30 K. Comparisons of far-IR line emission to shock models provided the estimate of pre-shock H_2 number densities of 10^4-10^5 cm^{-3} and UV radiation field strengths of 0.1-10 times the average interstellar radiation field in the cluster. The far-IR line spectroscopy revealed an ongoing star formation in Gy 3–7, dominated by intermediate-mass Class 0/I young stellar objects. The ratio of molecular-to-atomic far-IR line emission showed a decreasing trend with bolometric luminosities of the protostars, but we did not isolate the impact of low-metallicity.

Chapter 5: The NASA IRTF/SpeX survey of YSO candidates in the CMa-ℓ224 star-forming region showed that a number of YSO candidates in the CMa-ℓ224 region are characterized by on-going accretion, confirming their status as young stars. Among 14 sources with Na I , Ca I, and CO bandhead detections, 12 are dwarfs and 2 are candidate FU Orionis stars. The continuum emission in the K-band shows the evidence of excess emission due to accretion toward 6 sources, where sufficient lines have been detected. Median accretion luminosity of 0.32 $L_\odot$ obtained with SpeX is consistent with the survey with VLT/KMOS toward the other filament in the CMa-ℓ224 region (Itrich et al. 2023). It is also comparable to YSOs in the Solar neighborhood, in particular L1641 where YSOs are characterized by similar stellar luminosities as those in the CMa-ℓ224 region. Accretion luminosities of YSOs generally increase as a function of stellar luminosity and K-band magnitude. The observations does not support the earlier suggestions that accretion properties might be affected by metallicity of the environment (Ward et al. 2015, 2016). Similar to other study in the outer Galaxy (Kalari & Vink 2015), we find no evidence for the impact of metallicy on mass accretion onto YSOs.

The methodology presented in Chapter 3 sets a path toward the measurements of magnetic fields in other molecular clouds in our Galaxy. Unfortunately, the SOFIA mission was finished prematurely in 2022, and we could not obtain polarimetric observations of the CMa-ℓ224 region with HAWC+ (the proposal was submitted, but not evaluated). Observations in the millimeter regime (e.g., with the James Clerk Maxwell Telescope) could be used to assess magnetic fields in this region.

Similarly, far-IR observations of star-forming regions, as presented in Chapter 4, will not be accessible in the foreseeable future. Nonetheless, the MIRI instrument Rieke et al. (2015); Wright et al. (2015) on-board the James Webb Space Telescope is already providing high-resolution images of outflows from low-mass protostars, using e.g., multiple lines of H_2 and H_2O (Yang et al. 2022b). Similar observations for star-forming regions in the outer Galaxy would reveal any differences in molecular abundances and their impact on star formation.

Near-IR of YSOs is routinely done from the ground, and new generations of instruments could facilitate a more in-depth characterization of YSO candidates in the outer Galaxy. For example, the CRIRES+ instrument (Follert et al. 2014) on the Very Large Telescope offers extremely high spectral resolution observations, informing about gas kinematics. Integral field spectrographs such as KMOS already allow to obtain spectral cubes of large areas of the sky with high efficiency (Itrich et al. 2023); observations of additional regions at far outer Galaxy would help to identify the impact of metallicity on mass accretion rates.

List of Figures

List of Tables

Bibliography

Alcalá, J. M., Natta, A., Manara, C. F., et al. 2014, A&A, 561, A2

Andersson, B. G., Lazarian, A., & Vaillancourt, J. E. 2015, ARA&A, 53, 501

André, P. 2002, in EAS Publications Series, Vol. 3, EAS Publications Series, ed. J. Bouvier & J.-P. Zahn, 1–38

André, P., Belloche, A., Motte, F., & Peretto, N. 2007, A&A, 472, 519

Andre, P., Martin-Pintado, J., Despois, D., & Montmerle, T. 1990, A&A, 236, 180

André, P., Men'shchikov, A., Bontemps, S., et al. 2010, A&A, 518, L102

Andre, P., Montmerle, T., Feigelson, E. D., Stine, P. C., & Klein, K. L. 1988, in Activity in Cool Star Envelopes, ed. O. Havnes, B. R. Pettersen, J. H. M. M. Schmitt, & J. E. Solheim, Vol. 143, 293

Andre, P., Ward-Thompson, D., & Barsony, M. 2000, in Protostars and Planets IV, ed. V. Mannings, A. P. Boss, & S. S. Russell, 59

Antoniucci, S., García López, R., Nisini, B., et al. 2014, A&A, 572, A62

Arce, H. G., Shepherd, D., Gueth, F., et al. 2007, in Protostars and Planets V, ed. B. Reipurth, D. Jewitt, & K. Keil, 245

Arzoumanian, D., André, P., Didelon, P., et al. 2011, A&A, 529, L6

Arzoumanian, D., Furuya, R. S., Hasegawa, T., et al. 2021, A&A, 647, A78

Balser, D. S., Rood, R. T., Bania, T. M., & Anderson, L. D. 2011, ApJ, 738, 27

Benedettini, M., Molinari, S., Baldeschi, A., et al. 2020, A&A, 633, A147

Benson, P. J. & Myers, P. C. 1989, ApJS, 71, 89

Benz, A. O., Bruderer, S., van Dishoeck, E. F., et al. 2016, A&A, 590, A105

Bertoldi, F. & McKee, C. F. 1992, ApJ, 395, 140

Bica, E., Dutra, C. M., & Barbuy, B. 2003, A&A, 397, 177

Blitz, L. & Shu, F. H. 1980, ApJ, 238, 148

Bontemps, S., André, P., Kaas, A. A., et al. 2001, A&A, 372, 173

Bontemps, S., Andre, P., Terebey, S., & Cabrit, S. 1996, A&A, 311, 858

Borlaff, A. S., Lopez-Rodriguez, E., Beck, R., et al. 2023, arXiv e-prints, arXiv:2303.13586

Bressan, A., Marigo, P., Girardi, L., et al. 2012, MNRAS, 427, 127

Bronfman, L., Nyman, L. A., & May, J. 1996, A&AS, 115, 81

Brown, R. L. & Zuckerman, B. 1975, ApJ, 202, L125

Bruderer, S., Benz, A. O., Doty, S. D., van Dishoeck, E. F., & Bourke, T. L. 2009, ApJ, 700, 872

Buckle, J. V., Hills, R. E., Smith, H., et al. 2009, MNRAS, 399, 1026

Butner, H. M., Evans, Neal J., I., Harvey, P. M., et al. 1990, ApJ, 364, 164

Calvet, N., Muzerolle, J., Briceño, C., et al. 2004, AJ, 128, 1294

Caratti o Garatti, A., Garcia Lopez, R., Antoniucci, S., et al. 2012, A&A, 538, A64

Cardelli, J. A., Clayton, G. C., & Mathis, J. S. 1989, ApJ, 345, 245

Caselli, P. & Myers, P. C. 1995, ApJ, 446, 665

Chandrasekhar, S. & Fermi, E. 1953, ApJ, 118, 116

Chen, H. H.-H., Pineda, J. E., Goodman, A. A., et al. 2019, ApJ, 877, 93

Chen, Y., Bressan, A., Girardi, L., et al. 2015, MNRAS, 452, 1068

Chen, Y., Girardi, L., Bressan, A., et al. 2014, MNRAS, 444, 2525

Chuss, D. T., Andersson, B. G., Bally, J., et al. 2019, ApJ, 872, 187

Claria, J. J. 1974, AJ, 79, 1022

Clemens, D. P., Sarcia, D., Grabau, A., et al. 2007, PASP, 119, 1385

Connelley, M. S. & Greene, T. P. 2010, AJ, 140, 1214

Connelley, M. S. & Reipurth, B. 2018, ApJ, 861, 145

Cooper, H. D. B., Lumsden, S. L., Oudmaijer, R. D., et al. 2013, MNRAS, 430, 1125

Cortes, P. C., Girart, J. M., Hull, C. L. H., et al. 2016, ApJ, 825, L15

Coudé, S., Bastien, P., Houde, M., et al. 2019, ApJ, 877, 88

Crutcher, R. M. 2004, in The Magnetized Interstellar Medium, ed. B. Uyaniker, W. Reich, & R. Wielebinski, 123–132

Crutcher, R. M. 2012, ARA&A, 50, 29

Crutcher, R. M. & Kemball, A. J. 2019, Frontiers in Astronomy and Space Sciences, 6, 66

Crutcher, R. M., Wandelt, B., Heiles, C., Falgarone, E., & Troland, T. H. 2010, ApJ, 725, 466

Cushing, M. C., Vacca, W. D., & Rayner, J. T. 2004, PASP, 116, 362

Cyganowski, C. J., Brogan, C. L., Hunter, T. R., Churchwell, E., & Zhang, Q. 2011, ApJ, 729, 124

Cyganowski, C. J., Koda, J., Rosolowsky, E., et al. 2013, ApJ, 764, 61

Cyganowski, C. J., Whitney, B. A., Holden, E., et al. 2008, AJ, 136, 2391

Davies, R. I., Agudo Berbel, A., Wiezorrek, E., et al. 2013, A&A, 558, A56

Davis, C. J., Scholz, P., Lucas, P., Smith, M. D., & Adamson, A. 2008, MNRAS, 387, 954

Davis, L. 1951, Physical Review, 81, 890

Davis, L. & Greenstein, J. L. 1949, Phys. Rev., 75, 1605

de Zeeuw, P. T., Hoogerwerf, R., de Bruijne, J. H. J., Brown, A. G. A., & Blaauw, A. 1999, AJ, 117, 354

Devaraj, R., Clemens, D. P., Dewangan, L. K., et al. 2021, ApJ, 911, 81

Draine, B. T. & Weingartner, J. C. 1997, ApJ, 480, 633

Duarte-Cabral, A., Colombo, D., Urquhart, J. S., et al. 2021, The SEDIGISM survey: molecular clouds in the inner Galaxy, Monthly Notices of the Royal Astronomical Society, Volume 500, Issue 3, pp.3027-3049

Dunham, M. M., Allen, L. E., Evans, Neal J., I., et al. 2015, ApJS, 220, 11

Edwards, S., Fischer, W., Hillenbrand, L., & Kwan, J. 2006, ApJ, 646, 319

Elia, D., Merello, M., Molinari, S., et al. 2021, MNRAS, 504, 2742

Elia, D., Molinari, S., Fukui, Y., et al. 2013, ApJ, 772, 45

Elitzur, M., Hollenbach, D. J., & McKee, C. F. 1989, ApJ, 346, 983

Ennico, K., Becklin, E. E., Le, J., et al. 2018, Journal of Astronomical Instrumentation, 7, 1840012

Enoch, M. L., Evans, Neal J., I., Sargent, A. I., & Glenn, J. 2009, ApJ, 692, 973

Esplin, T. L. & Luhman, K. L. 2020, AJ, 159, 282

Esteban, C. & García-Rojas, J. 2018, MNRAS, 478, 2315

Evans, Neal J., I., Dunham, M. M., Jørgensen, J. K., et al. 2009, ApJS, 181, 321

Faúndez, S., Bronfman, L., Garay, G., et al. 2004, A&A, 426, 97

Fernández-Martín, A., Pérez-Montero, E., Vílchez, J. M., & Mampaso, A. 2017, A&A, 597, A84

Fiorellino, E., Manara, C. F., Nisini, B., et al. 2021, arXiv e-prints, arXiv:2103.03863

Fischer, C., Beckmann, S., Bryant, A., et al. 2018, Journal of Astronomical Instrumentation, 7, 1840003

Fischer, C., Iserlohe, C., Vacca, W., et al. 2021, PASP, 133, 055001

Fischer, W., Edwards, S., Hillenbrand, L., & Kwan, J. 2011, ApJ, 730, 73

Fischer, W. J., Padgett, D. L., Stapelfeldt, K. L., & Sewiło, M. 2016, ApJ, 827, 96

Fissel, L. M., Ade, P. A. R., Angilè, F. E., et al. 2016, The Astrophysical Journal, 824, 134

Flower, D. R. & Pineau Des Forêts, G. 2010, MNRAS, 406, 1745

Flower, D. R. & Pineau des Forêts, G. 2012, MNRAS, 421, 2786

Follert, R., Dorn, R. J., Oliva, E., et al. 2014, in Society of Photo-Optical Instrumentation Engineers (SPIE) Conference Series, Vol. 9147, Ground-based and Airborne Instrumentation for Astronomy V, ed. S. K. Ramsay, I. S. McLean, & H. Takami, 914719

Frank, A., Ray, T. P., Cabrit, S., et al. 2014a, in Protostars and Planets VI, ed. H. Beuther, R. S. Klessen, C. P. Dullemond, & T. Henning, 451

Frank, A., Ray, T. P., Cabrit, S., et al. 2014b, in Protostars and Planets VI, ed. H. Beuther, R. S. Klessen, C. P. Dullemond, & T. Henning, 451–474

Frerking, M. A., Langer, W. D., & Wilson, R. W. 1982, ApJ, 262, 590

Friberg, P., Bastien, P., Berry, D., et al. 2016, in Society of Photo-Optical Instrumentation Engineers (SPIE) Conference Series, Vol. 9914, Millimeter, Submillimeter, and Far-Infrared Detectors and Instrumentation for Astronomy VIII, ed. W. S. Holland & J. Zmuidzinas, 991403

Fukui, Y., Iwata, T., Mizuno, A., Bally, J., & Lane, A. P. 1993, in Protostars and Planets III, ed. E. H. Levy & J. I. Lunine, 603

Furuya, R. S., Kitamura, Y., Wootten, A., Claussen, M. J., & Kawabe, R. 2003, ApJS, 144, 71

Galitzki, N., Ade, P. A. R., Angilè, F. E., et al. 2014, in Society of Photo-Optical Instrumentation Engineers (SPIE) Conference Series, Vol. 9145, Ground-based and Airborne Telescopes V, ed. L. M. Stepp, R. Gilmozzi, & H. J. Hall, 91450R

Garcia Lopez, R., Nisini, B., Eislöffel, J., et al. 2010, A&A, 511, A5

Giannini, T., Massi, F., Podio, L., et al. 2005, A&A, 433, 941

Goicoechea, J. R., Cernicharo, J., Karska, A., et al. 2012, A&A, 548, A77

Goldreich, P. & Kylafis, N. D. 1981, ApJ, 243, L75

Goldsmith, P. F. & Langer, W. D. 1978, ApJ, 222, 881

Goldsmith, P. F. & Langer, W. D. 1999, ApJ, 517, 209

Graczyk, D., Pietrzyński, G., Thompson, I. B., et al. 2014, ApJ, 780, 59

Green, J. D., Evans, Neal J., I., Jørgensen, J. K., et al. 2013, ApJ, 770, 123
Green, J. D., Yang, Y.-L., Evans, Neal J., I., et al. 2016, AJ, 151, 75
Griffin, M. J., Abergel, A., Abreu, A., et al. 2010, A&A, 518, L3
Guerra, J. A., Chuss, D. T., Dowell, C. D., et al. 2021, ApJ, 908, 98
Guevara, C., Stutzki, J., Ossenkopf-Okada, V., et al. 2020, A&A, 636, A16
Gullbring, E., Hartmann, L., Briceño, C., & Calvet, N. 1998, ApJ, 492, 323
Güsten, R., Nyman, L. Å., Schilke, P., et al. 2006, A&A, 454, L13
Gyulbudaghian, A. L. 2012, Astrophysics, 55, 92
Habing, H. J. 1968, Bull. Astron. Inst. Netherlands, 19, 421
Hachisuka, K., Brunthaler, A., Menten, K. M., et al. 2006, ApJ, 645, 337
Hall, J. S. 1949, Science, 109, 166
Hamaguchi, K., Corcoran, M. F., & Imanishi, K. 2003, PASJ, 55, 981
Harju, J., Lehtinen, K., Booth, R. S., & Zinchenko, I. 1998, A&AS, 132, 211
Harper, D. A., Runyan, M. C., Dowell, C. D., et al. 2018, Journal of Astronomical Instrumentation, 7, 1840008
Hartmann, L. 1998, Accretion Processes in Star Formation
Hatchell, J. & van der Tak, F. F. S. 2003, A&A, 409, 589
He, J. H., Takahashi, S., & Chen, X. 2012, ApJS, 202, 1
Hennebelle, P. & Falgarone, E. 2012, A&A Rev., 20, 55
Hennebelle, P. & Inutsuka, S.-i. 2019, Frontiers in Astronomy and Space Sciences, 6
Henney, W. J., Arthur, S. J., de Colle, F., & Mellema, G. 2009, MNRAS, 398, 157
Herbst, W. & Assousa, G. E. 1977, ApJ, 217, 473
Herczeg, G. J., Karska, A., Bruderer, S., et al. 2012, A&A, 540, A84
Heyer, M. & Dame, T. M. 2015, ARA&A, 53, 583
Hildebrand, R. 1989, in Interstellar Dust, ed. L. J. Allamandola & A. G. G. M. Tielens, Vol. 135, 275
Hildebrand, R. H., Kirby, L., Dotson, J. L., Houde, M., & Vaillancourt, J. E. 2009, ApJ, 696, 567
Hiltner, W. A. 1949, Nature, 163, 283
Hinkle, K., Wallace, L., & Livingston, W. 1995, PASP, 107, 1042
Hoang, T. D., Ngoc, N. B., Diep, P. N., et al. 2022, ApJ, 929, 27
Hollenbach, D. & McKee, C. F. 1989, ApJ, 342, 306
Hollenbach, D. J. & Tielens, A. G. G. M. 1997, ARA&A, 35, 179
Houde, M., Rao, R., Vaillancourt, J. E., & Hildebrand, R. H. 2011, ApJ, 733, 109
Hwang, J., Kim, J., Pattle, K., et al. 2021, ApJ, 913, 85
Hwang, J., Pattle, K., Parsons, H., Go, M., & Kim, J. 2023, AJ, 165, 198
Immer, K., Reid, M. J., Menten, K. M., Brunthaler, A., & Dame, T. M. 2013, A&A, 553, A117
Iserlohe, C., Fischer, C., Vacca, W. D., et al. 2021, PASP, 133, 055002
Itrich, D., Karska, A., Sewiło, M., et al. 2023, arXiv e-prints, arXiv:2306.05502
Jakob, H., Kramer, C., Simon, R., et al. 2007, A&A, 461, 999
Jeans, J. H. 1928, Astronomy and cosmogony
Jiménez-Donaire, M. J., Meeus, G., Karska, A., et al. 2017, A&A, 605, A62
Johnstone, D., Fich, M., McCoey, C., et al. 2010, A&A, 521, L41
Kalari, V. M. & Vink, J. S. 2015, ApJ, 800, 113

Kandori, R., Kusakabe, N., Tamura, M., et al. 2006, in Society of Photo-Optical Instrumentation Engineers (SPIE) Conference Series, Vol. 6269, Society of Photo-Optical Instrumentation Engineers (SPIE) Conference Series, ed. I. S. McLean & M. Iye, 626951
Karska, A., Herczeg, G. J., van Dishoeck, E. F., et al. 2013, A&A, 552, A141
Karska, A., Herpin, F., Bruderer, S., et al. 2014a, A&A, 562, A45
Karska, A., Kaufman, M. J., Kristensen, L. E., et al. 2018, ApJS, 235, 30
Karska, A., Koprowski, M., Solarz, A., et al. 2022, A&A, 663, A133
Karska, A., Kristensen, L. E., van Dishoeck, E. F., et al. 2014b, A&A, 572, A9
Kauffmann, J., Bertoldi, F., Bourke, T. L., Evans, N. J., I., & Lee, C. W. 2008, A&A, 487, 993
Kaufman, M. J. & Neufeld, D. A. 1996, ApJ, 456, 611
Kaufman, M. J., Wolfire, M. G., & Hollenbach, D. J. 2006, ApJ, 644, 283
Kennicutt, R. C. & Evans, N. J. 2012, ARA&A, 50, 531
Klein, R., Beckmann, S., Bryant, A., et al. 2014, in Society of Photo-Optical Instrumentation Engineers (SPIE) Conference Series, Vol. 9147, Ground-based and Airborne Instrumentation for Astronomy V, ed. S. K. Ramsay, I. S. McLean, & H. Takami, 91472X
Klessen, R. S. & Glover, S. C. O. 2016, in Saas-Fee Advanced Course, Vol. 43, Saas-Fee Advanced Course, ed. Y. Revaz, P. Jablonka, R. Teyssier, & L. Mayer, 85
Koch, E. W. & Rosolowsky, E. W. 2015, MNRAS, 452, 3435
Kristensen, L. E., Gusdorf, A., Mottram, J. C., et al. 2017a, A&A, 601, L4
Kristensen, L. E., van Dishoeck, E. F., Bergin, E. A., et al. 2012, A&A, 542, A8
Kristensen, L. E., van Dishoeck, E. F., Mottram, J. C., et al. 2017b, A&A, 605, A93
Krumholz, M. R., Bate, M. R., Arce, H. G., et al. 2014, in Protostars and Planets VI, ed. H. Beuther, R. S. Klessen, C. P. Dullemond, & T. Henning, 243–266
Kuchar, T. A. & Bania, T. M. 1994, ApJ, 436, 117
Kudritzki, R. P. 2002, ApJ, 577, 389
Kwan, J., Edwards, S., & Fischer, W. 2007, ApJ, 657, 897
Kwon, J., Doi, Y., Tamura, M., et al. 2018, ApJ, 859, 4
Kwon, J., Tamura, M., Hough, J. H., et al. 2015, ApJS, 220, 17
Kwon, W., Pattle, K., Sadavoy, S., et al. 2022, ApJ, 926, 163
Lada, C. J. 1999, in NATO Advanced Study Institute (ASI) Series C, Vol. 540, The Origin of Stars and Planetary Systems, ed. C. J. Lada & N. D. Kylafis, 143
Lada, C. J. & Lada, E. A. 2003, ARA&A, 41, 57
Lada, C. J. & Wilking, B. A. 1984, ApJ, 287, 610
Ladd, E. F., Deane, J. R., Sanders, D. B., & Wynn-Williams, C. G. 1993, ApJ, 419, 186
Ladeyschikov, D. A., Gong, Y., Sobolev, A. M., et al. 2022, ApJS, 261, 14
Ladjelate, B., André, P., Könyves, V., et al. 2020, A&A, 638, A74
Lamarre, J. M., Puget, J. L., Ade, P. A. R., et al. 2010, A&A, 520, A9
Larson, R. B. 1969, MNRAS, 145, 271
Larson, R. B. 1981, MNRAS, 194, 809
Lazarian, A. 2007, J. Quant. Spectr. Rad. Transf., 106, 225
Lazarian, A. & Hoang, T. 2007, MNRAS, 378, 910
Lazarian, A. & Vishniac, E. T. 1999, ApJ, 517, 700
Lazarian, A., Yuen, K. H., & Pogosyan, D. 2022, ApJ, 935, 77
Lee, D., Berthoud, M., Chen, C.-Y., et al. 2021, ApJ, 918, 39

Leurini, S., Wyrowski, F., Wiesemeyer, H., et al. 2015, A&A, 584, A70

Lew, B. 2018, Experimental Astronomy, 45, 81

Lin, Z., Sun, Y., Xu, Y., Yang, J., & Li, Y. 2021, ApJS, 252, 20

Liseau, R., Justtanont, K., & Tielens, A. G. G. M. 2006, A&A, 446, 561

Liseau, R., Larsson, B., Lunttila, T., et al. 2015, A&A, 578, A131

Liseau, R., Lorenzetti, D., Nisini, B., Spinoglio, L., & Moneti, A. 1992, A&A, 265, 577

Litvak, M. M. 1969, Science, 165, 855

Liu, J., Zhang, Q., & Qiu, K. 2022, Frontiers in Astronomy and Space Sciences, 9, 943556

Lombardi, M., Alves, J., & Lada, C. J. 2011, A&A, 535, A16

Lopez-Rodriguez, E., Beck, R., Clark, S. E., et al. 2021, ApJ, 923, 150

Lopez-Rodriguez, E., Mao, S. A., Beck, R., et al. 2022, ApJ, 936, 92

Loren, R. B., Wootten, A., & Wilking, B. A. 1990, ApJ, 365, 269

Mackey, J. & Lim, A. J. 2011, MNRAS, 412, 2079

Manara, C. F., Frasca, A., Alcalá, J. M., et al. 2017, A&A, 605, A86

Manara, C. F., Testi, L., Rigliaco, E., et al. 2013, A&A, 551, A107

Manoj, P., Watson, D. M., Neufeld, D. A., et al. 2013, ApJ, 763, 83

Marsh, K. A., Whitworth, A. P., Lomax, O., et al. 2017, MNRAS, 471, 2730

Matuszak, M., Karska, A., Kristensen, L. E., et al. 2015, A&A, 578, A20

Maury, A., Hennebelle, P., & Girart, J. M. 2022, Frontiers in Astronomy and Space Sciences, 9, 949223

McKee, C. F. & Ostriker, E. C. 2007, ARA&A, 45, 565

Melnick, G. J. & Kaufman, M. J. 2015, ApJ, 806, 227

Menten, K. M., Reid, M. J., Pratap, P., Moran, J. M., & Wilson, T. L. 1992, ApJ, 401, L39

Mestel, L. 1966, MNRAS, 133, 265

Minier, V., André, P., Bergman, P., et al. 2009, A&A, 501, L1

Mirocha, A., Karska, A., Gronowski, M., et al. 2021, A&A, 656, A146

Molinari, S., Swinyard, B., Bally, J., et al. 2010a, A&A, 518, L100

Molinari, S., Swinyard, B., Bally, J., et al. 2010b, PASP, 122, 314

Mookerjea, B., Sandell, G., Vacca, W., Chambers, E., & Güsten, R. 2018, A&A, 616, A31

Mookerjea, B., Sandell, G., Veena, V. S., et al. 2021, A&A, 648, A40

Moscadelli, L., Reid, M. J., Menten, K. M., et al. 2009, ApJ, 693, 406

Motogi, K., Sorai, K., Habe, A., et al. 2011, PASJ, 63, 31

Motte, F., Andre, P., & Neri, R. 1998, A&A, 336, 150

Mottram, J. C., van Dishoeck, E. F., Kristensen, L. E., et al. 2017, A&A, 600, A99

Mouschovias, T. 2001, in Astronomical Society of the Pacific Conference Series, Vol. 248, Magnetic Fields Across the Hertzsprung-Russell Diagram, ed. G. Mathys, S. K. Solanki, & D. T. Wickramasinghe, 515

Mouschovias, T. C. & Ciolek, G. E. 1999, in NATO Advanced Study Institute (ASI) Series C, Vol. 540, The Origin of Stars and Planetary Systems, ed. C. J. Lada & N. D. Kylafis, 305

Mouschovias, T. C., Tassis, K., & Kunz, M. W. 2006, ApJ, 646, 1043

Muzerolle, J., Hartmann, L., & Calvet, N. 1998, ApJ, 116, 2965

Muzerolle, J., Hillenbrand, L., Calvet, N., Briceño, C., & Hartmann, L. 2003, ApJ, 592, 266

Nakano, M., Yoshida, S., & Kogure, T. 1984, PASJ, 36, 517
Nakano, T. & Nakamura, T. 1978, PASJ, 30, 671
Navarete, F., Damineli, A., Barbosa, C. L., & Blum, R. D. 2015, MNRAS, 450, 4364
Neckel, T. 1978, A&A, 69, 51
Nisini, B., Codella, C., Giannini, T., et al. 2007, A&A, 462, 163
Nisini, B., Santangelo, G., Antoniucci, S., et al. 2013, A&A, 549, A16
Nisini, B., Santangelo, G., Giannini, T., et al. 2015, ApJ, 801, 121
Oliveira, J. M., van Loon, J. T., Sewiło, M., et al. 2019, MNRAS, 490, 3909
Olmi, L., Cunningham, M., Elia, D., & Jones, P. 2016, A&A, 594, A58
Oort, J. H. 1954, Bull. Astron. Inst. Netherlands, 12, 177
Ortiz-León, G. N., Loinard, L., Kounkel, M. A., et al. 2017, ApJ, 834, 141
Ossenkopf, V., Röllig, M., Simon, R., et al. 2010, A&A, 518, L79
Ostriker, E. C., Stone, J. M., & Gammie, C. F. 2001, ApJ, 546, 980
Pabst, C., Higgins, R., Goicoechea, J. R., et al. 2019, Nature, 565, 618
Pabst, C. H. M., Goicoechea, J. R., Teyssier, D., et al. 2020, A&A, 639, A2
Pattle, K. & Fissel, L. 2019, Frontiers in Astronomy and Space Sciences, 6, 15
Pattle, K., Fissel, L., Tahani, M., Liu, T., & Ntormousi, E. 2022a, arXiv e-prints, arXiv:2203.11179
Pattle, K., Lai, S.-P., Di Francesco, J., et al. 2021, ApJ, 907, 88
Pattle, K., Lai, S.-P., Sadavoy, S., et al. 2022b, MNRAS, 515, 1026
Pattle, K., Ward-Thompson, D., Berry, D., et al. 2017, ApJ, 846, 122
Pattle, K., Ward-Thompson, D., Hasegawa, T., et al. 2018, ApJ, 860, L6
Pattle, K., Ward-Thompson, D., Kirk, J. M., et al. 2015, MNRAS, 450, 1094
Pickett, H. M., Poynter, R. L., Cohen, E. A., et al. 1998, J. Quant. Spectr. Rad. Transf., 60, 883
Pietrzyński, G., Graczyk, D., Gieren, W., et al. 2013, Nature, 495, 76
Pilbratt, G. L., Riedinger, J. R., Passvogel, T., et al. 2010, A&A, 518, L1
Pillai, T., Kauffmann, J., Wyrowski, F., et al. 2011, A&A, 530, A118
Pillai, T. G. S., Clemens, D. P., Reissl, S., et al. 2020, Nature Astronomy, 4, 1195
Planck Collaboration, Ade, P. A. R., Aghanim, N., et al. 2015, A&A, 576, A104
Planck Collaboration, Ade, P. A. R., Aghanim, N., et al. 2016, A&A, 586, A138
Plummer, H. C. 1911, MNRAS, 71, 460
Poglitsch, A., Waelkens, C., Geis, N., et al. 2010, A&A, 518, L2
Porter, J. M., Drew, J. E., & Lumsden, S. L. 1998, A&A, 332, 999
Pound, M. W. & Wolfire, M. G. 2011, PDRT: Photo Dissociation Region Toolbox
Primiani, R. A., Young, K. H., Young, A., et al. 2016, Journal of Astronomical Instrumentation, 5, 1641006
Purser, S. J. D., Lumsden, S. L., Hoare, M. G., & Kurtz, S. 2021, MNRAS, 504, 338
Ramirez, S. V., Depoy, D. L., Frogel, J. A., Sellgren, K., & Blum, R. D. 1997, AJ, 113, 1411
Rautela, B. S., Joshi, G. C., & Pandey, J. C. 2004, Bulletin of the Astronomical Society of India, 32, 159
Rayner, J. T., Cushing, M. C., & Vacca, W. D. 2009, ApJS, 185, 289
Rayner, J. T., Toomey, D. W., Onaka, P. M., et al. 2003, PASP, 115, 362
Reiter, M., Nayak, O., Meixner, M., & Jones, O. 2019, MNRAS, 483, 5211

Reynolds, R. J. & Ogden, P. M. 1978, ApJ, 224, 94

Rieke, G. H., Wright, G. S., Böker, T., et al. 2015, PASP, 127, 584

Risacher, C., Güsten, R., Stutzki, J., et al. 2018, Journal of Astronomical Instrumentation, 7, 1840014

Robitaille, T. P. 2017, A&A, 600, A11

Robitaille, T. P., Whitney, B. A., Indebetouw, R., & Wood, K. 2007, ApJS, 169, 328

Rodríguez-Kamenetzky, A., Carrasco-González, C., Araudo, A., et al. 2016, ApJ, 818, 27

Roman-Duval, J., Jackson, J. M., Heyer, M., Rathborne, J., & Simon, R. 2010, ApJ, 723, 492

Ruprecht, J. 1966, IAU Trans, 12B, 348

Russell, S. C. & Dopita, M. A. 1992, ApJ, 384, 508

Rygl, K. L. J., Brunthaler, A., Sanna, A., et al. 2012, A&A, 539, A79

Sadavoy, S. I., Stephens, I. W., Myers, P. C., et al. 2019, ApJS, 245, 2

Sandell, G. 2000, A&A, 358, 242

Sandell, G. & Sievers, A. 2004, ApJ, 600, 269

Santos, F. P., Chuss, D. T., Dowell, C. D., et al. 2019, ApJ, 882, 113

Schisano, E., Rygl, K. L. J., Molinari, S., et al. 2014, ApJ, 791, 27

Schöier, F. L., van der Tak, F. F. S., van Dishoeck, E. F., & Black, J. H. 2005, A&A, 432, 369

Sewiło, M., Whitney, B. A., Yung, B. H. K., et al. 2019, ApJS, 240, 26

Sharples, R., Bender, R., Agudo Berbel, A., et al. 2013, The Messenger, 151, 21

Sharpless, S. 1959, ApJS, 4, 257

Shevchenko, V. S. & Yakubov, S. D. 1989, Soviet Ast., 33, 370

Shu, F., Najita, J., Ostriker, E., et al. 1994, ApJ, 429, 781

Shu, F. H., Adams, F. C., & Lizano, S. 1987, ARA&A, 25, 23

Skalidis, R. & Tassis, K. 2021, A&A, 647, A186

Skrutskie, M. F., Cutri, R. M., Stiening, R., et al. 2006, AJ, 131, 1163

Soam, A., Maheswar, G., Lee, C. W., Neha, S., & Andersson, B. G. 2017, MNRAS, 465, 559

Soam, A., Maheswar, G., Lee, C. W., Neha, S., & Kim, K.-T. 2018, MNRAS, 476, 4782

Soares, J. B. & Bica, E. 2002, A&A, 388, 172

Soares, J. B. & Bica, E. 2003, A&A, 404, 217

Sodroski, T. J., Odegard, N., Arendt, R. G., et al. 1997, ApJ, 480, 173

Solomon, P. M., Rivolo, A. R., Barrett, J., & Yahil, A. 1987, ApJ, 319, 730

Stanke, T., McCaughrean, M. J., & Zinnecker, H. 2000, A&A, 355, 639

Storey, P. J. & Hummer, D. G. 1995, Monthly Notices of the Royal Astronomical Society, 272, 41

Szymczak, M., Hrynek, G., & Kus, A. J. 2000, A&AS, 143, 269

Szymczak, M., Olech, M., Wolak, P., Bartkiewicz, A., & Gawroński, M. 2016, MNRAS, 459, L56

Tahani, M., Bastien, P., Furuya, R. S., et al. 2023, ApJ, 944, 139

Tang, J., Bressan, A., Rosenfield, P., et al. 2014, MNRAS, 445, 4287

Tapia, M., Persi, P., Bohigas, J., & Ferrari-Toniolo, M. 1997, AJ, 113, 1769

Temi, P., Hoffman, D., Ennico, K., & Le, J. 2018, Journal of Astronomical Instrumentation, 7, 1840011

Testi, L., Birnstiel, T., Ricci, L., et al. 2014, in Protostars and Planets VI, ed. H. Beuther, R. S. Klessen, C. P. Dullemond, & T. Henning, 339–361
Tobin, J. J., Stutz, A. M., Manoj, P., et al. 2016, ApJ, 831, 36
Tram, L. N., Bonne, L., Hu, Y., et al. 2023, ApJ, 946, 8
Tram, L. N. & Hoang, T. 2022, Frontiers in Astronomy and Space Sciences, 9, 923927
Troland, T. H., Crutcher, R. M., Goodman, A. A., et al. 1996, ApJ, 471, 302
Tychoniec, Ł., Tobin, J. J., Karska, A., et al. 2018a, ApJS, 238, 19
Tychoniec, Ł., Tobin, J. J., Karska, A., et al. 2018b, ApJ, 852, 18
Uchida, Y. & Shibata, K. 1985, PASJ, 37, 515
Urquhart, J. S., Figura, C., Cross, J. R., et al. 2021, MNRAS, 500, 3050
Urquhart, J. S., Hoare, M. G., Lumsden, S. L., et al. 2012, MNRAS, 420, 1656
Urquhart, J. S., Morgan, L. K., Figura, C. C., et al. 2011, MNRAS, 418, 1689
Vacca, W., Clarke, M., Perera, D., Fadda, D., & Holt, J. 2020, in Astronomical Society of the Pacific Conference Series, Vol. 527, Astronomical Data Analysis Software and Systems XXIX, ed. R. Pizzo, E. R. Deul, J. D. Mol, J. de Plaa, & H. Verkouter, 547
Vacca, W. D., Cushing, M. C., & Rayner, J. T. 2003, PASP, 115, 389
Valdettaro, R., Palla, F., Brand, J., et al. 2001, A&A, 368, 845
van der Tak, F. F. S. 2012, Philosophical Transactions of the Royal Society of London Series A, 370, 5186
van der Tak, F. F. S., van Dishoeck, E. F., Evans, Neal J., I., Bakker, E. J., & Blake, G. A. 1999, ApJ, 522, 991
van Dishoeck, E. F., Kristensen, L. E., Benz, A. O., et al. 2011, PASP, 123, 138
van Dishoeck, E. F., Kristensen, L. E., & the WISH team. 2021, arXiv e-prints, arXiv:2102.02225
Visser, R., Kristensen, L. E., Bruderer, S., et al. 2012, A&A, 537, A55
Ward, J. L., Oliveira, J. M., van Loon, J. T., & Sewiło, M. 2015, MNRAS, 455, 2345
Ward, J. L., Oliveira, J. M., van Loon, J. T., & Sewiło, M. 2016, MNRAS, 464, 1512
Ward-Thompson, D., Karoly, J., Pattle, K., et al. 2023, ApJ, 946, 62
Ward-Thompson, D., Pattle, K., Bastien, P., et al. 2017, ApJ, 842, 66
White, G. J., Abergel, A., Spencer, L., et al. 2010, A&A, 518, L114
White, G. J., Drabek-Maunder, E., Rosolowsky, E., et al. 2015, MNRAS, 447, 1996
Wiesenfeld, L. & Goldsmith, P. F. 2014, ApJ, 780, 183
Wilking, B. A., Gagné, M., & Allen, L. E. 2008, in Handbook of Star Forming Regions, Volume II, ed. B. Reipurth, Vol. 5, 351
Wilson, B. A., Dame, T. M., Masheder, M. R. W., & Thaddeus, P. 2005, A&A, 430, 523
Wood, D. O. S. & Churchwell, E. 1989, ApJ, 340, 265
Wouterloot, J. G. A. & Brand, J. 1989, A&AS, 80, 149
Wright, G. S., Wright, D., Goodson, G. B., et al. 2015, PASP, 127, 595
Xu, Y., Reid, M. J., Menten, K. M., et al. 2009, ApJ, 693, 413
Yang, Y.-L., Evans, N. J., Karska, A., et al. 2022a, ApJ, 925, 93
Yang, Y.-L., Green, J. D., Evans, Neal J., I., et al. 2018, ApJ, 860, 174
Yang, Y.-L., Green, J. D., Pontoppidan, K. M., et al. 2022b, ApJ, 941, L13
Zinnecker, H. & Yorke, H. W. 2007, ARA&A, 45, 481
Zucker, C. & Chen, H. H.-H. 2018, ApJ, 864, 152

Publications

Publications in refereed journals

6. **Far-infrared line emission from the outer Galaxy cluster Gy 3-7 with SOFIA/FIFI-LS: Physical conditions and UV fields**

   Ngân Lê, Agata Karska, Miguel Figueira, Marta Sewiło, Agnieszka Mirocha, Christian Fischer, Maja Kaźmierczak-Barthel, Randolf Klein, Marcin Gawroński, Maciej Koprowski, Klaudia Kowalczyk, William J. Fischer, Karl M. Menten, Friedrich Wyrowski, Carsten König, and Lars E. Kristensen, 2023, A&A, 674, A64

   DOI: 10.1051/0004-6361/202346141 [arXiv:2304.08127]

5. **B-fields And dust in interstelLar fiLAments using Dust POLarization (BALLAD-POL): I. The massive filament G11.11-0.12 observed by SOFIA/HAWC+**

   Nguyen Bich Ngoc, Pham Ngoc Diep, Thiem Hoang, Le Ngoc Tram, Nguyen Chau Giang, Ngân Lê, Thuong Duc Hoang, Nguyen Thi Phuong, Nguyen Minh Khang, Dieu D. Nguyen, and Gia Bao Truong Le, 2023, ApJ, in press

   DOI: 10.48550/arXiv.2302.10543 [arXiv:2302.10543]

4. **Investigating the Impact of Metallicity on Star Formation in the Outer Galaxy. I. VLT/KMOS Survey of Young Stellar Objects in Canis Major** Dominika Itrich, Agata Karska, Marta Sewiło, Lars E. Kristensen, Gregory J. Herczeg, Suzanne Ramsay, William J. Fischer, Benoît Tabone, Will R. M. Rocha, Maciej Koprowski, Ngân Lê, and Beata Deka-Szymankiewicz, 2023, ApJS, in press

   DOI: 10.48550/arXiv.2306.05502 [arXiv:2306.05502]

3. **Studying Magnetic Fields and Dust in M17 Using Polarized Thermal Dust Emission Observed by SOFIA/HAWC+**

   Thuong Duc Hoang, Nguyen Bich Ngoc, Pham Ngoc Diep, Le Ngoc Tram, Thiem Hoang, Kate Pattle, Wanggi Lim, Ngan Le, Dieu D. Nguyen, Nguyen Thi Phuong, Nguyen Fuda, Tuan Van Bui, Kate Pattle, Gia Bao Truong Le, Hien Phan, and Nguyen Chau Giang,, 2022, ApJ, 929, 27

   DOI: 10.3847/1538-4357/ac5abf [arXiv:2108.10045]

2. **Physical Model of Dust Polarization by Radiative Torque Alignment and Disruption and Implications for Grain Internal Structures**

Hyeseung Lee, Thiem Hoang, Ngan Le, and Jungyeon Cho, 2020, ApJ, 896, 44

DOI: 10.3847/1538-4357/ab8e33 [arXiv:1911.00654]

1. **The MBHBM⋆ Project. I. Measurement of the Central Black Hole Mass in Spiral Galaxy NGC 3504 Using Molecular Gas Kinematics**

   Dieu D. Nguyen, Mark den Brok, Anil C. Seth, Timothy A. Davis, Jenny E. Greene, Michelle Cappellari, Joseph B. Jensen, Sabine Thater, Satoru Iguchi, Masatoshi Imanishi, Takuma Izumi, Kristina Nyland, Nadine Neumayer, Kouichiro Nakanishi, Phuong M. Nguyen, Takafumi Tsukui, Martin Bureau, Kyoko Onishi, Quang L. Nguyen, and Ngan M. Le, 2020, ApJ, 892, 68

   DOI: 10.3847/1538-4357/ab77aa [arXiv:1902.03813]

Publications in preparation

2. **Mapping and characterizing magnetic field in the Ophiuchus A molecular cloud with SOFIA/HAWC+**

   Ngân Lê, Le Ngoc Tram, Agata Karska, Thiem Hoang, Pham Ngoc Diep, Nguyen Bich Ngoc, Karl. M. Menten, Nguyen Thi Phuong, Dieu D. Nguyen, Thuong Duc Hoang, and Friedrich Wyrowski, to be submitted to A&A

1. **Near-Infrared Spectroscopy of Young Stellar Objects in the CMa-ℓ224 Star-Forming Region. II. Spectral Types, Extinction, and Mass Accretion**

   Ngân Lê, Agata Karska, Mariusz Tarnopolski, Dominika Itrich, William J. Fischer, Maciej Koprowski, Marta Sewilo, Lars E. Lars Kristensen, Will R. M. Rocha, and Beata Deka-Szymankiewicz, to be submitted to A&A

Non-refereed publications

1. **SOFIA/FIFI-LS spectroscopy of Gy 3-7 cluster in the Outer Galaxy**
   Ngân Lê, Agata Karska, Christian Fischer, Christian Fischer, MajaKaźmierczak-Barthel, Agnieszka Mirocha, Randolf Klein, Marta Sewiło, Lars E. Kristensen, and William J. Fischer, 2022, in XL Polish Astronomical Society Meeting, Vol. 12, 195–198

   [2022pas..conf..195L]

Acknowledgment

My PhD studies nearly come to an end. All Chapters of this manuscript are done and it is time for me to express the spectrum of my feelings and to acknowledge everyone who has helped and accompanied me during the past four years.

I will start with Professor Michał Hanasz, who kindly agreed to become my official supervisor so that I could move to Toruń and start my journey with Agata and other colleagues from the Molecular Astrophysics LAB (MA–LAB).Thank you, Michał, for your invaluable support whenever I needed your help with my Ph.D. study and with the bureaucracy during these years. I am also grateful for your careful reading of the manuscript and providing comments which improved this manuscript.

A super big thanks to Agata Karska, who offered this great thesis topic, got the fancy funding altogether, and laid her trust in me to carry out the projects presented in this thesis. You would never know how lucky I felt when I received your email about the interview on a cold day in November 2018 and later got the invitation to continue my study path in Toruń! Many thanks for your patience, guidance, teaching me everything from basics, and for bringing me to the fantastic international working environment.Even though there were difficult moments and high demands for the Ph.D. projects, I felt really grateful since you often asked me before our meetings started e.g., *“Did you spend any time to sleep last night?"*, or you encouraged me to take a long sleep after some of our big deadlines. I was truly touched because of these small things. Finally, many thanks for helping me to put everything together in this manuscript!

I would also like to express my big thanks to Tram Le Ngoc, who was my main mentor for the nice project about the role of magnetic fields in molecular clouds. I am grateful for introducing me to the VARNET group where I could connect and work with excellent Vietnamese researchers and students working around the world, from Vietnam (Diep, Ngoc) to South Korea (Thiem, Giang, Bao, Phuong), Japan (Thuong), France (Dieu), Germany (Tram), and the UK (Khang)!I thank you for your kind support both in science and social life, and fests of Vietnamese cuisine every time I visited Bonn. I also appreciate your advice concerning the thesis manuscript.

During the past years, I had many possibilities to collaborate with people from different awesome places: Toruń (Maciej, Dominika, Marcin, Klaudia, and Mariusz), Krakow (Aga), Warsaw (Miguel), Bonn (Carsten, Karl, and Tram), Stuttgart (André, Maja), Copenhagen (Lars), and even California (Christian and Randolf) and Maryland (Marta and Will)! Thank you for all your support!

I would like to also thank the staff at the administration of the Faculty of Physics, Astronomy and Informatics – especially Dominika, Dorota, Monika K., Monika Cz., and Asia – for helping me with procedures and paperwork.

I appreciate all my colleagues from the lab and friends in Toruń, who has been next to me when I needed them most. I might forget some of you as I am in a rush (as usual), so please forgive me! I thank Michał, Kasia, Dominika, Konrad, and Krzysiek from MA–LAB for helping me to settle down in Toruń already a long time ago. I especially thank Helena for sharing the office with me and reminding me about the food and breaks. There is now plenty of snacks in the office but I still need someone to play this sort of funny games with me again! I am also super grateful to be a member of the " ... *Gang*". I especially thank Nicolas for bringing me to the group and giving me advice whenever I needed it!I thank all of you guys for being friends, sharing life problems, and taking care of each other.I really appreciate the friendships that we all have made during these years. I thank you for our meetings which often came with plenty of food – from France (Quentin – thanks for the quiche, tartiflette, and your weird whisky sour), Italia (Matteo - admittedly, your tiramisu is pretty good though I keep complaining it is too sweet), India (your grilled Tandori chicken is pretty awesome, Ayush!). I thank Marius and Ele for listening to my dummy problems and helping me out in opening my mindset, less overthinking, and giving ideas for solve my problems! And I would never forget my bestie Tilak who always harmonizes with me in any joke! I wish all the best to you guys for your study and future! Special thanks also to Ashish for being my good friend at the Institute of Physics. We both got to the end of our PhDs and I wish you all the best for your future.

Last but not least, I would like to thank my mother, brothers, and sister who understand me best and who let me continue my long journey of study! Thanks so much for always supporting me from a very long distance. I appreciate it!